AD-A079 400 PENNSYLVANIA STATE UNIV UNIVERSITY PARK MATERIALS RE--ETC F/G 9/1
TARGETED BASIC STUDIES OF FERROELECTRIC AND FERROELASTIC MATERI--ETC(U)
DEC 79 L E CROSS , R E NEWNHAM , G R BARSCH N00014-78-C-0291

UNCLASSIFIED NL

1 OF 4
AD A 079400

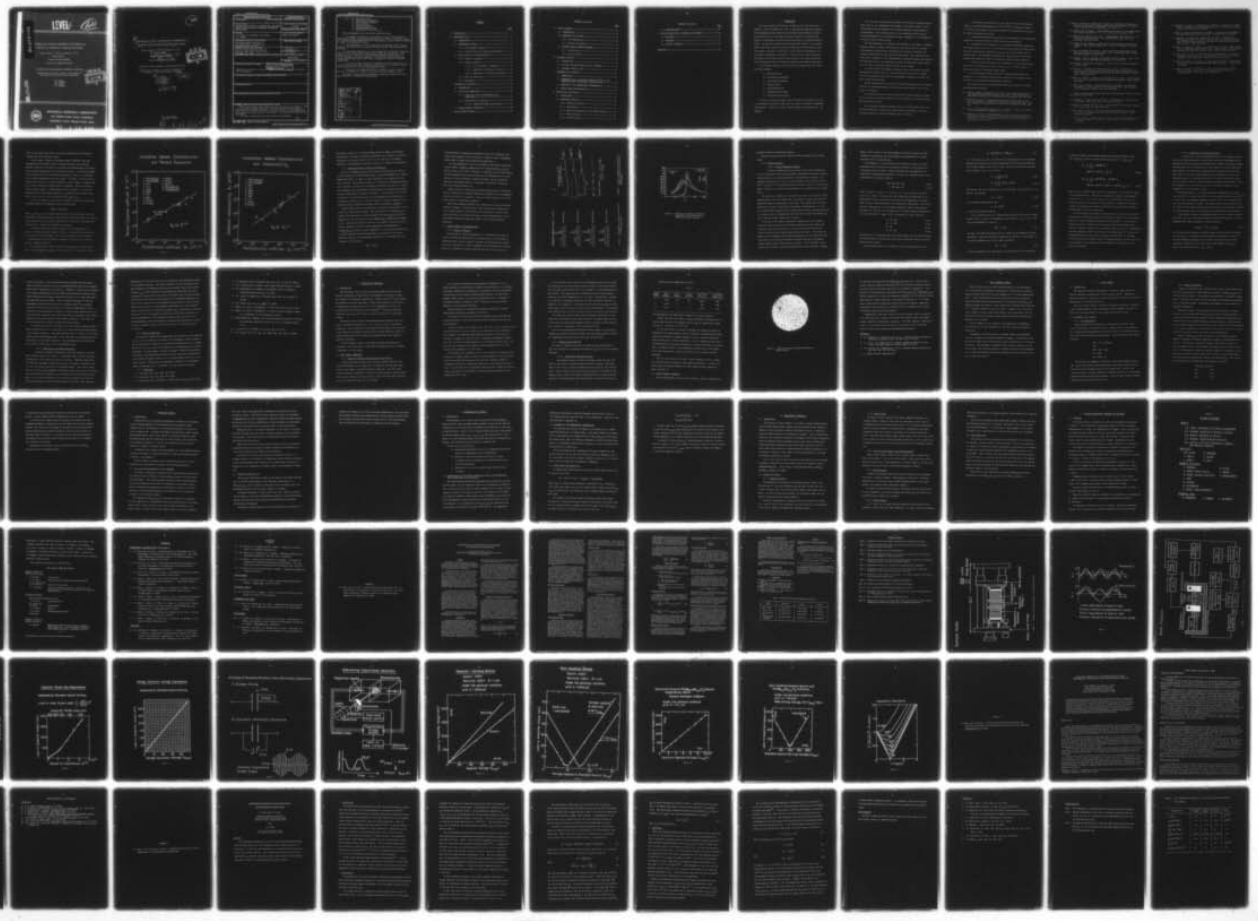

TARGETED BASIC STUDIES OF FERROELECTRIC AND FERROELASTIC MATERIALS FOR PIEZOELECTRIC TRANSDUCER APPLICATIONS

Period January 1, 1979 to December 31, 1979

Annual Report

OFFICE OF NAVAL RESEARCH

Contract No. N00014-78-C-0291

L.E. Cross
R.E. Newnham
G.R. Barsch
J.V. Biggers

MATERIALS RESEARCH LABORATORY
THE PENNSYLVANIA STATE UNIVERSITY
UNIVERSITY PARK, PENNSYLVANIA 16802

(12)

(6) TARGETED BASIC STUDIES OF FERROELECTRIC AND FERROELASTIC MATERIALS FOR PIEZOELECTRIC TRANSDUCER APPLICATIONS.

Period January 1, 1979 to December 31, 1979

(9) Annual Report, 1 Jan — 31 Dec 79

OFFICE OF NAVAL RESEARCH

(15) Contract No. N00014-78-C-0291

(10) L.E. Cross,
R.E. Newnham,
G.R. Barsch
J.V. Biggers

(12) 205

(11) Dec 79

220750

UNCLASSIFIED

SECURITY CLASSIFICATION OF THIS PAGE (When Data Entered)

REPORT DOCUMENTATION PAGE		READ INSTRUCTIONS BEFORE COMPLETING FORM
1. REPORT NUMBER	2. GOVT ACCESSION NO.	3. RECIPIENT'S CATALOG NUMBER
4. TITLE (and Subtitle) TARGETED BASIC STUDIES OF FERROELECTRIC AND FERROELASTIC MATERIALS FOR PIEZOELECTRIC TRANSDUCER APPLICATIONS		5. TYPE OF REPORT & PERIOD COVERED Annual Jan. 1, 1979 to Nov. 30, 1979 6. PERFORMING ORG. REPORT NUMBER
7. AUTHOR(s) L.E. Cross, R.E. Newnham, G.R. Barsch, J.V. Biggers		8. CONTRACT OR GRANT NUMBER(s) N00014-78-C-0291
9. PERFORMING ORGANIZATION NAME AND ADDRESS Materials Research Laboratory The Pennsylvania State University University Park, PA 16802		10. PROGRAM ELEMENT, PROJECT, TASK AREA & WORK UNIT NUMBERS
11. CONTROLLING OFFICE NAME AND ADDRESS Office of Naval Research, Room 619 Ballston Tower, 800 N. Quincy Street Arlington, CA 22217		12. REPORT DATE December 1979 13. NUMBER OF PAGES 283
14. MONITORING AGENCY NAME & ADDRESS (if different from Controlling Office)		15. SECURITY CLASS. (of this report) UNCLASSIFIED 15a. DECLASSIFICATION/DOWNGRADING SCHEDULE

16. DISTRIBUTION STATEMENT (of this Report)

This document has been approved for public release and sale; its distribution is unlimited.

Reproduction in whole or in part is permitted for any purpose of the United States Government.

17. DISTRIBUTION STATEMENT (of the abstract entered in Block 20, if different from Report)

18. SUPPLEMENTARY NOTES

19. KEY WORDS (Continue on reverse side if necessary and identify by block number)

20. ABSTRACT (Continue on reverse side if necessary and identify by block number)

This report details work carried out over the period from January 1, 1979 in the Materials Research Laboratory of The Pennsylvania State University under ONR contract N00014-78-C-0291. The work is part of a long-range (five-year) program of basic studies of ferroelectric and ferroelastic materials for transducers.

The work is organized under seven major topic headings:

DD FORM 1 JAN 73 1473 EDITION OF 1 NOV 65 IS OBSOLETE

SECURITY CLASSIFICATION OF THIS PAGE (When Data Entered)

A. Electrostriction
B. Piezoelectric Composites
C. Grain Oriented Ceramics
D. Crystal Growth
E. Processing Studies
F. Phenomenological Theory
G. Ferroelectric Bicrystals

Major achievements over the present period have been:

1. The design, construction, and testing of a new ultrasensitive AC dilatometer capable of resolving displacements of 10^{-3}Å over a frequency range of 4 to 200 Hz, which permits the direct measurement of electrostrictive strains in simple low permittivity solids.

2. The development of a more refined lattice dynamical theory for the origin of electrostriction in solids with alkali halide and with perovskite structure.

3. Excellent confirmation has been obtained for the original theoretical models for 3:1 connected PZT ceramic:plastic component transducers. With correct control of the scale of the macrostructure and volume fraction of PZT it has proven possible to generate a new hydrophone material with $g_h d_h$ product greater than 10,000 10^{-15} M^2/N as compared to $\sim$200 10^{-15} M^2/N for normal PZTs.

4. A new very simple fabrication technique has been developed for 3:3 plastic:PZT composites which permits the duplication of the property combinations available in the earlier replamineform ceramics.

5. The first clear indications that it might be possible to improve the d_{33} coefficient in a composite over that of either component phase.

The report contains nineteen appendices comprised of papers that have been published or submitted for publication.

CONTENTS

CONTENTS (Continued)

CONTENTS (Continued)

I. INTRODUCTION

This report details work that was carried out over the period from January 1, 1979, to November 30, 1979, in the Materials Research Laboratory of The Pennsylvania State University under ONR Contract N00014-78-C-0291. The work is part of a long range (five-year) program of "Targeted Basic Studies of Ferroelectric and Ferroelastic Materials for Transducer Applications." In the period covered by this second annual report of the program, many of the topics initially chosen for study have now been written up for publication. Reprints or preprints of these studies are presented in the 19 technical appendices to the report. The text of the report itself has been kept to a very brief narrative description of the current activities and of developing efforts in areas not covered in the technical appendices.

To facilitate reporting, the work has been organized under the following seven headings:

A. Electrostriction

B. Piezoelectric Composites

C. Grain Oriented Ceramics

D. Crystal Growth

E. Processing Studies

F. Phenomenological Theory

G. Ferroelectric Bicrystals

It should be stressed, however, that this mode of presentation is just for convenience and does not imply that the topics are separate, independent mini-projects. They are, in fact, closely coupled and interconnected. For example:

(a) The basic electrostriction studies will provide the reliable experimental data for the complementary development of the lattice theory of electrostriction, which is essential for a proper microscopic understanding of the phenomenon. Since electrostriction is the underlying elasto-electric coupling mechanism in all piezoelectric ceramic transducers, it is fundamental to the whole area of Navy interest.

(b) The development of a completely new approach to the design of composite materials based on a proper consideration of the crucial role of the phase interconnection (connectivity) has enabled the tailoring of important new property combinations from well known existing phases. Such composite structures will be essential if the technologically interesting relaxor ferroelectric electrostrictors are to be effectively utilized, and will have similar importance for other new materials being developed on the program.

(c) Crystal growth and ceramic processing studies are obviously essential underpinning activities vital for the fabrication of new types of composite and for the separation and study of the mechanisms of behavior in relaxor and other ceramic ferroelectrics.

(d) The phenomenological correlation draws continuously upon the continuing spectrum of property measurements and structural data generated in the other areas of the program.

(e) We believe that the bicrystal studies will provide essential information on the role of internal boundaries in the ceramics, both electrostrictive and piezoelectric systems.

The 19 technical appendices perhaps attest in a rather direct way to the productive advantage in having such coupled studies progressing in parallel. Outstanding among the current developments are, we believe:

1. The design and construction of a new type of precise AC dilatometer capable of resolving displacements $\sim 10^{-13}$ m (10^{-3} Å) in a frequency range of 4 to 200 Hz, which permits the direct measurement of electrostrictive strains in simple low-permittivity solids.

2. The excellent progress being made in the development of the theoretical framework of electrostriction in alkali halides and perovskites.

3. Confirmation of the behavior of 3:1 connected PZT:plastic composites. With proper control of the scale of the macrostructure versus the sample thickness, the piezoelectric responses (d_{33}, g_{33}, d_h, g_h) follow closely the theoretical model. For hydrophone-type materials, $d_h g_h$ products $\sim$10,000 appear possible and samples are stable to hydrostatic pressures beyond 2,000 psi.

4. The first clear indications that in composites of more complex macrostructure in the PZT:plastic systems d_{33} values can be achieved which are higher than those of the separate ceramic phase.

5. A new exceedingly simple fabrication technique which permits the formation of a 3:3 connected ceramic:plastic composite with properties close to those of the corresponding replamineform materials.

Over the past year the following papers have been presented at national and international meetings:

S.J. Jang, K. Uchino, S. Nomura and L.E. Cross. Electrostrictive Behavior of Lead Magnesium Niobate Based Ceramic Dielectrics. IEEE International Symposium on Applications of Ferroelectrics, Minneapolis, MN, June 1979.

K. Uchino and L.E. Cross. A Very High Sensitivity AC Dilatometer for the Direct Measurement of Piezoelectric and Electrostrictive Constants. IEEE Int. Symposium on Applications of Ferroelectrics, Minneapolis, MN, June 1979.

L.E. Cross. Phenomenological Theory for PZT. IEEE Int. Symposium on Applications of Ferroelectrics, Minneapolis, June 1979.

R.E. Newnham, D. Skinner, B. Hardiman and K. Klicker (Invited) Ferroelectric Ceramic:Plastic Composites of Controlled Macrostructure for Piezoelectric Applications. IEEE Int. Symposium on Applications of Ferroelectrics, Minneapolis, MN, June 1979.

L. Bowen, T. Shrout, W. Schulze and J. Biggers. Piezoelectric Properties of Internally Electroded PZT Multilayers. IEEE Int. Symposium on Applications of Ferroelectrics, Minneapolis, MN, June 1979.

D.A. Hankey and J.V. Biggers. Calcining-Reaction Kinetics of PZT Compositions. 81st Annual Meeting, Amer. Cer. Soc., Cincinnati, OH, April 1979.

H. McKinstry, A. Amin and L.E. Cross. A Thermodynamic Gibbs Function for the System of PZT Piezoceramics. 81st Annual Meeting, Amer. Cer. Soc., Cincinnati, OH, April 1979.

M.B. Holmes and R.E. Newnham. Preparation of Grain-Oriented Ferroelectric Ceramics. 81st Annual Meeting, Amer. Cer. Soc., Cincinnati, OH, April 1979.

A. Amin, R.E. Newnham and D.E. Cox. Neutron Diffraction Refinement of Low-Temperature Phase in the PZT System. Amer. Crystallogr. Assoc. Winter Meeting, Honolulu, HI, March 1979.

R.E. Newnham. Relaxor, Improper and Secondary Ferroic Crystals. Amer. Crystallogr. Assoc. Winter Meeting, Honolulu, HI, March 1979.

R.E. Newnham. Piezoelectric Composites. Amer. Chem. Soc. Meeting, Honolulu, HI, March 1979.

K. Takahashi, L.H. Hardy, R.E. Newnham and L.E. Cross. Pyroeffect in $Pb_5Ge_3O_{11}$ and $Pb_5Ge_2SiO_{11}$ Crystals Prepared by Glass Recrystallization. Second Meeting of Ferroelectric Materials and Their Applications (FMA 2), Kyoto, Japan, May 1979.

S. Nomura, K. Tonooka, J. Kuwata, R.E. Newnham and L.E. Cross. Second Meeting of Ferroelectric Materials and Their Applications (FMA 2), Kyoto, Japan, May 1979.

K. Uchino and L.E. Cross. A High-Sensitivity AC Dilatometer for the Direct Measurement of Piezoelectricity and Electrostriction. 33rd Frequency Control Symposium, Atlantic City, NJ, June 1979.

Papers listed below have been submitted for publication. The exact status is indicated in each case.

J.V. Biggers, T.A. Shrout and W.A. Schulze. Densification of PZT Cast Tape by Pressing. Bull. Amer. Ceram. Soc. 58, 516 (1979).

M. Holmes, R.E. Newnham and L.E. Cross. Grain Oriented Ferroelectric Ceramics. Bull. Amer. Ceram. Soc. 58, 872 (1979).

K. Uchino and L.E. Cross. A Very Sensitive AC Dilatometer for the Direct Measurement of Piezoelectric and Electrostrictive Constants. Ferroelectrics (accepted).

S.J. Jang, K. Uchino, S. Nomura and L.E. Cross. Electrostrictive Behavior of Lead Magnesium Niobate Based Ceramic Dielectrics. Ferroelectrics (accepted).

R.E. Newnham, D. Skinner, B. Hardiman and K. Klicker. Ferroelectric Ceramic: Plastic Composites of Controlled Macrostructure for Piezoelectric Applications. Ferroelectrics (accepted).

L. Bowen, T. Shrout, W. Schulze and J. Biggers. Piezoelectric Properties of Internally Electroded PZT Multilayers. Ferroelectrics (accepted).

T. Takahashi, L.H. Hardy, R.E. Newnham and L.E. Cross. Pyroeffect in $Pb_5Ge_3O_{11}$ and $Pb_5Ge_2SiO_{11}$ Crystal Prepared by Glass Recrystallization. Proc. Second Meeting of Ferroelectric Materials and Their Applications (FMA 2), Kyoto, Japan (accepted).

S. Nomura, K. Tanooka, J. Kuwata, R.E. Newnham and L.E. Cross. Electrostriction in $Pb(Mg_{1/3}Nb_{2/3})O_3$ Ceramics. Proc. Second Meeting of Ferroelectric Materials and Their Applications (FMA 2), Kyoto, Japan (accepted).

K. Uchino and L.E. Cross. A High Sensitivity AC Dilatometer for Direct Measurement of Piezoelectricity and Electrostriction. Proc. 33rd Annual Frequency Control Symposium. Atlantic City, NJ, June 1979.

K. Uchino, S. Nomura, L.E. Cross, S.J. Jang and R.E. Newnham. Electrostriction Effects in Lead Magnesium Niobate Single Crystals. J. Appl. Phys. (accepted).

S. Nomura, J. Kuwata, K. Uchino, S.J. Jang, L.E. Cross and R.E. Newnham. *Electrostriction in the Solid Solution System* $Pb(Mg_{1/3}Nb_{2/3})O_3$: $Pb(Mg_{1/2}W_{1/2})O_3$. Phys. Stat. Sol. (submitted).

2. ELECTROSTRICTION

2.1 INTRODUCTION

To reiterate our original proposal, the primary objectives of the studies on electrostriction were

(a) To develop a dilatometric system capable of measuring the exceedingly small (10^{-8}) electrostrictive strains which can be induced in simple solids of low permittivity.

(b) To develop in parallel with the experimental program the lattice dynamical theory of electrostriction for alkali halides, perovskites, and other simple solids. For this study the new experimental data will provide a powerful check of the theoretical development.

(c) To extend the study of high permittivity perovskite dielectrics with relaxor:ferroelectric properties which have technologically interesting strain:field levels so as to contribute to the understanding of the basic cause of the diffuse phase transition and the associated important properties.

2.2 EXPERIMENTAL STUDIES

2.2.1 AC Dilatometer Studies

A major experimental effort is being devoted to the completion of the ultrasensitive AC dilatometer first described in last year's annual report. This work was reported at the 33rd Annual Frequency Control Symposium in Atlantic City in June 1979. A copy of this paper is attached as Appendix 1. A second, more concise, description of the present system together with calibration data and a new study of d_{33} in PVF2 was presented at the ISAF 79 in Minneapolis, also in June, and is included as Appendix 2. These initial polymer studies presented at ISAF 79 have now been extended and the nonlinearity in d_{33} correlated with the electrostriction. A paper describing

this work, which was carried out in cooperation with Dr. Charles Hicks of Naval Ocean Systems Command, San Diego, has been prepared as a paper for submission to the Journal of Applied Physics and is presented in this report as Appendix 3.

In very brief summary:

(a) An AC dilatometer has been constructed that is capable of resolving displacements of 10^{-13} m (10^{-3} Å).

(b) A capacitance calibrator has been built and used to check d_{11} for quartz, giving values within 1% of accepted value.

(c) Comparative measurements have been made between quartz, wurtzite, and berlinite to establish both direct and relative measurement methods.

(d) Electrostriction has been measured in $Pb_3MgNb_2O_9$ ceramic and is close to the value determined from LVDT studies on the same material.

(e) Direct measurements have been made of d_{33} and the nonlinearity in d_{33} for several types of polyvinylidene, and related to the electrostriction in this material.

Having established unequivocally the principle of the AC dilatometric method and demonstrated its capability with known piezoelectrics, electrostrictors and polymers, we are now moving to measurements on alkali halides and other low-permittivity electrostrictors. In this work, new problems have arisen which appear to be associated with the effects of the Maxwell stresses and electrostrictive deformations of the holder structure under the very high voltages now required for these measurements.

The initial design of dilatometer used supported the high-potential electrode of the electrostrictor under study on a thick lucite (PMMA) plate. High, obviously spurious, values of the apparent Q coefficients were then traced to the fact that PMMA has electrostriction Q constants more than an

order of magnitude larger than in the alkali halides and field related M constant more than two orders larger.

In the course of seeking an alternate support insulator, data were assembled from all possible sources regarding Q_h values in insulators. Reliable values for this number are available from measurements of the hydrostatic pressure dependence of the dielectric stiffness. A correlation between the electrostriction and other measured properties likely to be controlled by the lattice anharmonicity was then sought. In Figure 1, the log of Q_h is plotted versus the log of thermal expansion α, and in Figure 2 a similar plot of Q_h versus isothermal compressibility is presented. While the relations are not exactly linear, a marked general trend is evident, i.e. soft high-expansion solids like polymers might have Q_h constants three orders of magnitude larger than the hard low-expansion $Pb(Mg_{1/3}Nb_{2/3})O_3$.

In fact, of course, for the holder structure it is the electrostrictive M constant which is of importance, and for linear solids

$$M_{ijmn} = Q_{ijkl}\eta_{kj}\eta_{nl}$$

where η_{km} and η_{nl} are the appropriate dielectric susceptibilities. Thus for exceedingly low electrostrictive response under high driving fields we require a very stiff solid of low thermal expansion and low dielectric susceptibility (permittivity). Fused silica appears most suitable.

A new sample holder has now been designed for the dilatometer on a coaxial configuration which produces a radial electrostrictive stress normal to the direction of measurement, with a broad fused silica ring insulator.

Measurements are now proceeding on samples of fused silica to confirm the low Q constants expected.

In the alkali halide crystals NaCl, KCl measurements in the new holder show a strong frequency dependence of induced strain. High frequency values

Correlation between Electrostriction and Thermal Expansion

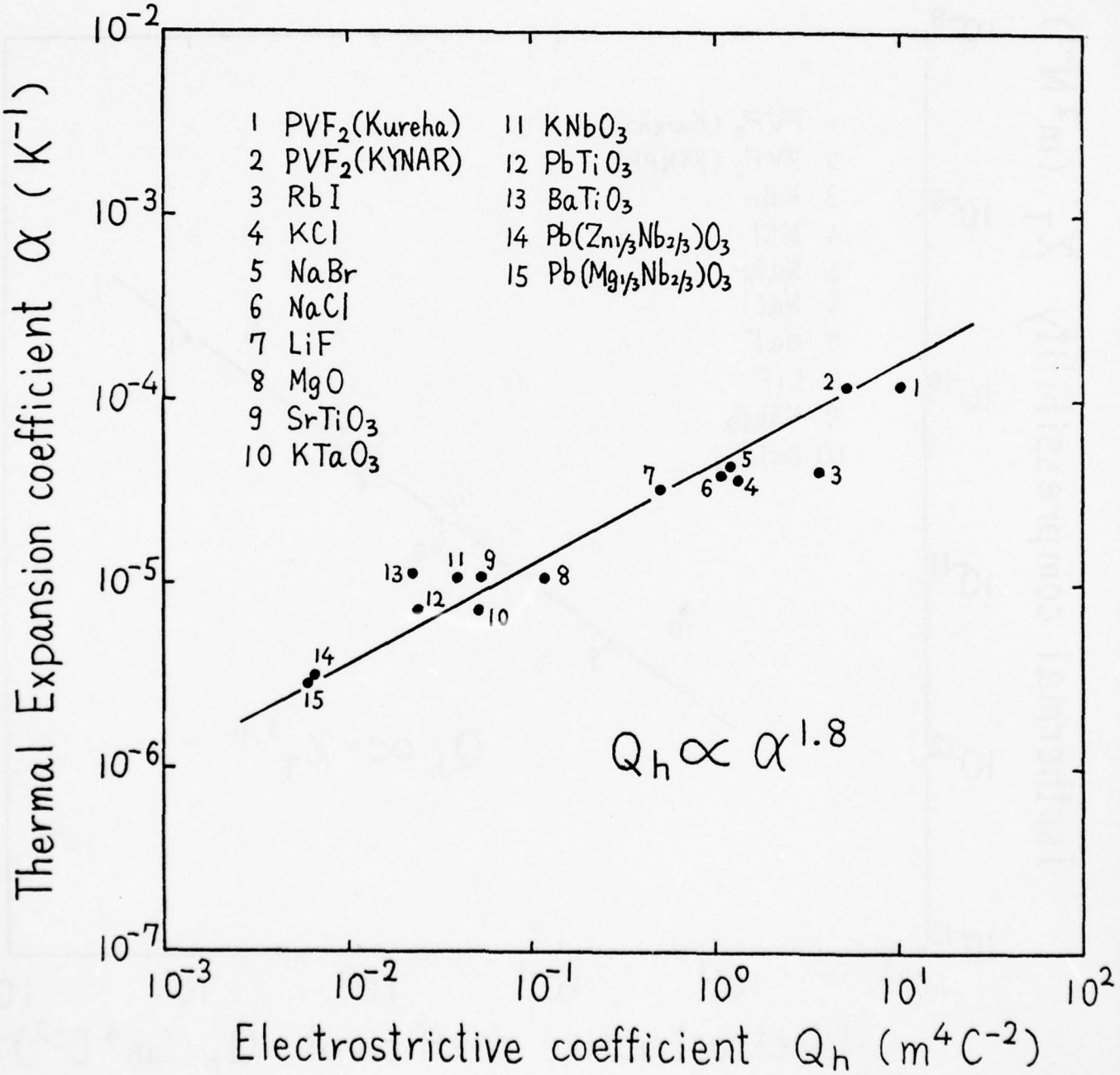

Figure 1

Correlation between Electrostriction and Compressibility

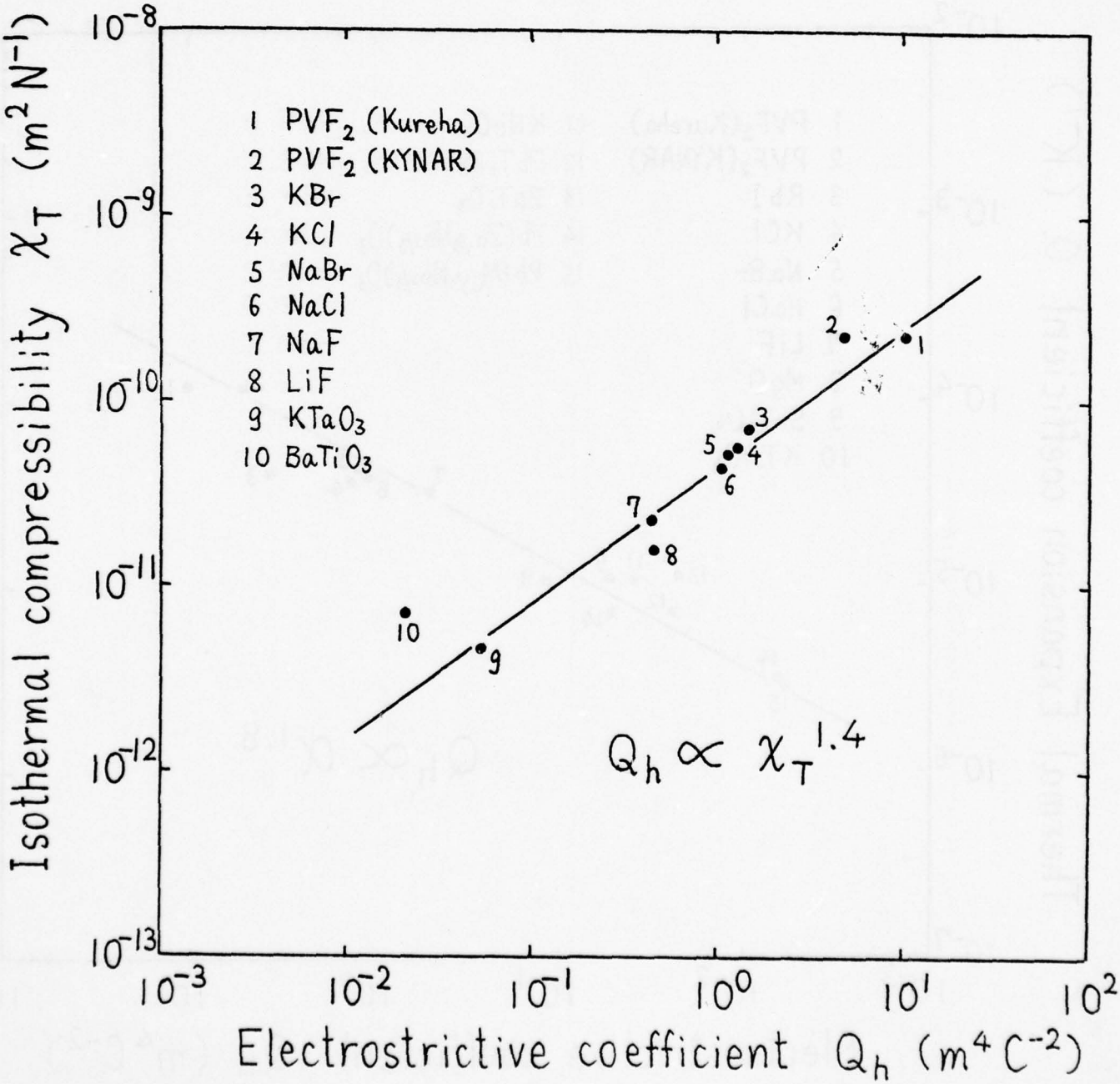

Figure 2

are within a factor of 3 of those measured earlier by Böhaty and Haussuhl. We believe that the high low frequency values may have an origin in dielectric heating due to a grossly hydrated surface layer. New very low frequency dielectric loss measurements are being carried out to check this possibility.

2.2.2 Electrostriction in Relaxor Ferroelectrics

Work on the $Pb(Mg_{1/3}Nb_{2/3})O_3$ based relaxor ferroelectrics for electrostrictive applications was initiated under an earlier DARPA:ONR joint funding (N00014-76-C-0515). A number of tasks initiated on that program have now been completed. Technological properties of interest in $Pb_3(Mg_1Nb_2)O_9$:$PbTiO_3$ solid solutions are discussed in Appendix 6 and joint work with Dr. S. Nomura and colleagues on this system which was presented at the applications meeting in Kyoto, Japan (FMA 2) is given in Appendix 9. The extensive work we have performed on electrostriction has also been summarized for presentation to colleagues in Japan by Dr. K. Uchino in a paper in Japanese submitted to the Japanese Journal of Electronic Ceramics which is included as Appendix 4.

Recent studies have now focused more on the physical explanation of the response in these relaxor systems. The low values of the averaged $\bar{Q}_{ij}$ in ceramics have been shown to increase rapidly with $Pb(W_{1/2}Mg_{1/2})O_3$ content (Appendix 7) as is the case also in the $PbMg_{1/3}Nb_{2/3}O_3$:$PbTiO_3$ system (Appendix 6). That the low values are not due to an unusual cancellation in the ceramic average $\bar{Q}$'s has been clearly demonstrated by measurements on $(Pb(Mg_{1/3}Nb_{2/3})O_3$ single crystals (Appendix 5). It has also been shown that a coherent and self-consistent explanation can be given for the elasto: dielectric behavior of the perovskite relaxors if it is assumed that the constant A in the formula

$$\omega_{TO}^2 = A(T-T_c)$$

which describes the temperature dependence of the soft transverse optic lattice mode frequency in these crystals is almost an order of magnitude smaller than in normal sharp transition ferroelectrics.

In a new fundamental attack on the origins of the diffuse transition, crystal chemical arguments suggested that the compound $Pb(Sc_{1/2}Ta_{1/2})O_3$ should be just on the limit of stability of ordering for the B site cations. For this compound it has now been shown that the diffuseness of the transition at T_c can be modified by thermal treatment, and the thermal and dielectric diffuseness related to the degree of structural ordering of the B site cations (Figures 3,4).

Single crystals of $Pb(Sc_{0.5}Ta_{0.5})O_3$ have been grown by a flux method, and for suitable heat treatments ordered and disordered B site arrangements produced and shown to correspond to sharp and diffuse behavior of the weak field dielectric permittivity (Figure 5.)

High field hysteresis behavior also correlates with sharp and diffuse transition behavior. We believe that these and additional studies that are now going forward on this material will provide for the first time a clear indication of the nature and scale of the microheterogeneity in the disordered perovskite systems which leads to the interesting relaxor properties.

2.3 LATTICE THEORY OF ELECTROSTRICTION

2.3.1 Purpose of Research

The objective of these investigations is to understand the effect of crystal structure and composition on the electrostriction coefficients of crystalline ionic solids in order to optimize the electrostriction coefficients and, ultimately, in order to maximize the electromechanical coupling factors of ferroelectric materials derived from centric prototypes via a

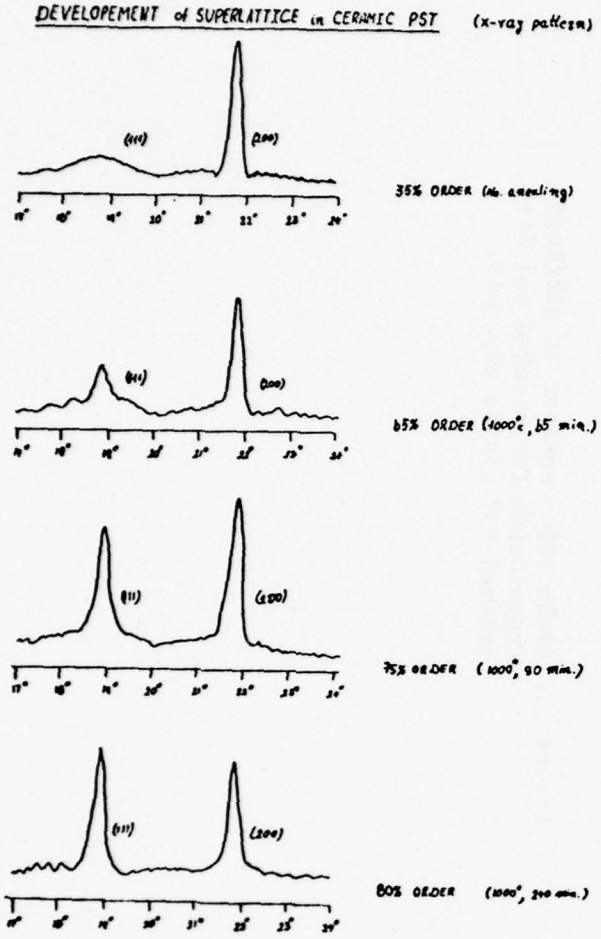

Figure 3. Development of order in the B site of $Pb(Sc_{1/2}Ta_{1/2})O_3$.

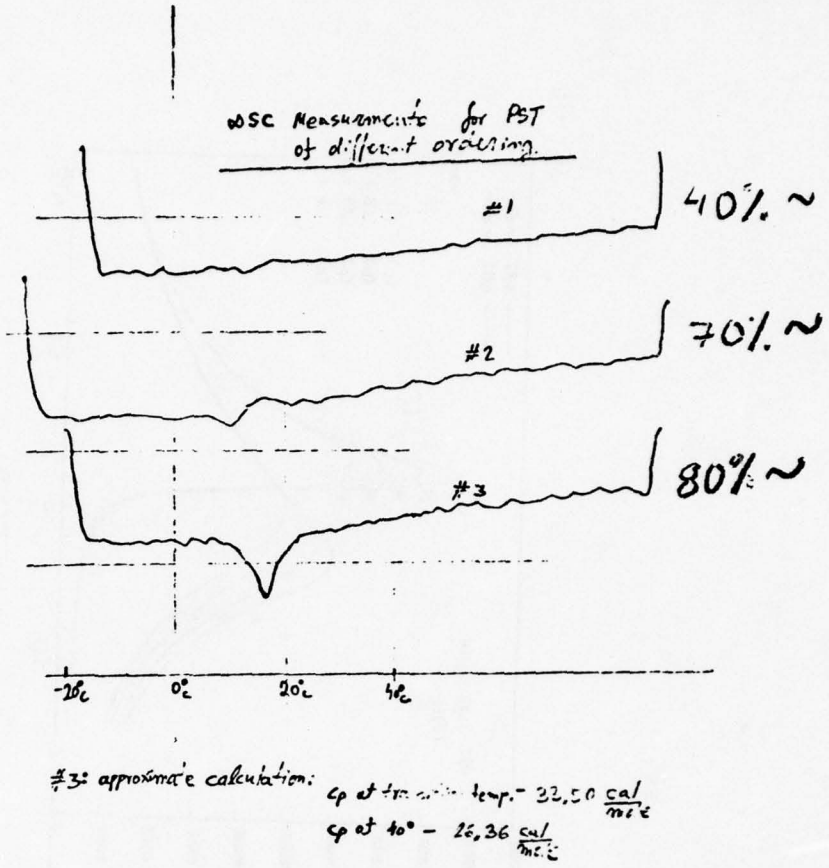

Figure 4. Heat of transition as related to degree of order in the B site of PST ceramic.

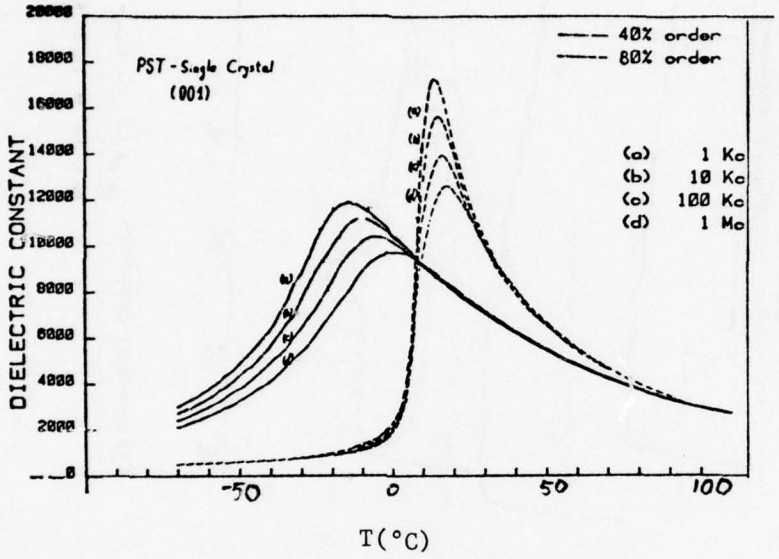

Figure 5. Dielectric constant at different frequencies for ordered and disordered PST single crystals.

systematic molecular engineering approach.

Progress during the present contract period encompasses the following items:

2.3.2 Technical Results

2.3.2.1 Lattice Dynamical Framework

The most comprehensive lattice theory of the elastic dielectric is due to Srinivasan[1], who has given general expressions for the photoelastic, electrostriction, and nonlinear dielectric susceptibility constants. All subsequent applications are based on this treatment and deal with the fluorite[2,6], rocksalt[3-5,7] and cesium chloride[4] structures. None of the theoretical models considered so far gives good agreement for the electrostriction coefficients.

The theoretical treatment of Srinivasan[1] is based on the rigid ion model. Generalization to the shell model (SM) is achieved by treating the shells as additional rigid-ion sublattices of zero mass. This implies that the shell-sublattices are partly restricted to the harmonic approximation, in so far as the shell model parameters (shell charges and core-shell coupling constants) are constants, and no anharmonicity other than that arising from Coulomb and short range shell-shell repulsion is included.

To provide a more general theoretical framework and a more rigorous derivation which would be free from these limitations we have derived the nonlinear constitutive relations of the elastic dielectric from lattice theory by using the shell model equations from the outset. The results are general for any anharmonic SM in which anharmonicity of both inter-ionic and intra-ionic forces (such as nonlinear core-shell coupling or deformation induced charge transfer effects) may be present. In the following a short outline will be given of the method used and the results obtained. Although

general results valid for non-centrosymmetric crystal structures have been obtained, for simplicity only centrosymmetric (non-piezoelectric) crystal structures will be considered here.

The derivation of the electrostriction constants is based on the long wavelength method as applied to the equations of motion in the presence of a macroscopic electric field. Using the approach and the nomenclature of Cowley[8] the time-independent equations of motion for a periodic motion in the approximation of the SM are given by

$$\omega^2 \tilde{M}\bar{U} = \tilde{A}\bar{U} + \tilde{B}\bar{W} - \tilde{Z}\bar{E} \tag{2.1a}$$

$$0 = \tilde{C}\bar{U} + \tilde{D}\bar{W} - \tilde{Y}\bar{E} \tag{2.1b}$$

$\bar{U}$, $\bar{W}$, $\bar{E}$ (with $\bar{U} = \{U_\alpha(\kappa)\}$, $\alpha = 1,2,3; \kappa = 1,2,\ldots s$: etc) denote vectors of rank 3s (s = number of ions per unit cell) specifying the amplitudes of the displacements of the cores and of the shells and the amplitude of the macroscopic electric field pertaining to all sublattices, respectively. $\tilde{M}$, $\tilde{Z}$ and $\tilde{Y}$ (with $\tilde{M} = \{M(x)\delta_{\alpha\beta}\delta_{\kappa\kappa'}\}$ etc) are diagonal matrices of rank 3s pertaining to the masses, to the total ionic charges and to the shell charges, respectively. $\tilde{A}$, $\tilde{B}$, $\tilde{C}$ and $\tilde{D}$ (with $\tilde{A} = \{A_{\alpha\beta}(\kappa\kappa')\}$ etc) are matrices of rank 3s given by

$$\tilde{A} = \tilde{R} + \tilde{Z}\tilde{C}\tilde{Z} \tag{2.2a}$$

$$\tilde{B} = \tilde{T} + \tilde{Z}\tilde{C}\tilde{Z} \tag{2.2b}$$

$$\tilde{C}^+ = \tilde{B}^* \tag{2.2c}$$

$$\tilde{D} = \tilde{S} + \tilde{Y}\tilde{C}\tilde{Y} \tag{2.2d}$$

The matrices $\tilde{R}$, $\tilde{T}$, $\tilde{S}$ describe short range interactions, and the terms involving the Coulomb matrix $\tilde{C}$ describe the electrostatic interactions between the point charges and the dipoles.

Using the definition for the components P_α of the polarization vector

$$P_\alpha = \frac{e}{V_c} \sum_\kappa \{(\tilde{Z}\bar{U})_\alpha(\kappa) + (\tilde{Y}\bar{W})_\alpha(\kappa)\} \tag{2.3}$$

(V_c = volume per unit cell) one obtains after performing the long wavelength expansion and eliminating the shell displacement $\bar{W}$ the following expressions for the high frequency limit and the static limit of the dielectric susceptibility tensor $\tilde{\chi} = (\chi_{ij})$ (i,j = 1,2,3):

$$\tilde{\chi}^\infty = \frac{1}{V_c} \sum_{\kappa\kappa'} [\tilde{Y}\tilde{D}^{-1}\tilde{Y}] \tag{2.4a}$$

$$\tilde{\chi}^o = \frac{1}{V_c} \sum_{\kappa\kappa'} [\tilde{X}\tilde{L}^{-1}\tilde{X} + \tilde{Y}\tilde{D}^{-1}\tilde{Y}] \tag{2.4b}$$

The sums are over all s sublattices, so that the result in each case is a 3 x 3 matrix. The quantity

$$\tilde{X} = \tilde{Z} - \tilde{B}\tilde{D}^{-1}\tilde{Y} \tag{2.5a}$$

is an effective charge matrix, and

$$\tilde{L} = \tilde{A} - \tilde{B}\tilde{D}^{-1}\tilde{B}^+ \tag{2.5b}$$

an effective interaction matrix.

For a strained crystal the coupling matrices $\tilde{A},\tilde{B},\tilde{C},\tilde{D}$ and the shell charge matrix $\tilde{Y}$ are functions of the Lagrangian strain tensor $\tilde{\eta} = (\eta_{ij})$. Up to first order this dependence is given by

$$\tilde{A}(\tilde{\eta}) = \tilde{A} + \tilde{\tilde{A}}\tilde{\eta} \tag{2.6}$$

etc, where the coefficient matrices $\tilde{\tilde{A}}$, etc, depend on the anharmonic coupling parameters. Using the perturbation expansion for $\bar{U},\bar{W},\bar{E}$ and ω with respect to the strain components up to first order according to

$$U(\tilde{\eta}) = U + \tilde{U}\tilde{\eta} \tag{2.7}$$

etc, and proceeding in the same manner as outlined above for the strain-free

crystal one obtains the following expressions for the photoelastic tensor $\tilde{\tilde{\chi}}^{\infty} = (\partial\chi^{\infty}_{ij}/\partial\eta_{kl})$ and for the electrostriction tensor $\tilde{\tilde{\chi}}^{o} = (\partial\chi^{o}_{ij}/\partial\eta_{kl})$:

$$\tilde{\tilde{\chi}}^{\infty} = \frac{1}{V_c} \sum_{KK'} \{-[\tilde{Y}\tilde{D}^{-1}\tilde{\tilde{D}}\tilde{D}^{-1}\tilde{Y}] + \\ +[\tilde{\tilde{Y}}\tilde{D}^{-1}\tilde{Y}] + [\tilde{Y}\tilde{D}^{-1}\tilde{\tilde{Y}}] + \frac{1}{V_c}\tilde{\chi}^{\infty}\tilde{I} \qquad (2.8a)$$

$$\tilde{\tilde{\chi}}^{o} = \frac{1}{V_c} \sum_{KK'} \{-[\tilde{X}\tilde{L}^{-1}\tilde{\tilde{L}}\tilde{L}^{-1}\tilde{X}] - [\tilde{Y}\tilde{D}^{-1}\tilde{\tilde{D}}\tilde{D}^{-1}\tilde{Y}] \\ +[\tilde{\tilde{X}}\tilde{L}^{-1}\tilde{X}] + [\tilde{X}\tilde{L}^{-1}\tilde{\tilde{X}}] + [\tilde{\tilde{Y}}\tilde{D}^{-1}\tilde{Y}] + [\tilde{Y}\tilde{D}^{-1}\tilde{\tilde{Y}}]\} + \frac{1}{V_c}\tilde{\chi}^{o}.\tilde{I} \qquad (2.8b)$$

Here $\tilde{I} = \{\delta_{\alpha\beta}\}$ denotes the unit tensor of rank three. Eqs (2.8a) and (2.8b) are the desired result. They show no resemblance, however, to Srinivasan's[1] equation (3.51). In fact, they constitute an alternative solution to the problem and have the advantages of higher generality, simplicity and greater lucidity in displaying the physical origin and the nature of the individual contributions in the final expression.

We have verified that numerical application of eqs (2.8) to the rocksalt structure for a conventional rigid shell model ($\tilde{Y}$ = const; $\tilde{\tilde{Y}} \equiv 0$) gives results identical to those obtained by Srinivasan and Srinivasan[2]. At this point it should be noted that Srinivasan and Srinivasan[2] state without proof that a factor 1/2 should be added to the last additive term in eq (3.51) of Srinivasan[1], and their numerical results[2] are based on the revised equation. We have also independently derived this correct equation, with the factor 1/2 included. It follows that for the special case of a rigid shell model the above eqs (2.8) are equivalent to the corrected form of Srinivasan's[1] eq (3.51), with the factor 1/2 included.

2.3.2.2 Application to Rocksalt Structure

As mentioned in our First Semiannual Report on the present contract, none of the existing theoretical models gives satisfactory agreement for the photoelastic and electrostriction coefficients of rocksalt type alkali halides. Possible causes for the deficiencies of these models are (a) that purely harmonic models for the electronic polarizability are used, and (b) that many-body effects in the short range interactions are included, if at all, in an inadequate manner. To investigate the first of these possibilities we have for the rocksalt structure considered several anharmonic shell models in which the anharmonicity of the intraionic forces is included in addition to the anharmonicity of the interionic forces.

The most obvious way to introduce intraionic anharmonicity is to add a cube term $k'W^3$ or a quartic term $k''W^4$ to the core-shell interaction potential[9,10]. It can be shown from symmetry arguments, however, that for the rocksalt structure the cube term does not arise. The quartic term, on the other hand, does not enter the first order electrostriction coefficient $\tilde{\tilde{\chi}}$, as given by eq (2.8b), but becomes apparent only in the second order electrostriction coefficients.

A mechanism for intraionic anharmonicity, which for the rocksalt structure does affect the first order electrostriction coefficient, consists of a strain dependent shell charge according to (tensor notation):

$$Y_{ij}(\eta_{kl}) = Y^{o}\delta_{ij} + Y_{ijkl}\eta_{kl} \qquad (2.9)$$

Eq (2.9) describes intraionic core-shell charge transfer under the influence of a strain η_{kl}. Y^{o} denotes the shell charge in the absence of strain. For the cubic symmetry pertaining to the rocksalt structure there are three independent components of the fourth rank charge transfer tensor Y_{ijkl}, namely (in Voigt notation) Y_{11}, Y_{12}, and Y_{44}.

We have incorporated the charge transfer mechanism defined by Eq (2.9) into a shell model for rocksalt-type materials in which general noncentral short range force between nearest neighbors, central forces between neighboring anions, and the polarizability of the anions are included. The model contains six harmonic and five anharmonic parameters. The harmonic parameters are, in the nomenclature explained in our First Semiannual Report, the nearest neighbor short range constants A_1, B_1, the second neighbor short range constants A_2, B_2, the anion core-shell coupling constant k, and the anion shell charge Y^o. The anharmonic parameters are the short range parameters C_1 and C_2 pertaining to first and second neighbor interaction, respectively, and the charge transfer parameters Y_{11}, Y_{12}, and Y_{44}. Numerical application to the alkali halides was made by fitting the harmonic parameters to the three elastic constants, to the static and to the high frequency limit of the dielectric constant, and to the transverse optical frequency. The anharmonic parameters were fitted to the first pressure derivatives of the elastic constants c_{11} and c_{44}, and to the three photoelastic constants.

In Table 1 the calculated results are compared with the experimental data for the photoelastic constants[11] (in Voigt notation)

$$p_{\mu\nu} = -\frac{1}{(\varepsilon^{\infty})^2} \left(\frac{\partial \varepsilon_{\mu}^{\infty}}{\partial \eta_{\nu}}\right) \tag{2.10}$$

and of the electrostriction constants[12]

$$f_{\mu\nu} = -\frac{1}{2} \left(\frac{\partial \varepsilon_{\mu}^{o}}{\partial \eta_{\nu}}\right) \tag{2.11}$$

For comparison the theoretical results of Goyal et al[7] are also included which are based on a shell model with angle bending forces.

It is apparent that the present model allows a perfect fit for the photoelastic constants, whereas for the model of Goyal et al[7] discrepancies up to a

Table 1. Comparison of experimental and theoretical values of photoelastic constants $p_{\mu\nu}$ (dimensionless) and first-order electrostriction coeffcients $f_{\mu\nu}$ (in 10^{-10} NV^{-2}) for four alkali halides.

		p_{11}	p_{12}	p_{44}	f_{11}	f_{12}	f_{44}
LiF	Experimental[11,12]	0.02	0.13	-0.045	-5.77	0.83	-5.08
	Theory (present)	0.02	0.13	-0.045	-5.33	0.08	-0.11
	Theory (Goyal et al[7])	0.082	0.274	0.024	-5.49	0.65	0.30
NaCl	Experimental[11,12]	0.115	0.161	-0.011	-2.67	0.62	-0.97
	Theory (present)	0.115	0.161	-0.011	-2.38	0.09	-0.033
	Theory (Goyal et al[7])	0.067	0.266	0.022	-2.56	0.19	-0.03
KBr	Experimental[11,12]	0.212	0.165	-0.026	-2.56	0.82	-0.66
	Theory (present)	0.212	0.165	-0.026	-1.87	0.076	-0.047
	Theory (Goyal et al[7])	0.230	0.260	0.024	-2.47	0.11	-0.08
RbI	Experimental[11,12]	0.262	0.167	-0.023	-3.30	0.95	-0.58
	Theory (present)	0.262	0.167	-0.023	-1.41	0.083	-0.038

factor of two occur. For the electrostriction constants both the present results and those of Goyal et al show considerable deviations from the experimental data[12], especially for f_{12} and f_{44}. Moreover, in spite of the inclusion of intraionic anharmonicity the calculated electrostriction constants do not differ drastically from values calculated on the basis of a rigid-shell model with many-body forces included[7]. One may therefore conclude (a) that the experimental electrostriction data for the alkali halides[12] are probably seriously in error, (b) that inclusion of intraionic anharmonicity, while essential for the photoelastic constants, is only of minor importance for the electrostriction constants, and (c) that the effect of many-body forces, while apparent in the second and third order elastic constants, is only small for the electrostriction constants, at least in alkali halides.

To substantiate the last conclusion (c) we have applied Keating's model of angle bending forces[13] up to third order in the four anion-cation-anion angles of the rocksalt structure. The results indicate that as a result of the crystal symmetry these angle bending forces do not contribute to the anharmonic potential energy in the rocksalt structure. Thus the many-body forces present in the rocksalt structure must be of a more general nature.

2.3.2.3 Application to Perovskite Structure

The lattice dynamical framework has also been applied to the perovskite structure ABO_3 on the basis of a rigid-shell model, with the electronic polarizability of all three ions taken into account. Numerical application to $SrTiO_3$ has been made by taking into account the thermal contribution from the soft zone center optic mode in an empirical manner. Good overall agreement for all first order anharmonic coefficients (third order elastic constants and electrostriction constants) can be obtained with only one empirical parameter (i.e. the third derivative of the short range repulsive potential for the Ti-O interaction) if the third derivatives of the short range repulsive

interaction for the Sr-O and for the O-O interaction are determined by means of a Born-Mayer potential. The results indicate (a) that the various first order anharmonic coefficients, especially the (largest) third order elastic constant c_{111} and the hydrostatic electrostriction coefficient Q_h, can be consistently accounted for on the basis of the model used, (b) that the Sr-O and the O-O overlap repulsive interactions are of comparable magnitude, but that the Ti-O interaction is the dominant interaction and is over ten times larger than the other two first-neighbor interactions, (c) that the hydrostatic electrostriction coefficient Q_h depends quite sensitively on the third derivative of the Ti-O repulsive interaction, and that this interaction is not well represented by the Born-Mayer potential form, and (d) that to a good approximation the electrostrictive constants are determined by only one anharmonic parameter, namely the third derivative of the Ti-O repulsive interaction.

2.3.3 Plans for Next Year

The results obtained clearly demonstrate the feasibility of the approach chosen, and it is hoped that the theory can be extended to predict trends of the electrostriction constants for isostructural compounds even if no experimental data (or only a few) are available for the determination of the model parameters. For this purpose it may be necessary to improve the previously used models by including many-body effects and/or intraionic anharmonicity, and to extend the general theory so as to include thermal effects in a consistent manner. Applications are envisaged for members of the perovskite family of compounds and, if successful, for other crystal structures.

2.3.4 References

1. R. Srinivasan, Phys. Rev. 165, 1041 (1968).

2. R. Srinivasan, Phys. Rev. 165, 1054 (1968).

3. R. Srinivasan and K. Srinivasan, J. Phys. Chem. Solids 33, 1079 (1972).

4. R. Srinivasan and K. Srinivasan, Phys. Stat. Sol. (b) 57, 757 (1973).

5. A.L. Larionov and B.Z. Malkin, Soviet Physics-Solid State 16, 21 (1974).

6. A.A. Kaplyanskii, B.Z. Malkin, V.N. Medvedev, and A.P. Skvortsov, Soviet Phys-Solid State 16, 221 (1974).

7. S.C. Goyal, R. Prakash and S. Tripathi, Phys. Stat. Sol. (b) 85, 477 (1978).

8. R.A. Cowley, Proc. Roy. Soc. A268, 121 (1962).

9. Migoni, R., Bilz, H. and Bäuerle, D. (1976) Phys. Rev. Lett. 37, 1155.

10. Migoni, R., Bilz, H. and Bäuerle, D. (1978) in Lattice Dynamics (edited by M. Balkanski), p. 650 (Flammarion, Paris).

11. Landolt-Börnstein, Numerical Data and Functional Relationships is Science and Technology, New Series, Group III, Vol. 11, Springer, Berlin (1979).

12. L. Bohaty and S. Haussühl, Acta Crysta. A33, 114 (1977).

13. P.N. Keating, Phys. Rev. 145, 637 (1966); Phys. Rev. 149, 674 (1966).

3. PIEZOELECTRIC COMPOSITES

3.1 INTRODUCTION

The second major area of study on the present ONR contract has been devoted to expanding and exploiting the development of new types of composite material for transducer applications. Earlier studies[1,2] have already established the cardinal importance of phase interconnection (connectivity) in piezoelectric composites, and led to the development of 3:3 and 3:1 connected materials fabricated by the replamine[3] technology which show exceptional g_{33} and g_h coefficients of potential interest for hydrophone systems.

New work has been concerned with developing model materials with precisely controlled macrostructure, so as to test and verify the predicted properties, with establishing a much simplified processing technology which closely mimics the replamine characteristics and with additional studies of potential applications for internally electroded PZT and other lamellar composite structures.

A concise summary of many of the present composite approaches was presented as an invited paper at ISAF 1979 in Minneapolis, and is included as Appendix 10 to this report.

3.2 PZT: PLASTIC COMPOSITES

3.2.1 Composites with Very High Hydrostatic Sensitivity

A simple extrusion technique has been used to develop PZT rods with controlled diameters in the range 800 to 200 μmeters, and PZT:epoxy composites of very regular 3:1 phase connection fabricated. Data from these studies presented in Appendix 11 verify the earlier proposed composite model and show that materials with $\bar{g}_h \bar{d}_h$ product almost 100 times larger than that that of the single PZT phase can be developed.

In a concurrent processing study discussed in Appendix 12, a very simple technique is described which permits the fabrication of a low density PZT:plastic composite with dominantly 3:3 connectivity which closely mimics the properties of the original replamine form materials. We note that a somewhat similar product has recently been produced by Dr. K. Okazaki of the Defense Academy in Yokosuka, Japan[4] which also has g_h d_h product superior to the constituent PZT phase.

Current studies are concerned with possible techniques for further improving the hydrostatic performance as follows:

By laying up the PZT rods along three orthogonal axes and poling from surface electrodes, a solid with three effective orthogonal polar axes has been developed.

Cursory assessment would suggest that a unit cube of this composite could be electroded on all six faces and the face electrodes series connected in such a manner as to generate under hydrostatic pressure three times the voltage of a single 3:1 connected array. Preliminary experiments, however, show that in fact the voltage generated is even further enhanced, due to the fact that the orthogonal PZT elements provide considerable relief of the radial stress components on the PZT rods.

The triaxial polar composite is only one of a number of composites that would have no simple ceramic or single crystal equivalent, that can be fabricated from the PZT rod structures, and we are now studying a number of arrangements using both straight and curved rods, coils, and helical structures. To avoid some of the complexities associated with poling the PZT from surface electrodes we have devised a continuous poling technique for the unsupported rod or fiber.

In the initial set-up, two pools of lead bismuth eutectic alloy solder were maintained by surface tension in small circular holes drilled through two thin copper plates spaced some 2 to 4 mm apart in a high temperature oil bath (150°C). The copper plates are insulated from each other and maintained at a potential difference of 3 ∿ 5 K Volts. The PZT fiber, attached to a fine wire, is threaded through the two holes and pulled vertically at speeds up to 0.5 mm/minute. The solder does not wet PZT, but makes a sufficient contact with the surface to pole the PZT longitudinally. PZT 501A rods with diameters from 10-25 mils have been poled to saturation by this method.

The solder does require rather careful handling, and recently we have found that a high density carbon foam attached to the copper plate in place of the solder dot makes quite adequate contact for poling at 80°C using the same conditions of separation, field, and pulling speed.

We are now experimenting with similar contact schemes for poling more complex coil, spiral, and helical shapes, and with longer parallel contacts for longitudinal surface poling of long tape cast PZT sheets.

3.2.2 Composites with High $\bar{d}_{33}$

Two types of composite structure are being explored which appear to offer the possibility of enhancing the effective $\bar{d}_{33}$ over that of the parent PZT phase.

3.2.2.1 Dimpled PZT Sheet:Epoxy Plastic

The dimpled structure is made by pressing a green tape cast PZT lightly over a mold of regularly spaced steel ball bearings. This green sheet is then fired to retain the dimpled structure and cast into a Spurrs epoxy. After potting top and bottom surfaces parallel to the plane of the dimpled ceramic, sheets are carefully ground down so as to expose the tips and bases of the PZT dimples then electroded with air-drying silver paint.

Initial data are summarized in Table 2.

Table 2

Sample Number	Ball Diameter	Array Elements	Number Measured	($\times 10^{-12}$ M/V) Best d_{33}	($\times 10^{-12}$ M/V) Average d_{33}
1	1/8"	20	20	1039	561
2	3/16"	9	5	980	585
3	1/4"	4	4	1273	611

All measurements were taken using a nominal 12 mil tape thickness.

Clearly more data are required to make any definite conclusions, but it may be noted that even the averaged values of $\bar{d}_{33}$ are significantly higher than d_{33} for the PZT5A $\sim 400\ 10^{-12}$ M/V.

In the second type of structure, techniques for making PZT spheres of uniform size are being explored, with the objective of generating thin sheet composites essentially 1 sphere thickness. So far, the best results have been obtained using a PZT:wax composition, held at a temperature well above the melting point of the wax and dripped at a constant rate into a warm water bath. By careful control of the temperature and drip rate of the PZT:wax, and of the cooling water, spherical particles of very uniform size were generated.

After a slow burn-out of the wax, a short sintering cycle on a support of loose PZT powder provided the final spherical particles. A typical composite made up using microspheres in a Spurrs Epoxy potting compound is shown in Figure 6.

3.3 CERAMIC:CERAMIC COMPOSITES

Tape casting methods have been used to produce a range of composite and

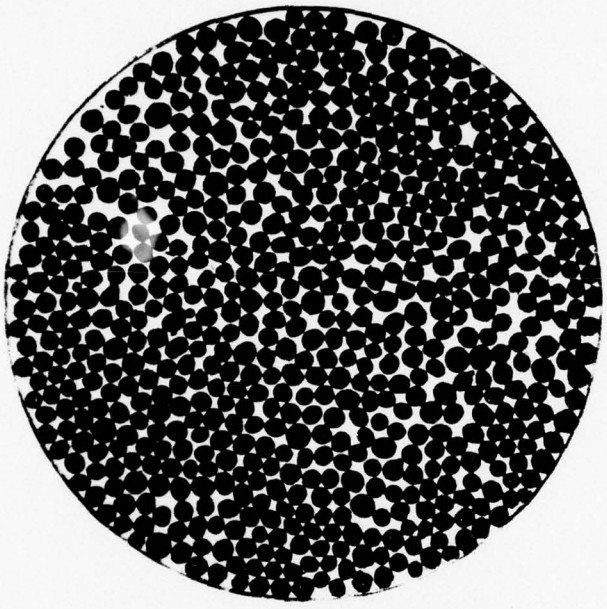

Figure 6. Composite formed using PZT microspheres in epoxy plastic.

of internally electroded PZT and $Pb(Mg_{1/3}Nb_{2/3})O_3$ materials. Typical applications using the impedance adjustment which such multilayer structures afford for both static and resonant applications are discussed in Appendix 13. The principle of using multilayer techniques with $Pb(Mg_{1/3}Nb_{2/3})O_3$:{$Pb(Mg_{1/3}Nb_{2/3})O_3$: $PbTiO_3$} composites to control the temperature dependence of the effective elastic compliances in resonant structures is discussed in Appendix 14. It is shown that a rather precise cancellation between positive and negative temperature coefficients can be effected by a suitable choice of components and an added stabilization against depoling developed.

Stemming from these early studies, it was also evident that the polarization level above the T_c range in the relaxor can strongly affect the clamped elastic compliance (antiresonant frequency). The effect suggests a significant role for the 6th order electrostriction constants which will be discussed further in the section dealing with phenomenological theories.

References

1. R.E. Newnham, D.P. Skinner and L.E. Cross, Connectivity and Piezoelectric-Pyroelectric Composites, Mat. Res. Bull. 13, 525 (1978).

2. L.E. Cross, J.V. Biggers and R.E. Newnham, Ceramic Piezoelectric Transducers, ONR Final Report on Contract N00014-76-C-0515.

3. D.P. Skinner, R.E. Newnham and L.E. Cross, Flexible Composite Transducers, Mat. Res. Bull. 13, 599 (1978).

4. K. Okazaki (Private Communication).

4. GRAIN ORIENTED CERAMICS

Effort on this topic has been confined primarily to the development of a technique for cost-effective fabrication of oriented grain structures. Using a eutectic molten salt process (Appendix 15) it has been demonstrated that 'c' axis oriented ceramics can be fabricated from microcrystalline-shape anisotropic particles precipitated in the compositions $Bi_4Ti_3O_{12}$ and Bi_2WO_6 by simple tape casting. X-ray studies have confirmed 100% orientation of 'c' normal to the plane of the cast sheet. Attempts to pole the anisotropic samples in these systems have, however, been frustrated by the very high coercivity and the rapidly rising conductivities with increasing temperature in both systems.

Current studies are now focusing on the preparation of $PbBi_2Nb_2O_9$. This material has a lower transition at 275°C which might aid markedly in the poling.

Arrangements are now being made to exchange samples and information with Dr. K. Okazaki at the Defense Academy in Yokosuka. His group has been fabricating similar grain oriented layer structure materials by hot extrusion processing. This exchange of information will, we hope, speed up our work in this whole topic area and provide an interesting effective intercomparison of two completely different processing techniques which achieve almost identical orientation factors.

5. CRYSTAL GROWTH

5.1 INTRODUCTION

The flux growth facility described in our initial annual report has been in continuous operation over the full contract period. Emphasis has been on the growth of crystals in the PZT solid solution family and of relaxor ferroelectrics of perovskite structure.

Over the contract period, the group has provided assistance to establish a new constant diameter control Czochralski pulling equipment that will be vital for continuing studies of the tungsten bronze-type crystals.

5.2 PEROVSKITE TYPE CRYSTALS

5.2.1 PZT Compositions

Growth attempts were concentrated on compositions with Zr/Ti ratio close to morphotropy. The approach was not aimed to produce large samples, but to develop small homogeneous crystals that would be of sufficient quality for optical and microdielectric measurements. Flux systems that were tested included:

PbF_2 - KF - $Pb_3(PO_4)_2$

PbO

PbO - PbF_2 - B_2O_3

KF - PbF_2

PbO - PbF_2 - KF

The systems that appeared to yield best results were KF:PbF_2 and pure PbO. Growth runs from pure PbO yielded small cube-shaped crystals, most of which were in the tetragonal phase at room temperature. In many cases, crystals encased in the melt appeared of excellent quality, but an extraction exhibited massive internal micro-cracking. Only very small irregular-shaped pieces were obtained free from the flux.

5.2.2 Relaxor Perovskites

A number of growth runs were carried through using a flux of excess PbO with minor B_2O_3 addition to grow additional crystals of $Pb(Mg_{1/3}Nb_{2/3})O_3$ for electrostriction studies. The procedure was described in the previous annual report. Crystals in the form of small rectangular parallelepipeds with edges up to 0.5 mm were produced. Experimental measurements on these samples are reported in Appendix 5.

Following a careful crystal chemical analysis and studies on ceramic materials, it was evident that $Pb(Sc_{1/2}Ta_{1/2})O_3$ could be produced either as a sharp transition (ordered) compound or with scandium and tantalum ions disordered on the B site giving diffusing transition behavior. Having verified by x-ray powder methods that order:disorder could be modified in this compound by the thermal treatments it was desirable to grow single crystals for precise dielectric, optical, elastic, and other property measurements.

Crystals of $Pb(Sc_{1/2}Ta_{1/2})O_3$ were grown by the following procedure. Powder was prepared by mixing the appropriate oxides in stoichiometric proportions. The powder was calcined by firing at 800°C for two hours in a closed platinum crucible, then grinding and refiring again at 1300°C for one hour. X-ray examination showed the resulting powder to be dominantly in the perovskite structure with only small traces of the pyrochlore modification. Flux systems tested included PbO, PbO-PbF_2, and PbO-PbF_2-B_2O_3. Best success was achieved with the PbO-PbF_2-B_2O_3 flux using mole fractions

$Pb(Sc_{1/2}Ta_{1/2})O_3$	:0.15
PbO	:0.40
PbF_2	:0.40
B_2O_3	:0.05

Growth was accomplished in a platinum crucible with a temperature cycle

25°C - 1250°C	Linear over six hours
1250°C	Soak for four hours
1250°C - 1000°C	Linear cooling at 3°C/hour
1000°C - 900°C	Linear cooling at 5°C/hour
900°C - Room T.	50°C/hour

The crystals obtained were pale yellow in color in the form of well developed cubes with 100 faces.

Unit cell size as determined by x-ray diffraction was 4.073Å, in good agreement with literature values for the ceramic material.

5.3 DIAMETER CONTROL GROWTH EXPERIMENT

5.3.1 Introduction

The major effort to establish an effective Czochralski pulling system for oxide crystals has been carried forward by Dr. Brun in MRL, under AFOSR sponsorship. In preliminary evaluation of available control methods, it was decided to use digital rather than analog control, and in view of our experience in this area the ferroelectrics group has been cooperating to help establish this important capability.

5.3.2 Control System

In Figure 7 the major components of the system are outlined in block form. The system is based on a control from the weight change of the melt and crucible as pulling proceeds. The melt and crucible located in the A.D. Little puller, or in a corresponding resistance heated puller, are continuously weighed by a top-loading electronic balance which is read at 1 second intervals by the LSI-11/2 computer. A temperature reading from a digital thermomenter is also inputted to the control computer for emergency shutdown

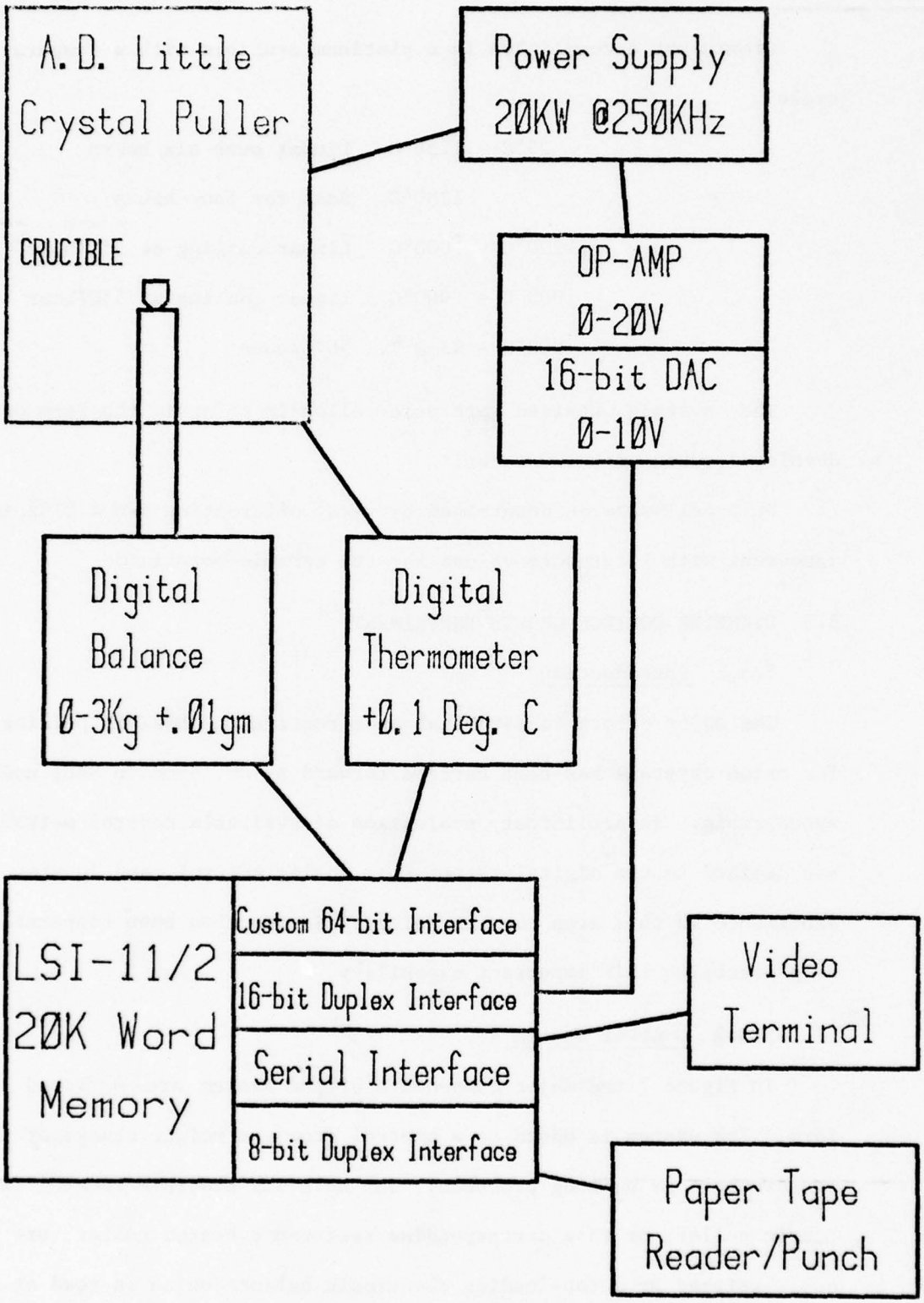
A.D. Little
Crystal Puller
CRUCIBLE
Power Supply
20KW @250KHz
OP-AMP
0-20V
16-bit DAC
0-10V
Digital
Balance
0-3Kg +.01gm
Digital
Thermometer
+0.1 Deg. C
LSI-11/2
20K Word
Memory
Custom 64-bit Interface
16-bit Duplex Interface
Serial Interface
8-bit Duplex Interface
Video
Terminal
Paper Tape
Reader/Punch

Figure 7

if necessary during pulling and to facilitate controlled cool-down after growth. A video terminal provides communication with the system.

In operation the computer reads the balance every second, then from accumulated readings it computes the rate of weight loss by a least squares fitting. This value is then compared to the desired loss (calculated from density and pulling rate) and the necessary correction control signal to the power supply calculated. In the inductive A.D. Little system power is controlled in the resistive heated system, then set point of the temperature controller is adjusted.

Preliminary tests on alkali halide crystals and with lead bismuth niobate show most encouraging results.

6. PROCESSING STUDIES

6.1 INTRODUCTION

Electrostriction and composite piezoelectrics studies on this program place continuing demands for the processing of new perovskite based ceramics and for the fabrication of conventional materials in new and unusual configurations. Our major involvement with PZT based ceramic systems has required careful study of the control of the partial pressure of PbO during sintering, and this study, which has been written up for publication, is presented in Appendix 16. The work also formed the basis of the MS thesis of K. Klicker in Ceramic Science.

An important step forward was the development of a new simple processing technique for making 3:3 connected PZT;plastic composites discussed earlier in Section 3 and Appendix 12.

Current studies are focused on the calcination reactions in the PZT system and on a more detailed evaluation of the sintering behavior.

6.2 CALCINING REACTION KINETICS IN PZT COMPOUNDS

This study is primarily concerned with the reaction mechanisms and reaction kinetics for the formation of $PbZrO_3$-$PbTiO_3$ ceramics from mixed oxide starting powders. The objective, besides obtaining a better understanding of the crucial forming reactions and their dependence on raw material parameters and processing conditions, was to determine the extent to which differences in the calcining conditions were reflected in the piezoelectric properties of the finished ceramic.

The composition $PbZr_{0.6}Ti_{0.4}O_3$ has been most thoroughly investigated. For this composition the constituent oxides were characterized by their phase purity, phase content, particle size, size and shape distributions, and surface areas. As well as these more normal indices, x-ray line broadening

has been used to give additional information on crystallite size and crystallite strain. These data are most important because the phenomenon of agglomeration can give confusing data using the simpler measuring methods. Particularly for the ZrO_2, modification of these parameters by high energy milling has been shown to have a profound effect on reaction kinetics.

Quantitative data of the phase assemblages at each stage of calcining have been obtained using the "matrix flushing technique" for x-ray diffraction analysis. Tests with artificial standards have shown this method to give better than 1% precision.

Kinetic data have been fitted using the Jonder equation for diffusion controlled reaction and activation energies obtained from Arrhenius plots of the rate constant for the $PbTiO_3$ and PZT formation.

Variations in the final electromechanical properties appear to be strongly related to the presence of incompletely reacted PbO solid solutions in the calcined powders and, as expected, to produce wider variations in properties as the composition is brought closer to the morphotropic composition.

6.3 SINTERING STUDIES ON PZT

This work was initiated to study (i) the effects of the phase distribution in calcined oxide powders on the sintering characterisics of $PbZr_{0.6}Ti_{0.4}O_3$; (ii) the effects of PbO vapor on the sintering; (iii) the mechanisms involved in the very early stages of sintering.

Isothermal sintering at 1,000, 1,100, 1,200, and 1,300°C for periods from 10 minutes to 12 hours, and dilatometer studies at constant 200°C/hour heating rate have been used to explore the densification of different starting phase assemblages.

Preliminary findings indicate (i) that densification and reactions to

complete the formation of the PZT can proceed independently; (ii) uncalcined and partially calcined oxide powders exhibit initial expansion during formation of $PbTiO_3$ and PbO solid solution phases; (iii) at very high heating rates the PbO solid solution phase is eliminated from the sequence.

7. PHENOMENOLOGICAL THEORIES

7.1 INTRODUCTION

The development of an elastic Gibbs function for the $PbZrO_3$:$PbTiO_3$ family materials using the ADAGE computer graphics system with the IBM 370: A description of this work has been submitted for publication in the Journal of Applied Physics. Detail of the fitting procedure used and of measurements of the spontaneous strains $x_{1(s)}$, $x_{2(s)}$, $x_{4(s)}$ have been given in a Ph.D. thesis by A. Amin (Phenomenological and Structural Studies of $PbZrO_3$:$PbTiO_3$ Ceramics, The Pennsylvania State University, November 1979).

Current work is concerned with

A. Measurement and prediction of the low temperature phase transitions for compositions close to Morphotropy.

B. Extension of the phenomenological function to include octahedral rotation coordinates and antiferroelectric sublattice polarizations.

C. Examination of the role of higher order electrostriction constants.

7.2 PHENOMENOLOGICAL AND NEUTRON DIFFRACTION STUDY OF LOW TEMPERATURE PHASE TRANSITIONS IN $PbZrO_3$:$PbTiO_3$

The Landau-Ginsburg-Devonshire phenomenology described above has been used to predict the low temperature course of the morphotropic boundary in PZT. The theory predicts that the phase boundary occurs at almost the same composition (Zr/Ti ratio) down to near 0°K. The extension of the single cell multicell (R3m-R3c) phase boundary in the rhombohedral phase field has been investigated by neutron diffraction in cooperation with Dr. E. Cox at Brookhaven. For a composition of $PbZr_{0.6}Ti_{0.4}O_3$ the diffraction data confirm that the transition is between 200°K and 9°K. Low temperature

pyroelectric measurements using the Chynoweth method exhibit a peak at 45 K identifying the transition point in this composition. Details of this work are given in Appendix 18.

7.3 EXTENSION OF THE THERMODYNAMIC PHENOMENOLOGY

The equations used earlier are based on the supposition of a simple proper ferroelectricity in $PbTiO_3$:$PbZrO_3$. They appear adequate for prediction of the properties for compositions up to $PbZr_{0.6}Ti_{0.4}O_5$ in the single cell phase fields. They are obviously inadequate to describe materials that exhibit the rhombohedral R3m-R3c phase transition, or for the high-zirconia antiferroelectric compositions.

We are now exploring the consequences of using an expanded two sublattice function, such as that used earlier by Cross for $(NaK)NbO_3$, and of including terms to describe the oxygen octahedral rotations as in the treatment by Axe for $SrTiO_3$ and by Darlington in $(KNa)NbO_3$.

7.4 HIGHER ORDER ELECTROSTRICTION

In simple proper ferroelectric crystals the elastic Gibbs function may be written in the form

$$\Delta G_1 = f(P_i) + f'(x_{ij}) - b_{ijk}P_1x_{jk} - Q_{ijkl}x_{kl}P_iP_j$$

where $f(P_i)$ is a power series expansion in components of P_i, including at least sixth power terms, $f(x_{ij})$ is the normal elastic stored energy and b_{ijk}, Q_{ijkl} the piezoelectric and electrostrictive couplings between polarization and stress.

For systems that stem from centric prototypes in which first order ferroelectric transitions obviously require the inclusion of 6th power terms in P, it appears unwise to consider only the 4th power cross terms (Q_{ijkl}). In current studies of 6th power cross terms of the form

$$-\Phi_{ijklmn} P_i P_j X_{xl} X_{mn} \qquad \text{and}$$

$$-\xi_{inklmn} P_i P_j P_k P_l X_{mn}$$

We have shown that in the $(Ba_{0.5}Si_{0.5})Nb_2O_6$ tungsten bronze the inclusion of the 6th order Φ_{ijklmn} terms explains well the electric bias effects on the elastic compliances in the high temperature paraelectric phase and the polarization dependence of the clamped compliances in the ferroelectric 4mm phase.

In bismuth titanate ($Bi_4Ti_3O_{12}$) a phenomenological analysis of the piezoelectric response in the single domain ferroelectric phase (m) clearly requires the inclusion of the 6th or ξ_{ijklm} terms to properly represent the symmetry in the lower temperature region.

8. FERROELECTRIC BICRYSTALS

8.1 INTRODUCTION

The objective of these studies is to produce "joining" between differently oriented ferroelectric crystals along an extended planar boundary to simulate as far as possible conditions that might occur at a crystallite: crystallite grain boundary in a ferroelectric ceramic. Since in normal ferroelectrics, the crystallite boundaries do encompass a wide range of perfection, width and chemical character, ranging from the near perfect joining along narrow angle grain boundaries in hot-forged single crystals to the very broad second phase inclusion in some deliberately diphasic materials, it is of interest to explore a broad range of joining techniques for a spectrum of different ferroelectric systems.

Over the past year we have still been in this exploratory mode working to generate representative planar bonded surfaces in triglycine sulfate [$(CH_2NH_2COOH)_3H_2SO_4$], quartz (SiO_2), lead potassium niobate, $PbKNb_3O_9$, $PbBiNb_5O_{15}$, $BaTiO_3$, and $LiNbO_3$.

8.2 PREPARATIVE STUDIES

8.2.1 Triglycine Sulfate

The preparation of bicrystals with bonding surfaces normal to the ferroelectric 'b' axis has proceeded along the lines outlined last year. In some 20 growth runs, only two good planar bonded crystal pairs were produced. For both of these cases, however, the interfacial region was $\sim$50 μmeters thick and obviously highly imperfect.

Dielectric measurements on capacitors with major surfaces cut normal to b, however, show a clear Curie-Weiss law, and analysis is now proceeding on the data to explore the permittivity thickness product.

8.2.2 Quartz (SiO_2)

To explore initial conditions for higher temperature diffusion controlled bonding, a number of tests were run using quartz crystal cuts as a nonferroelectric (but ferroic) model system. For the several orientations tried the crystals bonded most satisfactorily at temperature, but always cracked into many small pieces on traversing the β-α phase inversion at 573°C. Even with unconstrained single crystal samples, we find it most difficult to bring the crystal through the phase change intact, and it appears that the additional constraints in the bicrystal make this task exceedingly difficult.

8.2.3 Lead Potassium Niobate, Lead Bismuth Niobate

Using crystals kindly supplied by Dr. M. Brun, several attempts were made to bond simple 'c' axis cuts of PKN and PBN. Though again the crystals bond quite effectively at high temperature, the phase change at the Curie temperature in each case leads to catastrophic mechanical cracking.

8.2.4 Barium Titanate

A number of successful fabrication runs were carried out using Remeika flux grown 'c' plates of $BaTiO_3$. Unfortunately, in every case a detailed examination of the interface after bonding revealed pockets of flux segregated at the boundary surface during hot pressing.

We could not find pressing conditions that would bond the crystals without flux segregation, and further attempts with $BaTiO_3$ will be delayed until Czochralski grown crystals are available.

8.2.5 Lithium Niobate

For 'c' axis cuts of $LiNbO_3$ excellent bonding has been obtained by hot pressing at 1100°C, below the Curie temperature. In these crystals no problems

have been encountered in cooling, and optically clean interfaces are regularly reproduced.

Work is now in progress using single domain $LiNbO_3$ to explore the sign and orientation effects on the bonding. Following a visit by Dr. B. Auld from Stanford University, it is proposed to supply samples of the niobate bicrystals to Dr. Auld's group for evaluation by acoustic wave techniques.

8.3 CHARACTERIZATION

Most effort at this early stage has been committed to the fabrication of specimens. We have, however, been developing a cooperative program with Dr. Lawless in the Materials Science Department at the University of Virginia, to make use of their excellent facilities for transmission electron microscopy (TEM). Initial studies have been concentrated on PZT ceramics formed by the HIP process, to evaluate the ability of the TEM system to distinguish small second phase inclusions at the grain boundary and to give the Virginia group, who are more familiar with metal systems, experience with thinning and handling ceramics in the microscope.

Future work on this program will investigate domain/grain boundary interactions in the $PbZr_{0.6}Ti_{0.4}O_3$ and in the $LiNbO_3$ bicrystals.

9. PROGRAM ORGANIZATION: PERSONNEL AND EQUIPMENT

9.1 PERSONNEL

The people directly responsible for work on this program are summarized in Table 3. All activities are coordinated through the three co-principal investigators, L.E. Cross, R.E. Newnham and J.V. Biggers. Major responsibility for electrostriction studies is with L.E. Cross, who supervises the experimental activities by K. Uchino, J. Jang, and N. Setter. Theoretical work by B.N. Achar is under the direction of G. Barsch. Experimental and theoretical activities are kept in balance by regular meetings of this subgroup.

The composite piezoelectric studies are in general coordinated by R.E. Newnham, with B. Hardiman and A. Bhalla responsible for preparative and measurement aspects. Students involved with the composites include K. Klicker, T. Gururaja, A. Safari, K. Rittenmeyer and T. Shrout.

The many preparation and fabrication requirements are under the supervision of J.V. Biggers and W. Schulze working with B. Hardiman and L. Bowen. Students involved are T. Shrout, D. Hankey, K. Klicker, S. Venkataramani and A. Safari.

Phenomenological theoretical work is piloted by L.E. Cross, through A. Amin and K. Uchino. The small effort on grain oriented ceramics is supervised by R.E. Newnham, and the work carried through my M. Holmes.

Bicrystal studies are directed by L. Bowen working now with a visiting scientist from Peking, Dr. Yao Xi.

Excellent technical backup is provided by two technicians, R. Brenneman and R. Ormsby, and the cohesion of the group much aided by our secretary, S. LeFrancois.

In personnel, the group is now up to strength. Some minor rebalancing, however, will be required as our present postdoctoral fellows move through,

Table 3

DN BASIC PERSONNEL

FACULTY

L.E. CROSS, PROFESSOR OF ELECTRICAL ENGINEERING

R.E. NEWNHAM, PROFESSOR OF MATERIALS SCIENCE

G.R. BARSCH, PROFESSOR OF PHYSICS

J.V. BIGGERS, SENIOR RESEARCH ASSOCIATE

W.A. SCHULZE, ASSISTANT PROFESSOR OF CERAMICS AND MATERIALS RESEARCH

ASSOCIATES

B.N. ACHAR
A. BHALLA
L. BOWEN
B. HARDIMAN
K. UCHINO
A. AMIN

GRADUATE ASSISTANTS

T. GURURAJA
D. HANKEY (KODAK FELLOW)
M. HOLMES (BISMUTH INSTITUTE)
J. JANG*
K. KLICKER
K. RITTENMEYER
A. SAFARI (IRAN GOVERNMENT)
N. SETTER
T. SHROUT
S. VENKATARAMANI

TECHNICAL AIDES

R. BRENNEMAN
R. ORMSBY
S. LEFRANCOIS

to provide needed expertise in crystal growth and to open up new efforts on ferroelastic crystals and glass ceramics. It has been our decision to focus current major effort into the electrostriction and composite piezoelectric studies, and we believe that the results to date presented in this report justify that decision.

9.2 EQUIPMENT

Two major advances have been achieved over the current year:

1. The development, construction, and testing of the new high precision AC dilatometer. This instrument provides a unique capability for electrostriction measurements on simple solids and for detecting the nonlinear electrostriction contributions in simple piezoelectrics.

2. An HP9825 based automated measurement system has now been installed and the interfacing and software developed for:

(a) Measurements of dielectric permittivity and loss as a function of temperature and frequency, over a temperature range of 23°C to 1500°C and a frequency range of 100 Hz to 1 MHz. Measuring bridge and temperature program are under direct machine control. Output can be presented in tabulated form on a high-speed line printer or graphically on the HP four-color graphics terminal.

Graphical data can be scaled directly for reporting or presentation on viewgraph transparency.

(b) Electrical conductivity versus field and temperature: The measuring instrument used is a Keithley digital electrometer with interface to the HP 1B data bus. Current levels to 10^{-13} amps and potential up to 1000 volts can be encompassed.

(c) Pyroelectric measurement by the Byer-Roundy technique of controlled heating rate.

Currently we are evaluating a range of network analyzers from Hewlett Packard, Marconi and Tektronix, with a view to automating our measurements of the resonant response of piezoelectric crystals and ceramics.

Over the contract period an effort has been made to upgrade the precision of our electronic measurements by providing calibration facilities within the group for DC and AC voltage, time and frequency. Assistance has been provided for the development of a diameter control for Czochralski crystal growth, as discussed earlier in the text.

To facilitate the development of hydrophone-type materials, and to supplement data being provided for us by Charles LeBlanc and the group at New London we have designed and installed a very simple hydrostatic piezoelectric measuring system, using a pumped oil bath and a simple field effect integrator to determine charge release. The system is capable of repeated testing at pressures up to 5,000 psi.

During 1979 the Laboratory has acquired a new Philips automatic x-ray diffraction system, a Kevex x-ray fluorescence analyzer and a new IBSCA surface analysis facility. An ISI model 30 scanning microscope is on order, and this machine will have STEM capability. With these new facilities coming we believe that the group is in excellent shape for future characterization requirements on the new materials that are being developed.

9.3 ADVISORY COMMITTEE

The second meeting of the ONR Advisory Committee for this program was held at Penn State University on Monday and Tuesday, October 29th and 30th, 1979. Participants at the meeting were: A. Glass, Bell Telephone Labs; H. Anderson, University of Missouri-Rolla; B. Jaffe, Vernitron Corporation; W. Smith, Philips Laboratories; A. Diness, ONR, Washington; R. Pohanka, ONR,

Washington; P. Smith, NUSC, New London; R. Wollett, NUSC, New London. Participants from Penn State were L.E. Cross, J.V. Biggers, R.E. Newnham, B.R. Barsch, N. Achar, A. Amin, R. Betsch, A. Bhalla, L. Bowen, B. Hardiman, K. Hayashi, K. Klicker, W. Schulze, N. Setter and K. Uchino. Guests were J. Dougherty, Gulton Industries; R. Hansen, Litton Industries, and W. Harrison, Honeywell Ceramics Center.

The program of the meeting is outlined below:

ONR ADVISORY COMMITTEE MEETING

Monday, October 29
9:00 am to 12:30 pm

R. Pohanka	Introduction
L. E. Cross	Program outline, objectives and achievements
R. E. Newnham and K. E. Klicker	Composite Transducers
J. V. Biggers	New Processing for Composites. Discussion of present work and future possibilities for composite piezoelectrics

1:30 pm to 4:30 pm

Walk through Ferroelectric Labs

L. E. Cross	Electrostriction
K. Uchino and N. Setter	Experimental
G. R. Barsch	Theory
L. E. Cross	Phenomenological Theory
Discussion	

Tuesday, October 30
9:00 am to 12:00

C. LeBlanc	Measurements Taken at New London on Lamellar Electrostrictors. Polymer:Ceramic Composites. PVF2 Polymer Materials. Discussion of Data.

Proceedings of the group have been reported separately.

APPENDICES

EXPERIMENTAL ELECTROSTRICTION (Measurements)

1. K. Uchino and L.E. Cross. A High-Sensitivity AC Dilatometer for the Measurement of Piezoelect-icity and Electrostriction. Proc. 33rd Annual Symposium on Frequency Control, U.S. Army Electronics Command, Fort Monmouth, NJ (1979).

2. K. Uchino and L.E. Cross. A Very High Sensitivity AC Dilatometer for the Direct Measurement of Piezoelectric and Electrostrictive Constants. Ferroelectrics (in press).

3. K. Uchino, L.E. Cross and J.C. Hicks. Longitudinal Piezoelectric Strain Measurements of Polyvinylidene Fluoride Films.

4. K. Uchino, S. Nomura, L.E. Cross and R.E. Newnham. New Electrostrictive Materials for Displacement Transducers. J. Electronic Ceramics [Japan] (submitted).

5. K. Uchino, S. Nomura, L.E. Cross, S.J. Jang and R.E. Newnham. Electrostrictive Effect in Lead Magnesium Niobate Single Crystals. J. Appl. Phys. 51 (1980).

6. S.J. Jang, K. Uchino, S. Nomura and L.E. Cross. Electrostrictive Behavior of Lead Magnesium Niobate Based Ceramic Dielectrics (in press).

7. S. Nomura, J. Kuwata, K. Uchino, S.J. Jang, L.E. Cross and R.E. Newnham. Electrostriction in the Solid Solution System $Pb(Mg_{1/3}Nb_{2/3})O_3$-$Pb(Mg_{1/2}W_{1/2})O_3$. Phys. Stat. Sol. 57 (1980).

8. S. Nomura, K. Tonooka, J. Kuwata, R.E. Newnham and L.E. Cross. Electrostriction in $Pb(Mg_{1/3}Nb_{2/3})O_3$ Ceramics.

9. K. Uchino, S. Nomura, L.E. Cross and R.E. Newnham. An Estimate of Soft Modes in Relaxor Ferroelectrics.

COMPOSITES

10. R.E. Newnham, D.P. Skinner, K.A. Klicker, A.S. Bhalla, B. Hardiman and T. Gururaja. Ferroelectric Ceramic-Plastic Composites for Piezoelectric and Pyroelectric Applications. Proc. Int. Symp. Applications of Ferroelectrics, IEEE, Minneapolis, MN, June 1979.

APPENDICES
(Contd)

11. K.A. Klicker, J.V. Biggers and R.E. Newnham. Composites of PZT and Epoxy for Transducer Applications.

12. T.R. Shrout, W.A. Schulze and J.V. Biggers. Simplified Fabrication of PZT/Polymer Composites. Mat. Res. Bull. (submitted).

13. L.J. Bowen, T. Shrout, W.A. Schulze and J.V. Biggers. Piezoelectric Properties of Internally Electroded PZT Multilayers. Proc. Int. Symp. Applications of Ferroelectrics, Minneapolis, MN, June 1979.

14. T.R. Shrout, W.A. Schulze and James V. Biggers. Temperature Compensated Composite Resonator.

GRAIN ORIENTED

15. M. Holmes, R.E. Newnham and L.E. Cross. Grain-Oriented Ferroelectric Ceramics. Ceram. Bull. 58(9) 872 (1979).

PROCESSING STUDIES

16. K.A. Klicker and J.V. Biggers. Control of the Partial Pressure of PbO During the Sintering of PZT Ceramics.

PHENOMENOLOGICAL THEORY

17. A. Amin, R.E. Newnham and L.E. Cross. Phenomenological and Structural Study of a Low Temperature Phase Transition in the $PbZrO_3$-$PbTiO_3$ System.

MISCELLANEOUS

18. L.L. Tongson, A.S. Bhalla, L.E. Cross and B.E. Knox. Investigation of $BaTiO_3$ and $Gd_2(MoO_4)_3$ Crystal Surfaces by Complementary AES and ISS Techniques. Appl. Surf. Sci. (accepted).

19. K. Takahashi, L.H. Hardy, R.E. Newnham and L.E. Cross. Pyroeffect in $PbGe_3O_{11}$ and $Pb_5Ge_2SiO_{11}$ Crystals Prepared by Glass Recrystallization.

APPENDIX 1

K. Uchino and L.E. Cross. A High-Sensitivity AC Dilatometer for the Measurement of Piezoelectricity and Electrostriction. Proc. 33rd Annual Symposium on Frequency Control, U.S. Army Electronics Command, Fort Monmouth, NJ (1979).

A HIGH-SENSITIVITY AC DILATOMETER FOR THE DIRECT MEASUREMENT OF PIEZOELECTRICITY AND ELECTROSTRICTION

Kenji Uchino and Leslie E. Cross
Materials Research Laboratory, The Pennsylvania State University
University Park, Pennsylvania

Summary

A capacitance type dilatometer has been constructed which is capable of resolving low frequency AC linear displacements of 10^{-13} meters (0.001Å) and can be used for the direct measurement of piezoelectric and electrostrictive deformations.

The sensing element of the dilatometer system is a parallel plate capacitor with sputtered platinum electrodes supported on fused silica optical flats. Changes of plate separation are sensed by the associated change in dielectric capacitance which is monitored by a capacitance bridge. Slow drift in the capacitance due to thermally induced changes in the plate separation are reduced to an equivalent plate separation change of less than ±0.002Å/minute by a DC servo actuated by the bridge unbalance signal which corrects the capacitor plate position through ceramic piezoelectric PZT pushers.

For AC measurement, one plate of the dilatometer is driven along the axis of the capacitor at a frequency of 14 Hz by a standard piezoelectric quartz crystal. The second plate of the sensing capacitor is driven in phase at the same frequency by the piezoelectric or electrostrictor of interest. A narrow band phase locked detector isolates and amplifies the 14 Hz signal detected in the unbalance output of the bridge detector. By adjusting the magnitudes of the AC voltage applied to the standard and the unknown crystals to produce a null response at 14 Hz, the electromechanical constants of the two crystals can be compared with very high precision.

Some examples are given of piezoelectric and electrostrictive crystals and ceramics which have been measured on the instrument.

Introduction

Electrostriction which is the basic electromechanical coupling in all non-piezoelectric solids is at present very poorly understood. There are few reliable data for the separate components of the electrostriction tensor even in simple solids, and there is no theory which is adequate even for alkali halide crystals. Experimentally, the difficulty is clearly associated with the very small magnitude of the electrostrictive strains even at the highest possible field levels in simple low permittivity solids. Theoretically the absence of well authenticated experimental values has certainly been a major disincentive to development and none of the present theories is viable.

The instrument described in this paper has been designed to resolve AC linear displacements of 10^{-13} meters (10^{-3} Å) and to permit the precise measurement of the very small electrostrictive strains in low permittivity solids. (The work is a preliminary part of a larger program in the Materials Research Laboratory which focuses upon both the experimental measurement and the theoretical description of electrostriction.) The AC differential capacitance dilatometer which has been constructed is based upon an early design by Bohatý and Haussühl.[1]

In this paper, the principle of the capacitance dilatometer is described first, the DC servo stabilization of the sensing capacitor which is the key to improved stability and sensitivity discussed, and the experimental arrangement detailed. The development of a unique new AC calibration capacitor is briefly described and finally some examples are given of piezoelectric and electrostrictive crystals and ceramics which have been measured on the instrument.

Design of the Capacitance Dilatometer

The scheme of the dilatometer is shown in Fig.1. The strain sensing capacitor consists of two platinum sputtered fused silica plates (2" diameter). The electrostrictive (or piezoelectric) sample plated with sputtered platinum electrodes is rigidly mechanically connected through an insulating lucite support to the right plate of the sensing capacitor. If the sample crystal is driven electrically, the right plate will be excited mechanically through the electrostrictive (or piezoelectric) strain generated in the crystal. A standard piezoelectric crystal is mounted in a similar manner so that the piezoelectrically generated strain is communicated to the left plate. Since the sensing capacitance C is given by

$$C = \varepsilon \frac{A}{\ell} \qquad (1)$$

where ε is the permittivity of air at atmospheric pressure, A the plate area, and ℓ the separation, the capacitance change ΔC associated with a small change in ℓ ($\Delta\ell$) will be given by

$$\Delta C = \left(-\frac{\varepsilon A}{\ell^2}\right)\Delta\ell = K\Delta\ell \qquad (2)$$

If the electrostrictive and the piezoelectric standard crystals are driven with AC voltages at frequencies of ω and 2ω, both capacitor plates will be excited mechanically at a frequency of 2ω. When the phase and amplitudes of the electric fields of both crystals are suitably chosen, the capacitor plates will vibrate in exact synchronism producing a net zero modulation of the separation and thus of the capacitance at 2ω. Figure 2 shows the crystal deformations in the piezoelectric standard and the electrostrictive sample at the null condition. Clearly, if this null condition can be precisely established, then from the AC voltages applied to both crystals, their known dimensions and the piezoelectric coefficient of the standard crystal (quartz) the unknown electrostrictive coefficient can be calculated. For the piezoelectric sample the situation is slightly different.

A simple block diagram of the full measuring system is given in Fig. 3. The components of the mechanical circuit (a,b,c,d) are identical in principle to those used by Bohatý and Haussühl.[1] However, to sense and control the capacitor (b,c) a General Radio 1620 capacitance measuring assembly is used (j,k,l). To obtain maximum sensitivity, the capacitance bridge is operated at a frequency of 5 kHz, the standard piezoelectric crystal is driven at 14 Hz and the electrostrictor under study at 7 Hz. The phase locked detector is locked to the 14 Hz driving oscillator.

DC Servo Stabilization

Obviously the sensitivity constant K in Eq (2) can be made very large if the separation ℓ can be made very small. In a practical system, however, a limiting value of ℓ is set by slow dimension changes due to thermal drift. Even though the mechanical support for the sensing capacitor is made from super invar with a very small thermal expansion coefficient ($\lesssim 0.3 \times 10^{-6}$ deg^{-1}), and the assembly is put into a chamber controlled to ± 0.04°C, thermal dimension changes are still very much larger than the electrostrictive displacements induced at tolerable fields, and would take the bridge detector well out of its linear range. To overcome this problem, a DC output from the phase locked bridge detector is used to operate a Burleigh RC42 servo amplifier which actuates three parallel piezoceramic mechanical actuators made of PZT controlling the static plate separation (bc).

Instrument Examinations

Servo-Positioner Check

After the system has stabilized for some four hours, the DC servo system is disabled and the intrinsic drift rate of the capacitance determined by measuring the bridge unbalance signal as a function of time (Fig. 4). By rebalancing the bridge periodically the capacitance increment for a given unbalance voltage can be determined, and from the ΔC a corresponding $\Delta\ell$ can be calculated. It is evident from Fig. 4 that without compensation the drift rate corresponds to a plate separation change of 1 Å/minute. Maintaining the same conditions, the DC servo is now turned on, and at the same gain setting no drift is discernible. Turning the gain up by a factor of 100, however, (Fig. 4, right-hand scale) it is evident that the drift rate now corresponds to a linear dimension change of 0.002Å/minute.

Resolution Check

To check the AC sensitivity the standard quartz crystal was driven by a Wavetek Model 142 oscillator at 14 Hz. With 30 volts rms applied to the bridge, the lock-in output as a function of voltage applied to the quartz crystal is given in Fig. 5. The linear relation expected for a piezoelectric is clearly evident. Right-hand scale shows the actual deformation of the quartz crystal in Å rms, calculated by use of the absolute calibrator that will be discussed later. The experimental error is much smaller than the solid circles and is about ± 0.1 mV, which corresponds to $\pm 10^{-3}$ Å. This value is the smallest resolvable increment at present. Taking the quartz thickness value of $\ell = 5.45$ mm, the resolvable increment corresponds to the resolvable strain $\Delta\ell/\ell = \pm 2.10^{-11}$.

Further Checks

The lock-in output for a fixed value of drive voltage to the quartz standard (10.8 V rms) was recorded as a function of capacitor plate separation (Fig. 6) and of voltage applied to the capacitance bridge (Fig. 7). If the measured signal comes only from the capacitance bridge unbalance, this should scale linearly with the square of capacitance and with the bridge oscillator voltage as is evident in Figs. 6 and 7. A slight anomaly observed at 110 pF in Fig. 6 is caused by the sensitivity dial change of the capacitance bridge.

AC Calibration Capacitor

We have described, so far, a system in which the known piezoelectric coefficient of a standard quartz crystal has been used to calibrate the AC voltage output in terms of a calculated plate separation change. We propose a different way of deriving the sensitivity by using a very small 3-terminal variable air capacitor which can be driven at low AC. Figure 8 shows the principle of the absolute calibrator using an alternating capacitance. When the capacitor plate is driven mechanically by the electromechanically generated strain in the crystal (I), the capacitance bridge output (5 kHz) is modulated at 14 Hz as in the bottom figure. If we use the small alternating capacitance connected in parallel to the sensing capacitor instead of driving the sample (II), the same order of modulated output can be established. If we measure the lock-in output by driving this alternating capacitance, from the known alternating capacitance change and the capacitance of the sensing capacitor, we can calculate the equivalent AC linear deformation using Eq (2). The scheme of the alternating capacitance generator designed is shown in Fig. 9. The capacitance is made in a completely shielded aluminum box. When the central circular aluminum plate is in the vertical position, no electric flux can thread between the needles and the capacitance is almost equal to zero. In the horizontal position the capacitance shows a maximum. By rotating the

aluminum plate with a constant speed motor (Electro-Craft Motomatic System), a sinusoidal capacitance change (3-26 aF) can be obtained as shown in the bottom figure. The reference signal to the phase locked detector is produced by the photodiode and the rotating shutter fixed on the rotating axis.

If we obtain the lock-in output of V_{ACG} mV by driving the alternating capacitance generator under one instrument condition with the sensing capacitor of C pF, the sample crystal deformation in Å rms corresponding to the unit lock-in output in mV can be calculated as follows when measured under the same condition:

$$\left(\frac{\Delta \ell}{V_{ACG}}\right) = \frac{1430}{V_{ACG}\, C^2} \text{ [Å/mV]} \qquad (3)$$

Sample Measurements

To get the unknown piezoelectric or electrostrictive coefficient, there are three different ways of using the present instrument:

1. Absolute Calibration
   (using alternating capacitance generator)
2. Relative Calibration
   (using standard quartz driving)
   A. Separate vibrating method
   B. Null condition method
3. Sign Determination of Electrostrictive Coefficient
   (using electrostrictive standard PMN driving)

Absolute Calibration

By using the output from the alternating capacitance generator, the deformation corresponding to the lock-in output can be calculated. The piezoelectric or electrostrictive coefficient will, therefore, be given as follows:

$$d = \left(\frac{\Delta \ell}{V_{ACG}}\right) \times 10^{-10}\, V_{P,OUT}/V_{P,IN} \text{ [mV}^{-1}\text{]} \qquad (4a)$$

or

$$M = \sqrt{2}\left(\frac{\Delta \ell}{V_{ACG}}\right) \times 10^{-10}\, \ell_E\, V_{E,OUT}/V_{E,IN}^{\,2} \text{ [m}^2\text{V}^{-2}\text{]} \qquad (4b)$$

where V_{OUT} is the lock-in output voltage in mV, V_{IN} is the voltage applied to the sample in V rms and ℓ the thickness of the sample in m. Figure 5 is a good example for the piezoelectric case. We obtained the piezoelectric coefficient of quartz as $d_{11} = 2.27 \pm 0.01 \times 10^{-12}$ mV^{-1} from the data.

Separate Vibrating Method

The lock-in output was recorded separately for the piezoelectric wurtzite and quartz under the optimum condition (Fig. 10). By using the output ratio of wurtzite and quartz at the same applied voltage and the quartz piezoelectric coefficient, the wurtzite piezoelectric coefficient can be calculated as follows:

$$d_S = \frac{V_{S,OUT}}{V_{Q,OUT}}\, d_Q \qquad (5)$$

Null Condition Method

With a fixed value of drive voltage to the wurtzite sample, the lock-in output as a function of voltage applied to the standard quartz crystals was measured (Fig. 11). The null condition is established at the output minimum position. By using the ratio of the voltage applied to the wurtzite and the minimum position voltage and the quartz piezoelectric coefficient, the wurtzite coefficient can also be calculated as follows:

$$d_S = \frac{V_{Q,IN}}{V_{S,IN}}\, d_Q \qquad (6)$$

where crystal driving voltages are treated as root mean square values. Both methods gave the same value of the wurtzite piezoelectric coefficient ($d_{33} = 3.20 \pm 0.02 \times 10^{-12}$ mV^{-1}).

Figures 12 and 13 show the data for the electrostrictive sample $Pb(Mg_{1/3}Nb_{2/3})O_3$ ceramic. Lock-in output was completely proportional to the square of applied voltage (Fig.12). Very clear null condition can also be obtained at about 100 V rms to the standard quartz (Fig. 13). In this case the electrostrictive coefficient is calculated as follows:

$$M_S = \sqrt{2}\, \ell_S d_Q V_{Q,IN}/V_{S,IN}^{\,2} \qquad (7)$$

where $V_{S,IN}$ and $V_{Q,IN}$ are voltages applied to the sample and to quartz standard at the output minimum position, ℓ_S the sample thickness.

It is worth mentioning here that in a practical case, however, the lock-in output minimum is not exactly equal to zero because of a slight phase difference between the vibrations of both crystals. The details are discussed in the appendix.

Sign Determination of Electrostrictive Coefficient

To determine the sign of the unknown electrostrictive coefficient is rather complicated in a system which consists of the piezoelectric standard and the unknown electrostrictor, not only because the electric field frequency applied to the sample is different from the frequency for the standard, but also because the vibrational phase of the piezoelectric has two possibilities (180° difference) due to the crystal setting. We propose to use a known electrostrictor as a standard instead of quartz crystal, since the electrostrictive strain is not affected by 180° setting difference.

$Pb(Mg_{1/3}Nb_{2/3})O_3$ ceramic with perovskite-type structure is one of the best examples, which has a positive electrostrictive coefficient ($M = 1.05 \pm 0.01 \times 10^{-16}$ m^{2}V^{-2}).[2]

Example Data and Discussion

Some example data of piezoelectric and electrostrictive crystals and ceramics measured by the established instrument are listed in Table I, compared with the previous data. Coincidence between the values determined by the present and previous works for quartz and wurtzite indicates the precision of the established instrument. It is worth mentioning that the error is ten times smaller than the ones in the previous works. We emphasize that the resolution of ±0.001Å is equal to the greatest one in the world and corresponds to the resolvable strain $\Delta\ell/\ell \leq \pm 10^{-10}$, the order of which other measurements (e.g. x-ray diffractometer) cannot attain to.

Further measurements about many samples including alkali halide crystals will be made in the near future.

Acknowledgments

This work was sponsored by the Office of Naval Research through Contract N00014-78-C-0291. We also wish to thank our colleague Dr. Barsch at the Materials Research Laboratory for his many samples.

References

1) Bohatý, L. and Haussühl, S. (1977) Acta Cryst. A33, 114.
2) Cross, L.E., Jang, S.J., Newnham, R.E., Nomura, S. and Uchino, K. Ferroelectrics (submitted).
3) Bottom, V.E. (1970) J. Appl. Phys. 41, 3941.
4) Kobyakov, I.B. and Pado, G.S. (1968) Soviet Phys. Solid State 9, 1707.
5) Chang, Z.P. and Barsch, G.R. (1976) IEEE Trans.-Sonics and Ultrasonics 3, 127.

Appendix

Superposition of Two Waves with Different Phases

When a_1 and a_2 are the amplitudes of AC deformations of the sample and the standard crystals respectively and δ the phase difference, the change of the sensing capacitor separation $\Delta\ell$ will be given as follows:

$$\begin{aligned}\Delta\ell &= a_1 \sin \omega t - a_2 \sin(\omega t+\delta) \\ &= (a_1 - a_2 \cos\delta) \sin\omega t - a_2 \sin\omega \cos\omega t \\ &= [a_1^2 - 2a_1a_2 \cos\delta + a_2^2]^{1/2} \sin(\omega t - \psi) \qquad (8)\end{aligned}$$

where $\tan\psi = a_2 \sin\delta / (a_1 - a_2\cos\delta)$.

$[1-2r\cos\delta+r^2]^{1/2}$ term represents, therefore, the normalized shape of the dilatometer output curve as a function of driving voltage applied to the quartz standard. Figure 14 shows the theoretical calculation of the null condition method for various phase differences.

Table I. Some example data of electromechanical coefficients

Sample	Coefficient	Present	Previous
Quartz <100>	d_{11} ($\times 10^{-12}$ mV^{-1})	+2.27 (±0.01)	+2.27[3]
Wurtzite <001>	d_{33} ($\times 10^{-12}$ mV^{-1})	+3.20 (±0.02)	+3.2 (±0.2)[4]
Berlinite <100>	d_{11} ($\times 10^{-12}$ mV^{-1})	-3.98 (±0.05)	-5.3 (±1.6)[5]
$Pb(Mg_{1/3}Nb_{2/3})O_3$ (ceramic)	M'_{11} ($\times 10^{-16}$ m^2V^{-2})	+1.05 (±0.01)	+1.4 (±0.2)[2]

Figure Captions

Fig. 1 Schematic of the capacitance dilatometer and support structure.

Fig. 2 Crystal deformations induced in the piezoelectric and the electrostrictor at null condition.

Fig. 3 Schematic diagram of the AC dilatometer.

Fig. 4 DC plate separation change $\Delta\ell$ as a function of time with and without the drift compensation servo amplifier.

Fig. 5 Dilatometer output and the actual deformation as a function of driving voltage applied to the quartz standard crystal.

Fig. 6 Dilatometer output as a function of capacitor plate separation.

Fig. 7 Dilatometer output as a function of bridge oscillator voltage for fixed 10.8 V rms applied to the quartz crystal.

Fig. 8 Principle of the absolute calibrator. (I) sample driving; (II) equivalent alternating capacitance.

Fig. 9 Scheme of the alternating capacitance generator.

Fig. 10 Separate vibrating method for wurtzite and quartz.

Fig. 11 Null condition method between wurtzite and quartz.

Fig. 12 Dilatometer output as a function of square of driving voltage applied to $Pb(Mg_{1/3}Nb_{2/3})O_3$ ceramic.

Fig. 13 Null condition method between PMN and quartz.

Fig. 14 Theoretical calculation of the null condition method for various phase differences between the sample and the standard vibrations.

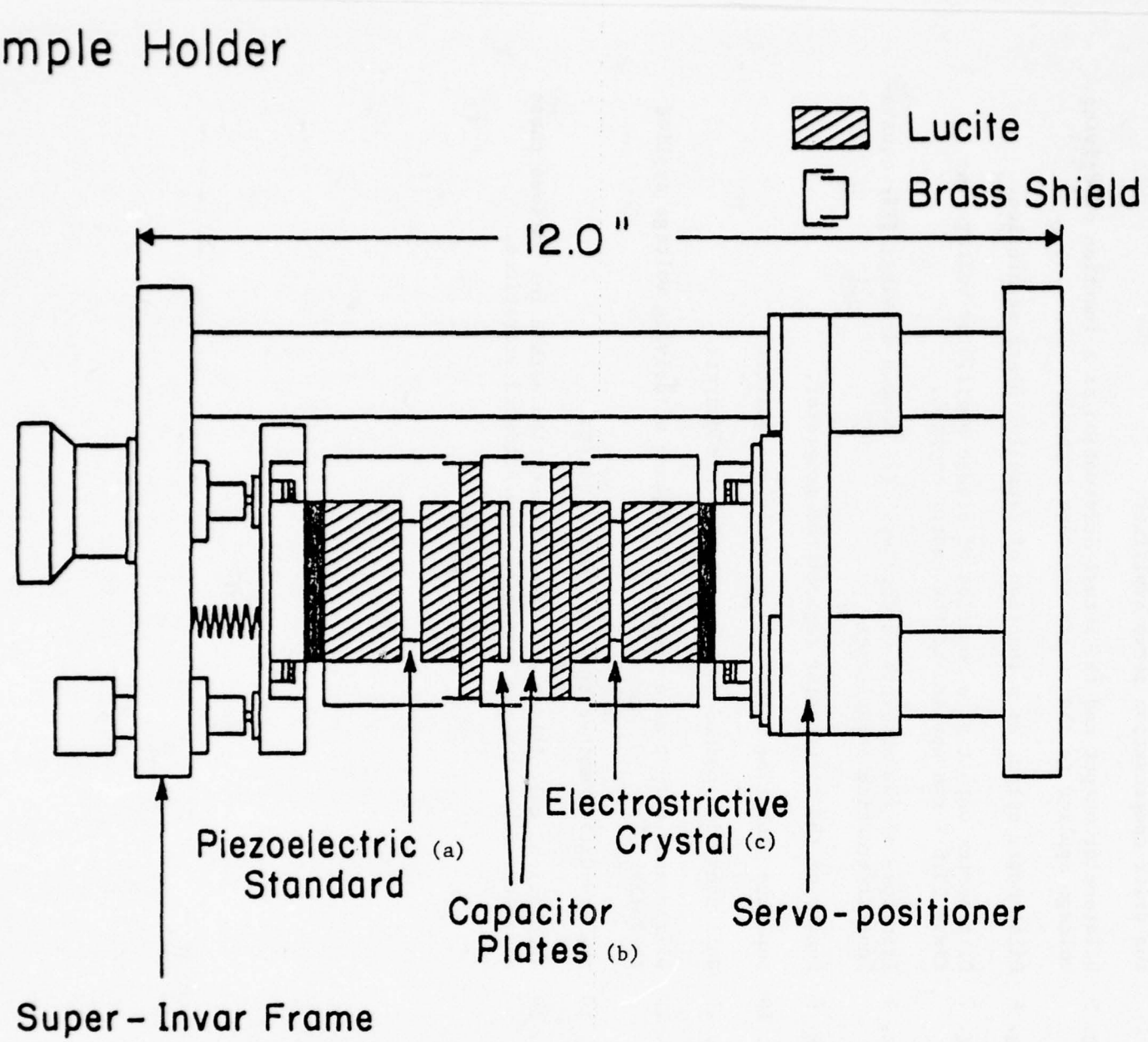

Figure 1. Schematic of the dilatometer and support structure.

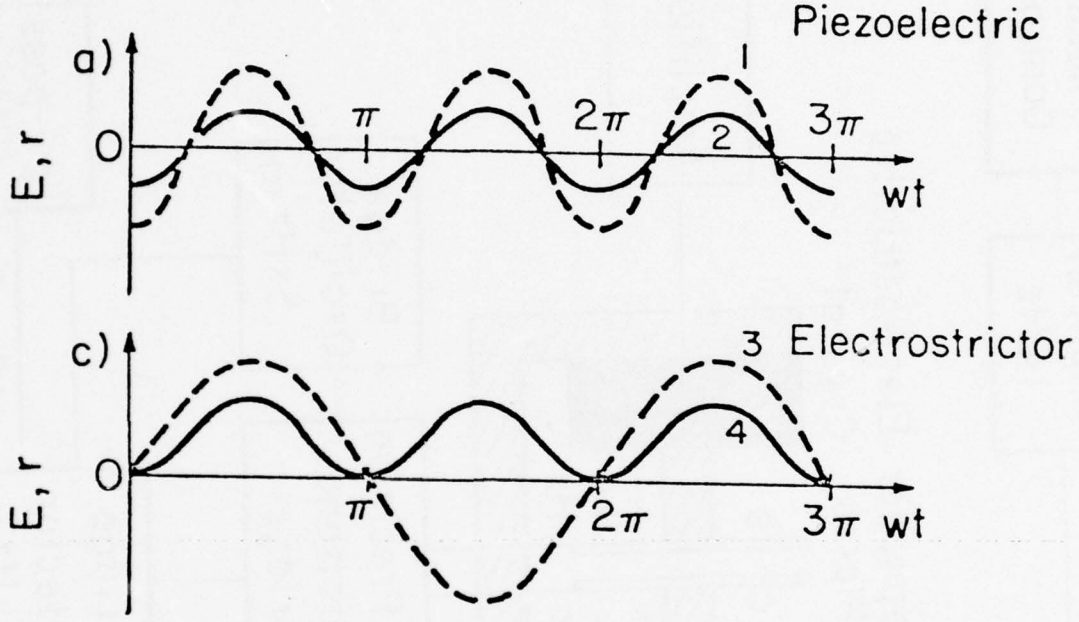

1) time dependence of electric field
2) strain induced in a piezoelectric sample
3) time dependence of electric field
4) strain induced in an electrostrictive sample

Figure 2

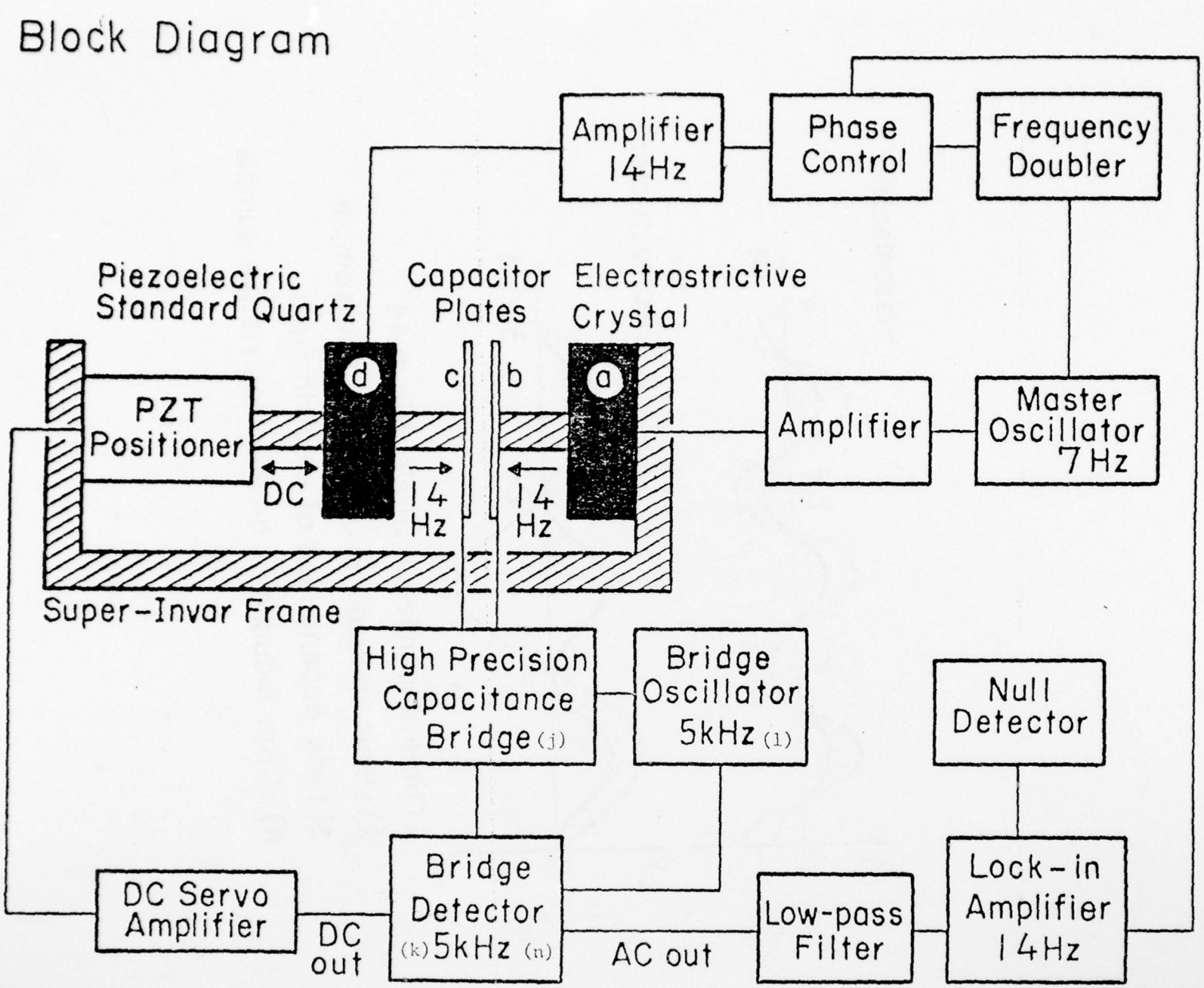

Figure 3. Schematic diagram of the AC dilatometer.

SERVO-POSITIONER CHECK

TEMPERATURE FLUCTUATION $\Delta T \sim \pm 0.04^{o}C$

CAPACITOR PLATES GAP CHANGE $\Delta l \sim \pm 20$ Å

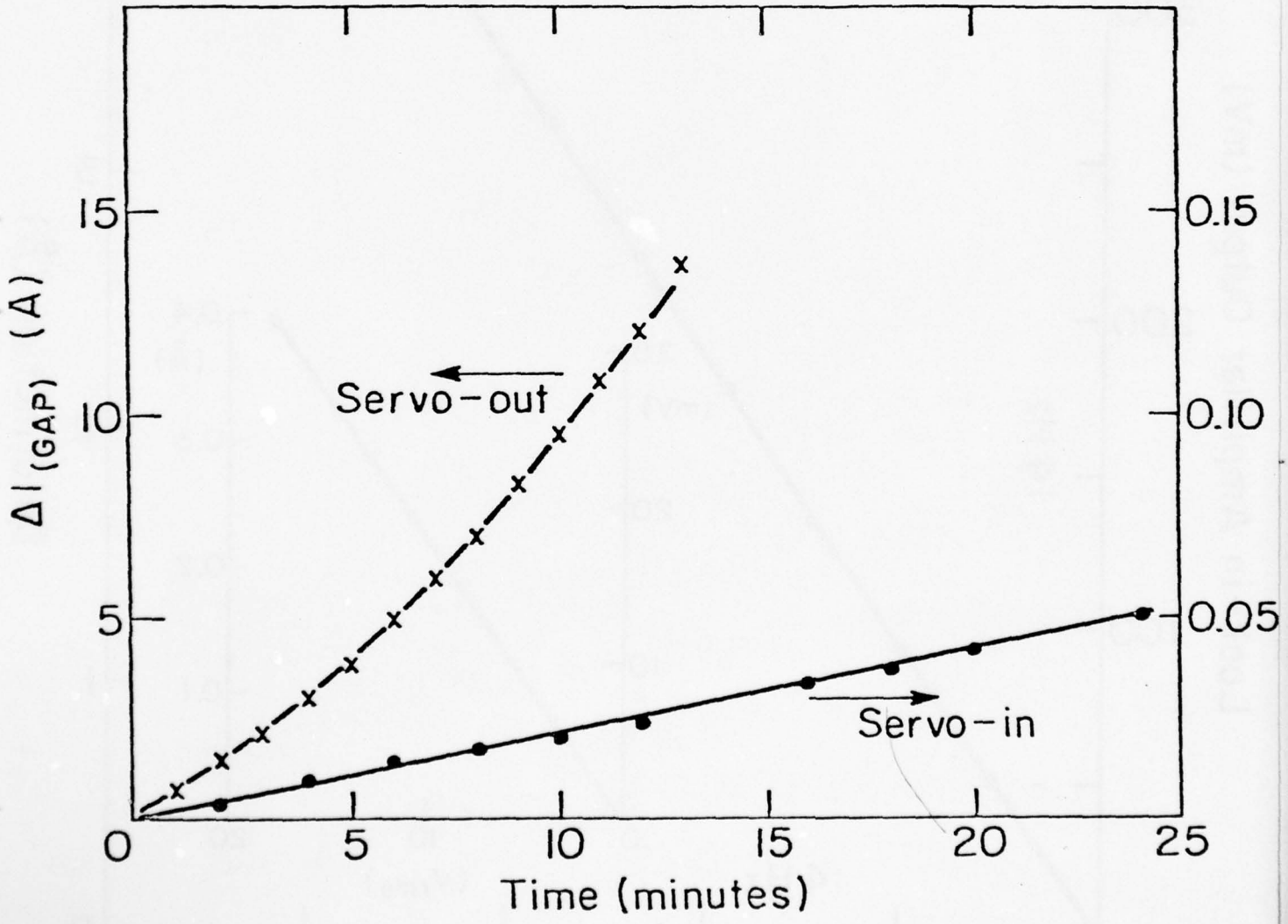

Figure 4. DC plate separation change $\Delta\ell$ as a function of time with and without the drift compensation Servo amplifier.

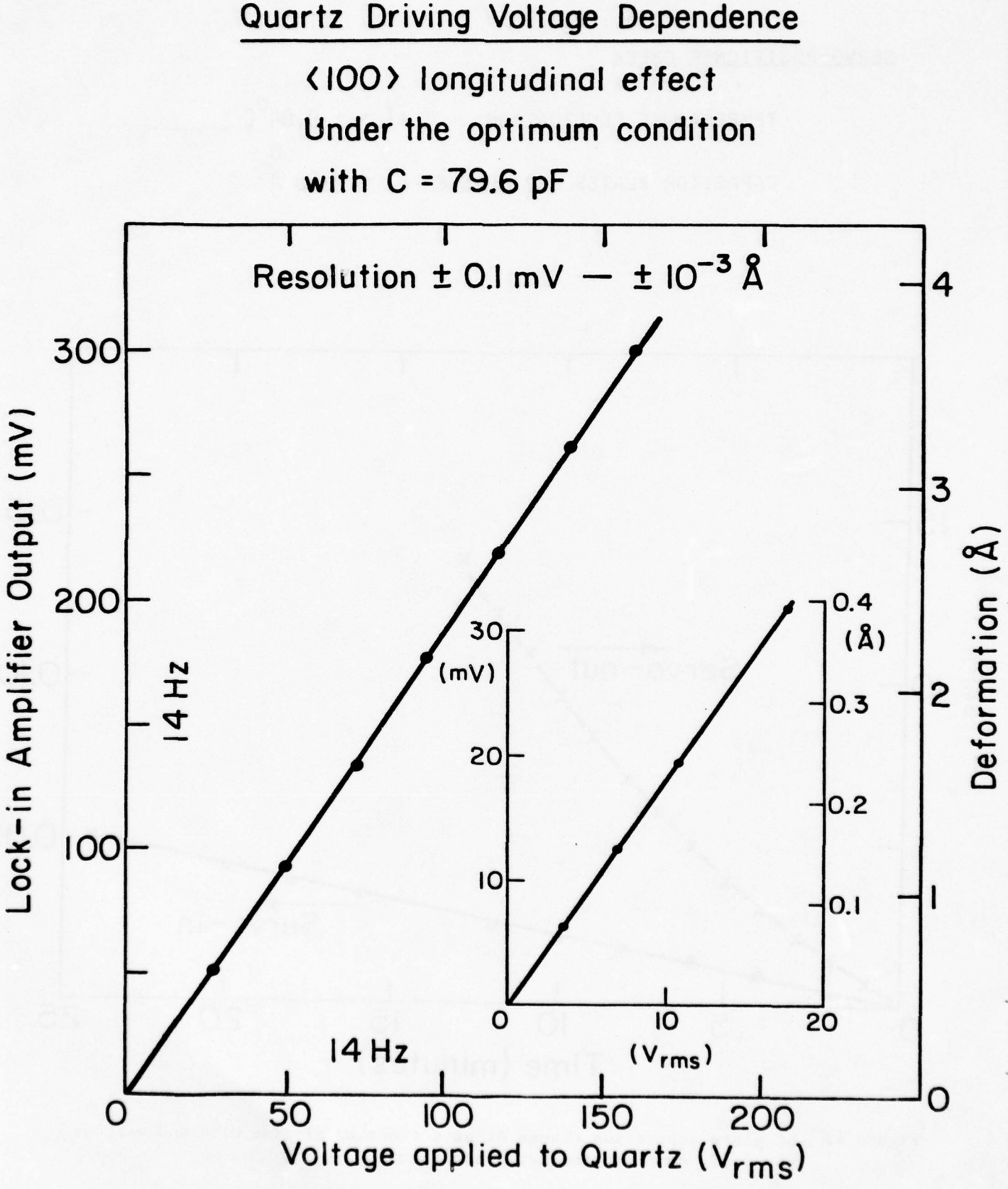
Quartz Driving Voltage Dependence
⟨100⟩ longitudinal effect
Under the optimum condition
with C = 79.6 pF
Resolution ± 0.1 mV — ± 10⁻³ Å
Lock-in Amplifier Output (mV)
Deformation (Å)
14 Hz
14 Hz
(mV)
(Å)
(Vrms)
Voltage applied to Quartz (Vrms)
0
50
100
150
200
300
1
2
3
4
10
20
30
0.1
0.2
0.3
0.4

Figure 5

Capacitor Plates Gap Dependence

measured by Standard Quartz Driving

Lock-in Amp. Output $\propto \Delta C = \left(-\frac{\Delta \ell}{\epsilon_0 A}\right) C^2$

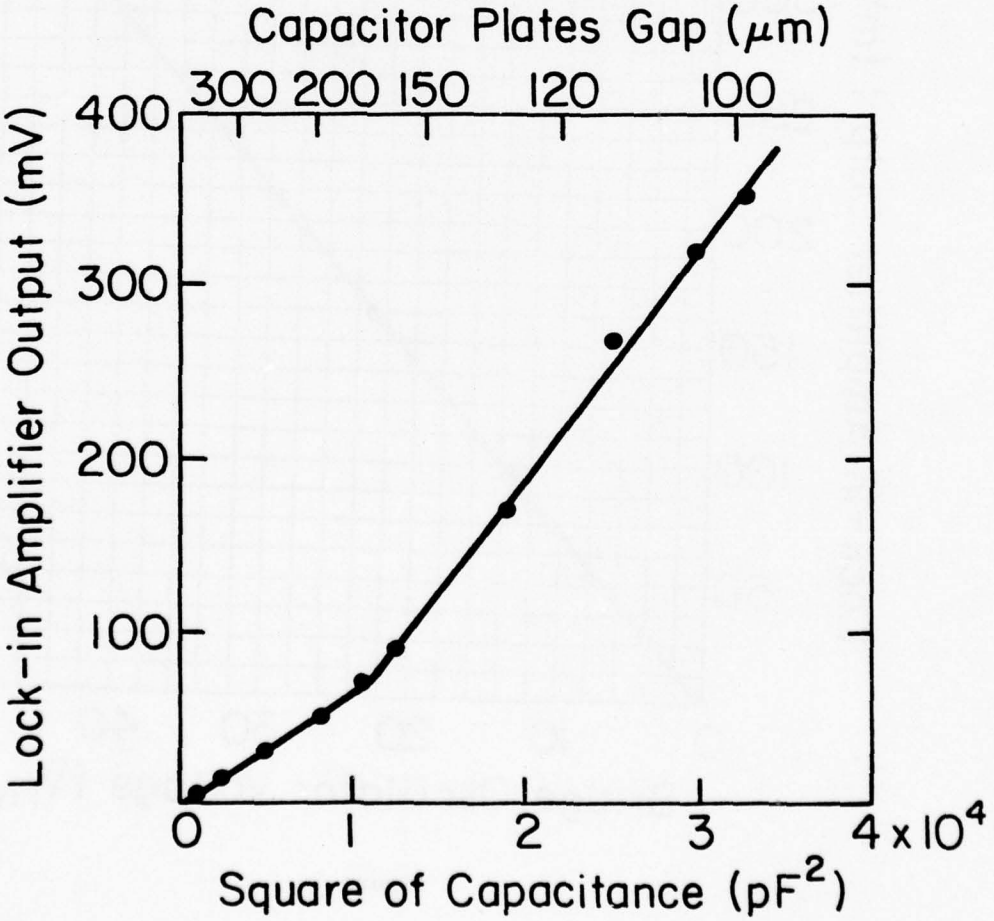

Figure 6

Bridge Oscillator Voltage Dependence

measured by Standard Quartz Driving

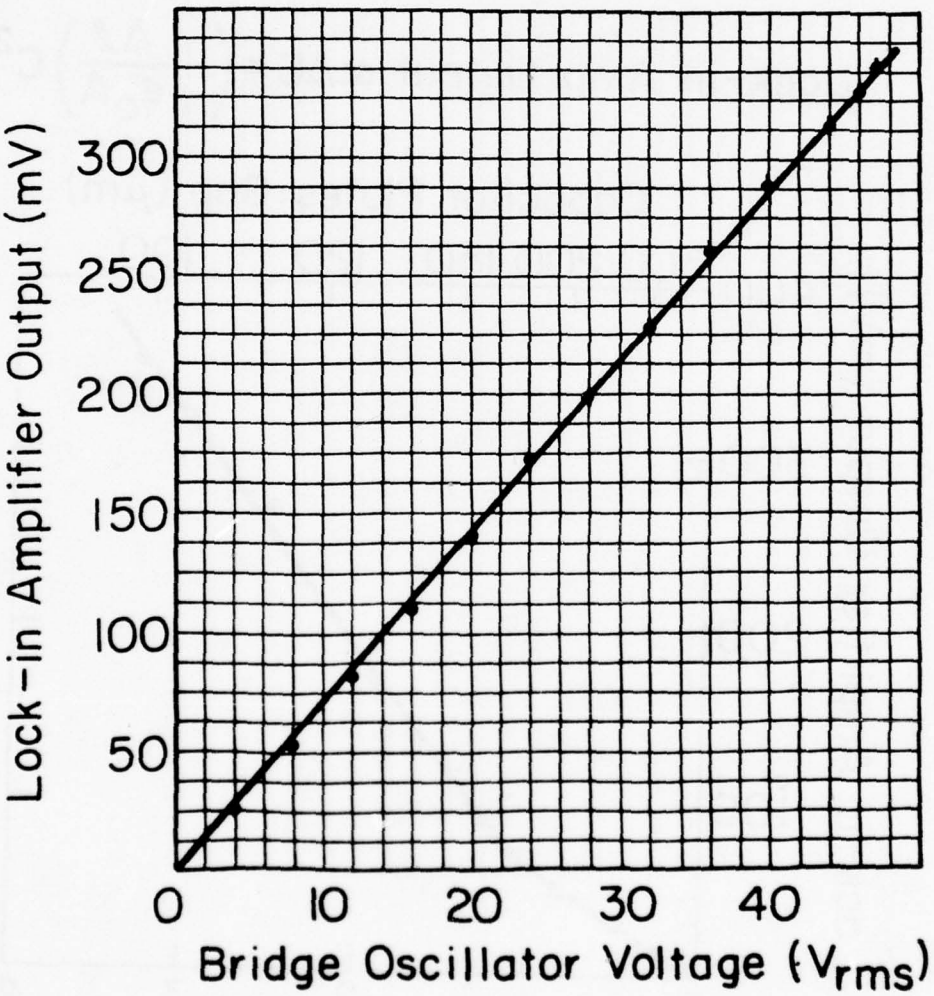

Figure 7

Principle of Absolute Standard using Alternating Capacitance

I) Sample Driving

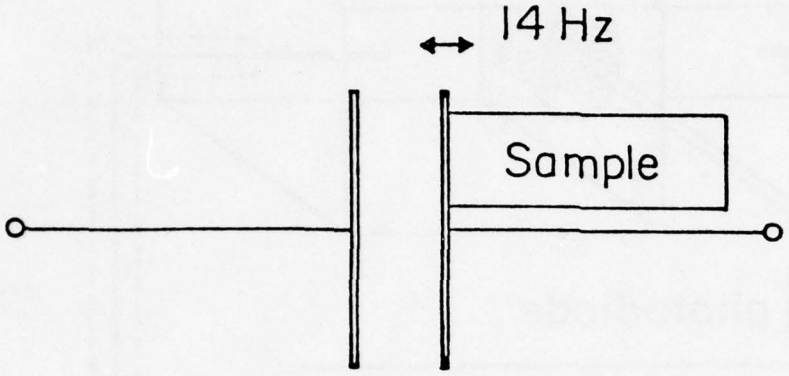

II) Equivalent Alternating Capacitance

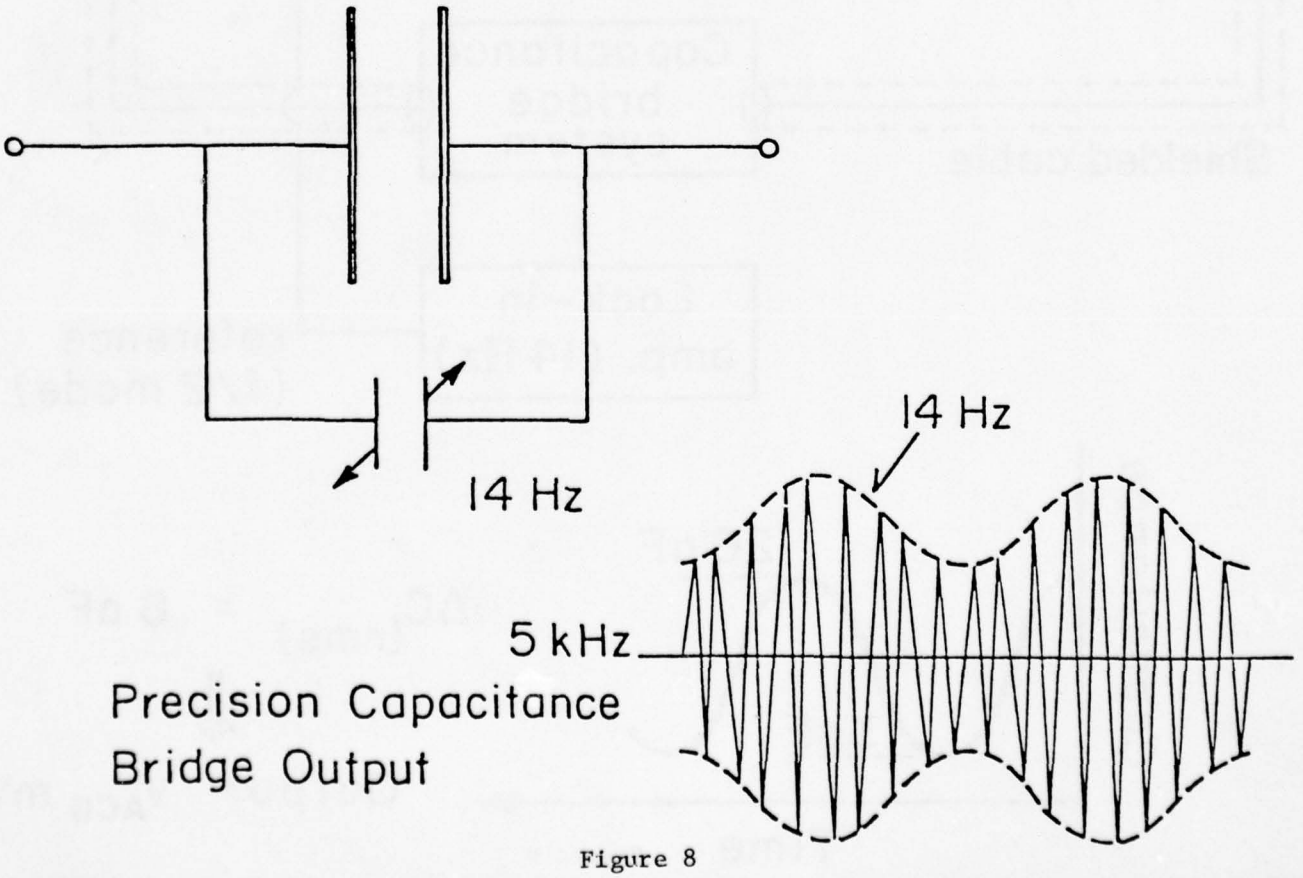

Figure 8

Alternating Capacitance Generator

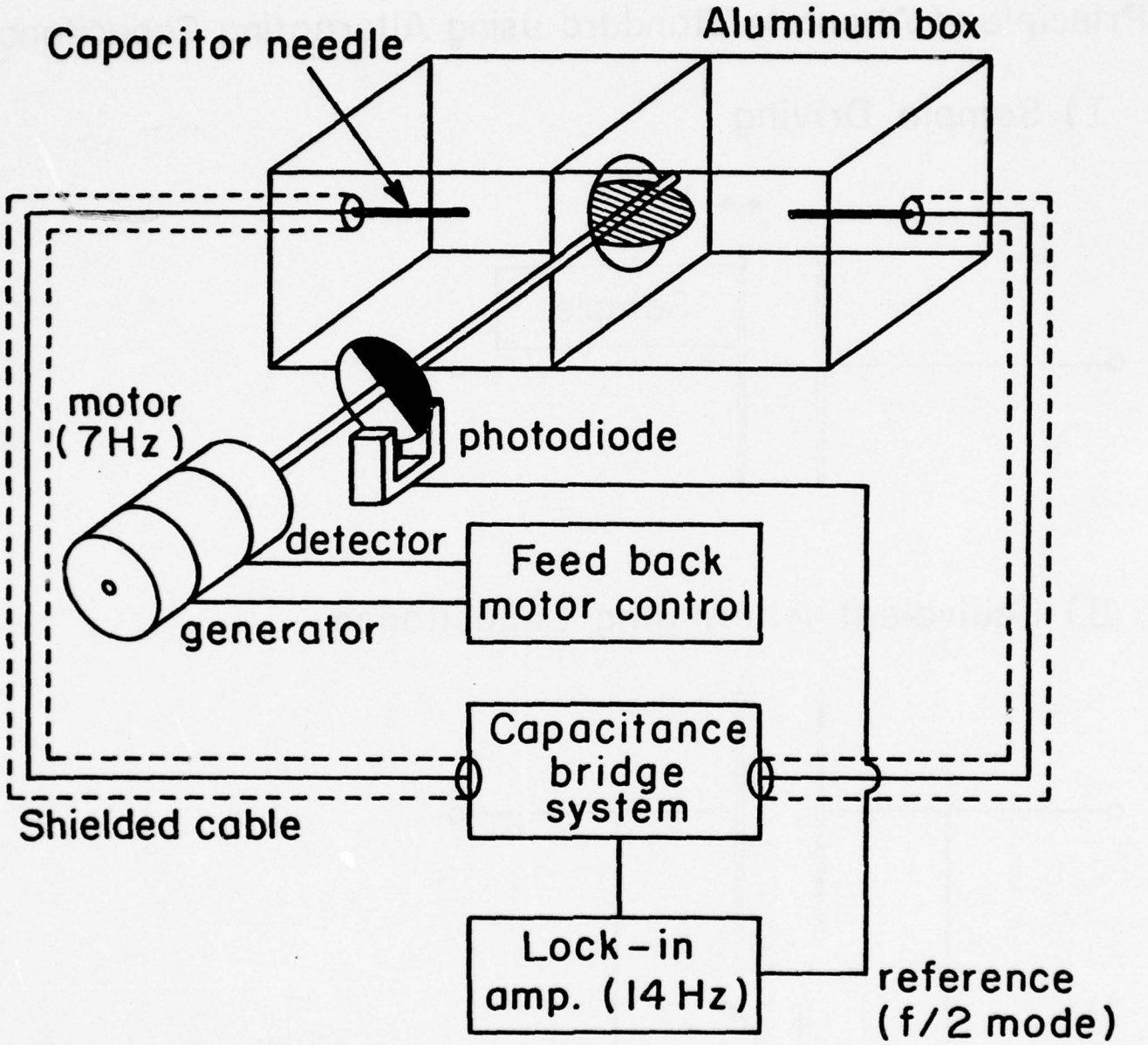

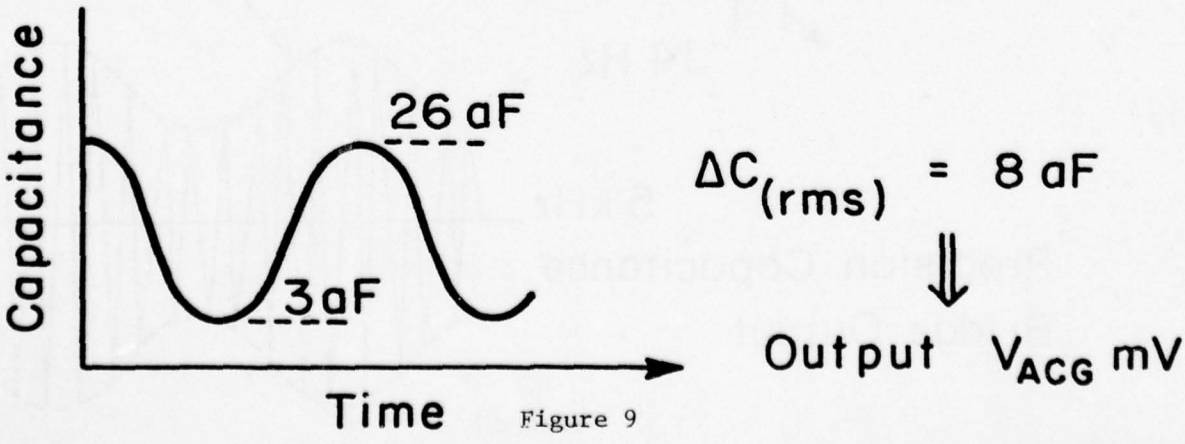

Figure 9

Separate – vibrating Method

Quartz ⟨100⟩

Wurtzite ⟨001⟩ R = 1.39

Under the optimum condition

with C = 105.5 pF

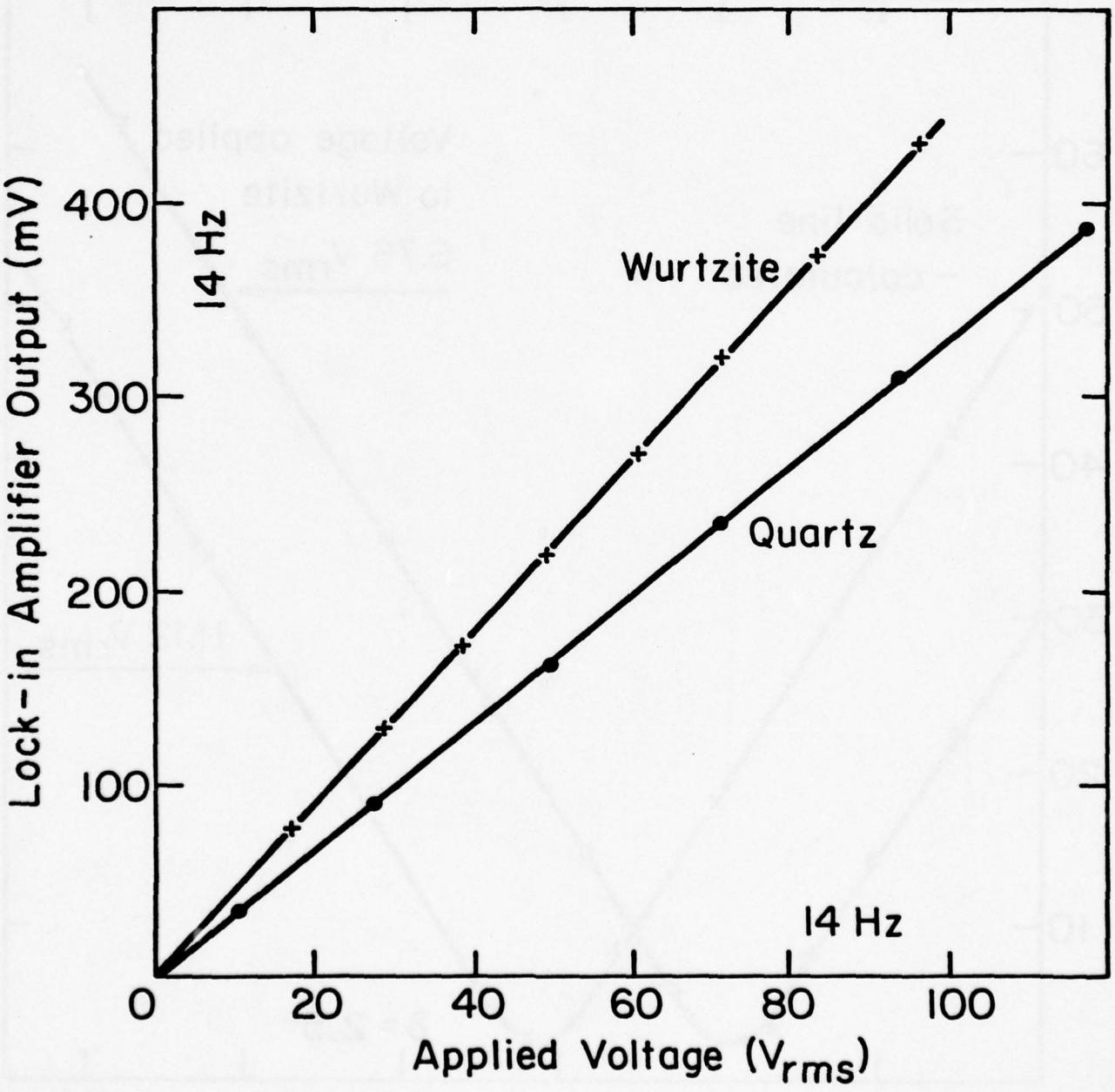

Figure 10

Null-condition Method

Quartz ⟨100⟩

Wurtzite ⟨001⟩ R = 1.41

Under the optimum condition

with C = 105.5 pF

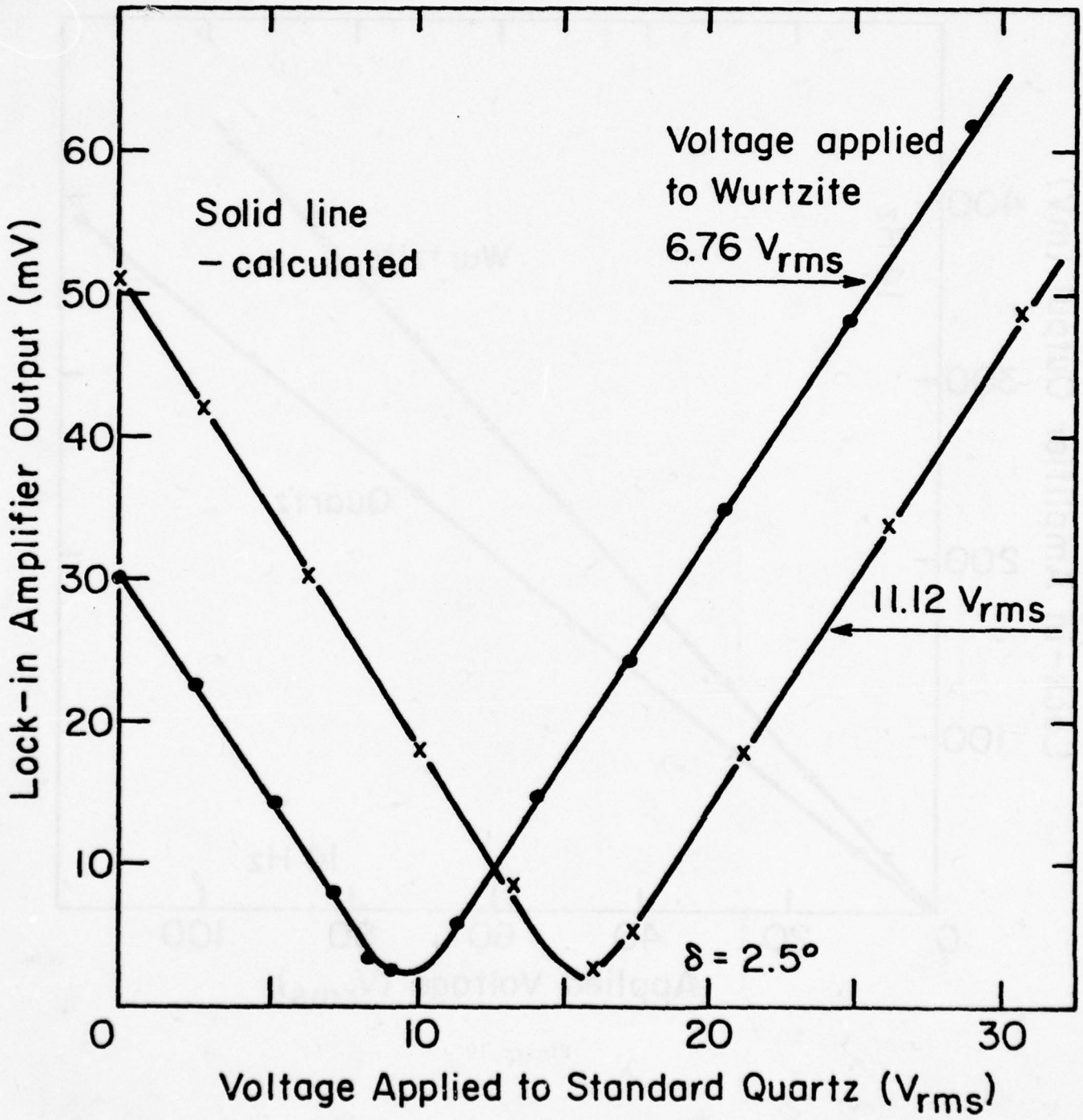

Figure 11

Electrostriction of $Pb(Mg_{1/3}Nb_{2/3})O_3$ Ceramic
longitudinal effect

Sample thickness = 3.68 mm

Under the optimum condition
with C = 74.1 pF

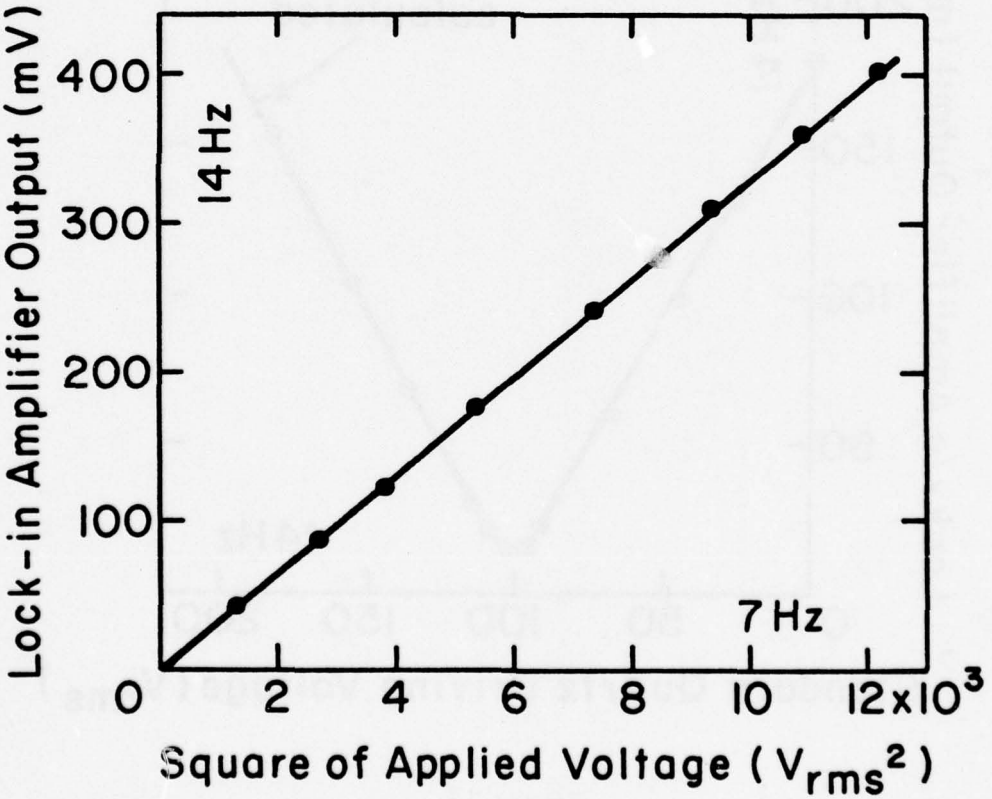

Figure 12

Null-condition between Quartz and $Pb(Mg_{1/3}Nb_{2/3})O_3$ Vibration

Under the optimum condition
with C = 74.0 pF
PMN Driving Voltage: 74.7 V_{rms} (7Hz)

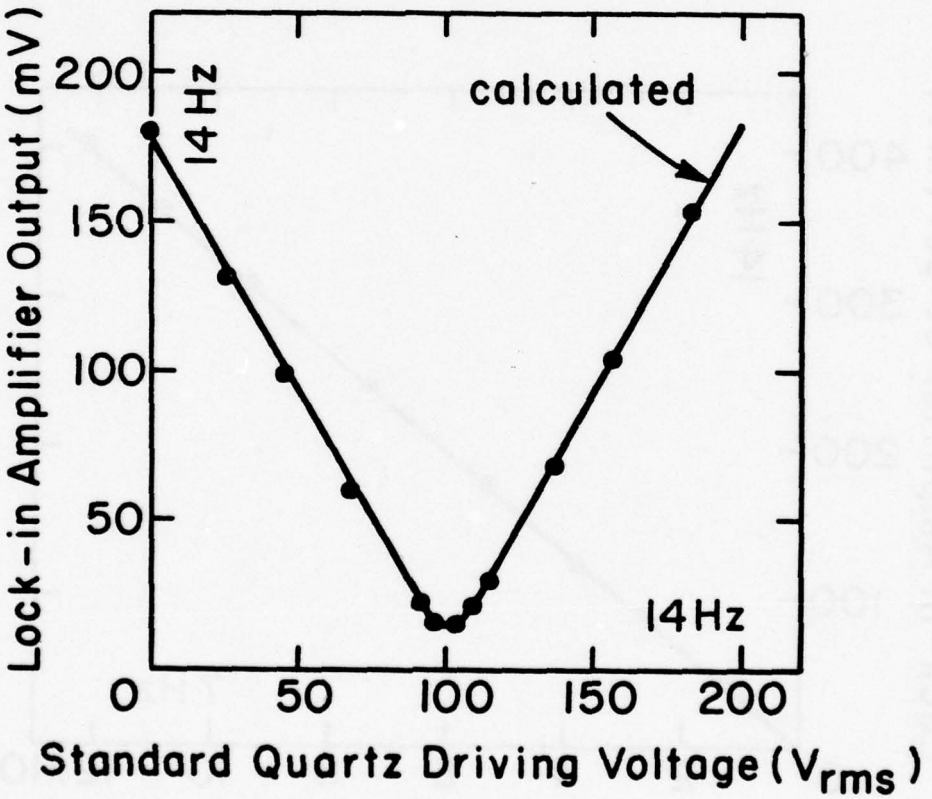

Figure 13

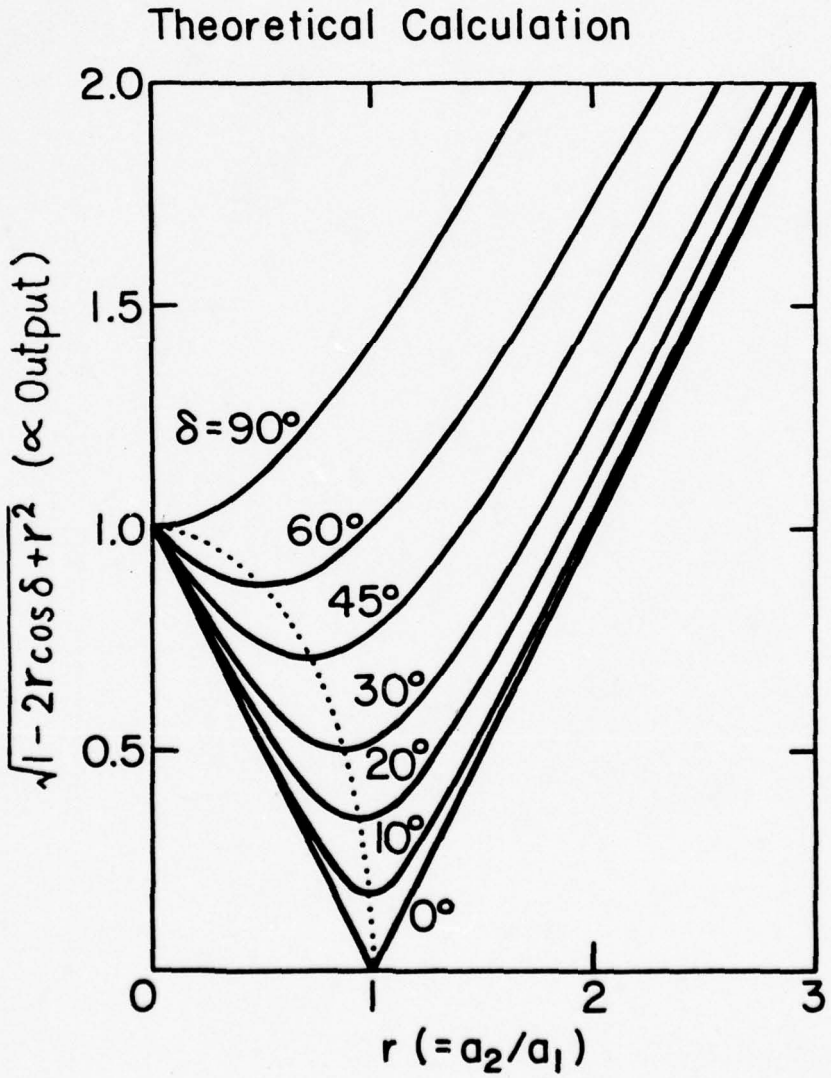
Theoretical Calculation
2.0
1.5
1.0
0.5
0
1
2
3
$\sqrt{1-2r\cos\delta+r^2}$ (∝ Output)
r (= a_2/a_1)
δ=90°
60°
45°
30°
20°
10°
0°

Figure 14

APPENDIX 2

K. Uchino and L.E. Cross. A Very High Sensitivity AC Dilatometer for the Direct Measurement of Piezoelectric and Electrostrictive Constants. Ferroelectrics (in press).

A VERY HIGH SENSITIVITY AC DILATOMETER FOR THE DIRECT MEASUREMENT OF PIEZOELECTRIC AND ELECTROSTRICTIVE CONSTANTS

KENJI UCHINO* and LESLIE E. CROSS
Materials Research Laboratory
The Pennsylvania State University
University Park, Pennsylvania 16802

A capacitance type dilatometer has been constructed which is capable of resolving low frequency AC linear displacements of 10^{-13} meter (0.001Å) and can be used for the direct measurement of piezoelectric and electrostrictive deformation. Using the DC servo stabilization of the sensing element, the mode of sensing the capacitance change generated by the crystal deformation has been radically improved. Some experimental data are given of piezoelectric and electrostrictive crystals and ceramics which have been measured by the established instrument.

INTRODUCTION

There are many physical and technological problems whose resolution depends on a capability of making precise measurements of exceedingly small displacements. Examples in the field of the electromechanical coupling are: (a) The measurement of electrostriction in simple low permittivity solids; (b) Detection of slight nonlinearity in piezoelectric deformations; (c) Determination of the piezoelectric strain in a very thin specimen, etc.

Capacitance-type dilatometers, which make use of the very high precision with which current dielectric bridge equipment can measure the capacitance of a parallel plate air capacitor and therefore can monitor the separation of the plates, have been used extensively in the past and have been summarized by White,[1] Pereira,[2] and Brändle.[3] For all of the instruments, however, the highest sensitivities reported are in resolving displacements of about 10^{-10} meters (1.0Å).

The instrument described in this paper has been designed to resolve AC linear displacements of 10^{-13} meters (10^{-3}Å) and to permit the precise measurement of the very small electromechanical strains. It is based upon an earlier design by Bohatý and Haussühl.[4]

We have described the detailed construction of the capacitance dilatometer in a recent paper.[5] In this paper the design of the instrument is reviewed briefly. The DC servo stabilization of the sensing capacitor, which is the key to improved stability and sensitivity, is discussed, and the experimental arrangement is summarized. Some experimental data are given for piezoelectric and electrostrictive coefficients measured on the instrument. Finally a typical application using very thin piezoelectric PVF_2 samples is presented.

*Permanent address: Department of Physical Electronics, Tokyo Institute of Technology, Ookayama, Meguro-ku, Tokyo 152, Japan.

KENJI UCHINO and LESLIE E. CROSS

DESIGN OF THE INSTRUMENT

A block diagram of the system constructed for electrostriction measurements is shown in Fig. 1.

The heart of the system is the mechanical circuit which incorporates the parallel plate sensing capacitor, one plate (c) of which is driven mechanically by a standard piezoelectric crystal (d), while the other plate (b) is driven by the electrostrictive sample (a). The first plate also has its position controlled by PZT piezoelectric pushers.

Capacitance, which is a direct measure of the plate separation of the sensing capacitor, is measured by a precision capacitance bridge (j,k,l). A signal proportional to the DC unbalance at the bridge is determined by the bridge detector, amplified and applied to the PZT piezoelectric pushers. Thus, if through thermal drift the plates begin to separate, a feedback voltage is applied to the PZT piezoids which keeps the capacitor plates in position. Because of this servo action, the bridge detector may be operated at maximum sensitivity without being driven beyond its linear range.

To measure the electrostriction constants, an electric field at 7 Hz is applied to the crystal through a suitable oscillator amplifier combination. This sets the capacitor plate vibrating at 14 Hz. A phase locked signal at 14 Hz is then also applied to the standard quartz crystal. The lock-in amplifier which is phase-locked to the 14 Hz driving frequency senses any component in the bridge output (capacitance) which is at 14 Hz and in phase with the driving oscillator.

By manipulating the voltage applied to the unknown and standard crystals, a null condition can be achieved. The unknown constant can then be derived from the voltage ratio and the appropriate geometrical constants.

OPERATION OF THE INSTRUMENT

Operation of the DC stabilization servo is evident from the data in Fig. 2. After the system enclosure has stabilized to ±0.04°C at 29°C, the DC servo is disconnected. The resulting capacitance change corresponds to about 1Å/minute separation change caused by slow thermal drifts. Reconnecting the servo amplifier, the drift rate decreases remarkably and now corresponds to less than 0.002 Å/minute. At this servo level, the bridge can be operated at high detector amplification about 80 dB.

To check the output sensitivity, a standard quartz crystal was driven at 14 Hz, without applying any voltage to the crystal on the counter plate (Fig. 3). The expected linear relation between voltage and output is clearly evident. For the gain settings used, the minimum resolvable increment in the lock-in amplifier was 0.1 mV. Taking the d_{11} of quartz as 2.3×10^{-12} (mV^{-1}) gives a minimum resolvable displacement of 1×10^{-3} Å rms. This resolution corresponds to a resolvable strain $\Delta\ell/\ell \leq \pm 10^{-10}$, far superior to other measurement techniques (e.g. x-ray diffraction).

To check this sensitivity, the AC calibration capacitor was set up to give a capacitance modulation of 8 aF rms at 14 Hz. For a sensing capacitance of 79.6 pF this gave an output voltage (mV) at the same gain settings as that used with the quartz driving. This back calculates to give a d_{11} for quartz of $2.27 \pm 0.01 \times 10^{-12}$ (mV^{-1}).

SPECIMEN MEASUREMENTS

As an example of the null condition method the d_{33} of piezoelectric wurtzite was compared with the d_{11} of quartz. After proper adjustment of phase with two different voltage levels applied to the wurtzite crystal, the output curves obtained as a function of voltage applied to the quartz standard, are shown in Fig. 4. Balances occurred at 9.54 and 15.68 volts on quartz, giving $d_{33} = 1.41\ d_{11}$ (quartz), or $3.20 \pm 0.02 \times 10^{-12}$ (mV^{-1}), in very good agreement with the value for wurtzite quoted in Landolt Börnstein.[6]

TABLE I. Some example data of electromechanical coefficients

SAMPLE	COEFFICIENT	PRESENT	PREVIOUS
QUARTZ (100)	$d_{11}(\times10^{12}\ mV^{-1})$	+2.27 (±0.01)	+2.27 [7]
WURTZITE (001)	$d_{33}(\times10^{-12}\ mV^{-1})$	+3.20 (±0.02)	+3.2 (±0.2)[6]
BERLINITE (100)	$d_{11}(\times10^{-12}\ mV^{-1})$	-3.98 (±0.05)	-5.3 (±1.6)[8]
PVF_2[a]			
UNORIENTED	$d_{33}(\times10^{-12}\ mV^{-1})$	-5.4 (±0.2)	-9[b]
ORIENTED	$d_{33}(\times10^{-12}\ mV^{-1})$	-20.2 (±0.4)	-20[b]
$Pb(Mg_{1/3}Nb_{2/3})O_3$ (CERAMIC)	$M'_{11}(\times10^{-16}\ m^2V^{-2})$	+1.05(±0.01)	+1.4 (±0.2)[9]
PMMA (POLYMETHYL-METHACRYLATE)[c]	$M'_{11}(\times10^{-17}\ m^2V^{-2})$	-1.6 (±0.1)	0

[a] KYNAR 7200
[b] PRIVATE COMMUNICATION; ESTIMATED VALUES BY HICKS (1979)
[c] SAMPLE SUPPORT MATERIAL

As a check the two crystals were driven independently to give the slopes (separate vibrating method). Again the ratio of the two slopes is 1.39 corresponding to a d_{33} in in wurtzite of $3.17 \pm 0.02 \times 10^{-12}$ (mV^{-1}).

Some measured data of piezoelectric and electrostrictive crystals and ceramics compared to standard literature values are listed in Table I. The agreement with the previously reported values for quartz and wurtzite indicates the high precision of our instrument. It is worth mentioning that the error is much smaller than those of previous measurements.

FURTHER APPLICATION TO THIN FOIL PVF_2

Using a normal dilatometer, the direct measurement of the thickness change of a very thin sample is very difficult. For this reason, there is, to our knowledge, no direct measurement of d_{33} for PVF_2 films.

Two kinds of PVF_2 (unoriented and oriented KYNAR 7200 with thicknesses of 193 μm and 69 μm, respectively) were driven under optimum instrument conditions (Fig. 5). The initial slopes of the strain curves gave d_{33} values of $-5.4 \pm 0.2 \times 10^{-12}$ (mV^{-1}) and $-20.2 \pm 0.4 \times 10^{-12}$ (mV^{-1}) respectively (Table I), which are in good agreement with the values estimated from the g_{31} and g_{32} coefficients determined by Hicks (1979; private communication).

A non-linear relation between the AC applied voltage and the output (which is to be expected in piezoelectric crystals at high electric field levels) was observed in both samples. To determine the field dependence of d_{33}, the lock-in output for a small fixed value of AC drive voltage to the PVF_2 sample was recorded as a function of DC bias field (Fig. 6. Hysteresis could also be detected by this method, and almost the same values of the average slopes ($\sim0.13\%/10^5 Vm^{-1}$) were obtained for both samples.

Further measurements on other interesting piezoelectric and electrostrictive materials will be made in the near future.

ACKNOWLEDGMENTS

This work was sponsored by the Office of Naval Research, Contract No. N00014-78-C-[illegible]. We also thank Dr. J.C. Hicks, Naval Ocean Systems Center, and Dr. G.R. Barsch of the Pennsylvania State University, for supplying us with samples.

HIGH SENSITIVITY AC DILATOMETER

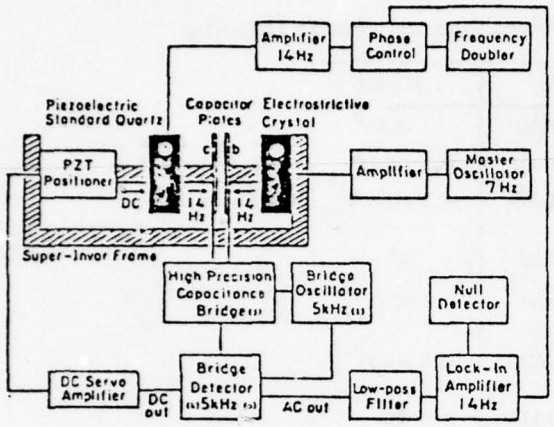

FIGURE 1. Schematic diagram of the AC dilatometer.

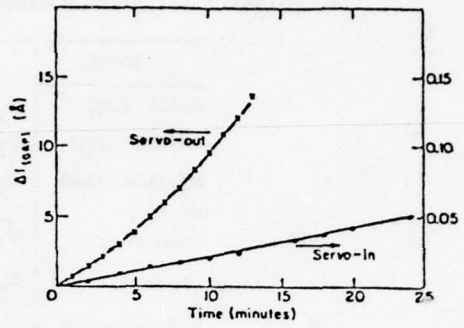

FIGURE 2. DC plate separation change as a function of time with and without servo.

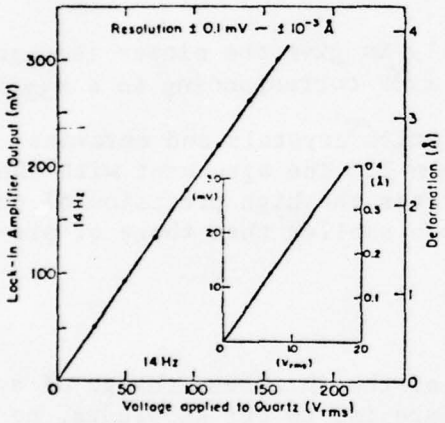

FIGURE 3. Dilatometer output and actual deformation as a function of quartz driving voltage.

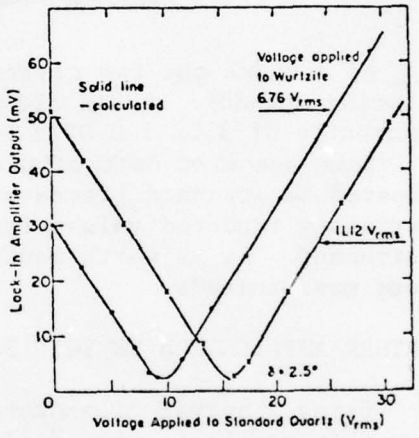

FIGURE 4. Null condition method between wurtzite and quartz.

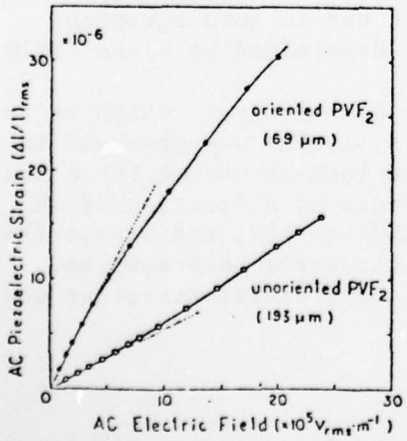

FIGURE 5. Piezoelectric strains as a function of AC driving field applied to each PVF_2.

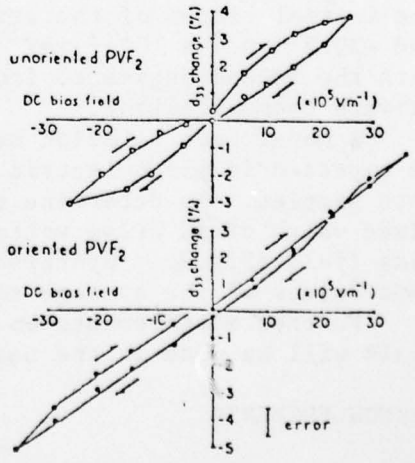

FIGURE 6. DC bias field dependence of d_{33} values of PVF_2.

REFERENCES

1. G. K. White, Cryogenics GB1, 151 (1968).
2. F. N. Pereira, C.H. Barnes and G.M. Graham, J. Appl. Phys. 41, 5050 (1970).
3. G. Brändle and R. Griessen, Cryogenics GB13, 299 (1973).
4. L. Bohatý and S. Haussühl, Acta Cryst. A33, 114 (1977).
5. K. Uchino and L.E. Cross, Proc. 33rd Annual Symposium on Frequency Control, U.S. Army Electronics Command, Fort Monmouth, NJ (1979).
6. I.B. Kobyakov and G.S. Pado, Soviet Phys.-Solid State 9, 1707 (1968).
7. V.E. Bottom, J. Appl. Phys. 41, 3941 (1970).
8. Z.P. Chang and G.R. Barsch, IEEE Trans.-Sonics and Ultrasonics 3, 127 (1976).
9. L.E. Cross, S.J. Jang, R.E. Newnham, S. Nomura and K. Uchino, Ferroelectrics (submitted).

APPENDIX 3

K. Uchino, L.E. Cross and J.C. Hicks. Longitudinal Piezoelectric Strain Measurements of Polyvinylidene Fluoride Films.

Longitudinal Piezoelectric Strain Measurements of Polyvinylidene Fluoride Films

K. Uchino and L.E. Cross

Materials Research Laboratory
The Pennsylvania State University
University Park, Pennsylvania 16802

and

J.C. Hicks

Naval Ocean Systems Center
San Diego, California 92152

Abstract

The longitudinal piezoelectric strain of polyvinylidenefluoride (PVF_2) films has been measured at room temperature using a high-sensitivity AC dilatometer. The DC bias field dependence of the piezoelectric strain coefficient d_{33} has been observed. The polarization related electrostrictive coefficient Q_{33} obtained is several hundred times larger with the opposite sign than the value in normal piezoelectric oxide crystals.

1. Introduction

The polymer PVF_2 (polyvinylidene fluoride) has been extensively studied since the discovery of its large piezoelectric coefficients in 1969[1]. Rolling and stretching the films at elevated temperatures during their preparation enhances the crystallization of the polar phase (form I) with polymer chains oriented preferentially along the tensile stress axis. After an electric field of sufficient magnitude (about 10^8 Vm^{-1}) is applied normal to the film at elevated temperatures, large piezoelectric coefficients can be measured. Though the transverse piezoelectric effect is rather easily detected, few studies have attempted to measure directly the longitudinal piezoelectric strain induced by an applied electric field because of thinness of films (usually less than 100 μm). The first direct observation of the piezoelectric coefficient d_{33} was made by Burkard and Pfister using a capacitance-type dilatometer[2]. This static measurements were carried out at 0.3 K to avoid length fluctuations due to thermal expansion.

Using a newly developed high-sensitivity AC dilatometer[3,4], we have measured precisely the longitudinal piezoelectric coefficients of PVF_2 films at room temperature. Moreover, we have observed the DC bias electric field dependence of the piezoelectric coefficient d_{33} (electrostrictive effect).

2. Experimental

The samples were cut from 193-μm-thick unoriented and 69-μm-thick oriented Kynar 7200 sheets (Pennwalt Chemicals Co.) and from 25-μm-thick oriented sheets obtained from Kureha Chemical Industries, after the samples had been poled in the manner described above.

Two systems were used to measure the electric-field-induced strain in these sample films. For the transverse piezoelectric effect, a strain gauge

technique was applied, the sample being placed such that the deformation produced a stress on a strain gauge. The piezoelectric coefficients d_{31} and d_{32} obtained are listed in Table I. The piezoelectric coefficient d_h ($= d_{31} + d_{32} + d_{33}$) was determined with the conventional method of applying a time-varying hydrostatic pressure to the film. The values of d_h are almost the same for the three specimens ($\sim -1 \times 10^{-12}$ mV^{-1}). From the values of d_{31}, d_{32}, d_h we can evaluate the piezoelectric coefficients d_{33}, which are also shown in Table I.

For the longitudinal piezoelectric measurement we applied a newly developed high-sensitivity AC dilatometer whose minimum resolvable displacement is less than 10^{-3} Å rms. Figure 1 shows the block diagram of this system, the details of which have been reported in previous papers[3,4]. To measure the piezoelectric strain, an alternating electric field at 14 Hz is applied to the PVF_2 sample film through a suitable oscillator amplifier combination, which sets the capacitor plate vibrating at 14 Hz. The lock-in amplifier which is phase-locked to the 14 Hz driving frequency senses any component in the bridge output (capacitance modulation) which is at 14 Hz and in phase with the driving oscillator. To check the output calibration factor, a standard quartz crystal is then driven at 14 Hz without applying any voltage to the film.

To avoid separation changes of the sensing capacitor plates due to thermal expansion, the DC unbalance signal of the capacitance bridge is fed back to the PZT pushers through an amplifier. This servo-system is the key to high sensitivity and stability of the instrument.

In Fig. 2(a) and (b) we show the observed longitudinal strain (root-mean-square value) for an oriented and an unoriented Kynar and an oriented Kureha film, respectively, under a sinusoidal electric field at 14 Hz.

The piezoelectric coefficient d_{33} is calculated from the slope of linear relation between strain and electric field near zero field. Deviation from the straight line at higher electric fields is caused by the hysteresis effect and the nonlinear (higher order) coupling. A determination of the negative sign of d_{33} is made from the 180° phase difference between the lock-in amplifier outputs of the PVF_2 and the standard quartz crystal.

To obtain the electrostrictive effect separately from the hysteresis effect, we measured the DC bias field dependence of the piezoelectric coefficient d_{33}. When a DC electric field E_o is superposed with a sinusoidal electric field $2E_1 \sin\omega t$, the induced strain X_3 is represented as

$$X_3 = d_{33}(E_o + \sqrt{2}E_1 \sin\omega t) + M_{33}(E_o + \sqrt{2}E_1 \sin\omega t)^2 \quad (1)$$

where M_{33} is the field related electrostrictive coefficient. The root-mean-square value of the strain at a frequency of $\omega, X_3(\omega)$ is given as

$$(\omega) = d_{33}^{eff}(E_o)E_1 \quad (2)$$

where

$$d_{33}^{eff}(E_o) = d_{33}\left(1 + \frac{2M_{33}}{d_{33}} E_o\right) \quad (3)$$

The lock-in amplifier output for a constant AC electric field ($E_1 \sim 10^5$ Vm^{-1}) was plotted as a function of the DC electric field. Figure 3(a) and (b) are the results showing the change of effective piezoelectric coefficient d_{33}^{eff} with the DC bias field E_o. An obvious hysteresis curve could be obtained in the relation between d_{33}^{eff} and E_o for all samples. The average d_{33}^{eff} change (neglecting the hysteresis) with the DC field is considered to give the electrostrictive effect approximately. The piezoelectric coefficient d_{33} (experimentally observed) and the field-related electrostrictive coefficient

M_{33} for three specimens are listed in Table I. Correction of the M_{33} value due to the Maxwell electrostatic stress is less than 10% of the apparent value. The polarization related electrostrictive coefficient Q_{33}, which is defined as $x_3 = Q_{33}P_3^2$, was calculated approximately as follows:

$$Q_{33} = M_{33}/\varepsilon_3^2 \tag{4}$$

where ε_3 is the permittivity.

3. Discussion

Oshiki and Fukada determined precisely the piezoelectric stress coefficient e_{31} and the electrostrictive stress coefficient γ_{31} (transverse effect) of PVF_2 by applying a sinusoidal electric field and detecting induced stresses[5]. They reported a marked hysteresis curve of e_{31} with the cyclic change of the DC bias field, which is very similar to that in Fig. 3 showing the dependence of d_{33} on the DC bias field. The low-frequency piezoelectric stress coefficient e_{31} decreases by about one order of magnitude from its room-temperature value of $\sim 10^{-2}$[C m^{-2}] on cooling the sample to -150°C. At 0.3 K the longitudinal piezoelectric strain coefficient d_{33} measured by Burkard and Pfister is of the order of $-10^{-13} \sim -10^{-12}$[mV^{-1}][2]. The difference of one to two orders of magnitude between their data and our d_{33} data is explained by the large temperature dependence of d_{33}. Their electrostrictive data were not so reliable as ours, but are still consistent with our measurement.

Using the piezoelectric resonance method, Ohigashi determined the piezoelectric strain coefficients (d_{31} and d_{32}) and the piezoelectric stress coefficient (e_{33}) in a high-frequency region[6]. At room temperature the d_{33} value ($\sim 15 \times 10^{-12}$ mV^{-1}) estimated from an approximate relation ($d_{33} \simeq e_{33}/c_{33}^D$) is almost of the same order as our observed data. No electrostrictive data could be obtained by the resonance method.

Let us discuss now a phenomenological interpretation for the piezoelectricity in poled PVF_2 in terms of *electrostriction*, which was first introduced by Oshiki and Fukada[5]. After poling, a preferred orientation of dipoles is produced in the film, which results in the spontaneous polarization P_s and the spontaneous strain x_s. The coupling of the electrostriction (which may be determined by the film preparation technique) with this spontaneous polarization produces piezoelectricity. In the phenomenological expression, the strain x_3 in the poled film of PVF_2 under an electric field E is given by

$$x_3 \simeq Q_{33} (P_s + \varepsilon_3 E)^2 \tag{5}$$

Then, by analogy with Eq (1) we may describe

$$x_3 = Q_{33} P_s^2 \tag{6}$$

$$d_{33} = 2Q_{33} P_s \varepsilon_3 \tag{7}$$

and

$$M_{33} = Q_{33} \varepsilon_3^2 \tag{4'}$$

By using $P_s \sim 0.5 \times 10^{-2} [Cm^{-2}]$ which was determined in our recent paper describing the effect of an AC annealing technique on the remanent polarization[7] we can evaluate the piezoelectric strain coefficient from Eq (7). Good agreement between the product value $2Q_{33} P_s \varepsilon_s$ and the d_{33} values observed for all three specimens shown in Table I, suggests the validity of the phenomenological treatment. The electromechanical data of normal piezoelectric $LiNbO_3$ are listed in Table I for comparison. In addition to the sign difference of d_{33} and Q_{33}, it is also interesting that the Q_{33} values in PVF_2 are two to three orders of magnitude larger than in $LiNbO_3$, while the P_s values are two

to three orders of magnitude smaller. In consequence, there follows almost the same magnitude piezoelectric coefficient d_{33} (though with the opposite sign).

Acknowledgment

We wish to thank the Office of Naval Research for their support of our work through Contract No. N00014-78-C-0291.

References

1. H. Kawai, Japan. J. Appl. Phys. 8, 975 (1969).

2. H. Burkard and G. Pfister, J. Appl. Phys. 45, 3360 (1974).

3. K. Uchino and L.E. Cross, Proc. 33rd Annual Symposium on Frequency Control, U.S. Army Electronics Command, Fort Monmouth, NJ (1979).

4. K. Uchino and L.E. Cross, Ferroelectrics (in press).

5. M. Oshiki and E. Fukada, J. Mat. Sci. 10, 1 (1975).

6. H. Ohigashi, J. Appl. Phys. 47, 949 (1976).

7. J.C. Hicks and T.E. Jones, Proc. Meeting of Amer. Phys. Soc. No. 77.80 (March, 1979).

8. R.T. Smith and F.S. Welsh, J. Appl. Phys. 42, 2219 (1971).

9. T. Yamada, J. Appl. Phys. 43, 329 (1972).

Figure Captions

Fig. 1 Block diagram of a high sensitivity AC capacitance-type dilatometer.

Fig. 2 Induced longitudinal strain under a sinusoidal electrical field at 14 Hz, (a) for the oriented and unoriented KYNAR 7200 and (b) for the oriented Kureha film.

Fig. 3 The effective piezoelectric coefficient d_{33}^{eff} change with the DC bias field E_o, (a) in the oriented and unoriented KYNAR 7200 and (b) in the oriented Kureha film.

Table I. Electromechanical properties of polarized PVF_2 films (compared with $LiNbO_3$).

Coefficients	Unoriented KYNAR	Oriented KYNAR	Oriented Kureha	$LiNbO_3$
ε_3 $(x\varepsilon_o)$	9.9	11	12	28.7[8]
$d_{31}(x10^{-12}mV^{-1})$	4.3	16.1	21.2	-0.85[9]
$d_{32}(x10^{-12}mV^{-1})$	4.2	1.9	2.4	0
$d_{33}^{calc}(x10^{-12}mV^{-1})$	-9	-19	-25	0
$d_{33}^{obs}(x10^{-12}mV^{-1})$	-5.5 ± 0.2	-20.2 ± 0.4	-24.2 ± 0.6	6.73
$M_{33}(x10^{-20}m^2V^{-2})$	-3.6	-13.6	-34.1	0
$Q_{33}(xm^4C^{-2})$	-5	-15	-30	0.016[8]
$2Q_{33}P_s\varepsilon_3(x10^{-12}mV^{-1})$	-4.4	-15	-31	5.8

AD-A079 400 PENNSYLVANIA STATE UNIV UNIVERSITY PARK MATERIALS RE--ETC F/G 9/1
TARGETED BASIC STUDIES OF FERROELECTRIC AND FERROELASTIC MATERI--ETC(U)
DEC 79 L E CROSS , R E NEWNHAM , G R BARSCH N00014-78-C-0291

UNCLASSIFIED NL

2 OF 4
AD A 079400

APPENDIX 4

K. Uchino, S. Nomura, L.E. Cross and R.E. Newnham. New Electrostrictive Materials for Displacement Transducers. J. Electronic Ceramics [Japan] (submitted).

新しい電歪材料

内野研二，野村昭一郎，L.E.Cross*，R.E.Newnham*

東京工大，工学部

ペンシルバニア州立大，物性研究所

要約

ポジション・コントロール用の新しい電歪材料の開発背景，諸特性，および応用例について述べる。　緩和型強誘電体（PMN系）の利用により，従来の圧電体（PZT，BT系）歪材料と比較して，より大きな歪，優れた反復再現性，非常に小さな誘電損係数をもつ材料を作り出した。後半，理論的研究を目的に作製したアルカリ・ハライド系の電歪効果測定用高感度ACディラトメータについて，その原理，構成，測定例を述べる。

§1．緒言

電歪効果（electrostrictive effect）は基本的な電気機械結合の一種であるにもかかわらず，実験的，理論的研究は遅れている。　その原因は，2次効果であるために通常誘起される歪は非常に小さく，実験的駐さをもたらしている点にある。　信頼のおける単結晶の電歪定数もほとんど決められていない現在，その理論的（微視的）解明は望むべくもない。　また応用面からの社会的要請がなかったことも大きく影響している。

ところが近年，天文学，光学の分野において，光角度，光路長を微動にコントロールする変位素子（displacement transducer）が所望されるようになった[1]。　ここに至り初めて電歪が注目されるようになった。

ポジション・コントロール用素子として備えるべき性質を列記しておく。

1．感度（変位／電界）
2．反復再現性（ヒステリシス）
3．安定性（温度，エージング）
4．応答時間，共鳴減衰
5．絶縁破壊強度等
6．サイズ，重量

素子材料としてまず考えられるのが，磁歪材料あるいは圧電材料であろう。　磁歪（magnetostriction）は大きさ（$\Delta l/l$）が10^{-5}～10^{-4}と圧電歪（piezoelectric strain）の10^{-4}～10^{-2}に比べて1桁以上小さく，その上コイル等の大きな駆動デバイス（大きな電力）を必要とするので使いにくい。　圧電歪の問題点は，ヒステリシスとエージングである。非晶質結晶における電歪（electrostriction）においては，原理的にヒステリシス，エージングはなく，応答時間も強誘電体の分域回転に比べて速い。　加えてめんどうなポーリング過程を必要としない。　このような背景のもとに，大きな電歪効果（従来の常識に反する！）をもつ物質を発見する動きが活発になってきた。　それと同時に電歪の起源の理論的解明も必要となってきている。

本稿は，東京工大とペンシルバニア州立大との共同研究の内容を中心に，新しい電歪材料開発の背景および応用について述べる。プロジェクトは大きく見て次の3つのブランチから進められている。

a．材質研究：素子材料として最適なものを合成する。
b．意匠研究：デバイスのデザイン（積層構造，2次元配列等）を考える。
c．理論研究：アルカリ・ハライド系結晶の電歪を測定し，電歪理論を組み立てる。

§2．電歪の現象論

まず電歪の物理的意味をはっきりさせるために，簡単な現象論的取扱いにふれておく。　熱力学関数としては弾性エンタルピー$H(X,P,S)$を用いるのが便利である。

$$dH = -x_{ij}\,dX_{ij} + E_m\,dP_m + T\,dS$$

電歪のような2次効果の場合，温度効果は小さく無視でき，応力X_{ij}と電気分極P_mが独立変数となる。　歪x_{ij}と電界E_mはそれらで次のように展開される。

$$x_{ij} = \left(\frac{\partial x_{ij}}{\partial X_{kl}}\right)_P dX_{kl} + \left(\frac{\partial x_{ij}}{\partial P_n}\right)_X dP_n + \frac{1}{2!}\left[\frac{\partial^2 x_{ij}}{\partial X_{kl}\partial X_{qr}} dX_{kl} dX_{qr}\right.$$

$$\left. + 2\frac{\partial^2 x_{ij}}{\partial X_{kl}\partial P_n} dX_{kl} dP_n + \frac{\partial^2 x_{ij}}{\partial P_n \partial P_o} dP_n dP_o\right] + \cdots \qquad (1)$$

$$E_m = \left(\frac{\partial E_m}{\partial X_{kl}}\right)_P dX_{kl} + \left(\frac{\partial E_m}{\partial P_n}\right)_X dP_n + \frac{1}{2!}\left[\frac{\partial^2 E_m}{\partial X_{kl}\partial X_{qr}} dX_{kl} dX_{qr}\right.$$

$$\left. + 2\frac{\partial^2 E_m}{\partial X_{kl}\partial P_n} dX_{kl} dP_n + \frac{\partial^2 E_m}{\partial P_n \partial P_o} dP_n dP_o\right] + \cdots \qquad (2)$$

(1)式の第1，2項は，弾性定数 s^P_{ijkl}，圧電定数 g^X_{ijn} として知られている。2次効果の大括弧内，ここでは電歪を記述する第3項だけを考慮し，他の2項を無視する。4階の電歪テンソル Q_{ijno} を次の形で導入する。

$$Q_{ijno} = \frac{1}{2}\left(\frac{\partial^2 x_{ij}}{\partial P_n \partial P_o}\right) \qquad (3)$$

(2)式の第2項は，逆誘電率 β^X_{mn} であり，第1項はマックスウェル関係式 $(\partial x_{ij}/\partial P_k)_X = -(\partial E_k/\partial X_{ij})_P$ を考慮すると圧電定数 $-g^X_{klm}$ に等しくなる。大括弧内，第2項が電歪効果を記述しており，他の2項は考えない。従って電歪効果による項は，次のように書き直される。

$$x_{ij} = Q_{ijno} P_n P_o \qquad (4)$$

$$E_m = -2 Q_{mnkl} P_n X_{kl} \qquad (5)$$

言い換えると，電歪は「電気分極の平方に比例する歪を生ずる現象」として定義されよう*。電歪は2次の効果で一般に小さく，純粋には中心対称性のある非ピエゾ結晶においてだけ観測される。

---

* 常識的な関係式 $x_{ij} = M_{ijkl} E_k E_l$ が成立するのは，電界が小さく線形関係 $P_n = \varepsilon_{nm} E_m$ が成り立つ範囲においてである。

ここで電歪テンソルが次の2様に書けることに注意しよう。

$$Q_{ijno} = \frac{1}{2}\left(\frac{\partial^2 x_{ij}}{\partial P_n \partial P_o}\right)$$

$$= -\frac{1}{2}\left(\frac{\partial^2 E_n}{\partial X_{ij}\partial P_o}\right) = -\frac{1}{2}\left(\frac{\partial \beta^X_{no}}{\partial X_{ij}}\right) \qquad (6)$$

これらの式は，電歪テンソル成分決定の2様の実験手段，すなわち

a. 電界（誘起分極）印加による歪の測定（直接測定法），

および

b. 応力印加による（逆）誘電率の測定（間接測定法）

を示唆している。

§3. 材質研究

電歪効果は，アルカリ・ハライドのような低誘電率化合物においても見られるが，歪は小さく実用材料とはほど遠い。(4)式が，ほぼ $x = QP^2 = Q\varepsilon^2 E^2$ と書けることから，誘電率の大きな物質に興味が持たれる。まず考えつくのがペロブスカイト型酸化物の $BaTiO_3$ 系，PZT系強誘電体の常誘電相の利用であり，実際にこの固溶系については米国ハニーウェル社によって研究が進められている[2]。

我々は以前より複合ペロブスカイトの緩和型強誘電体（relaxor ferroelectrics）に関する研究をしてきているが，それらにおいては，誘電率の大きさは通常のペロブスカイト強誘電体より1桁大きく，大きな利点として，非常に散漫な相転移（diffuse phase transition）をともなうために温度安定性をもつ。典型的な（最もよく研究されている）$Pb(Mg_{1/3}Nb_{2/3})O_3$（PMN）を主成分に取上げ，$PbTiO_3$（PT）との固溶系セラミクスにおいて，従来の $BaTiO_3$ 系セラミクスの電歪の10倍程度の大きさを有し，ヒステリシス，エージング効果の小さな優れた材質を得ることができた。

$Pb(Mg_{1/3}Nb_{2/3})O_3$ は，0°C近傍に平均的キュリー点をもつ強誘電体である。ペロブスカイト構造のB位置を Mg^{2+} と Nb^{5+} イオンがランダムに占めるが，その分布に統計的な不均一が生ずるので，キュリー温度が局所的に異なると考えられている[3]。このことが散漫な相転移を引き起こし，相転移温度領域において電界をかけると強くポーリングされ電界を除くと微小分域に分かれ残留分極をもたない好都合な条件を生

じている。

PMNセラミクス自身すでにBT系セラミクスの電歪効果を凌いでいるが，相転移温度を室温近傍まで引き上げればより優れた材料が期待できる。ここでは $Pb(Mg_{1/3}Nb_{2/3})O_3$ - $PbTiO_3$ 固溶系のうち，0.9 PMN - 0.1 PTについてのデータを示しておく[4]。キュリー温度領域は20°C近傍にあり，誘電率は7000 (1kHz 測定) 程度である。電歪は通常のストレイン・ゲージ法（直接測定法）を用いて測定した。図1に室温における横縮み効果の電界依存性を示した。比較のためにミラー・コントロール用として商品化されている PZT 8の圧電歪の電界依存性も示してある。歪の大きさ自身 PZT 8を凌いでおり，電界印加反復による再現性は，はるかに優れている。電歪横効果は

$$x_2 = \bar{Q}_{12} P_1^2 \quad (\bar{Q}_{12}: 多結晶体平均電歪定数) \qquad (7)$$

で表わされるが，図2はその性質が，0.9 PMN-0.1 PTセラミクスのように高い誘電率をもつ物質においても成り立つことを端的に現わしている。分極値はソーヤ・タウワ法（0.05 Hz）によって測定したものを用いた。直線の勾配から電歪定数 $\bar{Q}_{12}$ は $-0.9\times10^{-2}\ m^4C^{-2}$ と計算され，この値は他のペロブスカイトと同程度の大きさである。（ちなみに $BaTiO_3$, $SrTiO_3$, $Pb(Zr,Ti)O_3$, $LiTaO_3$ 等のセラミクスの $\bar{Q}_{12}$ 値はすべて約 $-1\times10^{-2}\ m^4C^{-2}$。）従って $BaTiO_3$ 系セラミクスの10倍もの電歪をもたらしている原因は，大きなカップリング定数によるのではなく，むしろ異常に大きな誘起分極，誘電率によるのである。図3には，縦および横電歪定数 Q_{11}, $\bar{Q}_{12}$ の $PbTiO_3$ 固溶割合依存性を示した。ほぼ直線的に増加している点が注目される。（§5.1 参照）

飽和型強誘電体のもうひとつの興味ある利点は，相転移近傍において熱膨張が非常に小さいことである。図4に 0.9 PMN-0.1 PT の熱膨張曲線を示した。実用温度領域（-50～100 °C）において熱線膨張係数は $1\times10^{-6}\ K^{-1}$ 以下と小さく，この値は溶融石英の値に匹適している。400°C 以上において通常のペロブスカイトの熱膨張係数（$10\times10^{-6}\ K^{-1}$）に近づく。熱膨張が電歪に比べて充分小さいことは，変位素子応用上好都合である。例えば，室温近傍において温度が 10°C 変化しても，それによる熱膨張は約 5×10^{-6} であり，この歪は熱電対起電圧のフィードバック増幅によるわずか 200 V/cm の電界で容易に補償できる。

PMN-PT 系の他の成分に関する詳細なデータ，および改良固溶系 $Pb(Mg_{1/3}Nb_{2/3})O_3$ - $PbTiO_3$ - $Ba(Zn_{1/3}Nb_{2/3})O_3$（温度安定性と低温におけるとステリシスの改良）に関するデータについては，文献 (5), (6), (7) を参照されたい。

§4. 意匠研究

電歪素子の実用化に拍車をかけたもののひとつに積層コンデンサーの技術がある。図5に電歪素子デザインの例を掲げたが，(a) の多層型を考えると，外部電圧と総厚みが一定の条件で，総変位量が，圧電材料の場合には層数に比例するのに対して電歪材料の場合には，層数の2乗に比例するのでその効用は非常に大きい。

ここでは，予備的に市販のソフト PZT を用いて行なった，電極内蔵多層型変位素子（internally electroded multilayer displacement transducer）の作製，特性について述べる[8]。図5 (a) は積層コンデンサーのデザインと同じもので，この型では1層おきにポーリング方向は逆であるが，変位は相和される。(b) は単層型，(c) は電極サンドイッチ型であり共に比較のために作製した。市販の PZT 501A (Ultrasonic Powders, Inc.) と結合剤 B42 (Cladan Inc.) の混合物を用い，標準テープ・カスチング法を適用した。乾燥したカスト・テープ（～250μm）間に，スクリーン・プリント プラチナ・インク（Englehard Industries, ～25μm）を内部電極としてほどこし，多層にしたものをプレスし標準的に焼成した。密度95%程度のものが焼成されるが，これをさらに 20 MNm^{-2} アルゴン圧中で HIP (hot isostatic press) 焼成し理論密度に近いものを作製した。図6にソフト PZT に関する圧電歪の電界依存性を示した。サンドイッチ型は単にバルク内部に等電位面をもうけるだけで，歪にほとんど影響しない。多層型では2種の電極が交互に入り組み，周囲に絶縁領域が必要なため電圧効果を若干減じている。このクランプ効果があるとは言え，5層型試験素子において，単層型と同じ変位を生ずるのに要する電圧は 1/3 以下であった。

多層型変位素子の実用性を示すために，0.9 PMN-0.1 PT を用いて，100 層素子を作製した。250 V 印加によって，約 25 mm 長素子の変位は 12 μm ($\Delta l/l \sim 5\times10^{-4}$) であり，反復再現性も良好であった。ちなみに 10°C の室温変化による熱膨張は 0.4 μm 以下である。カスト・テープ厚を減ずれば，印加電圧をそれだけ下げることができる。

図7には，ミラー・コントロール用としての実際使用例を示した。(a) は前述の多層型変位素子（縦効果素子），(b) は押し出し法により作製したハニカム型変位素子（筒の内壁に電極を塗布した横効果素子）の利用を示している。いずれの場合にも各々に適当な電圧を印加することにより，ミラーの位置および傾きを微妙にコントロールすることができる。

§5. 理論研究

イオン結晶中の電歪効果は，剛体イオンモデルにおける格子振動の非調和成分によって引きおこされるのであるが，最も単純な結晶構造をもつアルカリ・ハライドにおいてさえ，従来信頼のおける実験データがなかったために，電歪効果の微視的な解析法は確立されていない．強誘電体の電歪については多くのデータが存在するが[9]，（3種以上の元素イオンを含み）結晶構造が単純でないために，その解析は現象論的取扱いの域を出ていないものが多い．
ここでは最近の我々の研究から，緩和型強誘電体ペロブスカイト結晶 $Pb(Mg_{1/3}Nb_{2/3})O_3$ と $Pb(Zn_{1/3}Nb_{2/3})O_3$ の電歪効果に関する議論と，アルカリ・ハライドの電歪測定技術の2点にトピックスをしぼり述べる．

5.1. 緩和型強誘電体の電歪効果

$Pb(Mg_{1/3}Nb_{2/3})O_3$ と $Pb(Zn_{1/3}Nb_{2/3})O_3$ 単結晶の電歪を歪ゲージを用いて測定した．独立に誘電率の静水圧依存性から電歪定数 Q_h ($= Q_{11}+2Q_{12}$) を求めた（(10) 式参照）[10-12]．静水圧印加装置は市販のプレクソル油圧ポンプ（Pressure Products Industries）を用い，0～6 kbarの測定を行なった．表Iに得られた電歪定数 Q_{11}, Q_{12}, Q_h およびキュリー・ワイス定数，キュリー温度の圧力依存性等を，通常のペロブスカイト強誘電体（$BaTiO_3$, $PbTiO_3$, $KTaO_3$, $SrTiO_3$）の値と比較してまとめた．一見して緩和型強誘電体の電歪定数が通常の強誘電体の定数より1桁小さいことがわかる．さらに興味深いことは，緩和型のキュリー・ワイス定数 C がその分大きく[13]，結局積 Q_hC（あるいは電歪定数と誘電率の積）が，すべてのペロブスカイト型強誘電体でほぼ一定の値をもつことである†．
この関係を説明するために，我々は通常の強誘電体における，格子振動TOモードのソフト化のモデルを用いることを試みた．ソフト・モード振動数 ω_{TO} の温度依存性が

$$\omega_{TO}^2 = A\,(T - T_C) \qquad (T_C:\text{(平均)キュリー温度}) \tag{8}$$

で与えられるとし，定数 A の値が緩和型においては通常の値より1桁小さいと仮定する．この仮定はモードのソフト化が緩慢であることを意味し，緩和型強誘電体の特徴である散漫な相転移（diffuse phase transition）とも矛盾しない．格子振動と静的誘電率（ε_s）を結びつける Lyddane-Sachs-Teller 関係式を，光学的屈折率（ε_∞^2），LOモード振動数，ソフト化しないTOモード振動数が，すべてのペロブスカイトに対してほぼ同じであるとの仮定の下で書き下すと，

$$1/\varepsilon_s = K\omega_{TO}^2 \tag{9}$$

となる．また誘電率の静水圧依存性と電歪効果の間には，式(6)を考慮すれば次の関係がある．

$$\partial(1/\varepsilon_s)/\partial p = 2(Q_{11}+2Q_{12}) = 2Q_h \tag{10}$$

式(8)～(10)から

$$C = 1/KA \tag{11}$$

$$Q_h = \left[-\tfrac{1}{2}(\partial T_C/\partial p)\right] KA \tag{12}$$

すべてのペロブスカイト強誘電体において $(\partial T_C/\partial p) \sim -5\ K\,kbar^{-1}$ という実験事実（このことは積 Q_hC が一定であることと等価）を用いれば，C と Q_h の値の大小は A の値の大きさに帰着する．
$A/Q_h \sim 5\times10^2\ [cm^{-2}K^{-1}/m^4C^{-2}]$ なる関係を用いて $Pb(Mg_{1/3}Nb_{2/3})O_3$ と $Pb(Zn_{1/3}Nb_{2/3})O_3$ のソフト・モード振動数 ω_{TO} を予測計算すると，相転移温度近傍で約7 cm^{-1}（2×10^{11} Hz）となる．この波数ベクトル値は，ラマン散乱実験の限界値以下であり，従来この実験法でTOモードのソフト化が観測されていないのも道理である[14]．また誘電率の周波数依存性において，10^{-2}～2×10^9 Hz の範囲で大きな分散効果が見られるのも[15]上記の波数ベクトル値を支持している．より詳しい議論は文献(16)を参照されたい．

5.2. アルカリ・ハライドの電歪測定技術

アルカリ・ハライドは最も単純な結晶構造をもつイオン結晶であるため，電歪の微視的な解析も比較的容易である[17]．現在我々が試みているモデルには次のようなものがある[18]．

† 実際には，全く分極過程の異なった KDP（$Q_h = 0.94\ m^4C^{-2}$, $C = 3.3\times10^3$ K）等の強誘電体においてもほぼ同じ関係が存在している．

a．剛体イオンモデル（rigid ion model）
b．電荷移動モデル　（charge transfer model）
c．殻モデル　　　　（shell model）
d．非調和殻モデル　（anharmonic shell model）

しかしながら，信頼のおけるデータがない現在，モデルの適合性を評価できない状態にある。
また表Ⅱには各種八面体イオン配位をとるイオン結晶の電歪定数をまとめてあるが，アルカリ・ハライド，酸化マグネシウム，ペロブスカイト，タングステン・ブロンズのタイプ順の符号と値の変化は興味がもたれる問題である。

ともあれここではアルカリ・ハライドの電歪効果を直接測定するために，我々が新たに作製した高感度ACディラトメータに関して述べる[19]。アルカリ・ハライドの電歪の大きさを評価すると，厚さ1mmのサンプルに1kV印加したとき約0.1Å程度と言われている（$\Delta l/l \sim 10^{-8}$）。従って精度よく電歪定数を測定するためには10^{-3}Åの分解能が要求される。

キャパシタンス・ブリッジの改良にともない，近年平行プレート空気キャパシターを利用したディラトメータの作製がさかんになってきたが，従来の装置の分解能はせいぜい$\Delta l \sim 1$Åであった[20]。
我々はBohatý とHaussühlの作製した装置[21]に改良を加え，最大感度10^{-3}Åをもつディラトメータを作製した。図8にそのブロック・ダイアグラムを示した。検出キャパシターの片プレート（c）は標準圧電結晶（水晶）(d)の片面に接合され，片プレート（b）は試料電歪結晶(a)の片面に機械的に接合されている。前者全体はさらにPZTの変位素子上に接合され，ポジション・コントロールされている。検出キャパシターのプレート間隔変化は，それに比例した容量変化として精密キャパシタンス・ブリッジ（j,k,l）によって検知される。容量変化の直流分（<0.1Hz）は増幅されPZT圧電歪素子に印加される。このフィードバック・システムによって温度変動にともなう熱膨張ドリフトを抑えることができる。図9はシステム全体を29.0±0.04℃に保ったときのプレート間隔変化を時間に対してプロットしたものである。D.C.サーボシステムを使用しない場合には間隔は1Å/分程度の熱膨張ドリフトをともない，キャパシタンス・ブリッジを80dB程度の高い増幅レンジにしておくと数分で線形的な作動領域をオーバーしてしまう。サーボの使用により，ドリフトを0.002Å/分以下に抑えることが可能になったために，システム全体の安定性，精度は飛躍的に向上した。

電歪結晶に7Hz正弦波を増幅器を通して印加すると，キャパシタープレート（b）は14Hzで駆動され，一方標準圧電結晶に位相同期させ14Hz正弦波を印加するとやはりプレート（c）は14Hzで駆動される。両結晶に印加する電圧と位相を適当に調整して，両プレートの振動を同期させると容量変化（交流分）を零にすることができる。図10に両結晶に電界を印加して生ずる歪を模式的に示した。この零位状態が実現できれば，両結晶の厚さ，印加電圧，標準結晶の圧電定数から未知の電歪定数は簡単に計算される。
図11は，装置の分解能を調べるために，試料電歪結晶には電圧を印加せず，標準水晶にだけ電圧印加したときの，出力，圧電歪をプロットしたものである。最適条件で，ロック・イン・アンプの最小分解能は0.1mVで，これは変位の分解能10^{-3}Åに相当する。
図12に圧電結晶ZnS（wurtzite）zカット板と水晶xカット板との間で測定した零位法の例を示した。位相調整後ZnSに一定の電圧を印加しておき，水晶印加電圧に対してロック・イン・アンプ出力をプロットした。出力最低の位置が零位状態とみなせ，両結晶に印加した電圧比から直ちに，d_{33}(wurtzite) = 1.41 d_{11}(quartz) の関係が導ける。

表Ⅲには，各種圧電および電歪定数の測定例を，従来の報告値と比較してまとめたが，両定数値の一致はよく精度は1桁以上向上している。このことはすなわち，新しく作製したACディラトメータの信頼性を示すものである。装置の構成の詳細については文献(22)を参照されたい。アルカリ・ハライド結晶の信頼おける電歪定数の測定が今後の課題である。

§6．結言

内容を要約しておく。
1）$0.9Pb(Mg_{1/3}Nb_{2/3})O_3 - 0.1PbTiO_3$セラミクスの電歪は，通常の圧電歪の大きさを凌ぎ，反復再現性も優れており変位素子材料として有望である。加えて実用温度領域の熱膨張が非常に小さいという利点をもつ。電歪素子では，めんどうなポーリング過程を必要としないことも注目される。
2）積層型デザインの使用により電歪素子の実用化が容易になった。厚さ100μm程度のカスト・テープを用いれば，印加電圧100Vで，$\Delta l/l \sim 10^{-3}$程度の電歪を生ずる素子を作製できる。
3）緩和型強誘電体の電歪定数Qは，通常のペロブスカイト強誘電体の値に比べて1桁小さい。反面キュリー・ワイス定数は1桁大きいために（誘起分極が大きく），結局，緩和型強誘電体の電歪の大き

さは通常の強誘電体より1桁大きいことがわかる。
4) アルカリ・ハライドの電至測定用の容量型高感度ACディラトメータを作製した。分解能 $\Delta l \sim 10^{-3}$ Å ($\Delta l/l \lesssim 10^{-10}$)は、他の測定法(例えばX線回折等)によっては到達し得ない値である。

電至効果はイオン性結晶において見られる一般的な現象(歪の電界依存性)であり、熱膨張(thermal expansion, 歪の温度依存性)や圧縮率(compressibility, 歪の圧力依存性)と密接な関係があることが、現象論的に予想される。図13は、PVF_2, アルカリ・ハライド, 酸化マグネシウム, ペロブスカイト強誘電体, 緩和型強誘電体等各種について、電至定数 Q_h と線熱膨張係数 α を対数プロットしたものである。関係式 $Q_h \propto \alpha^2$ の明確な説明はないが興味ある事実である。

本稿が今後の電至デバイスの研究あるいは理論的研究の指針の一役を担えれば筆者らの幸いである。最後に試料作製, 電至測定に尽力いただいた S.J. Jang 君(ペンシルバニア州立大)と桑田純君(東京工大)および財政的援助の Office of Naval Research (米国) と作工会(日本)に感謝の意を表する。

文献

1) Sientific American, Scientific American Inc. (New York), 239, 70 (1978).
2) K.M. Leung, S.T. Liu and J. Kyonka, Ferroelectrics (印刷中).
3) V.A. Bokov and I.E. Myl'nikova, Fiz. Tverd. Tela, 3, 841 (1961).
4) L.E. Cross, S.J. Jang, R.E. Newnham, S. Nomura and K. Uchino, Ferroelectrics (印刷中).
5) S.J. Jang, K. Uchino, S. Nomura and L.E. Cross, Ferroelectrics (印刷中).
6) S.J. Jang, L.E. Cross, S. Nomura and K. Uchino, Phys. Stat. Sol. (投稿中).
7) S.J. Jang, Ph D. Thesis, The Pennsylvania State University (1979).
8) L.J. Bowen, T. Shrout, W.A. Schulze and J.V. Biggers, Ferroelectrics (印刷中).
9) Landolt-Börnstein, Group III, Volume II, Springer-Verlag (1979).
10) J. Yoshimoto, B. Okai and S. Nomura, J. Phys. Soc. Japan, 31, 307 (1971).
11) S. Nomura, J. Kuwata, S.J. Jang, L.E. Cross and R.E. Newnham, Mat. Res. Bull. 14, 769 (1979).
12) K. Uchino, S. Nomura, L.E. Cross, S.J. Jang and R.E. Newnham, J. Appl. Phys., (投稿中)
13) J. Kuwata, K. Uchino and S. Nomura, Ferroelectrics, 22, 863 (1979).
14) G. Burns and B.A. Scott, Commun. Solid State Phys. 13, 417 (1973).
15) V.V. Kirillov and V.A. Isupov, Ferroelectrics 5, 3 (1973).
16) K. Uchino, S. Nomura, L.E. Cross and R.E. Newnham, (投稿予定).
17) W. Kinase and M. Itoh, J. Phys. Soc. Japan, 42, 895 (1976).
18) L.E. Cross, R.E. Newnham, G.R. Barsch and J.V. Biggers, Annual Report to Office of Naval Research through Contract No. N00014-78-C-0291, 19 (1978
19) K. Uchino, L.E. Cross, Ferroelectrics (印刷中).
20) G. Brändle and R. Griessen, Cryogenics GBB, 299 (1973).
21) L. Bohatý and S. Haussühl, Acta Cryst. A33, 114 (1977).
22) K. Uchino and L.E. Cross, Proc. 33rd Annual Symposium on Frequency Control, U.S. Army Electronics Command, Forlmonmouth, N.J. (1979).
23) V.E. Bottom, J. Appl. Phys. 41, 3941 (1970).
24) I.B. Kobyakov and G.S. Pado, Soviet Phys.- Solid State 9, 1707 (1968).
25) F. Lissalde and J.C. Peuzin, Ferroelectrics 14, 579 (1976).
26) Z.P. Chang and G.R. Barsch, IEEE Trans.- Sonics and Ultrasonics 3, 127 (197

目次 [2]

Table I. Electrostrictive coefficients, Curie-Weiss constants, the variation of Curie temperature with hydrostatic pressure, and the coefficients related to the temperature dependence of the soft-mode frequency for some perovskite-type ferroelectrics.

Substance	Q_{11}	Q_{12}	Q_h	C	dT_c/dp	A
	($\times 10^{-2}\ m^4C^{-2}$)			($\times 10^5$ K)	(K kbar^{-1})	($cm^{-2}K^{-1}$)
$BaTiO_3$	11.0	-4.5	2.0	1.5	-5.5	—
$PbTiO_3$	8.0	-2.9	2.2	1.7	<-8.0	8.2
$KTaO_3$	10.8	-2.8	5.2	0.5	—	29.1
$SrTiO_3$	8.0	-1.5	5.0	0.77	—	28.6
$Pb(Mg_{1/3}Nb_{2/3})O_3$	2.52[12]	-0.96[12]	0.60[12]	4.7[6]	-4.8[12]	3.0*
$Pb(Zn_{1/3}Nb_{2/3})O_3$	2.38[11]	-0.86[11]	0.66	4.7[13]	-5.5[10]	3.3*

(Data quoted from the reference (9) Landolt-Börnstein.)

* Estimated values from the equation $A = 500\,Q_h$.

Table II. Electrostrictive coefficients Q of ionic crystals (in m^4C^{-2})

Materials		Q_{11}	Q_{12}	$Q_{11}+2Q_{12}$
Alkali halide	RbI	-13.4	4.72	-3.95
	NaCl	- 3.52	1.26	-1.01
	LiF	- 1.66	0.59	-0.47
MgO		—	—	-0.18
Perovskite type	$PbTiO_3$	0.080	-0.029	0.022
	$BaTiO_3$	0.110	-0.045	0.020
	$KNbO_3$	0.130	-0.047	0.036
Tungsten bronze type	$Ba_2NaNb_5O_{15}$	0.104	-0.018	0.068
	$Pb_2KNb_5O_{15}$	0.201	-0.015	0.171

(Data quoted from the references (9) and (21))

Table III. Some example data of electromechanical coefficients

Sample	Coefficient	Present	Previous
Quartz ⟨100⟩	$d_{11}(\times 10^{-12}\ mV^{-1})$	+2.27 (±0.01)	+2.27[23]
Wurtzite ⟨001⟩	$d_{33}(\times 10^{-12}\ mV^{-1})$	+3.20 (±0.02)	+3.2 (±0.2)[24]
$LiNbO_3$ ⟨001⟩	$d_{33}(\times 10^{-12}\ mV^{-1})$	+6.73 (±0.04)	+6.1 (±0.5)[25]
Berlinite ⟨100⟩	$d_{11}(\times 10^{-12}\ mV^{-1})$	-3.98 (±0.05)	-5.3 (±1.6)[26]
PVF_2 (Kynar 7200)	$d_{33}(\times 10^{-12}\ mV^{-1})$	-20.2 (±0.4)	-20*
PVF_2 (Kureha)	$d_{33}(\times 10^{-12}\ mV^{-1})$	-24.2 (±0.6)	-25*
$Pb(Mg_{1/3}Nb_{2/3})O_3$ (Ceramic)	$M'_{11}(\times 10^{-16}\ m^2V^{-2})$	+1.92 (±0.02)	+1.8 (±0.2)[6]

* Private communication ; estimated values by J.C. Hicks (1979)

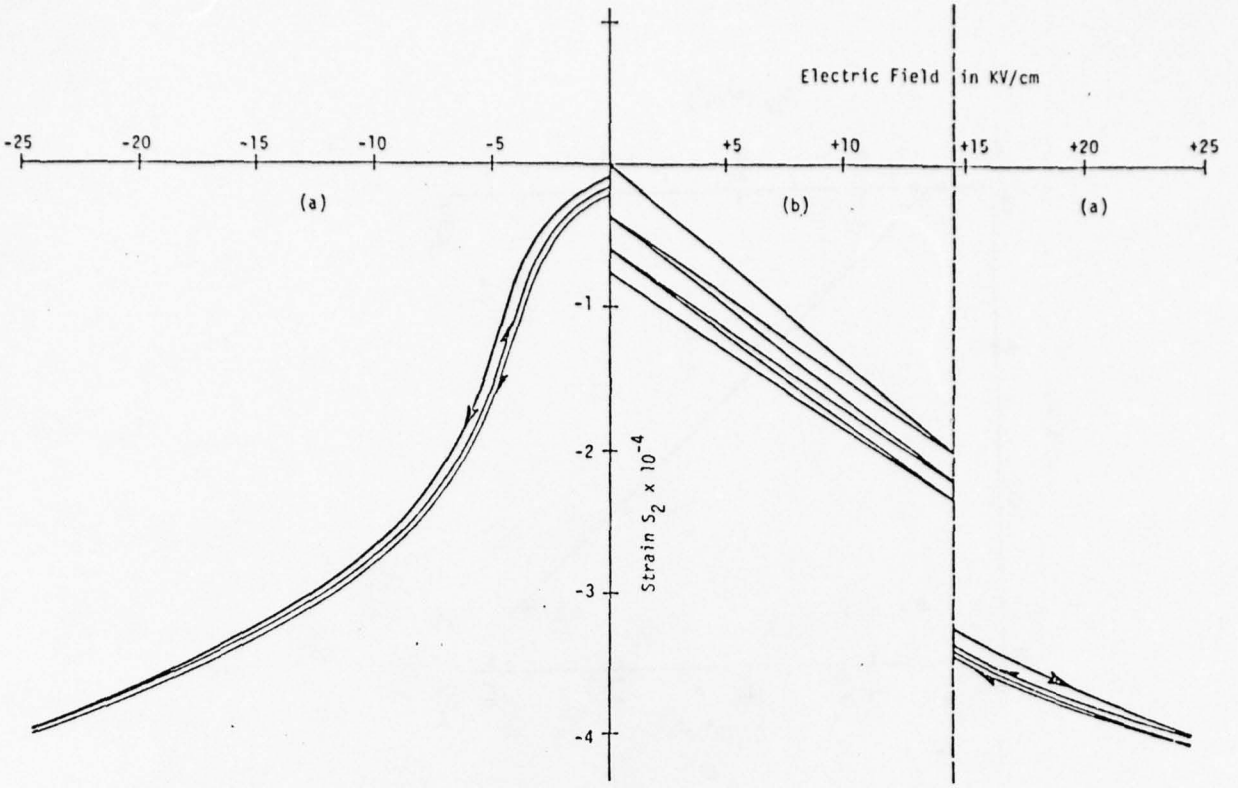
Electric Field in KV/cm
-25
-20
-15
-10
-5
+5
+10
+15
+20
+25
(a)
(b)
(a)
-1
-2
-3
-4
Strain $S_2 \times 10^{-4}$

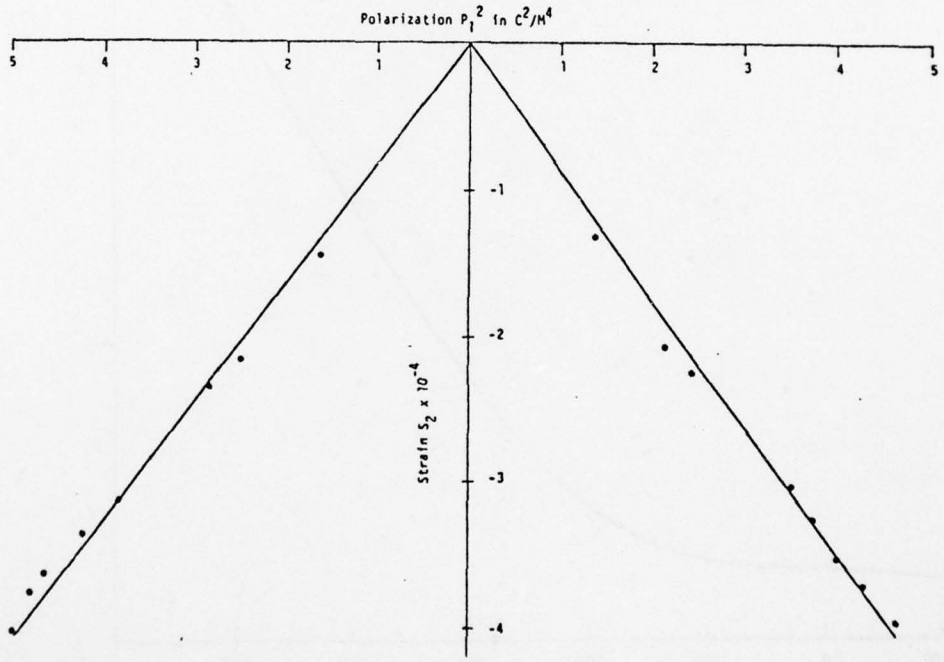
Polarization P_1^2 in C^2/M^4
5
4
3
2
1
1
2
3
4
5
-1
-2
-3
-4
Strain $S_2 \times 10^{-4}$

Temperature in °C
-200
-100
0
100
200
300
400
500
Strain x 10-4
0
5
10
15
20
25
30

Fig. 2

Q12 (M4/C2)
X10-2
-1.0
-0.8
-0.6
-0.4
-0.2
PMN
Q12
Q11
MOLE % OF PT
5
10
15
Q11 (M4/C2)
X10-2
3.0
2.4
1.8
1.2
0.6

Fig. 3

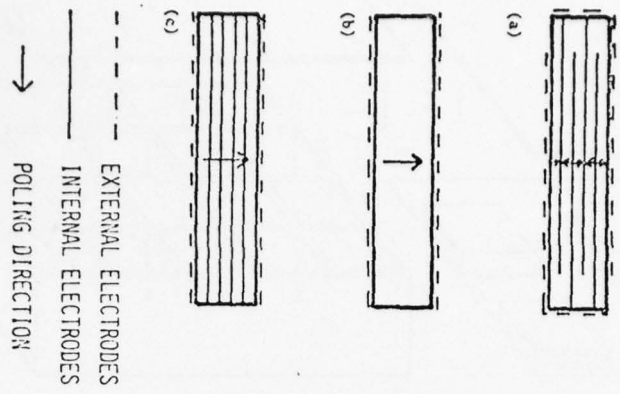
(c)
(b)
(a)
EXTERNAL ELECTRODES
INTERNAL ELECTRODES
POLING DIRECTION

Fig 5

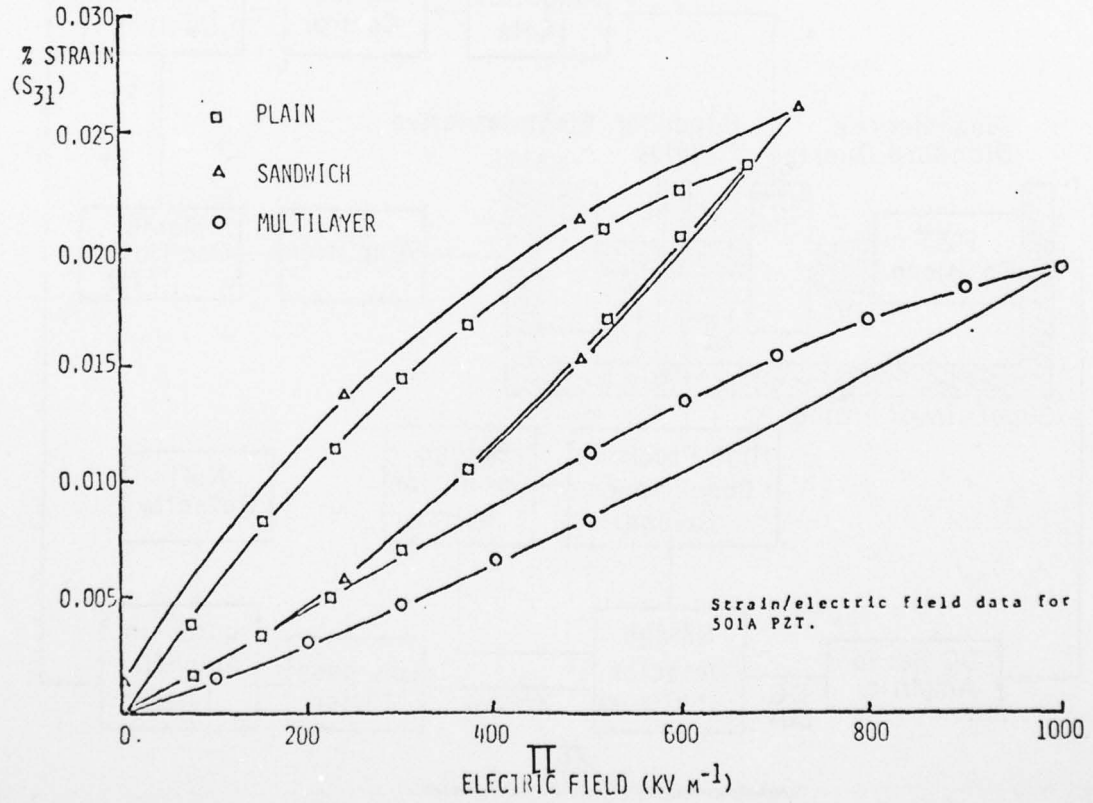
0.030
% STRAIN
(S_{31})
0.025
0.020
0.015
0.010
0.005
PLAIN
SANDWICH
MULTILAYER
Strain/electric field data for
501A PZT.
0
200
400
600
800
1000
ELECTRIC FIELD (KV M^{-1})

Fig 6

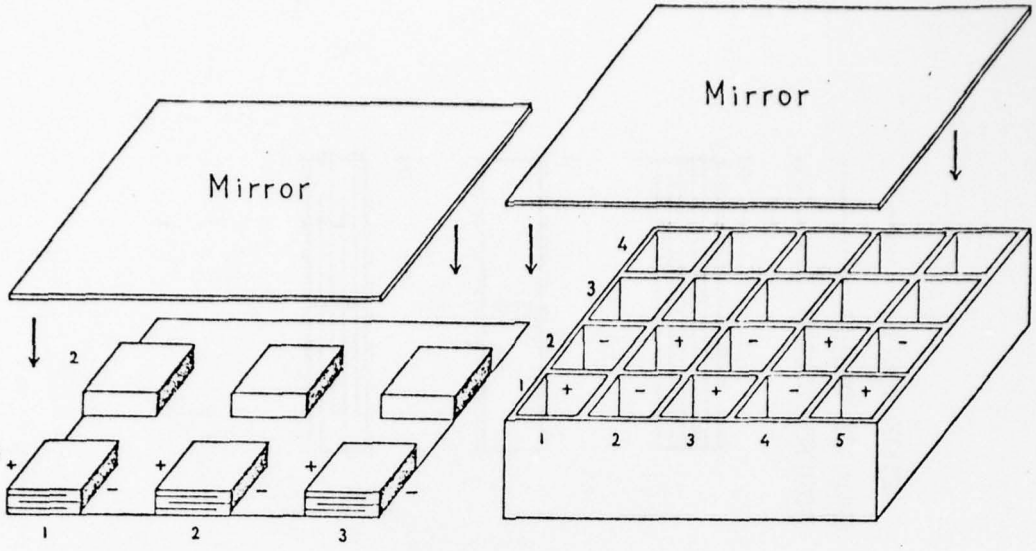

Block Diagram

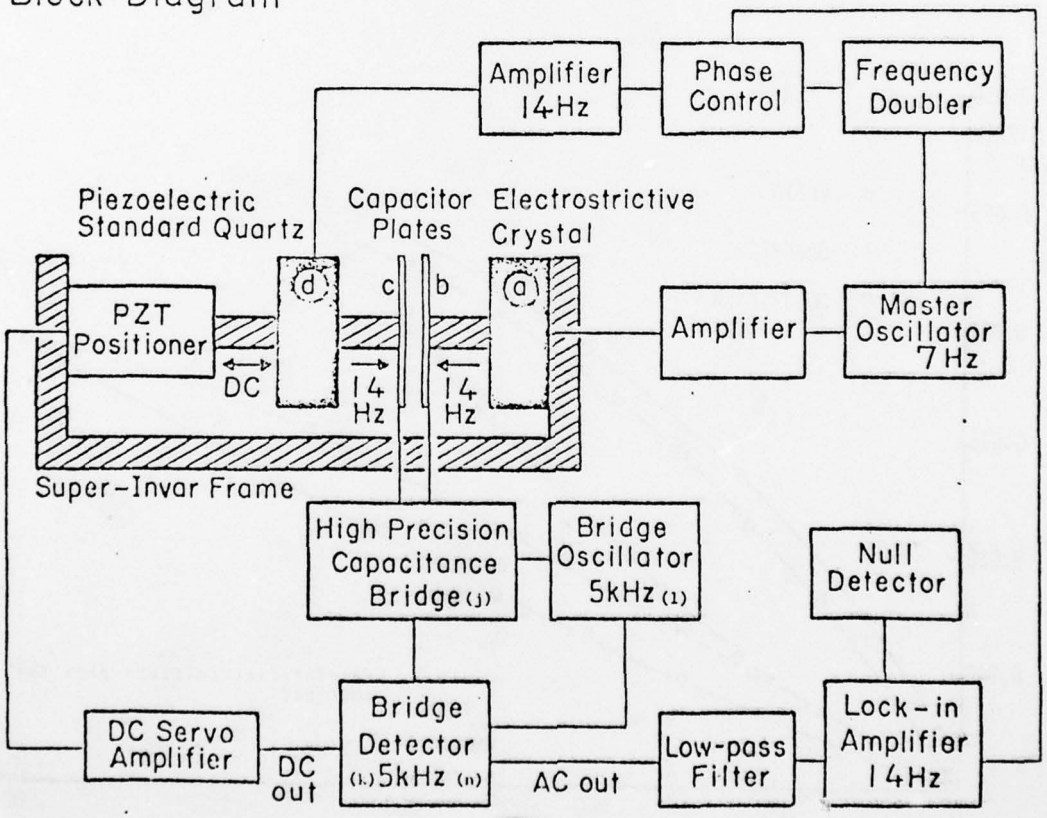

Schematic diagram of the AC dilatometer.

SERVO-POSITIONER CHECK

TEMPERATURE FLUCTUATION $\Delta T \sim \pm 0.04^{o}C$

CAPACITOR PLATES GAP CHANGE $\Delta l \sim \pm 20\ \overset{o}{A}$

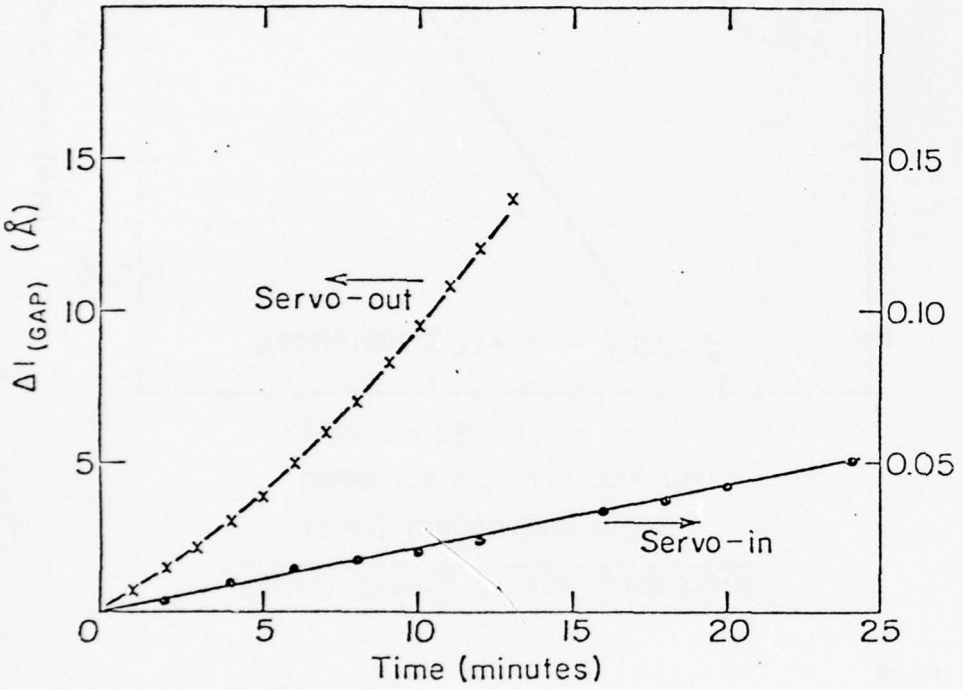

DC plate separation change $\Delta\ell$ as a function of time with and without the drift compensation Servo amplifier.

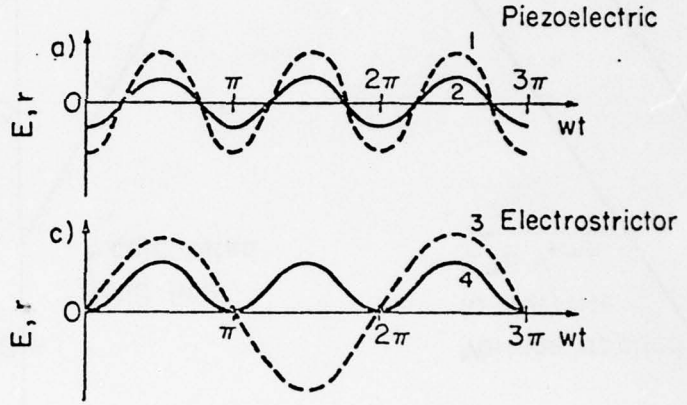

1) time dependence of electric field
2) strain induced in a piezoelectric sample
3) time dependence of electric field
4) strain induced in an electrostrictive sample

Quartz Driving Voltage Dependence

⟨100⟩ longitudinal effect
Under the optimum condition
with C = 79.6 pF

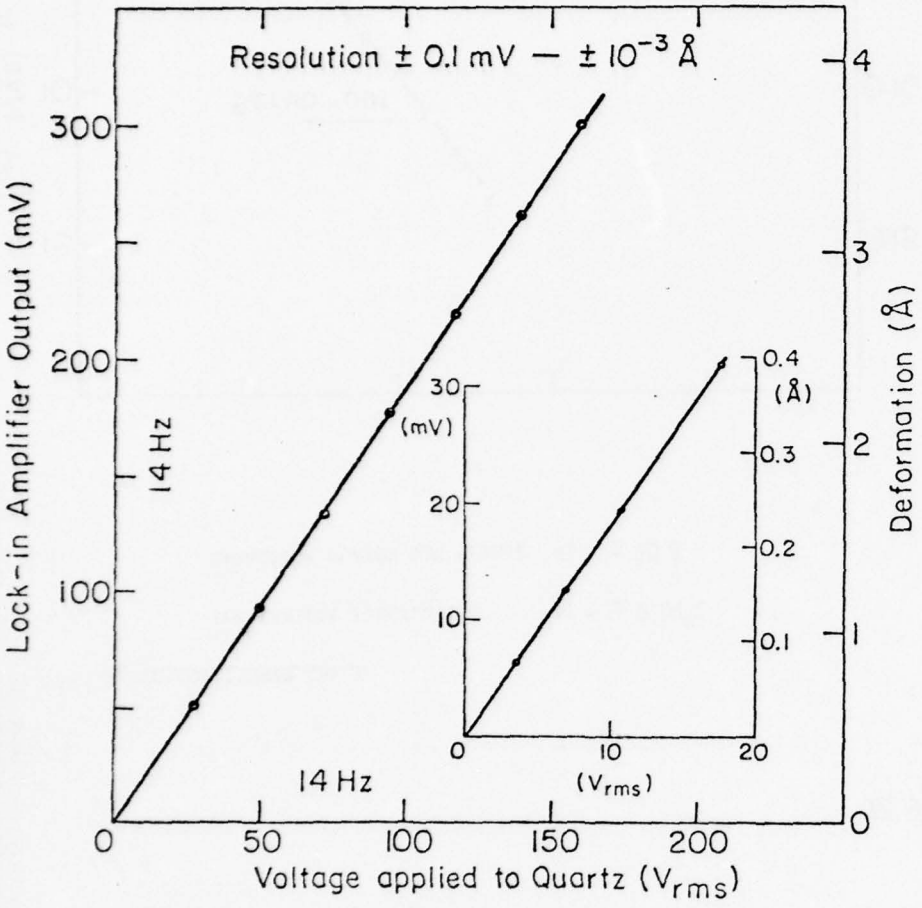

Null-condition Method

Quartz ⟨100⟩
Wurtzite ⟨001⟩ R = 1.41
Under the optimum condition
with C = 105.5 pF

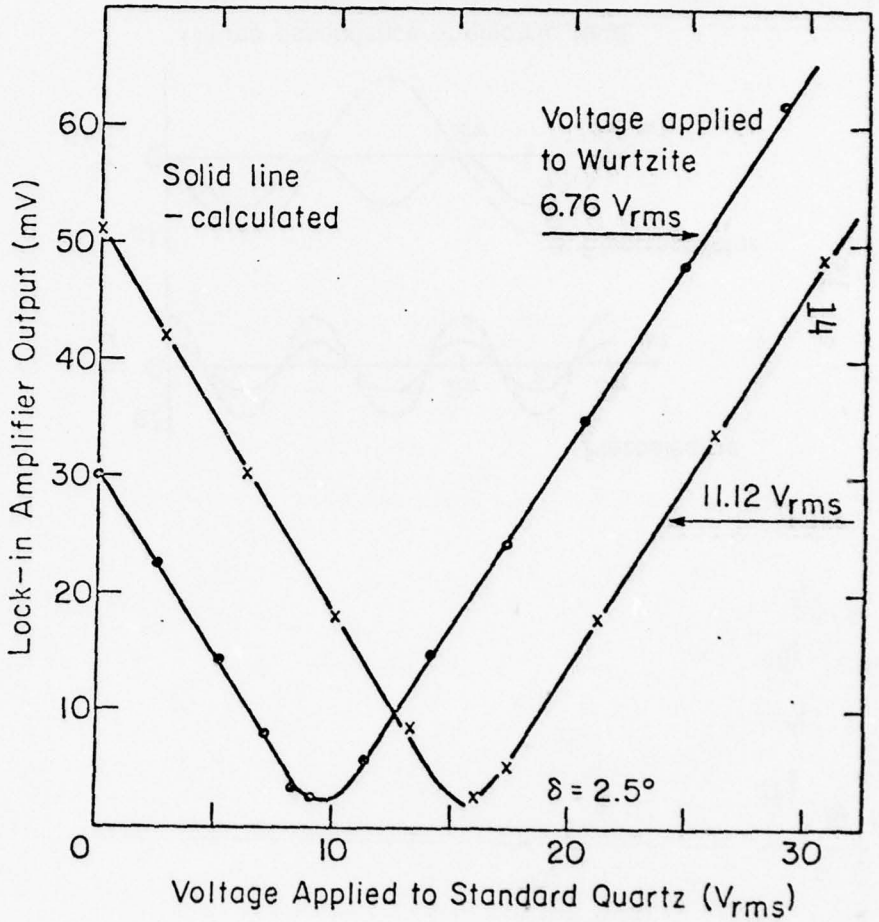

Correlation between Electrostriction and Thermal Expansion

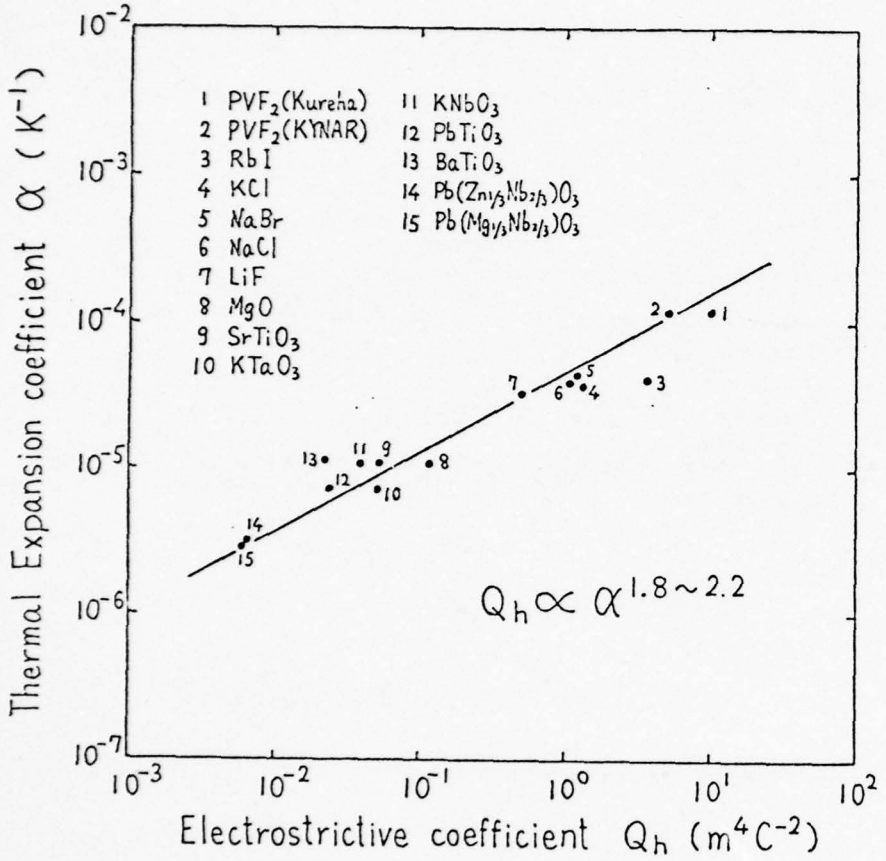

APPENDIX 5

K. Uchino, S. Nomura, L.E. Cross, S.J. Jang and R.E. Newnham. Electrostrictive Effect in Lead Magnesium Niobate Single Crystals. J. Appl. Phys. 51 (1980).

ELECTROSTRICTIVE EFFECT IN LEAD MAGNESIUM NIOBATE SINGLE CRYSTALS

K. Uchino and S. Nomura
Department of Physical Electronics, Faculty of Engineering
Tokyo Institute of Technology, Ookayama, Meguro-ku, Tokyo 152

and

L.E. Cross, S.J. Jang and R.E. Newnham
Materials Research Laboratory, The Pennsylvania State University
University Park, Pennsylvania 16802

Abstract

Transverse and longitudinal elastic strain have been measured for electric fields applied along the <100> direction in single crystals of lead magnesium niobate ($Pb(Mg_{1/3}Nb_{2/3})O_3$), using a bonded strain gauge technique. A quadratic electrostrictive relation holds between induced elastic strain and electric polarization for temperatures near the low frequency dielectric maximum. The electrostriction coefficients are almost temperature independent with values $Q_{11} = 2.50 \times 10^{-2}$ m^4/C^2 and $Q_{12} = -0.96 \times 10^{-2}$ m^4/C^2. To check the direct measurements, the hydrostatic Q coefficient was determined independently by measuring the pressure dependence of the dielectric permittivity. The value $Q_h = 0.60 \times 10^{-2}$ m^4/C^2 obtained is in good agreement with that calculated from the direct measurements.

INTRODUCTION

Recently we have reported in several papers the electrostrictive effects in $Pb(Mg_{1/3}Nb_{2/3})O_3$ based ceramics[1-4]. We suggested in these papers that the polarization related electrostriction constants Q in the relaxor type ferroelectrics are almost an order of magnitude smaller than in most normal ferroelectric perovskites.

To confirm this, the electrostriction in $Pb(Mg_{1/3}Nb_{2/3})O_3$ single crystals has been investigated using a bonded strain gauge method. The hydrostatic pressure dependence of electric susceptibility was also measured in order to support the direct electrostriction measurements. The results are discussed in conjunction with similar data for single crystal $Pb(Zn_{1/3}Nb_{2/3})O_3$ and compared to the electrostrictive behavior of simple (non-relaxor) perovskite ferroelectrics.

EXPERIMENTAL RESULTS

Electrostrictive Measurement

The polarization related electrostriction coefficients of a cubic perovskite type crystal are defined by the following equations

$$Q_{11} = \frac{1}{2}\left(\frac{\partial^2 x_1}{\partial P_1^2}\right) \tag{1}$$

and

$$Q_{12} = \frac{1}{2}\left(\frac{\partial^2 x_2}{\partial P_1^2}\right) \tag{2}$$

where x_1 and x_2 are the longitudinal and transverse induced strains, respectively. By plotting the strain as a function of the square of the electric polarization P_1^2, the values of Q can be calculated from the slope.

Flux-grown crystals of $Pb(Mg_{1/3}Nb_{2/3})O_3$ with rectangular plate shape oriented parallel to (100) ($\sim$2.7 x 2.5 x 1.3 mm^3) were used for our investigation. Gold

electrodes were sputtered onto the faces and a polyimide foil strain gauge (Kyowa, KFR-02-C1-11) was bonded with cement (Kyowa, PC-6) on the face of the crystal. Measurements were carried out by a DC method, using a double bridge technique. The electrostrictive strains x_1 and x_2 were measured as a function of the applied electric field (0.002 Hz) at various temperatures in the range from -10°C to 80°C. The curves of longitudinal strain are shown in Fig. 1, where the strain is corrected by multiplying a constant fractional error due to the gauge and sample geometry.

The induced electric polarization was measured at 0.05 Hz using a Sawyer-Tower circuit (Fig. 2).

Values of the electrostrictive coefficients derived from these measurements are shown in Fig. 3 as a function of temperature. It is evident that the electrostriction constants do not change significantly through the relaxation range (Q_{11} = 2.50 (±0.14) x 10^{-2} m^4 C^{-2}, Q_{12} = -0.96(±0.02) x 10^{-2} m^4 C^{-2}).

Pressure Dependence of Permittivity

By using the Maxwell relation, eqs (1) and (2) are transformed as follows:

$$Q_{11} = -\frac{1}{2}\left(\frac{\partial^2 E_1}{\partial X_1 \partial P_1}\right) = -\frac{1}{2}\left(\frac{\partial \chi_1}{\partial X_1}\right) \tag{3}$$

and

$$Q_{12} = -\frac{1}{2}\left(\frac{\partial^2 E_1}{\partial X_2 P_1}\right) = -\frac{1}{2}\left(\frac{\partial \chi_1}{\partial X_2}\right) \tag{4}$$

These equations indicate that the electrostrictive coefficients can be obtained by measuring stress X dependence of reciprocal susceptibility χ. When hydrostatic pressure p is applied to a centrosymmetric paraelectric crystal, the pressure dependence of the reciprocal susceptibility χ is represented by

$$\left(\frac{\partial \chi_1}{\partial p}\right) = -\left[\left(\frac{\partial \chi_1}{\partial x_1}\right) + \left(\frac{\partial \chi_1}{\partial x_2}\right) + \left(\frac{\partial \chi_1}{\partial x_3}\right)\right] \tag{5}$$

$$= 2Q_h,$$

where $Q_h = Q_{11} + 2Q_{12}$

The effect of hydrostatic pressure on the electric susceptibility of single crystal $Pb(Mg_{1/3}Nb_{2/3})O_3$ was investigated up to 6 kbar. A rectangular plate specimen about 1.5 x 1.5 x 0.6 mm^3 was used for our measurement. The capacitance of the sample was measured at frequencies of 1 and 100 kHz with an automatic capacitance bridge (Hewlett-Packard 4270A).

Hydrostatic pressure was generated in an air-driven intensifier pump (Pressure Products Industries). Plexol was used as the pressure medium. The value of pressure was monitored by a Heise gauge with the accuracy of ±5 bar. Temperature was varied with a lamp heater and an A-C thermocouple was set inside the cell.

Figure 4 shows isotherms of the reciprocal permittivity $1/\varepsilon$ measured as a function of hydrostatic pressure. Whereas for a single crystal $BaTiO_3$ the slope of the $1/\varepsilon$ versus p curve does not depend significantly on temperature[5], a gradual increase of the slope was observed for $Pb(Mg_{1/3}Nb_{2/3})O_3$ with increase of temperature. This effect can be explained by the diffused phase transition theory which will be proposed in the next section. From the averaged value of the slope for higher temperatures (48.2°C, 56.5°C) and eq (5) we calculated the electrostrictive coefficient Q_h as $0.60(\pm 0.08) \times 10^{-2}$ m^4 C^{-2}, which is in good agreement with the value calculated from the direct electrostrictive strain measurements ($0.58(\pm 0.18) \times 10^{-2}$ m^4 C^{-2}).

Figure 5 shows the hydrostatic pressure effect on the difference between dielectric constant (or dissipation factor) measured at 1 kHz and at 100 kHz,

that is the intensity of relaxation.

EXPANDED DIFFUSED PHASE TRANSITION THEORY

Integrating eq (5) we obtain

$$1/\varepsilon = \chi^\circ + 2Q_h p, \tag{6}$$

where $\chi^\circ = (T-T_o)/C$, T is temperature, T_o Curie temperature, and C Curie-Weiss constant. In other words, we obtain the expanded Curie-Weiss law, that is

$$1/\varepsilon = (T-T_o(p))/C \tag{7}$$

where $T_o(p) = T_o - 2Q_h C\, p$, or

$$1/\varepsilon = 2Q_h(p-p_o(T)) \tag{8}$$

where

$$p_o(T) = (T_o-T)/2Q_h C$$

These equations are known to be valid for single crystal $BaTiO_3$[5] and other simple perovskite crystals. But for $Pb(Mg_{1/3}Nb_{2/3})O_3$, eq (8) is not true as is evident in Fig. 4.

For ferroelectrics with a diffused phase transition the law $1/\varepsilon \sim (T-T_o)^2$ has been shown to hold over a wide temperature range instead of the normal Curie-Weiss law[6]. Considering the local Curie temperature distribution to be Gaussian, the reciprocal permittivity can be written in the form:

$$\frac{1}{\varepsilon} = \frac{1}{\varepsilon_m} \exp[(T-T_o)^2/2\delta^2] \tag{9}$$

where δ is a parameter describing the intensity of the diffused phase transition. A series expansion, neglecting terms with $(T-T_o)^4$ and higher gives

$$\frac{1}{\varepsilon} = \frac{1}{\varepsilon_m} + \frac{(T-T_o)^2}{2\varepsilon_m \delta^2} \tag{10}$$

Here, we propose an expanded theory where T_o is replaced by $T_o(p)$, since under pressure each local micro-region follows a slightly different Curie-Weiss law

$$\frac{1}{\varepsilon} = \frac{1}{\varepsilon_m} + \frac{(T-T_o(p))^2}{2\varepsilon_m \delta^2} \tag{11}$$

or

$$\frac{1}{\varepsilon} = \frac{1}{\varepsilon_m} + \frac{(2Q_h C)^2 (p-p_o(T))^2}{2\varepsilon_m \delta^2} \tag{12}$$

where $T_o(p)$, $p_o(T)$ are the same as previously described.

Figure 6 shows dependence of $1/\varepsilon$ on $(T-T_o)^2$ for a single crystal of $Pb(Mg_{1/3}Nb_{2/3})O_3$. From this curve with the aid of eq (10) we can find δ, the parameter that determines the diffuseness of the phase transition. The values of the fitted parameters are T_o = 269 K, $1/\varepsilon_m = 5.6 \times 10^{-5}$, and δ = 45 K.

The parameters of eq (12) are determined so that the slopes of the $1/\varepsilon$ versus $(p-p_o(T))^2$ curves have a constant value. The procedure is shown in Fig. 7(b) and the parameters deduced are T_o = 269 K, $1/\varepsilon_m = 4.6 \times 10^{-5}$, δ = 41 K, $2Q_h C$ = 4.9 K/kbar, which are in good agreement with the previous values. If we use the value $C = 4.5 \times 10^5$ determined from the slope of the $1/\varepsilon$ - T curve at higher temperatures, we calculate an electrostrictive coefficient $Q_h = 0.61 \times 10^{-2}$ m^4 C^{-2}. Figure 7(a) shows the temperature dependence of $p_o(T)$ determined experimentally. An almost linear relation supports our proposed procedure. The gradient is an estimate of the variation of Curie temperature with pressure and gives a consistent result with the Q_h value obtained.

DISCUSSION

Electrostrictive coefficients and the pressure derivatives of Curie temperature for $Pb(Mg_{1/3}Nb_{2/3})O_3$ and $Pb(Zn_{1/3}Nb_{2/3})O_3$ are summarized in Table I

in comparison with the data for $BaTiO_3$ and $PbTiO_3$. The Q_{11} values are slightly corrected by considering the (dT_c/dp) values. It is evident from these data that the polarization related electrostriction constants Q_{ij} in relaxor ferroelectric crystals are several times smaller than in most normal ferroelectric perovskites. On the other hand, the Curie-Weiss constants in the relaxor crystals are known to be several times larger[12] and consequently there follows an interesting effect, in that the (dT_c/dp) value is almost the same for all ferroelectric perovskites (See eq (7)).

A further study on the microscopic origin of electrostriction is in progress.

Acknowledgment

We wish to thank the Office of Naval Research for their support of our work, through Contract No. N00014-78-C-0291. We also owe our colleagues at the Materials Research Laboratory for the sample preparation and their assistance. The work by K. Uchino was in part supported by the Sakkokai Foundation in Japan.

References

1. L.E. Cross, S.J. Jang, R.E. Newnham, S. Nomura and K. Uchino, Ferroelectrics (accepted).
2. S.J. Jang, K. Uchino, S. Nomura and L.E. Cross, Ferroelectrics (in press).
3. S. Nomura, K. Tonooka, J. Kuwata, L.E. Cross and R.E. Newnham, Proc. 2nd Meeting on Ferroelectric Mater. & Appl. (in press).
4. S.J. Jang, L.E. Cross, S. Nomura and K. Uchino, Phys. Stat. Sol. (submitted).
5. G.A. Samara, Phys. Rev. 151, 378 (1963).
6. V.V. Kirillov and V.A. Isupov, Ferroelectrics 5, 3 (1973).
7. T. Yamada, J. Appl. Phys. 43, 328 (1972).
8. G.A. Samara, J. Phys. Soc. Japan, 28S, 399 (1970).
9. V.G. Gavrilyachenko and E.G. Fesenko, Soviet Phys.-Cryst. 16, 549 (1971).
10. S. Nomura, J. Kuwata, S.J. Jang, L.E. Cross and R.E. Newnham, Mat. Res. Bull. 14, 769 (1979).
11. J. Yoshimoto, B. Okai and S. Nomura, J. Phys. Soc. Japan 31, 307 (1971).
12. J. Kuwata, K. Uchino and S. Nomura, Ferroelectrics (in press).

Table I. Electrostrictive coefficients and the variation of Curie temperature with hydrostatic pressure for some perovskite-type crystals.

substance	$Q_{11}(x10^{-2}\ m^4\ C^{-2})$	$Q_{12}(x10^{-2}\ m^4\ C^{-2})$	$Q_h(x10^{-2}\ m^4\ C^{-2})$	dTc/dp (K $kbar^{-1}$)
$BaTiO_3$	11.0[7]	-4.5[7]	2.0	-5.5[8]
$PbTiO_3$	8.0[9]	-2.9[9]	2.2	-8.0[8]
$Pb(Zn_{1/3}Nb_{2/3})O_3$	2.38[10]	-0.86[10]	0.66	-5.5[11]
$Pb(Mg_{1/3}Nb_{2/3})O_3$	2.52	-0.96	0.60	-4.8

Figure Captions

Fig. 1 Electric field dependence of the longitudinal electrostriction at various temperatures.

Fig. 2 Electric field dependence of the induced polarization at various temperatures.

Fig. 3 Temperature dependence of the electrostrictive coefficients of $Pb(Mg_{1/3}Nb_{2/3})O_3$ single crystals.

Fig. 4 Hydrostatic pressure dependence of the reciprocal permittivity at various temperatures.

Fig. 5 Hydrostatic pressure dependence of the difference between dielectric susceptibility (or dissipation factor) measured at 1 kHz and at 100 kHz.

Fig. 6 Dependence of $1/\varepsilon$ on $(T-T_o)^2$ for $Pb(Mg_{1/3}Nb_{2/3})O_3$.

Fig. 7 Hydrostatic pressure dependence of permittivity:

(a) $p_o(T)$ versus $(T-T_o)$.

(b) $(1/\varepsilon - 1/\varepsilon_m)^{1/2}$ versus p.

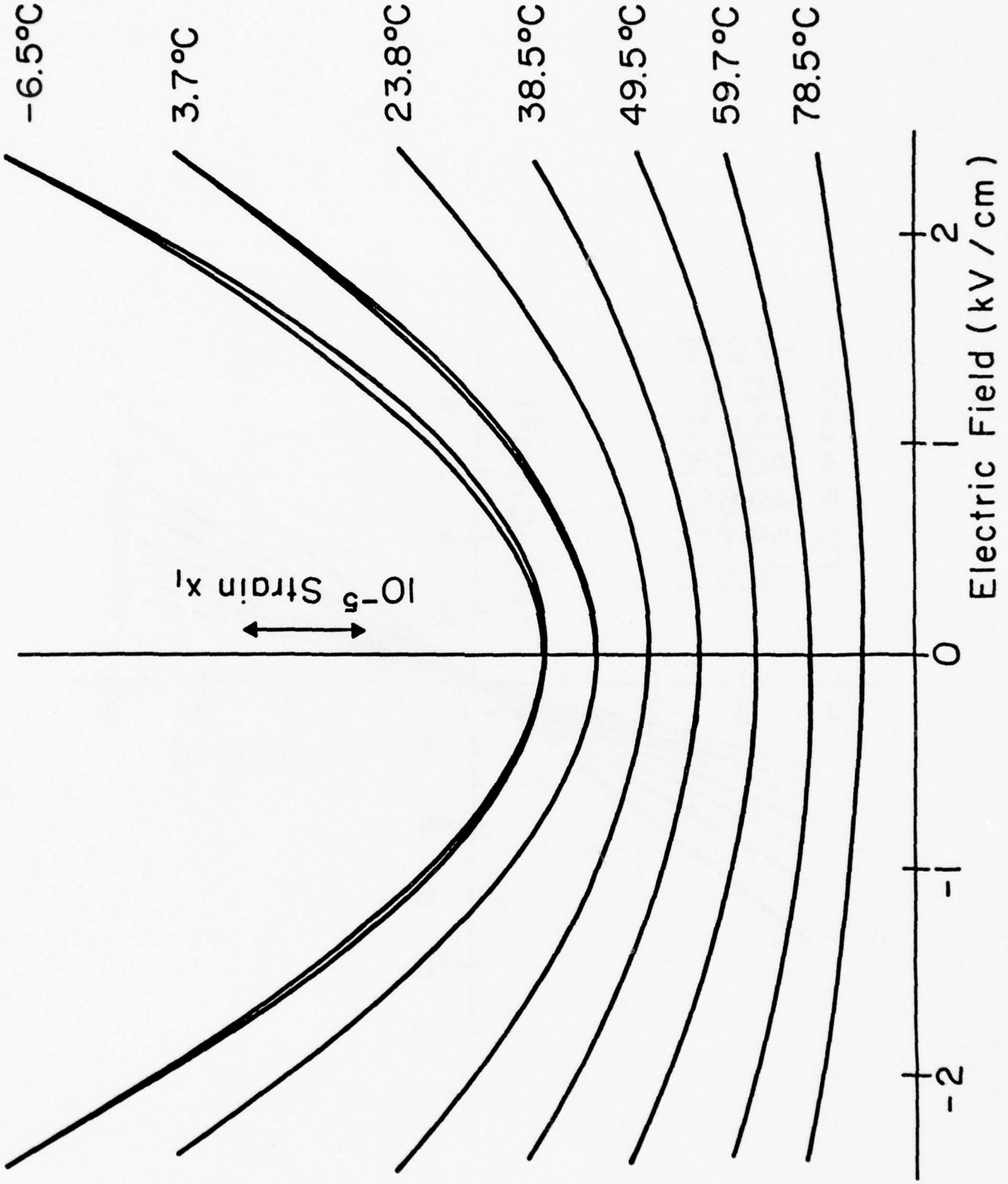
-6.5°C
3.7°C
23.8°C
38.5°C
49.5°C
59.7°C
78.5°C
10^{-5} Strain x_1
Electric Field (kV/cm)
2
1
0
-1
-2

Figure 1

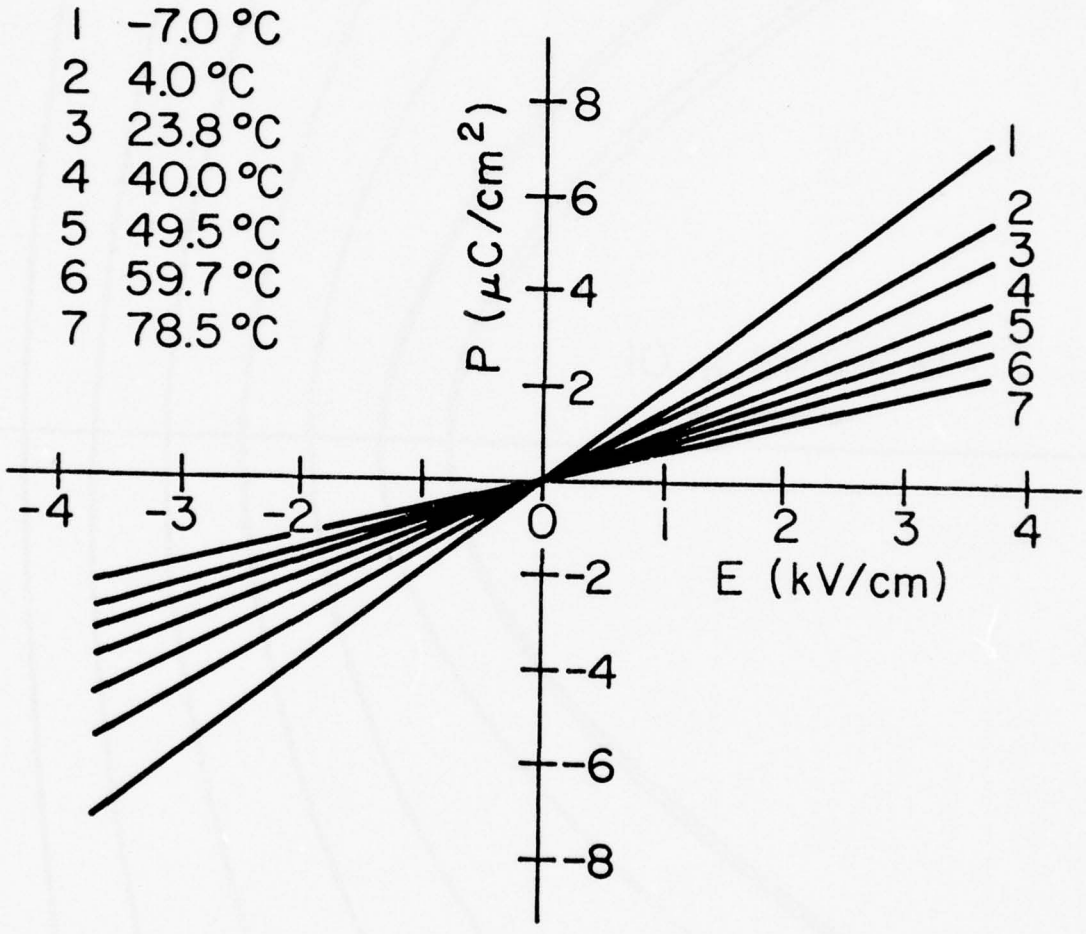
1 -7.0 °C
2 4.0 °C
3 23.8 °C
4 40.0 °C
5 49.5 °C
6 59.7 °C
7 78.5 °C
P (μC/cm²)
8
6
4
2
-2
-4
-6
-8
-4
-3
-2
0
1
2
3
4
E (kV/cm)
1
2
3
4
5
6
7

Figure 2

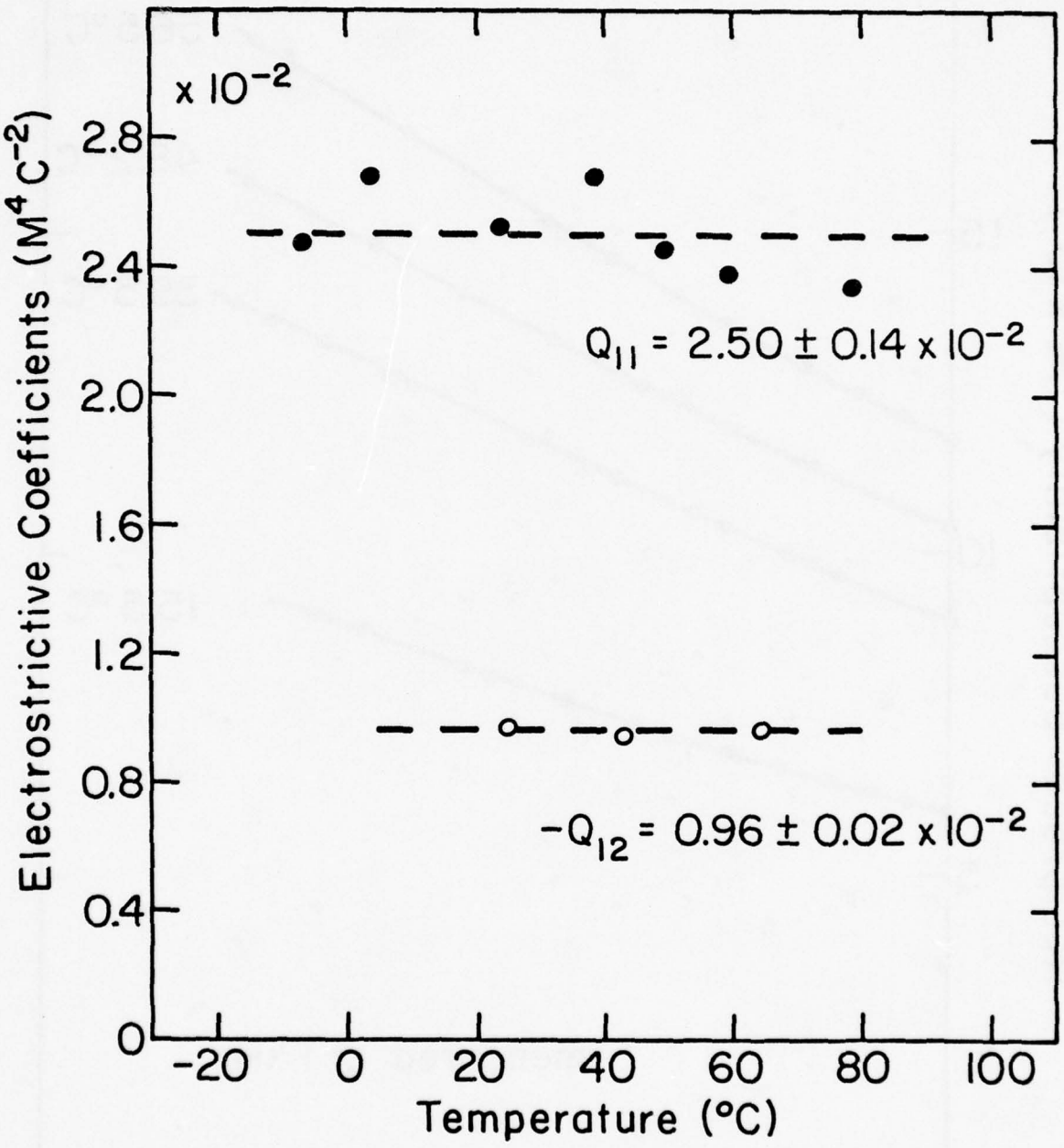
x 10⁻²
Electrostrictive Coefficients (M⁴C⁻²)
2.8
2.4
2.0
1.6
1.2
0.8
0.4
0
Q11 = 2.50 ± 0.14 x 10⁻²
-Q12 = 0.96 ± 0.02 x 10⁻²
-20
0
20
40
60
80
100
Temperature (°C)

Figure 3

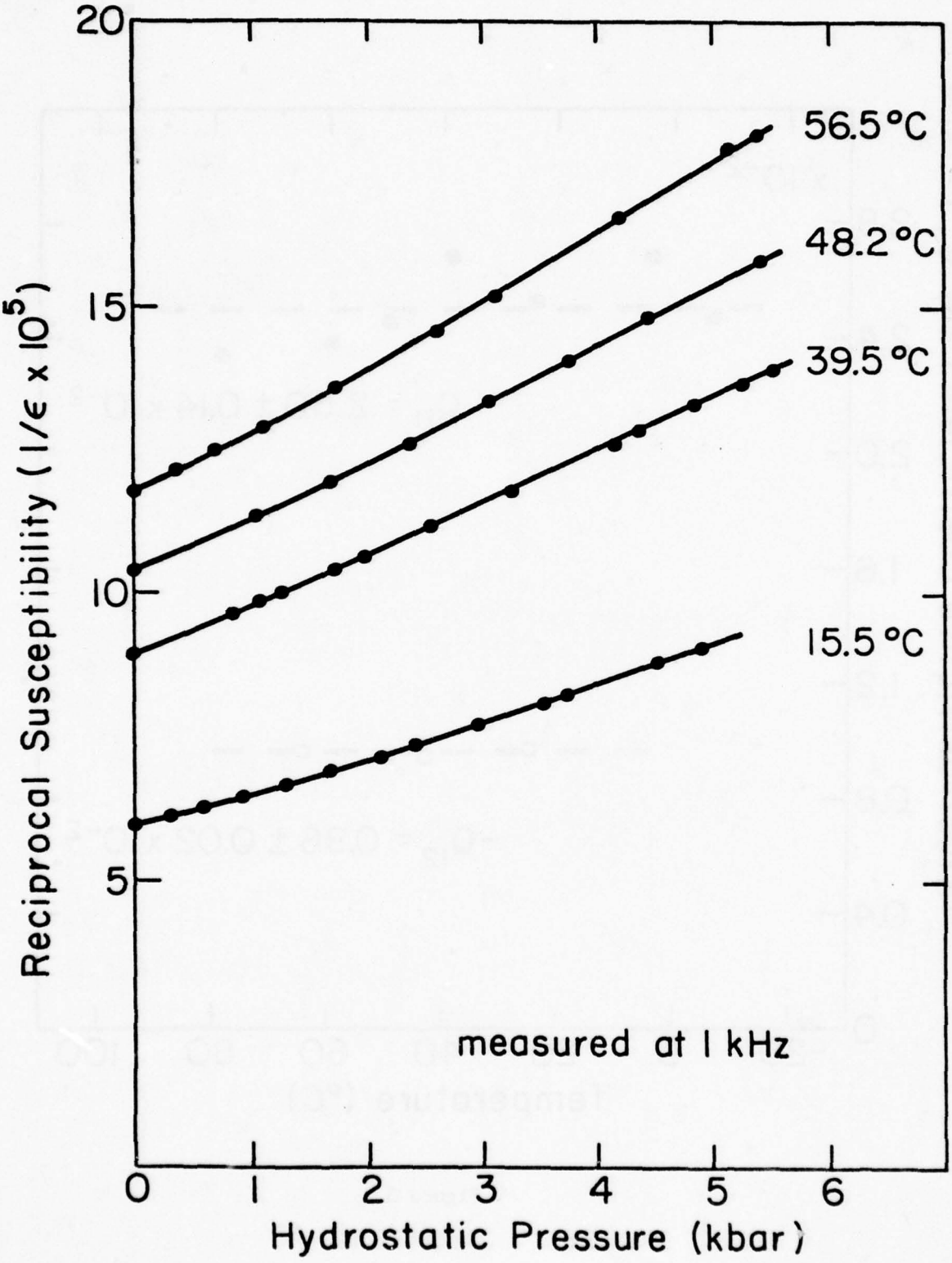
20
15
10
5
Reciprocal Susceptibility (1/ε x 10^5)
56.5 °C
48.2 °C
39.5 °C
15.5 °C
measured at 1 kHz
0
1
2
3
4
5
6
Hydrostatic Pressure (kbar)

Figure 4

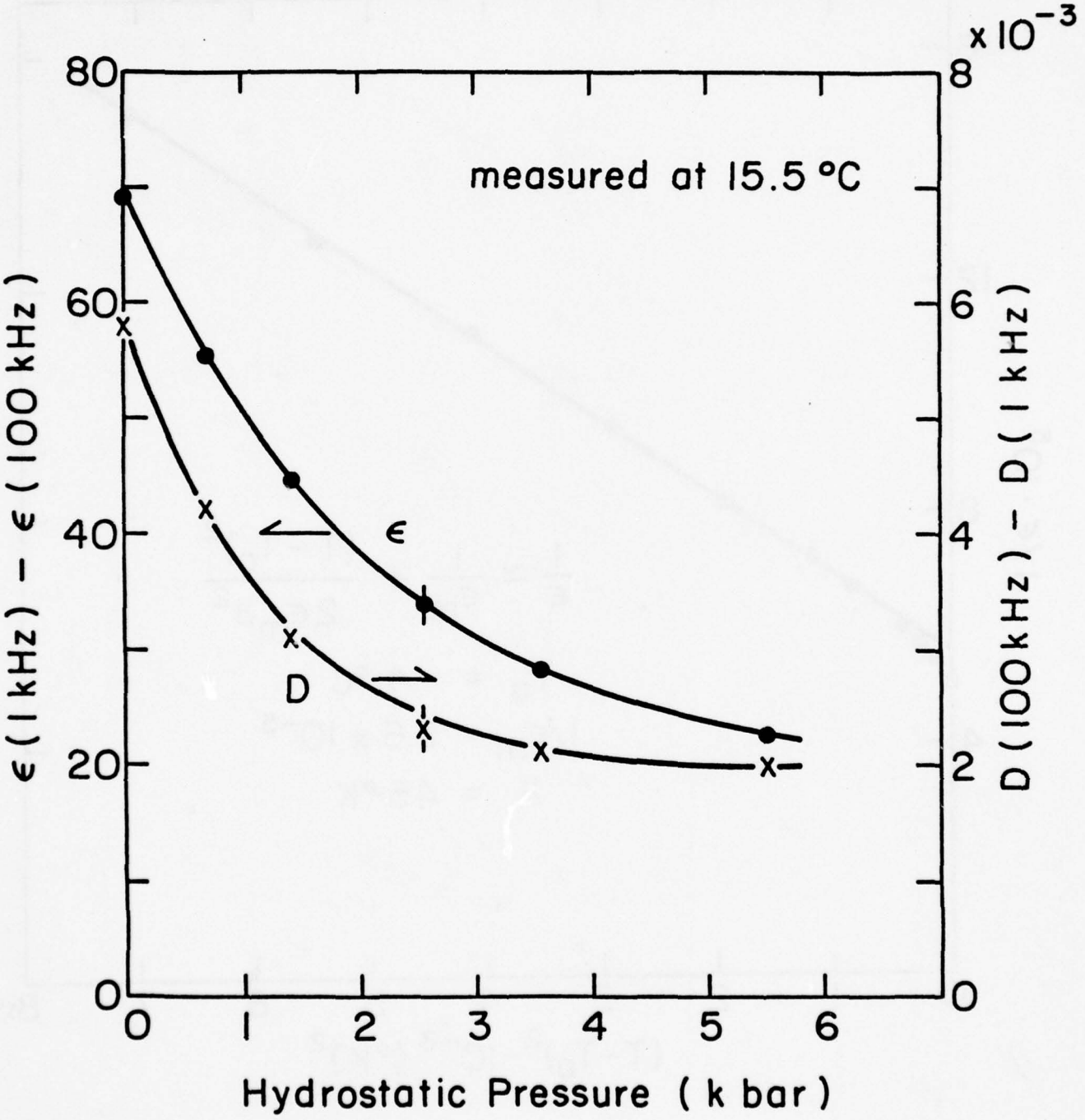
measured at 15.5 °C
ε
D
ε(1 kHz) − ε(100 kHz)
D(100 kHz) − D(1 kHz)
x 10⁻³
Hydrostatic Pressure (k bar)
0
20
40
60
80
0
2
4
6
8
0
1
2
3
4
5
6

Figure 5

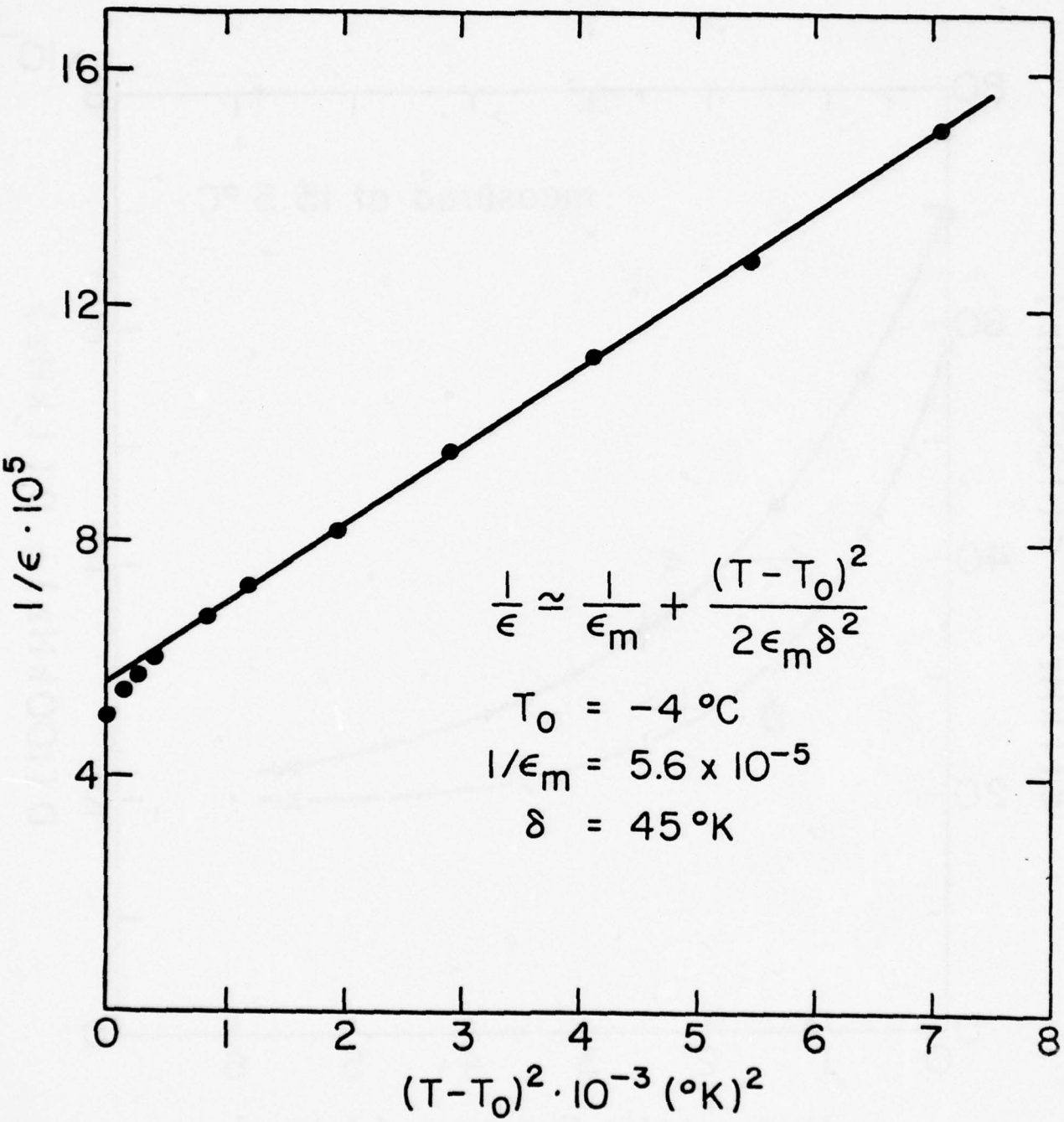
16
12
8
4
$1/\epsilon \cdot 10^5$
$\frac{1}{\epsilon} \simeq \frac{1}{\epsilon_m} + \frac{(T-T_0)^2}{2\epsilon_m \delta^2}$
$T_0 = -4\ ^\circ C$
$1/\epsilon_m = 5.6 \times 10^{-5}$
$\delta = 45\ ^\circ K$
0
1
2
3
4
5
6
7
8
$(T-T_0)^2 \cdot 10^{-3}\ (^\circ K)^2$

Figure 6

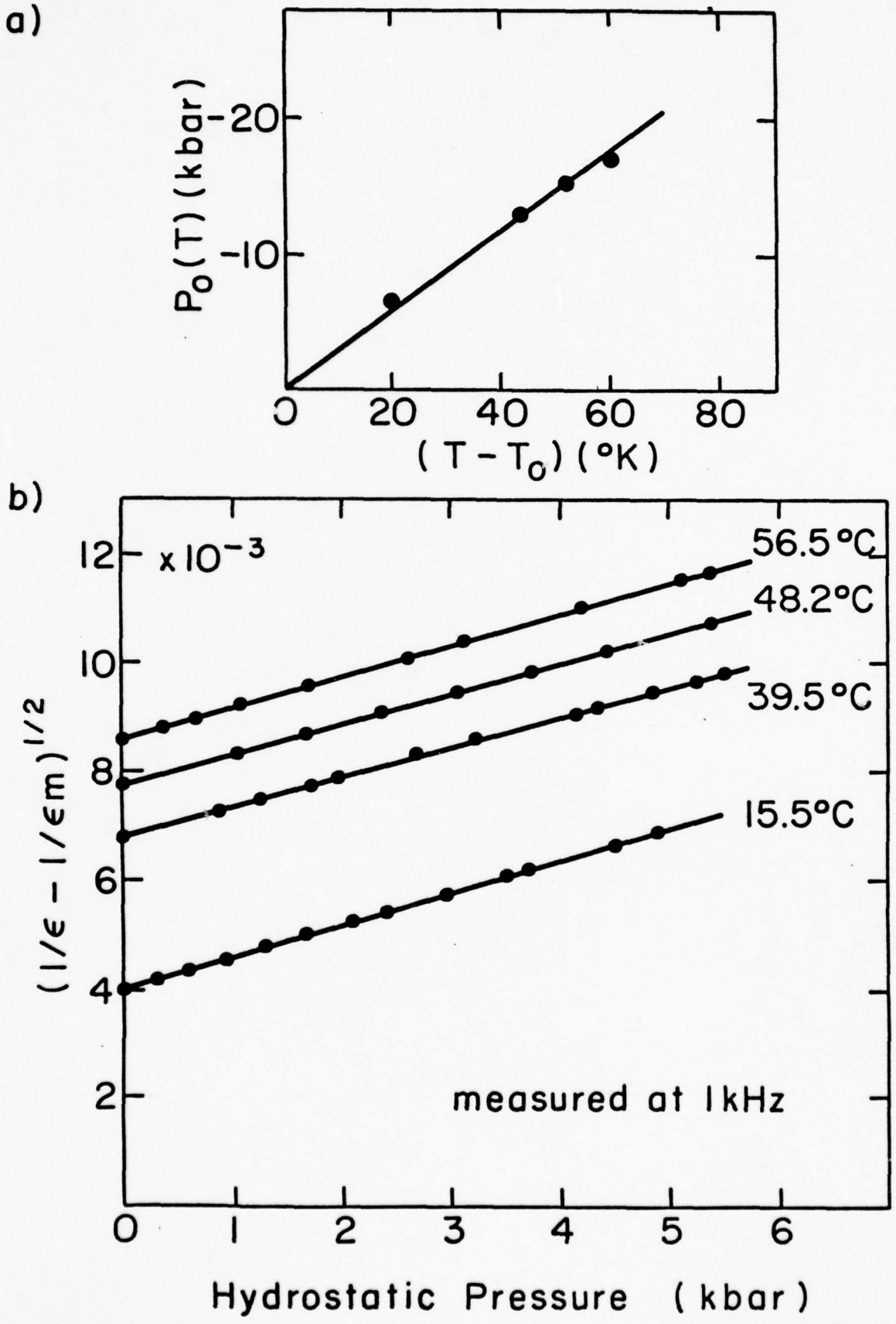
a)
$P_o(T)$ (kbar)
-20
-10
0
20
40
60
80
$(T - T_o)$ (°K)
b)
x 10^{-3}
12
10
8
6
4
2
$(1/\epsilon - 1/\epsilon m)^{1/2}$
56.5°C
48.2°C
39.5°C
15.5°C
measured at 1kHz
0
1
2
3
4
5
6
Hydrostatic Pressure (kbar)

Figure 7

APPENDIX 6

S.J. Jang, K. Uchino, S. Nomura and L.E. Cross. Electrostrictive Behavior of Lead Magnesium Niobate Based Ceramic Dielectrics (in press).

ELECTROSTRICTIVE BEHAVIOR OF LEAD MAGNESIUM NIOBATE BASED CERAMIC DIELECTRICS

S.J. JANG, K. UCHINO, S. NOMURA† and L.E. CROSS
Materials Research Laboratory
The Pennsylvania State University
University Park, Pennsylvania 16802

The electrostrictive strains induced by high electric fields have been measured for compositions in the solid solution system $Pb(Mg_{1/3}Nb_{2/3})O_3$:$PbTiO_3$ (PMN:PT) containing up to 20 mole% PT. Large anhysteretic quadratic strains (up to 1,000 x 10^{-6}) can be induced at room temperature with no evidence of remanence. In pure $Pb(Mg_{1/3}Nb_{2/3})O_3$ the electrostriction constants $\bar{Q}_{11}$ and $\bar{Q}_{12}$ are significantly smaller than in normal perovskites and the large induced strains may be traced to the high polarizability of the relaxor. With the addition of PT, the Q constants increase and the relaxation range shortens, with compositions close to 10 mole% PT providing maximum quadratic sensitivity. Over the relaxation range of temperatures, the thermal expansion is extremely small and comparable to the best thermally stable glasses and ceramics.

INTRODUCTION

Ceramic samples for these studies were prepared from reagent grade oxides, PbO, MgO, Nb_2O_5, and TiO_2. Careful control of the initial calcining reaction is required to avoid the formation of a low permittivity phase with pyrochlore structure. A detailed description of the preparation and densification has been given elsewhere.[1] X-ray powder diffraction, scanning electron microscopy, microprobe analysis, optical and etch studies of polished sections were used to confirm phase purity and solid solution formation.

Weak field dielectric measurements, as a function of frequency and temperature (Fig. 1), confirm relaxor behavior across the whole range of solid solutions up to 20 mole% PT, with the dispersion range narrowing with increasing PT content. Low frequency Sawyer and Tower measurements (10 Hz to 0.001 Hz) show S-shaped saturation curves for samples up to 10 mole% PT with an increasing remanence and more normal hysteresis for higher PT content.

Electrostrictive deformations were measured by two independent methods. At room temperature both longitudinal and transverse strains were measured by recording the direct dilatation (or contraction) of the sample with an LVDT gauge. For variable temperature measurements a bonded strain gauge method was used.[2] In transverse measurement the two techniques agree to better than ±10%. For longitudinal measurement it is difficult to avoid deformation of the field distribution by the bonded gauge, but the strain gauge method still provides reliable relative measurements.

Typical transverse strain measurements taken at room temperature for compositions with increasing PT content are shown in Fig. 2, and the reproducibility of the strain as compared to a conventional PZT8 piezoelectric ceramic in Fig. 3 for the 0.9 PMN:0.1 PT composition. The "walk-off" in the piezoceramic due to de-aging in the high forward field is clearly evident, and the greater reproducibility of the ceramic is evident.

---

†Now at Tokyo Institute of Technology.

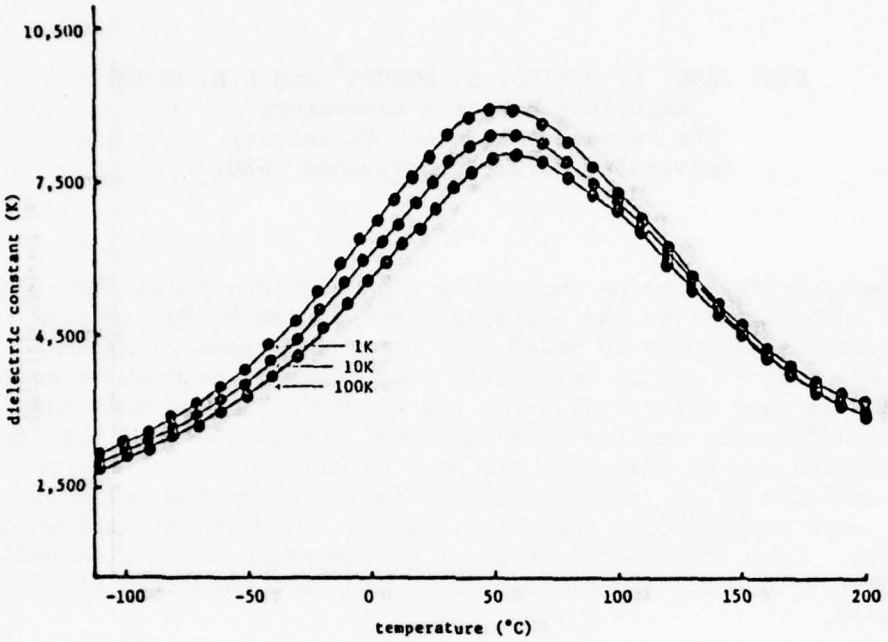

FIGURE 1. Dielectric constant as a function of temperature and *frequency in* 0.87 x PMN:0.13 x PT.

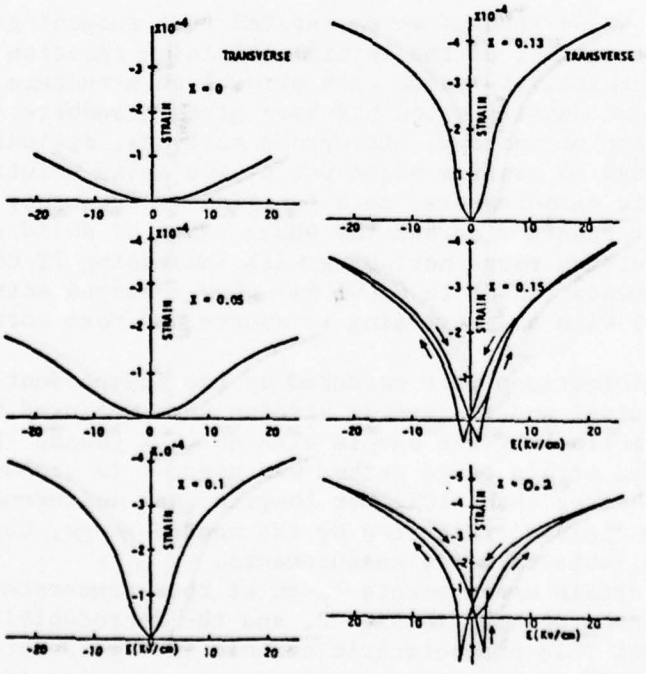

FIGURE 2. Transverse strain as a function of electric field in (1-x) PMN: (X) PT.

ELECTROSTRICTIVE BEHAVIOR OF CERAMIC DIELECTRICS

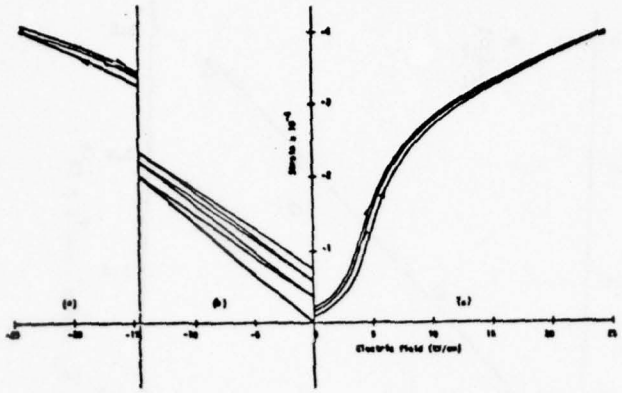

FIGURE 3. Transverse strain in ceramic 0.9 X PMN: 0.1 X PT sample (a) and a typical hard PZT 8 piezoceramic (b).

FIGURE 4. Transverse strain as a function of P^2 in (1-X)PMN: (X) PT system.

That the strain is dominantly electrostrictive in all compositions up to 0.87 PMN: 0.13 PT is evident from plots of the strain versus square of electric polarization (Fig. 4) where the polarization levels have been read from low frequency P versus E loops.

Confirmation that the $\bar{Q}_{12}$ values is low in pure PMN and increases with PT content is shown in Fig. 5.

Thermal expansion was measured using a conventional dilatometer over the temperature range from -200 to +600°C. It is evident that over the relaxation range of temperatures the thermal strain is anomalously small (Fig. 6) as compared to normal non-relaxor perovskites.

The combination of high stable electrostrictive deformations, coupled with low thermal expansion appear to make the PMN:PT electrostriction ceramics suitable candidates for a number of specialized transducer applications in micro-positioners and in adaptive optic systems. The lower values of electrostrictive Q constants observed here in PMN, and also evident in $Pb(Zn_{1/3}Nb_{2/3})O_3$[2] and in a number of relaxors of tungsten bronze structure[3] may play an important role in de-stabilizing the macro-domain structure of the normal ferroelectric state.

This work was supported by joint DARPA:ONR funding under Contract No. N00014-76-C-0515, Project No. 3203.

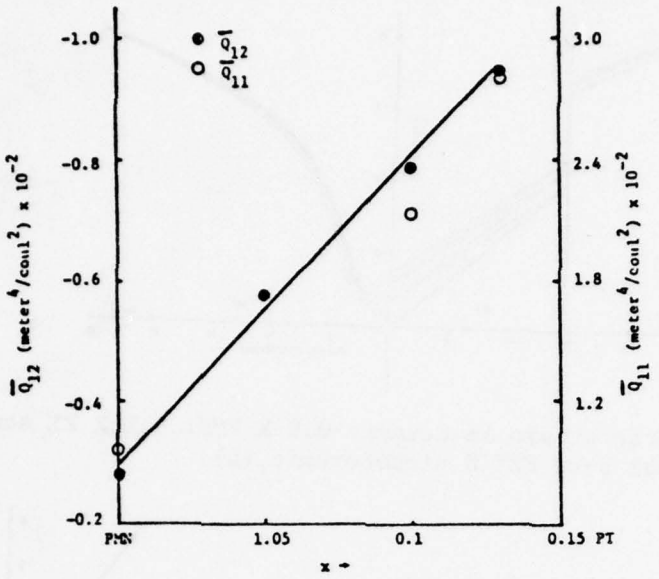

FIGURE 5. Electrostriction constants $\bar{Q}_{12}$ and $\bar{Q}_{11}$ as a function of composition.

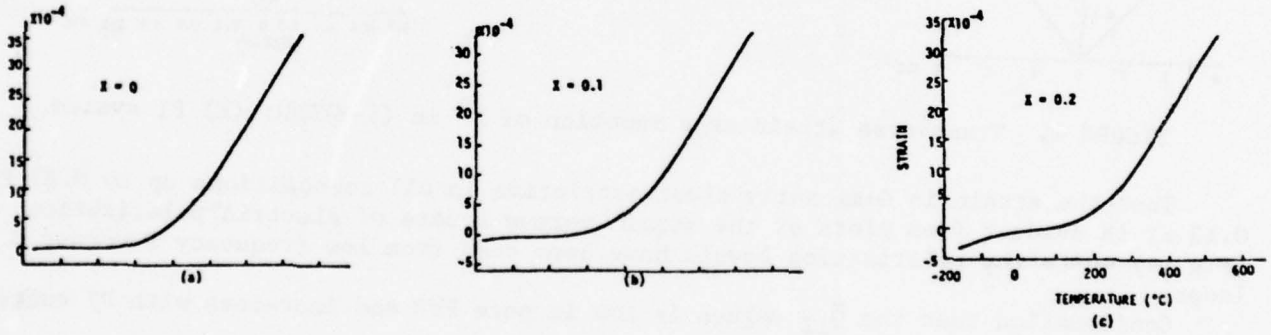

FIGURE 6. Thermal expansion of (1-X) PMN: (X) PT system.

REFERENCES

1. L.E. Cross, R.E. Newnham, J.V. Biggers. "Ceramic Piezoelectric Transducers," Final Report Contract N00014-76-C-0515, June 1979.
2. S. Nomura, J. Kuwata, S.J. Jang, L.E. Cross, R.E. Newnham. Mat. Res. Bull. 14, 769 (1979).
3. S.J. Jang, PhD Thesis, Solid State Science, The Pennsylvania State University (1979).

APPENDIX 7

S. Nomura, J. Kuwata, K. Uchino, S.J. Jang, L.E. Cross and R.E. Newnham. Electrostriction in the Solid Solution System $Pb(Mg_{1/3}Nb_{2/3})O_3$-$Pb(Mg_{1/2}W_{1/2})O_3$. Phys. Stat. Sol. 57 (1980).

ELECTROSTRICTION IN THE SOLID SOLUTION SYSTEM $Pb(Mg_{1/3}Nb_{2/3})O_3$-$Pb(Mg_{1/2}W_{1/2})O_3$*

S. Nomura, J. Kuwata, K. Uchino†, S.J. Jang, L.E. Cross, R.E. Newnham

Abstract

Electrostriction in the solid solution system of $(1-x)Pb(Mg_{1/3}Nb_{2/3})O_3$-$xPb(Mg_{1/2}W_{1/2})O_3$ ($x \leq 0.7$) has been measured by using a strain gauge technique. The electrostrictive Q coefficients were determined from the analysis of the induced strain versus polarization curves in the paraelectric phase. The Q values of $Pb(Mg_{1/3}Nb_{2/3})O_3$ increase rapidly in the region of $x \leq 0.2$ with the increase of $Pb(Mg_{1/2}W_{1/2})O_3$ mole fraction and reach nearly constant values in $x > 0.2$. The situation is compared with the case of $Pb(Mg_{1/3}Nb_{2/3})O_3$-$PbTiO_3$.

Die Elektrostriktion von $(1-x)Pb(Mg_{1/3}Nb_{2/3})O_3$-$xPb(Mg_{1/2}W_{1/2})O_3$ ($x \leq 0.7$) Mischkristallen wurde mit Hilfe von Dehnungsmeßstreifen untersucht. Aus dem Verlauf der Kurven Spannung gegen Polarisation im paraelektrischen Bereich wurden die elektrostriktiven Q Koeffizienten bestimmt. Die Q Werte von $Pb(Mg_{1/3}Nb_{2/3})O_3$ steigen im Bereich $x \leq 0.2$ rasch mit der Zunahme des $Pb(Mg_{1/2}W_{1/2})O_3$ Anteiles an und erreichen nahzu konstante Werte für $x \geq 0.2$. Ein Vergleich zwischen diesen Ergebnissen und den Resultaten einer Untersuchung von $Pb(Mg_{1/3}Nb_{2/3})O_3$-$PbTiO_3$ wird diskutiert.

---

*This work was supported by the Department of the Navy through the Office of Naval Research.

†Permanent address: Department of Physical Electronics, Tokyo Institute of Technology, Ookayama, Meguro-ku, Tokyo.

1. Introduction

Over the past year the major effort on materials for potential application in electrostriction transducer systems has focused on a study of the ferroelectric relaxor dielectrics. It has been proposed (1-3) that in these systems there is a microscopic composition fluctuation that causes a broad spatial distribution of ferroelectric Curie temperatures. A rather flat temperature dependence, therefore, can be expected in the electrostriction over a wide temperature range. $Pb(Mg_{1/3}Nb_{2/3})O_3$ (hereafter abbreviated PMN) may be a typical example in the perovskite family of ferroelectrics.

We have previously reported the electrostrictive data measured on ceramic samples for PMN (4) and some of its solid solutions: $Pb(Mg_{1/3}Nb_{2/3})O_3$-$PbTiO_3$ (5,6), $Pb(Mg_{1/3}Nb_{2/3})O_3$-$PbTiO_3$-$Ba(Zn_{1/3}Nb_{2/3})O_3$ (7).

Apart from the previous materials that are aimed at direct application, we have another interest in the role of a cation-ordered arrangement on the electrostrictive effect, since it is suggested that the electrostrictive Q constants in the disordered type complex perovskites are almost an order of magnitude smaller than in most "normal" ferroelectric perovskites (6). $Pb(Mg_{1/2}W_{1/2})O_3$ (abbreviated PMW) is a well-known example which has the NaCl-type cation-ordered arrangement in the B-sites of the ABO_3 perovskite structure (8). The crystal structures and the dielectric properties of the solid solution system PMN-PMW have been reported in our recent papers (9,10). The superstructure of a doubling of the perovskite subcell was observed for compositions containing more than 20 mole% PMW.

In this paper the electrostriction in the solid solutions is measured to examine how the values of electrostrictive coefficients depend upon the composition.

2. Experimental

The ceramic compounds were prepared from reagent grade PbO, MgO, Nb_2O_5, and WO_3. The constituent oxides were mixed in appropriate proportions, ball milled in alcohol, then dried and calcined in air in a closed alumina crucible. Calcining temperatures ranged from 800 to 1000°C depending on composition for a calcine time of 15 hours. The resulting calcine was ground and refired for two additional 15-hour periods to ensure complete reaction. Samples were prepared by cold pressing into disks 2.54 cm diameter and firing on zirconia setters in air. A 2-hour sintering was used and the temperature ranged from 1000 to 1280°C depending on composition.

The electrostriction was measured by a strain gauge method. Silver electrodes were evaporated onto the faces of a ceramic plate, and a polymid foil strain gauge (Kyowa, KFH-02-350) was bonded with a cement (Kyowa, PC-6) on the face of the sample. The measurement was done by the AC method (180 Hz) using a phase sensitive detector and a double bridge system to buck out the residual AC signal. The induced strain was measured under low frequency cyclic electric fields at various temperatures.

In a ceramic sample with cubic symmetry, there are two independent electrostrictive coefficients, $\bar{Q}_{11}$ and $\bar{Q}_{12}$. These coefficients are defined by the following equations:

$$x_1 = \bar{Q}_{11} P^2,$$
$$x_2 = \bar{Q}_{12} P^2.$$

Here x_1 and x_2 are the induced strains parallel and perpendicular to the direction of the electric polarization P respectively. The electric polarization P was measured against the electric field E by using a Sawyer-Tower circuit at 50 Hz.

3. Results

The average Curie temperature of the PMN-PMW system varies with the composition as shown in Fig. 1. The electrostrictive strains were measured on several samples containing less than 80 mole% PMW around each Curie temperature. The electrostriction could not be detected for the compositions containing more than 80 mole% PMW because of the small magnitude due to antiferroelectricity in that region.

The induced strain x_2 versus electric field E curves for 0.8PMN-0.2 PMW are given in Fig. 2. The measurements were done under a quasistatic condition of increasing and decreasing electric field. The curves are not accompanied by a hysteresis above the mean Curie temperature ($\sim -45°C$), but are accompanied by a slim loop behavior below that temperature. The samples containing more than 40 mole% PMW showed no appreciable hysteresis in the x_2-E curve even below the mean Curie temperature. In other words the activity of ferroelectric domains may be strongly suppressed by adding antiferroelectric PMW.

The magnitudes of x_1 and x_2 at room temperature vary with the composition as shown in Fig. 3. The marked decrease of the induced strain with the increase of PMW composition may be understandable basically in terms of the magnitude of dielectric constant which is given in Fig. 4. In general the magnitude of induced strain is supposed to be proportional to the square of the dielectric constant when a relatively low electric field is applied.

To obtain the electrostrictive Q coefficients, we analyzed the data of induced strain as a function of electric polarization P. The values of x_1 and x_2 in the paraelectric phase were plotted against the induced polarization corresponding to the same field as used for the strain on a log-log scale. (A similar plot was shown for the $Pb(Zn_{1/3}Nb_{2/3})$ single crystal in reference (11)). The straight line representing the quadratic relation ($x=QP^2$) could be obtained.

The Q values are almost independent of temperature in the paraelectric phase as in the cases of PMN-PT (6) and PZN (11).

The values of $\bar{Q}_{11}$ and $\bar{Q}_{12}$ coefficients are plotted against the composition in Fig. 5. Due to the accuracy limit of the measuring apparatus, reliable values of the Q coefficients, in particular $\bar{Q}_{11}$, could not be obtained for the solid solutions containing a large amount of $Pb(Mg_{1/2}W_{1/2})O_3$ because of the decreasing dielectric constant. The remarkable increase of the Q coefficients, however, is evident with the increase of PMW content in the region containing less than 20 mole% PMW, the identical region where the ionic ordered arrangement of B-sites grows rapidly in the short range.

4. Discussion

Electrostrictive Q coefficients have been measured on various kinds of perovskite type oxides. According to Yamada (12), the electrostrictive Q coefficients, which are obtained by assuming that the piezoelectric effect in the ferroelectric phase is due to the electrostrictive effect in the paraelectric phase biased by the spontaneous polarization, are nearly constant with the value $Q_{11} = 0.10\ m^4/C^2$, $Q_{12} = -0.034\ m^4/C^2$. It is known that generally the Q values obtained from the direct measurements of electrostriction in the paraelectric phase are nearly in agreement with the corresponding values described above. Ceramic $BaTiO_3$, $SrTiO_3$, $Pb(Zr,Ti)O_3$, and $ITaO_3$ all have $\bar{Q}_{12}$ values of about $-1 \times 10^{-2}\ m^4/c^2$.

In the previous paper concerning the PMN-PT system (6), we speculated that the polarization related electrostriction constants Q in such relaxor crystals as $Pb(Mg_{1/3}Nb_{2/3})O_3$ and $Pb(Zn_{1/3}Nb_{2/3})O_3$ (11) are almost an order of magnitude smaller than in most normal ferroelectric perovskites. The factor that may be responsible is a large internal stress that is induced by the disordered arrangement of the B ions. The internal stress may have a depressing effect on the electrostrictive strain in the paraelectric phase.

The present work supports the model mentioned above. In the case of the PMN-PT system, the large internal stress of PMN will be reduced with increasing $PbTiO_3$ content. For the PMN-PMW system the same order or larger reducing effect may be expected with increasing $Pb(Mg_{1/2}W_{1/2})O_3$ content, because the ordering tendency of Mg and W ions is considered to promote a stress relief effect. In Fig. 5 the Q coefficient values increase rapidly with the increase of PMW mole fraction in the region containing less than 20 mole% PMW. It is notable that this mole fraction corresponds to the one above which the superstructure of a doubling of the perovskite subcell is detected. In the region with the superstructure, the Q values of the solid solutions are nearly constant regardless of the composition and almost of the same value as for most normal ferroelectric perovskites. Further experimental study on electrostriction of $Pb(Mg_{1/3}Nb_{2/3})O_3$ single crystals is now proceeding.

Acknowledgment

The authors would like to thank K. Tonooka and Y. Watanabe for help with the experiments.

[1] G.A. SMOLENSKII and A.I. AGRANOVSKAYA, Soviet Phys.-Solid State 1, 1429 (1959).

[2] V.A. BOKOV and I.E. MYLNIKOVA, Soviet Phys.-Solid State 3, 613 (1961).

[3] L.E. CROSS and J.W. SMITH, Ferroelectrics 1, 137 (1970).

[4] S. NOMURA, K. TONOOKA, J. KUWATA, L.E. CROSS and R.E. NEWNHAM, Proc. 2nd Meeting on Ferroelectric Mat. and Appl. (in press).

[5] L.E. CROSS, S.J. JANG, R.E. NEWNHAM, S. NOMURA and K. UCHINO, Ferroelectrics (in press).

[6] S.J. JANG, L.E. CROSS, S. NOMURA and K. UCHINO, Phys. Stat. Sol. (submitted).

[7] S. J. JANG, Ph.D. Thesis, Solid State Science, The Pennsylvania State University (1979).

[8] A.I. ZASLAVSKII and M.F. BRYZHINA, Kristallografiya 1, 709 (1962).

[9] A. AMIN, R.E. NEWNHAM, L.E. CROSS, S. NOMURA and D.E. COX, Acta Cryst. (submitted).

[10] S. NOMURA, S.J. JANG, L.E. CROSS and R.E. NEWNHAM, J. Amer. Ceramic Soc. (in press).

[11] S. NOMURA, J. KUWATA, S.J. JANG, L.E. CROSS and R.E. NEWNHAM, Mat. Res. Bull. 14, 769 (1979).

[12] T. YAMADA, J. Appl. Phys. 43, 328 (1972).

Figure Captions

Fig. 1 Average Curie temperature in the $Pb(Mg_{1/3}Nb_{2/3})O_3$-$Pb(Mg_{1/2}W_{1/2})O_3$ system determined from the measurement of dielectric constant at various frequencies.

Fig. 2 Induced strain x_2 versus electric field E in $0.8Pb(Mg_{1/3}Nb_{2/3})O_3$-$0.2Pb(Mg_{1/2}W_{1/2})O_3$ ceramic at various temperatures.

Fig. 3 Induced strain x_1 for $E = 10^5$ V/m and x_2 for $E = 10^6$ V/m at room temperature as a function of composition.

Fig. 4 Dielectric constant at room temperature as a function of composition.

Fig. 5 Electrostrictive coefficients $\bar{Q}_{11}$ and $\bar{Q}_{12}$ as a function of composition.

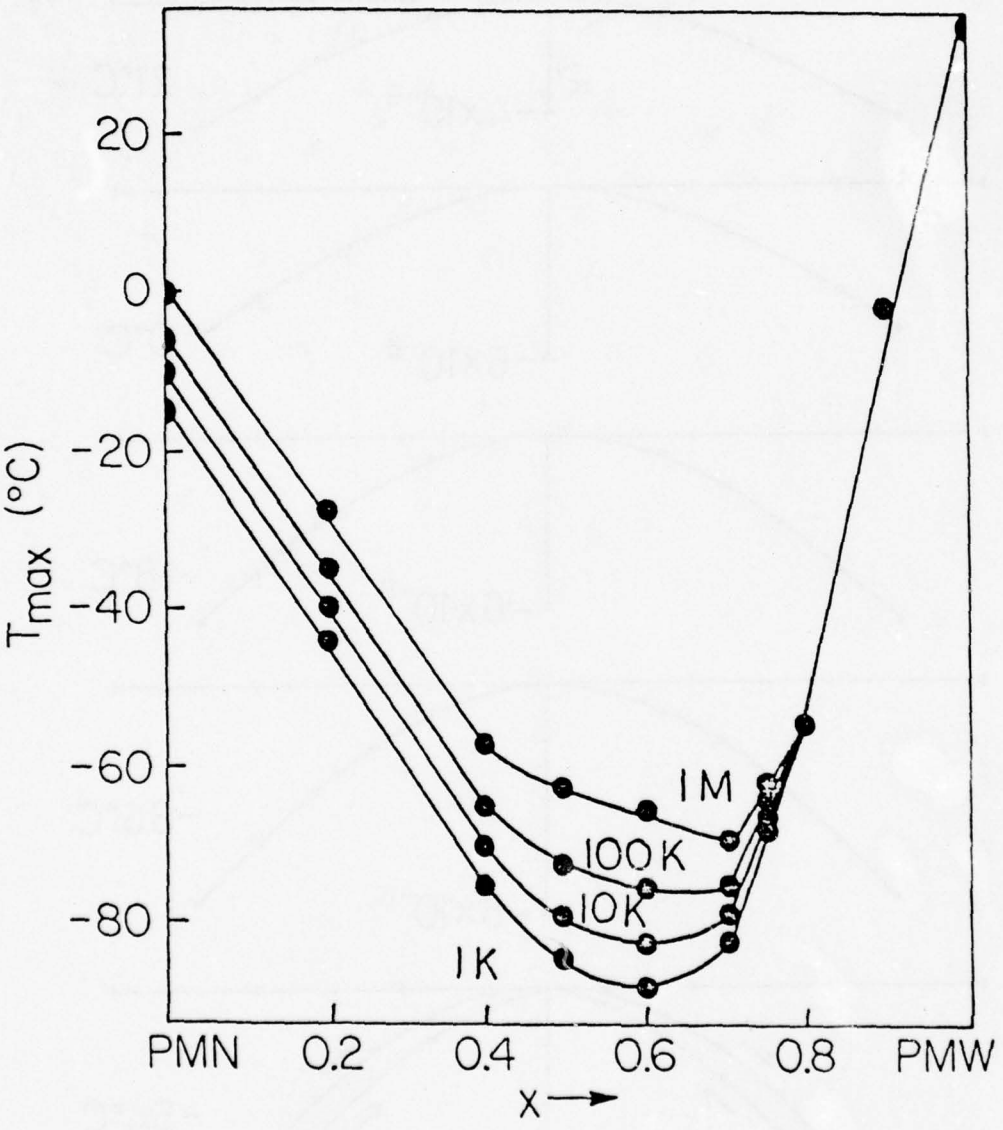

Figure 1

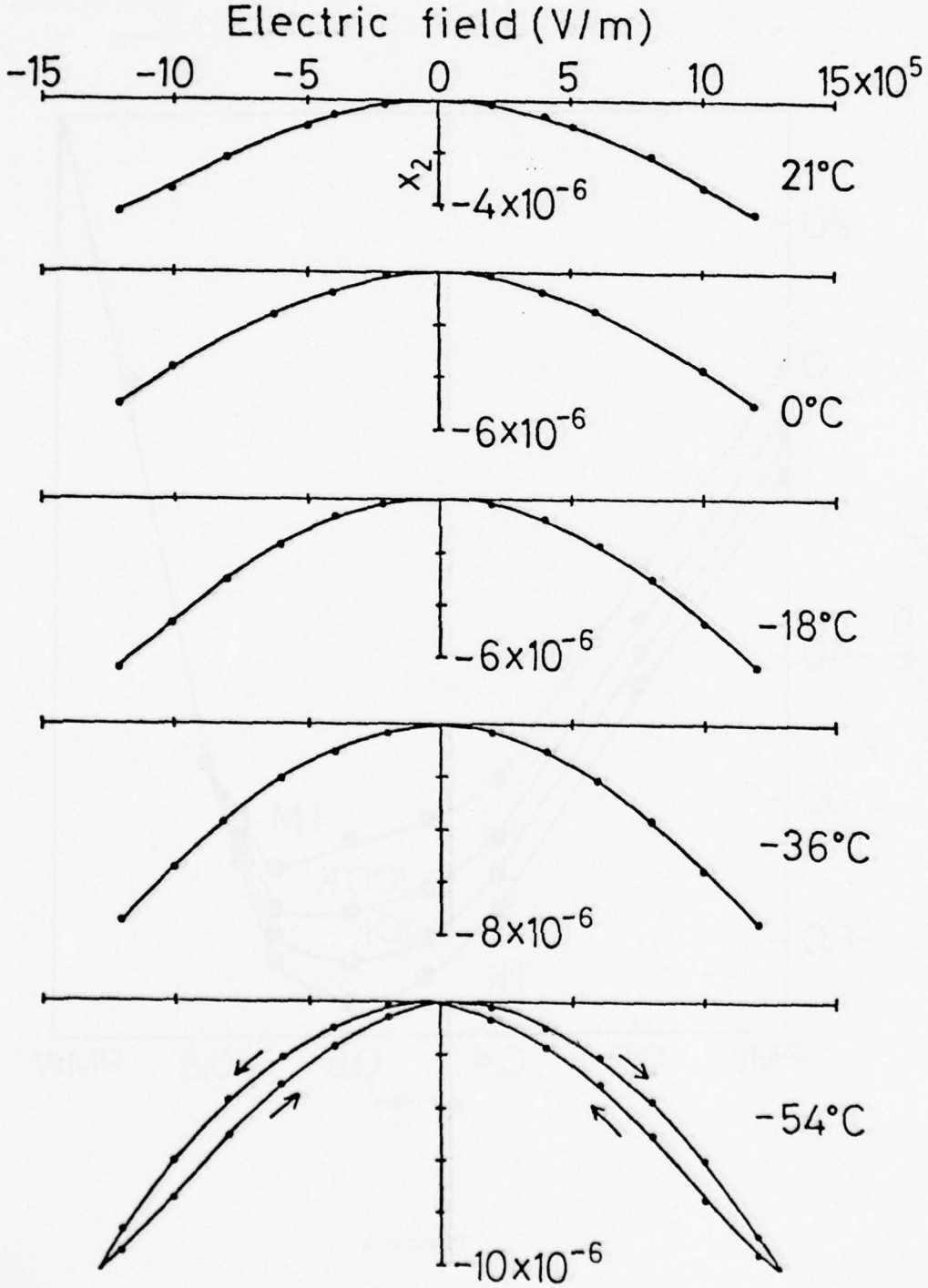
Electric field (V/m)
-15
-10
-5
0
5
10
15x10^5
x2
-4x10^-6
21°C
-6x10^-6
0°C
-6x10^-6
-18°C
-8x10^-6
-36°C
-10x10^-6
-54°C

Figure 2

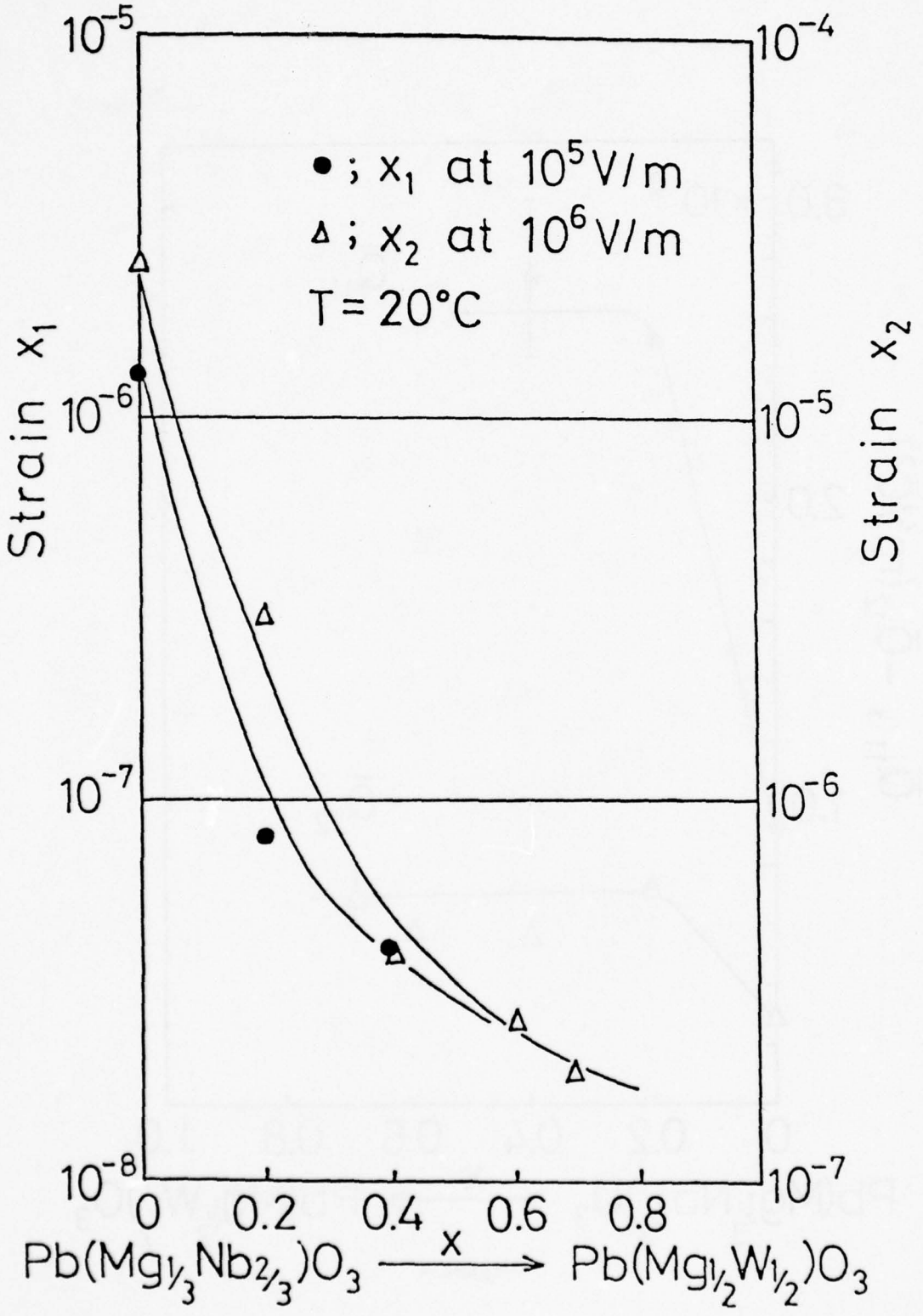
10^-5
10^-4
• ; x1 at 10^5 V/m
Δ ; x2 at 10^6 V/m
T = 20°C
Strain x1
Strain x2
10^-6
10^-5
10^-7
10^-6
10^-8
10^-7
0
0.2
0.4
0.6
0.8
x
Pb(Mg1/3Nb2/3)O3
Pb(Mg1/2W1/2)O3

Figure 3

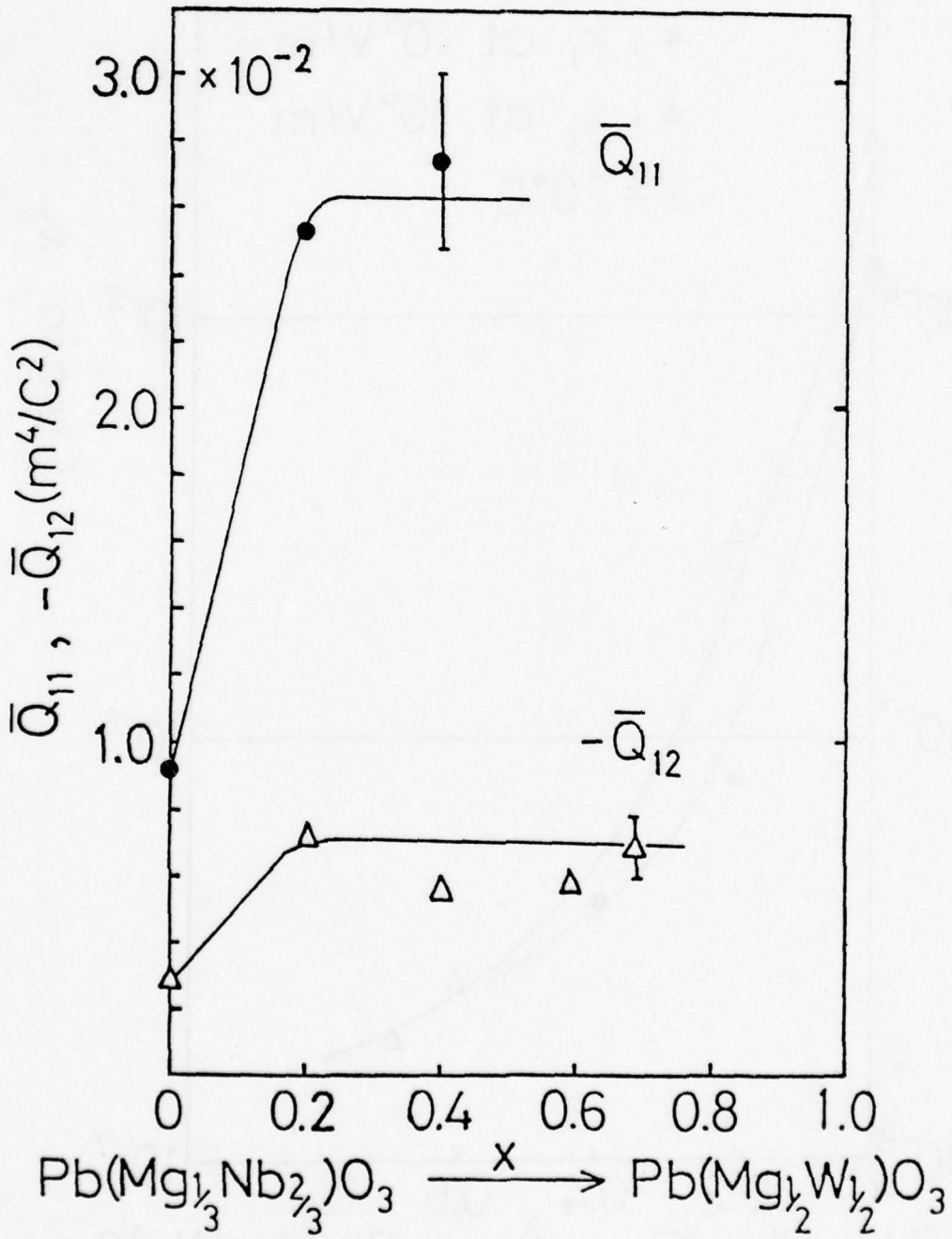
3.0
× 10⁻²
2.0
1.0
$\bar{Q}_{11}$
$-\bar{Q}_{12}$
$\bar{Q}_{11}$, $-\bar{Q}_{12}$ (m⁴/C²)
0
0.2
0.4
0.6
0.8
1.0
x
Pb(Mg1/3Nb2/3)O3
Pb(Mg1/2W1/2)O3

Figure 4

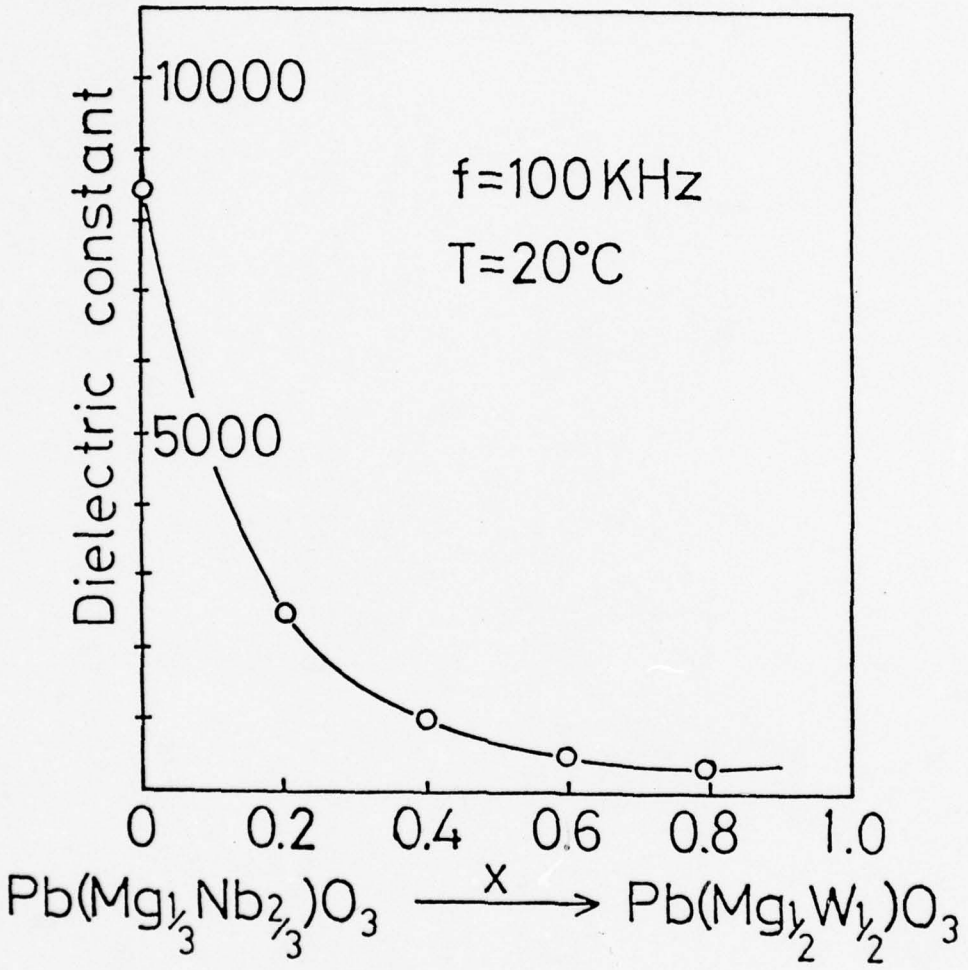
Dielectric constant
10000
5000
f=100 KHz
T=20°C
0
0.2
0.4
0.6
0.8
1.0
Pb(Mg1/3Nb2/3)O3
X
Pb(Mg1/2W1/2)O3

Figure 5

APPENDIX 8

S. Nomura, K. Tonooka, J. Kuwata, R.E. Newnham and L.E. Cross. Electrostriction in $Pb(Mg_{1/3}Nb_{2/3})O_3$ Ceramics.

A - 6

Electrostriction in $Pb(Mg_{1/3}Nb_{2/3})O_3$ Ceramics

Shoichiro NOMURA, Kazuhiko TONOOKA and Jun KUWATA

Department of Physical Electronics, Faculty of Engineering, Tokyo Institute of Technology, Meguro-ku, Tokyo 152

L.E.CROSS and R.E.NEWNHAM

Materials Research Laboratory, The Pennsylvania State University, University Park, Pennsylvania 16802

Electrostriction in $Pb(Mg_{1/3}Nb_{2/3})O_3$ ceramics is studied by two methods using strain gauge and a piezoelectric resonance. The electrostriction Q coefficients are determined from the analysis of the induced strain vs. polarization curves in the paraelectric phase, as $Q_{11}=(2.8\pm0.2)\cdot10^{-2}\ m^4/C^2$ and $Q_{12}=-(0.6\pm0.1)\cdot10^{-2}\ m^4/C^2$. In the determination of k_p in the paraelectric phase, the piezoelectric admittance is numerically analysed in the vicinity of the resonance frequency, using a hyperbolic approximation. The k_p factor increases in proportion to the applied d.c. field, from which the value of Q_{12} is calculated as $-(0.71\pm0.05)\cdot10^{-2}\ m^4/C^2$.

1. Introduction

$Pb(Mg_{1/3}Nb_{2/3})O_3$ belongs to the ferroelectric crystals with a diffuse phase transition.[1] The phase transition covers a wide range of temperature with an average Curie temperature of 0°C[1]. In the paraelectric phase, the crystal belongs to the cubic point group O_h, in which Mg^{2+} and Nb^{5+} ions are randomly distributed, occupying the centers of an octahedron formed by oxygen ions. The transition occurs gradually because different regions of the crystal have unequal Curie temperature due to fluctuation in composition. To elucidate the mechanism of the diffuse phase transition and also to explore its possibility for device application, various kinds of studies, in particular dielectric and optical ones have been intensively studied[2]. Few studies, however, have been reported so far regarding electrostrictive properties.[3]

Electrostriction is a phenomenon which give rise to a strain proportional to the square of the applied electric field. Strains in crystal due to electrostrictive effect, in general, are small. In ferroelectric crystal strain caused by the application of an electric field, is due to the combined effects of piezoelectricity and electrostriction. Pure electrostriction can be observed only in non-piezoelectric compounds or in a paraelectric state of ferroelectrics.

It is interesting to investigate the electrostrictive properties of $Pb(Mg_{1/3}Nb_{2/3})O_3$ in a temperature region of diffuse phase transition, where the two phases of ferroelectric and paraelectric coexist. We have determined the Q coefficients of $Pb(Mg_{1/3}Nb_{2/3})O_3$ ceramics from two different measurements : a direct measurement of electrostriction using a strain gauge, and an indirect measurement of induced piezoelectric resonance of the ceramic disk under applying d.c. field. To compare with the data of $Pb(Mg_{1/3}Nb_{2/3})O_3$, electrostrictive coefficient Q_{12} of $(Ba_{0.6}Sr_{0.4})TiO_3$ ceramics was

measured in the paraelectric phase by the piezoelectric resonance method.

2. Sample preparation

The ceramic compounds were prepared from reagent grade PbO, MgO, and Nb_2O_5. The constituent oxides were mixed in appropriate proportion ball-milled in alcohol, then dried and calcined in air for 15 hr in a closed alumina crucible. The calcining temperature was about 1000°C. The resulting calcine was ground and refired at 1100°C to ensure complete reaction. Ceramic sample was prepared by pressing into a disk 1.6 cm diameter and firing on a platium sheet in alumina crucible at about 1230°C for 4 hr. The similar method of preparation was applied to the ceramic sample of $(Ba_{0.6}Sr_{0.4})TiO_3$. The firing temperature was 1500°C.

3. Measurement of electrostriction by a strain gauge method

For a ceramic sample with cubic symmetry, the independent electrostriction coefficients are Q_{11} and Q_{12}, which are defined by following equations,

$$x_1 = Q_{11}P^2 \quad (1)$$

$$x_2 = Q_{12}P^2 \quad (2)$$

where x_1 and x_2 are the induced strain parallel and perpendicular to the direction of the induced electric polarization P respectively.[4)]

The measurement of induced strain was carried out by a strain gauge. Silver electrodes were evaporated onto the faces of ceramic plate, and then a polymid foil strain gauge (Kyowa, KFH-02-350) was bonded with a cement (Kyowa, PC-6) on the face of the sample. The dimension of the ceramic plate is 28 mm^2 area, 3 mm thickness for the measurement of x_1, and 15 mm^2 area, 0.22 mm thickness for x_2. The measurement was done by the a.c. method (180 Hz), using a phase sensitive detector and a double bridge to buck out the residual a.c. signal. The dummy gauge was bonded on a copper cube which was contained in a copper block together with the sample to obtain a good uniformity of the temperature between them. The induced strain was quasistatically measured, step by step with increasing and decreasing the applied field at various temperatures. The electric polarization P was measured at 0.1 Hz, by using a modified Sawyer-Tower circuit.

4. Measurement of the induced piezoelectric resonance

The transmission method[5)] was used for determination of the planer coupling factor k_p of disk resonator of $Pb(Mg_{1/3}Nb_{2/3})O_3$ ceramics under appling d.c. field. The dimension of sample is 8.6 mm diameter and 0.38 mm thickness. Since the magnitude of k_p is relatively small (less than 10 %) in the paraelectric phase, the application of the convensional formula for k_p[6)], i.e.

$$k_p^2 = \frac{2.51}{2}\,\frac{f_{min}^2 - f_{max}^2}{f_{min}^2} \quad (3)$$

where f_{min} is the frequency at minimum admittance of the ceramic disk, and f_{max} is the frequency at maximum admittance, leads to noticeable error in the measurement of the induced piezoelectric resonance. Hereafter we denote the coupling factor k_p calculated by equ. (3) as k_p' to distinguish from the correct k_p value.

To obtain the k_p factor, we expanded the admittance of the electrostrictive disk surrounding the resonance point in a hyperbolic formula as a function of the frequency, and determined the parameters involved in the formula so that the calculated admittance curve can be fitted to the observed one on the skirt of the resonance curve. The coupling factor k_p was numerically determined in this fitting process.

The planar coupling factor k_p is related to the piezoelectric strain constant d_{31} as follows,[5]

$$d_{31} = \sqrt{\frac{\varepsilon_{33}^T}{2\rho(1+\sigma^E)}}\,\frac{\eta_1}{2\pi r f_r}\,k_p \qquad (4)$$

where ε_{33}^T is the dielectric constant, which depends upon the applied d.c. field, ρ is the density, r is the radius, f_r is the resonance frequency, σ^E is the Poisson's ratio, and η_1 is the lowest positive root of the equation : $(1-\sigma^E)J_1(\eta) = \eta J_0(\eta)$. The Poisson's ratio σ^E was determined from the ratio of the first overtone to the fundamental frequency. The numerical values of $Pb(Mg_{1/3}Nb_{2/3})O_3$ ceramic sample are ρ=7.3 g/cm^3, f_r=316 kHz, σ^E=0.30, and η_1=2.05 respectively. The dielectric constant $\varepsilon_{33}^T/\varepsilon_o$ is about 8000 at 170 kHz, and the value decreases with increasing the d.c. bias field. In our numerical calculation of d_{31}, we used different values of ε_{33}^T, depending upon the value of bias field.

On the other hand, the induced piezoelectric strain constant d_{31} can be expressed in terms of the electrostriction constant Q_{12} by

$$d_{31} = 2\varepsilon_{33}^T Q_{12} P \qquad (5)$$

in the paraelectric phase.[4] From the measurement of the field dependence of k_p, and using equs. (4) and (5), the magnitude of Q_{12} can be determined.

5. Results

The relationship between the induced strain x_2 and the electric field for the $Pb(Mg_{1/3}Nb_{2/3})O_3$ ceramic sample are shown in Fig.1. Below the average Curie temperature of 0°C, the curves are accompanied by a hysteresis, which is caused by the ferroelectric domains. Near the Curie temperature the hysteresis is very skinny, which is different from that of ferroelectrics with simple perovskite structure. At -115°C, far below the Curie temperature a typical butterfly-shaped hysteresis is obtained. The curves of induced strain x_1 vs. electric field E were measured only in the paraelectric phase, which are shown in Fig.2. The sign of

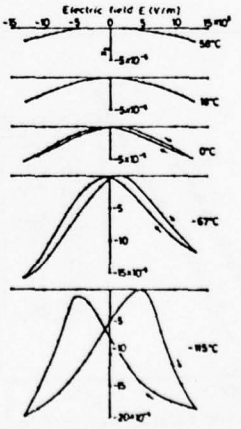

Fig.1 Strain x_2 vs. electric field E in $Pb(Mg_{1/3}Nb_{2/3})O_3$ ceramics.

x_1 is positive, and that of x_2 is negative as expected.

To obtain the electrostriction Q coefficients, the induced strains in the paraelectric phase were plotted against the electric polarization P on a log-log scale, as shown in Fig.3. The straight line in this figure represents the quadratic relation : $x \propto QP^2$. Just above the average Curie temperature, the quadratic relation does not hold. The Q values of the $Pb(Mg_{1/3}Nb_{2/3})O_3$ ceramics were plotted as a function of temperature in Fig.4.

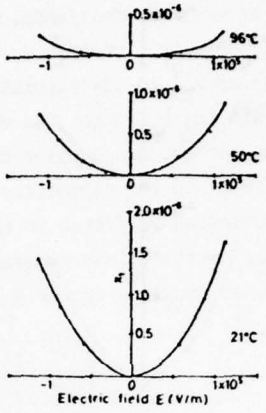

Fig.2 Strain x_2 vs. E in $Pb(Mg_{1/3}Nb_{2/3})O_3$ ceramics.

By using equ.(3) the planar coupling constant k_p' was calculated as a function of the electric field at various temperatures. The results are shown in Fig.5. At -115°C the sample shows a ferroelectric character and the value of k_p' reaches 10 %. At 0°C the curve is accompanied by a skinny hysteresis but the remanance is vanishing. At 50°C, the $k_p'^2$ vs. E curve is quadratic, but it does not pass through the origin, i.e. the k_p' at zero applied field has a non-vanishing value (denoted by $k_p'(0)$). As mentioned in §4, this is resulted from the inaccurate approximation, using equ.(3).

The corrected value of k_p calculated by the numerical fitting method are plotted against the electric field E, in Fig.6, together with the values of $\sqrt{k_p'^2 - k_p'(0)^2}$ and $\sqrt{k_p'^2}$. The value of k_p increases in proportional to the electric field and the line passes through the origin. The interesting result is that the $\sqrt{k_p'^2 - k_p'(0)^2}$ is also a linear function of E, and both the lines have the same gradient. In other words, the correct value of k_p can be obtained by $\sqrt{k_p'^2 - k_p'(0)^2}$.

The value of d_{31} was calculated as a function of polarization P or electric field

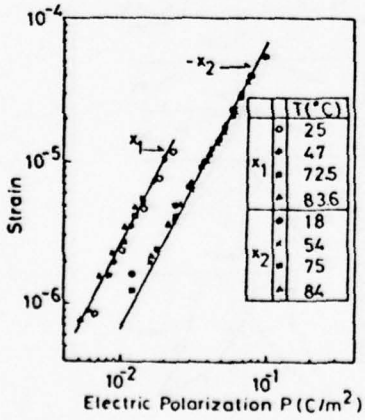

Fig.3 Strain x_1 and x_2 vs. P in $Pb(Mg_{1/3}Nb_{2/3})O_3$ ceramics.

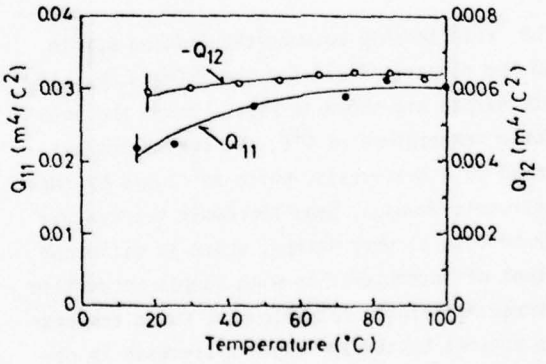

Fig.4 Temperature dependence of Q_{11} and Q_{12} in $Pb(Mg_{1/3}Nb_{2/3})O_3$ ceramics.

E, from which the value of Q_{12} was determined. In Fig.7, the value of d_{31} is plotted against the value of $\varepsilon_{33}^{T^2}E$, where a linear relation holds between them. The Q_{12} value was determined as $(0.71 \pm 0.05)\cdot 10^{-2} m^4/C^2$, which is very close to that obtained from the direct measurement by the strain gauge method. To compare with the data of $Pb(Mg_{1/3}Nb_{2/3})O_3$, we determined the values of k_p' and k_p of $(Ba_{0.6}Sr_{0.4})TiO_3$ ceramics at 40°C, which has a simple perovskite structure with the Curie temperature of 15°C. The result was analogous to that of the $Pb(Mg_{1/3}Nb_{2/3})O_3$. The electrostriction coefficient Q_{12} was determined as $1.0\cdot 10^{-2} m^4/C^2$ for the $(Ba_{0.6}Sr_{0.4})TiO_3$ ceramic sample.

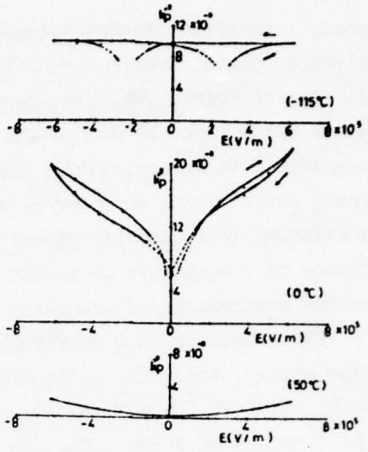

Fig.5 Electromechanical coupling factor k_p^2 determined by using equ.(3)(denoted by $k_p'^2$) vs. E in $Pb(Mg_{1/3}Nb_{2/3})O_3$ ceramics.

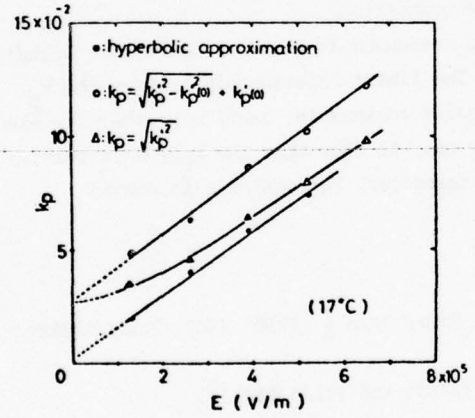

Fig.6 k_p vs. E in $Pb(Mg_{1/3}Nb_{2/3})O_3$ ceramics. $k_p'(0)$ is the value of k_p' at E=0.

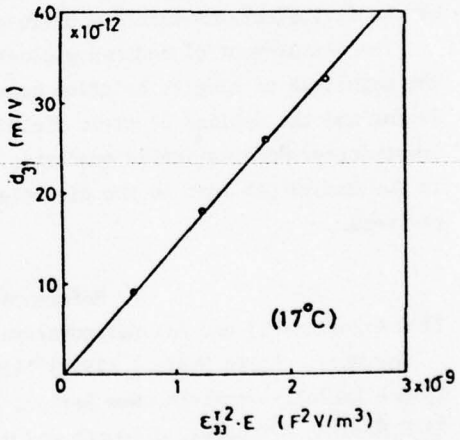

Fig.7 d_{31} vs. $\varepsilon_{33}^{T^2}E$ in $Pb(Mg_{1/3}Nb_{2/3})O_3$.

6. Discussion

Since the ferroelectric phase transition occurs gradually in $Pb(Mg_{1/3}Nb_{2/3})O_3$, the relationship between induced strain vs. electric polarization shows a deviation from quadratic in the temperature range just above the average Curie temperature, where the two phases of ferroelectric and paraelectric coexist, but it is not accompanied by a large hysteresis. This is a characteristic of the ferroelectrics with the diffuse

phase transition. We determined the Q coefficients from the measurements in the paraelectric phase, confirming their quadratic relation. Since the thermal expansion coefficient of $Pb(Mg_{1/3}Nb_{2/3})O_3$ ceramics is about $0.6 \cdot 10^{-6} \cdot C^{-1}$ at room temperature, the error which might be due to the electrocaloric effect upon the electrostriction is considered to be negligiblly small in our measurement. The temperature dependence of the Q coefficients observed in the paraelectric phase is probably due to the effect of coexisting ferroelectric phase, the fraction of which gradually decreases with the increase of temperature above 0°C. The similar temperature dependence has been observed in the measurement of quadratic electrooptic effect of $Pb(Mg_{1/3}Nb_{2/3})O_3$.[7)]

Electrostriction Q coefficients have been measured on various kinds of perovskite-type oxides. According to Schmidt,[8)] the Q values of $BaTiO_3$ ceramics are reported to be $Q_{11}=5.76 \cdot 10^{-2}$ m^4/C^2, and $Q_{12}=-1.242 \cdot 10^{-2}$ m^4/C^2. In comparison with these values, the Q values of $Pb(Mg_{1/3}Nb_{2/3})O_3$ ceramics are about half in magnitude. We have measured electrostrictive Q coefficients of $Pb(Zn_{1/3}Nb_{2/3})O_3$ crystal, which belongs to the ferroelectric crystals with a diffuse phase transition similar to $Pb(Mg_{1/3}Nb_{2/3})O_3$. The Q values determined in the paraelectric phase are $Q_{11}=1.6 \cdot 10^{-2}$ m^4/C^2, $Q_{11}=-0.86 \cdot 10^{-2}$ m^4/C^2, and $Q_{44}=0.85 \cdot 10^{-2}$ m^4/C^2 the magnitudes of which are nearly the same as those of $Pb(Mg_{1/3}Nb_{2/3})O_3$. It is not certain at this point whether the smaller values of Q is a common characteristic of the perovskite-type oxides containing Pb^{2+} ion or of the ferroelectrics with the diffuse phase transition.

The measurement of induced piezoelectric resonance is a useful method to evaluate the magnitude of electrostriction constant. The linear relationship between the k_p factor and the applied electric field E is quite reasonable, confirming that the electrostrictive deformation is quadratic. It is easy to show that the $k_p'(0)$ is related to the mechanical loss in the piezoelectric resonater. The analysis is now in progress.

Reference

1) G.A.Smolenskii and A.I.Agranovskaya ; Fiz Tverd Tera 1 (1959) 1562. Translation : Sov.Phys.- Solid State 1 (1959) 1429.

2) See Landolt-Börnstein, New Series, III/3 (1969) and III/9 (1975).

3) S.Nomura, K.Tonooka, J.Kuwata and M.Abe ; Abstracts, Annual Meeting of Jap.J.Appl. Phys.Soc. (1978) 47.

4) I.S.Zheludev ; Physics of Crystalline Dielectrics 2 (1971) 600 (Plenum Press)

5) "IRE Standars on Piezoelectric Crystals : Measurements of Piezoelectric Ceramics, 1961 ", Proc.IRE 49, 1161 (1961)

6) M.Marutake ; " Approximation Method of Calculating Electromechanical Coupling Factor ", Proc.IRE 49, 967 (1961)

7) N.N.Krainik, V.A.Trepakov, L.S.Kamujina, D.G.Sakharov, B.A.Volik, V.A.Pis'mennyi and K.P.Skornyakova ; Fiz Tverd Tera 17 (1975) 208. Translation : Sov.Phys.- Solid State 17 (1975) 122.

8) G.Schmidt ; Z.Phys. 145 (1956) 534.

APPENDIX 9

K. Uchino, S. Nomura, L.E. Cross and R.E. Newnham. An Estimate of Soft Modes in Relaxor Ferroelectrics.

An Estimate of Soft Modes in Relaxor Ferroelectrics

K. Uchino and S. Nomura

Department of Physical Electronics, Tokyo Institute of Technology

Ookayama, Meguro-ku, Tokyo 152, Japan

and

L.E. Cross and R.E. Newnham

Materials Research Laboratory, The Pennsylvania State University

University Park, Pennsylvania 16802

Abstract

The effect that the polarization related electrostrictive coefficients Q in the relaxor type ferroelectrics are almost an order of magnitude smaller than in most normal ferroelectric perovskites is reasonably explained under the assumption that the temperature dependence of the soft-mode TO phonon frequency is given as $\omega_{TO}^2 = A(T-T_c)$, where the coefficient A in relaxor ferroelectrics is an order of magnitude smaller than the value in normal ferroelectric perovskites. The assumption also concludes that the Curie-Weiss constants C in the relaxor crystals are several times larger than in the normal ferroelectrics. The soft-mode frequency in the $Pb(Mg_{1/3}Nb_{2/3})O_3$ crystal is predicted to be below 10 cm^{-1} near the mean Curie temperature.

1. Introduction

In our recent papers we have reported the pressure dependence of dielectric constants and the electrostrictive effects in $Pb(Mg_{1/3}Nb_{2/3})O_3$ [1] and $Pb(Zn_{1/3}Nb_{2/3})O_3$ [2,3] single crystals. We indicated in these papers that the polarization related electrostrictive coefficients Q in the relaxor type ferroelectrics are almost an order of magnitude smaller than in most normal ferroelectric perovskites. On the other hand, the Curie-Weiss constants C in the relaxor crystals are several times larger[4] and consequently the products QC (or Qx permittivity) are almost the same for all ferroelectric perovskites (See Table I).

To explain these phenomena, a soft-mode model of relaxor ferroelectrics is proposed in the temperature range near the low frequency dielectric maximum. Numerical prediction of the transverse optic phonon mode softening is made for $Pb(Mg_{1/3}Nb_{2/3})O_3$ and $Pb(Zn_{1/3}Nb_{2/3})O_3$ and compared to the soft-mode frequency of simple (non-relaxor) perovskite ferroelectrics.

2. Soft-Mode Model in Relaxor Ferroelectrics

Though the lattice vibrations of a disordered atomic assembly are not equivalent to unique vibrations in a regular lattice, the elastic vibrations of long wavelength are approximately similar plane waves, which are scarcely aware of the atomicity of the materials[5].

For the soft phonon near the zone center ($k \approx 0$) the energy-wave vector curve in a disordered crystal is expected to behave similarly to the one in an ordered crystal, although a sharply defined dispersion function in an ordered lattice is broadened in energy and/or momentum by incoherent scattering from the disordered assembly of atoms.

We presume that the temperature dependence of the transverse optical soft-phonon frequency in a disordered perovskite crystal is represented in a similar fashion to the one in simple perovskite ferroelectrics.

$$\omega_{TO}^{soft\ 2} = A(T-T_c) \tag{1}$$

Here we assume that the A value in a relaxor ferroelectric is an order of magnitude smaller than the value in a normal ferroelectric perovskite, since the diffuse temperature dependence of ω_{TO} in a wide temperature range is expected in the relaxor type.

The connection between ferroelectricity and lattice dynamics is made by means of the Lyddane-Sachs-Teller (LST) relation[6,7].

$$\varepsilon_s/\varepsilon_\infty = \prod_{i-1}^{N-1}[\omega_{LO}^{(i)}/\omega_{TO}^{(i)}]^2 \tag{2}$$

where ω_{LO} and ω_{TO} are longitudinal and transverse optical phonon mode frequencies at zero wave vector, N is the number of atoms per unit cell, ε_s is the static dielectric constant and ε_∞ is the square of the optical index of refraction. If we suppose that the frequency of one of TO phonon modes approaches zero (soft-mode) and that ε_∞ and $\omega_{LO}^{(i)}$s and other $\omega_{TO}^{(i)}$s are relatively insensitive to the compounds, we describe the LST relation as follows:

$$1/\varepsilon_s = K\omega_{TO}^{soft\ 2} \tag{3}$$

where K is almost constant for all ferroelectric perovskites.

There is also a relation between the stress dependence of ε_s and the electrostriction, since these two effects are derivable from the same term in the free energy[8].

$$\partial(1/\varepsilon_s)\partial p = 2(Q_{11} + 2Q_{12}) = 2Q_h \tag{4}$$

where p is the hydrostatic pressure and Q_s are the polarization related electrostrictive coefficients.

The relations between the Curie-Weiss constant C or the electrostrictive

coefficient Q_h and the temperature derivative of the square of the soft-phonon frequency A are derived from Eqs (1), (3), and (4) under the assumption that C is insensitive to the hydrostatic pressure[9].

$$C = 1/KA \tag{5}$$

$$Q_h = [-\tfrac{1}{2}(\partial T_c/\partial p)]KA \tag{6}$$

If we accept the experimental result that the $(\partial T_c/\partial p)$ value is almost constant for every ferroelectric perovskite[1,10], a large Curie-Weiss constant and a small electrostrictive coefficient can be derived from the one-order of magnitude smaller A value in relaxor type ferroelectrics. Electrostrictive coefficients, Curie-Weiss constants, pressure derivative of Curie temperature, and temperature derivative of the square of the soft-mode frequency for some perovskite-type ferroelectrics are summarized in Table I. The A values for $Pb(Mg_{1/3}Nb_{2/3})O_3$ and $Pb(Zn_{1/3}Nb_{2/3})O_3$ are estimated from the equation

$$A/Q_h \approx 570\ [cm^{-2}\ K^{-1}/m^4C^{-2}] \tag{7}$$

3. Discussion

There is a significant fact that no soft modes have been observed in the Raman spectra of a large number of mixed (relaxor) ferroelectrics[23]. If the soft-mode model in relaxor ferroelectrics (Eq (1)) is true, then the mode (ω_{TO}) must lie in the frequency range below 20 cm^{-1}, which is inaccessible to Raman scattering studies.

In the transition temperature range, temperature dependence of TO mode frequency may be slightly corrected for relaxor ferroelectrics in terms of diffuseness of the phase transition owing to disordered atomic arrangement[24]. Considering the local Curie temperature distribution as of Gaussian type, the TO mode frequency may be represented as follows:

$$[\omega_{TO}^{soft}(T)]^2 = \int_0^T A(T-T_c)\exp[-(T_c-T_{av})^2/2\delta^2]dT_c \Big/ \int_0^\infty \exp[-(T_c-T_{av})^2/2\delta^2]dT \tag{8}$$

where T_c, a local Curie temperature, T_{av}, the mean Curie temperature and δ is the parameter, describing the diffuseness of the phase transition. In the case of $Pb(Mg_{1/3}Nb_{2/3})O_3$ single crystal ($A = 3.4\ cm^{-2}K^{-1}$, $\delta = 41$ K), ω_{TO} is supposed to have a finite value ($\sim 7\ cm^{-1}$) even at $T = T_{av}$. The temperature dependence of its dielectric constant shows a considerable dispersion in a frequency range from 10^{-2} to 10^{9} Hz[25]. Kirillov et al. reported that maxima of the temperature dependence of the permittivity ε shift to higher temperatures with increasing measuring frequency. Although the frequency dependence of dielectric constant may be different below the mean Curie temperature because of the interaction between polar regions or the contribution of domain wall vibrations, the extrapolation of the curve $\ln\omega = f(T_{av})$ to a higher temperature ($\sim$310 K) leads to an almost similar magnitude of wavenumber 2 cm^{-1} to the one predicted above ($\sim 7\ cm^{-1}$).

Dielectric measurements in a frequency range from 10^{9} to 10^{12} Hz (microwave) or precise Raman scattering studies will be desired. If we will be able to make both ordered and disordered crystals with the same composition, only by changing the annealing process, the lower Curie temperature, the larger Curie-Weiss constant, and the smaller electrostrictive coefficient are expected in a disordered crystal than in an ordered crystal.

Acknowledgment

We wish to thank the Office of Naval Research for their support of our work through Contract No. N00014-78-C-0291.

References

1. K. Uchino, S. Nomura, L.E. Cross, S.J. Jang and R.E. Newnham, J. Appl. Phys. 51 (to be submitted).
2. J. Yoshimoto, B. Okai and S. Nomura, J. Phys. Soc. Japan 31, 307 (1971).
3. S. Nomura, J. Kuwata, S.J. Jang, L.E. Cross and R.E. Newnham, Mat. Res. Bull. 14, 769 (1979).
4. J. Kuwata, K. Uchino and S. Nomura, Ferroelectrics 22, 863 (1979).
5. J.M. Ziman, Models of Disorder, p. 439, Oxford:Cambridge University Press (1979).
6. R.H. Lyddane, R.G. Sachs and E. Teller, Phys. Rev. 59, 673 (1941).
7. W. Cochran, Advan. Phys. 10, 401 (1961).
8. F. Jona and G. Shirane, Ferroelectric Crystals, New York:Macmillan (1962).
9. G.A. Samara, Phys. Rev. 151, 378 (1966).
10. G.A. Samara, J. Phys. Soc. Japan 28S, 399 (1970).
11. T. Yamada, J. Appl. Phys. 43, 328 (1972).
12. C.J. Johnson, Appl. Phys. Lett. 7, 221 (1965).
13. V.G. Gavrilyachenko and E.G. Fesenko, Soviet Phys.-Cryst. 16, 549 (1971).
14. E.G. Fesenko, V.G. Gavrilyachenko and E.V. Zarochentsev, Bull. Acad. Sci. USSR, Phys. Ser. 34, 2262 (1970).
15. G. Shirane, J.D. Axe, J. Harada and J.P. Remeika, Phys. Rev. B2, 155 (1970).
16. H. Uwe and T. Sakudo, J. Phys. Soc. Japan 38, 183 (1975).
17. H. Uwe, H. Unoki, Y. Fujii and T. Sakudo, Commun. Solid State Phys. 13, 737 (1973).
18. G. Shirane, R. Nathans and V.J. Minkiewicz, Phys. Rev. 157, 396 (1967).
19. G. Schmidt and E. Hegenbarth, Phys. Stat. Sol. 3, 329 (1963).
20. R.O. Bell and G. Rupprecht, Phys. Rev. 129, 90 (1963).

21. P.A. Fleury and J.M. Worlock, Phys. Rev. 174, 613 (1968).

22. S. Nomura, S.J. Jang, L.E. Cross and R.E. Newnham, J. Amer. Ceram. Soc. (in press).

23. G. Burns and B.A. Scott, Commun. Solid State Phys. 13, 417 (1973).

24. G.A. Smolenskii, J. Phys. Soc. Japan 28, 26 (1970).

25. V.V. Kirillov and V.A. Isupov, Ferroelectrics 5, 3 (1973).

Table I. Electrostrictive coefficients, Curie-Weiss constants, the variation of Curie temperature with hydrostatic pressure and the temperature derivative of the swuare of the soft-mode frequency for some perovskite-type ferroelectrics.

Substance	Q_h $X10^{-2}m^4 \cdot C^{-2}$	C $(x10^5 K)$	$(\partial T_c/\partial p)$ $(K \cdot kbar^{-1})$	A $(cm^{-2}K^{-1})$
$BaTiO_3$	2.0[11]	1.5[12]	-5.5[10]	--
$PbTiO_3$	2.2[13]	1.7[14]	<-8[10]	8.2[15]
$KTaO_3$	5.2[16]	0.5[17]	--	29.1[18]
$SrTiO_3$	5.0[19]	0.77[20]	--	28.6[21]
$Pb(Mg_{1/3}Nb_{2/3})O_3$	0.60[1]	4.7[22]	4.8[1]	3.4*
$Pb(Zn_{1/3}Nb_{2/3})O_3$	0.66[3]	4.7[4]	-5.5[2]	3.8*

*Estimated values from the equation $A \approx 570\ Q_h$.

COMPOSITES

APPENDIX 10

R.E. Newnham, D.P. Skinner, K.A. Klicker, A.S. Bhalla, B. Hardiman and T. Gururaja. Ferroelectric Ceramic-Plastic Composites for Piezoelectric and Pyroelectric Applications. Proc. Int. Symp. Applications of Ferroelectrics, IEEE, Minneapolis, MN, June 1979.

FERROELECTRIC CERAMIC-PLASTIC COMPOSITES FOR PIEZOELECTRIC AND PYROELECTRIC APPLICATIONS

R.E. NEWNHAM, D.P. SKINNER, K.A. KLICKER, A.S. BHALLA,
B. HARDIMAN and T.R. GURURAJA
Materials Research Laboratory
The Pennsylvania State University
University Park, Pennsylvania 16802

Consideration of the influence of crystal symmetry, macrosymmetry, and interphase connectivity have been used to explore possible macrostructures of interest as piezoelectric or pyroelectric composites. Based on these design considerations, ceramic-plastic composites have been fabricated with 3-3 phase connectivity by the replication of natural template structures such as coral. Composites prepared in this way have piezoelectric g_{33} and g_h coefficients more than an order of magnitude higher than the coefficients of the homogeneously poled ferroelectric ceramic. Large voltage coefficients were also obtained from 3-1 piezoelectric composites made by embedding PZT fiber arrays in epoxy cement. Processing methods are described for producing straight and helical piezoelectric fibers by both extrusion and casting of PZT slips. Pyroelectric measurements on ceramic-plastic composites led to two interesting results: thermal expansion mismatch between the two phases can couple to the piezoelectric coefficients to give a large secondary pyroelectric effect, and, secondly, boracite-plastic composites have extremely large voltage coefficients (p/ε), comparable to boracite single crystals and the very best vidicon materials.

INTRODUCTION

Progress in materials science—like progress in most fields—follows the curve of history (Fig. 1). When a new effect such as ferroelectricity is discovered, scientific development is rather slow at first, until its importance is recognized. Then follows a period of rapid growth when practical applications and many new materials are discovered. Rapid changes take place in selecting the "best" material for each application. Eventually the field matures as the choices are made, and the curve of history saturates.

We see this saturation effect in many fields of materials science. PZT has been the best transducer material for 25 years. $BaTiO_3$ has been the best high K capacitor material for 30 years. Similar trends can be noted in magnetic materials, semiconductors, and superconductors. Despite intensive search for new compounds, relatively little progress has been made in the past ten or twenty years.

Where then do we go from here? Heterogeneous systems optimized for particular applications are certainly one possibility. Examples include semiconductor integrated circuits, fiber-reinforced metals, and barrier-layer ferroelectric capacitors. For the past three years we have been investigating some piezoelectric and pyroelectric composites, hoping to improve some of the properties of homogeneous materials. A summary of the basic ideas was published last year.[1] Connectivity is a critical parameter in composites designed for use as piezoelectric transducers or as pyroelectric detectors.

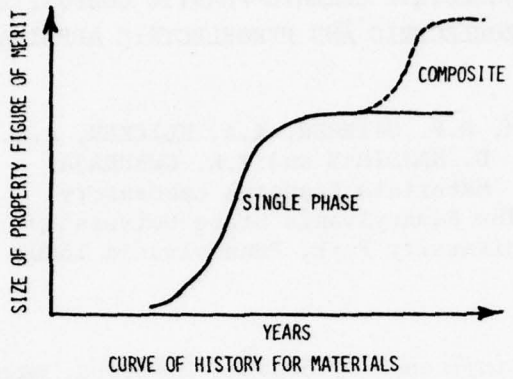

CURVE OF HISTORY FOR MATERIALS

Fig. 1

There are ten connectivity patterns in diphasic solids, ranging from a 0-0 unconnected checkerboard pattern to a 3-3 intertwined skeleton pattern in which both phases are three-dimensionally self-connected.

When the two phases are connected in parallel, the longitudinal piezoelectric voltage coefficient is

$$\bar{g} = \frac{v_I d_I s_{II} + v_{II} d_{II} s_I}{(v_I s_{II} + v_{II} s_I)(v_I \varepsilon_{II} + v_{II} \varepsilon_I)} \qquad (1)$$

In this expression, v_I and v_{II} are the volume fractions of the two phases. The piezoelectric coefficient, elastic compliance, and electric permittivity are represented by d, s, and ε, respectively. The composite of interest here is a mechanically stiff ferroelectric (phase I) in parallel with a soft compliant polymer (phase II), then $d_I >> d_{II}$, $s_I << s_{II}$, $\varepsilon_I >> \varepsilon_{II}$, and $\bar{g} \cong d_I/v_{II}\varepsilon_I$. Thus the voltage coefficient of the composite can easily exceed that of the solid ferroelectric.

In this paper we describe some processing methods for making 3-3 and 3-1 connectivity patterns which place the two phases in parallel. The composites give large voltage coefficients, as predicted by the theory.

A number of other research groups are also investigating the properties of ferroelectric composites with interesting connectivity patterns. Among the papers presented at this conference, there are examples of 3-0, 3-1, 3-3, and 2-2 patterns. The flexible PZT-polymer films described by Liu and Harrison[2] are 3-0 structures altered to 3-1 by grinding, while the properties of a ladder-type structure with 3-3 connectivity were reported by Miyashita and coworkers[3]. The internally electroded PZT multilayers investigated by Bowen and coworkers[4] are an excellent example of a metal-ceramic composite with 2-2 connectivity.

REPLAMINE TRANSDUCERS

Theoretical calculations indicate that a composite with 3-1 connectivity will have the best voltage coefficients, but 3-3 connectivity offers certain advantages in sample preparation; interconnections between the PZT fibers maintain the fiber orientation during the ceramic processing steps. In a 3-3 composite, both phases are self-connected in all these directions. Microstructures of this type occur in foams, phase-separated glasses, wood, and coral.

Coral skeletons are characterized by a narrow channel size distribution with complete interconnectivity. In the goniopera coral used in this study, the largest channel diameters are about 600 μm.

FERROELECTRIC CERAMIC-PLASTIC COMPOSITES

A lost-wax technique has been developed to replicate skeletal structures in other materials.[5,6] As illustrated in Fig. 2, the first step is to machine the coral in the desired shape. Using vacuum suction, the coral template is then impregnated with Kerr Inlay casting wax, after which the $CaCO_3$ skeleton is dissolved away in hydrochloric acid. The wax negative is reinvested with a PZT slip (43 volume% PZT, 53% H_2O, 4% poly (vinyl alcohol)). Ultrasonics PZT-501A with an average grain size of 1.6 μm was used in the process. The wax negative was burned off at 300°C, leaving a coral replica of PZT which was then sintered at 1280°C for one hour. The PZT replica was later back-filled with a high-purity silicone rubber (Dow Corning MDX-4-4210 Elastomer). After attaching silver-loaded silicone rubber electrodes, the composite was poled for five minutes at 100°C under an electric field of 14 kV/cm.

As poled, the PZT-rubber replica is mechanically rigid, but flexing the composite fractures the ceramic skeleton and improves the piezoelectric properties. Shearing the structure lowers the permittivity without appreciably affecting the piezoelectric d coefficient. As a result, the longitudinal voltage coefficient g_{33} is greatly enhanced.

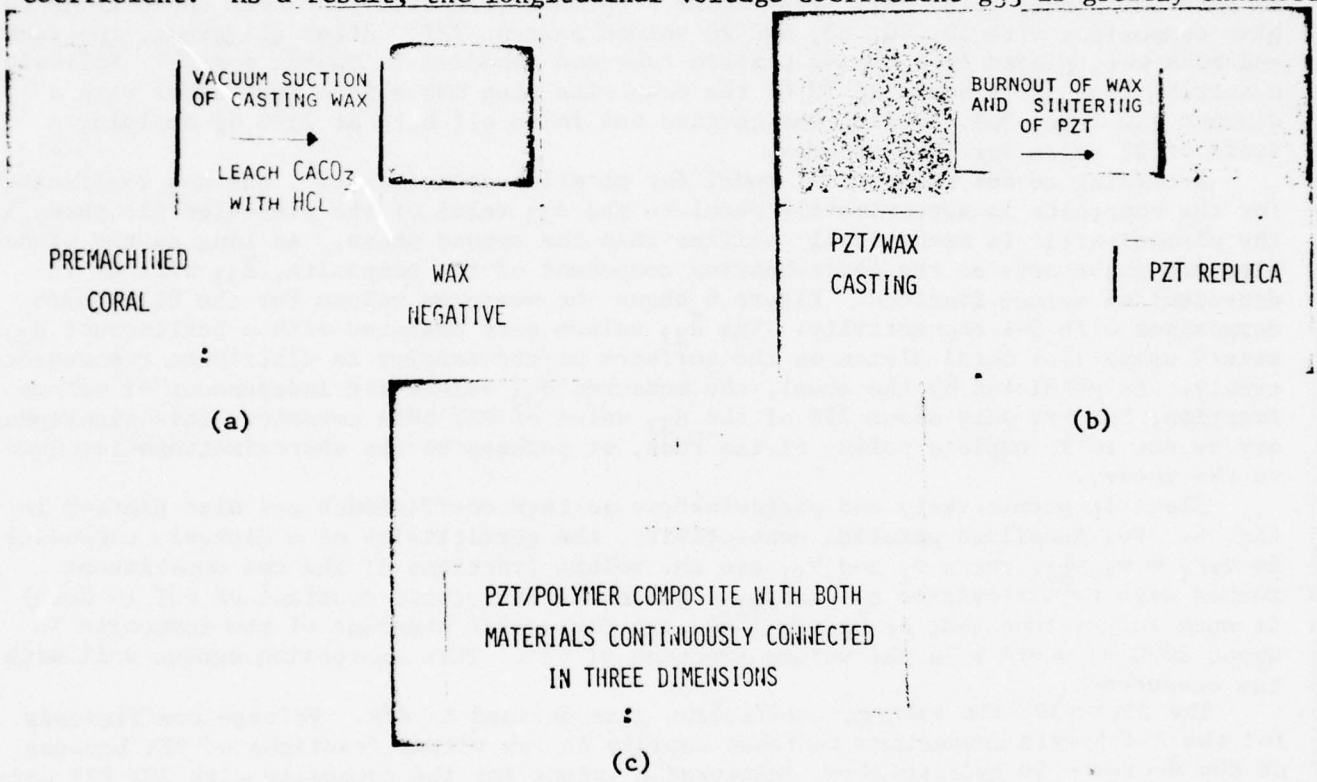

Fig. 2 A lost-wax technique to replicate skeletal structures.

The measured values are $K_{33} = 40$, $d_{33}=100\times10^{-12}$ C/N, and $g_{33} = 300\times10^{-3}$ Vm/N, about fifteen times better than a solid PZT ceramic of similar composition. Three other advantageous properties of the composite are low density, high felxibility, and high tensile strength.

PIEZOELECTRIC FIBERS IN PLASTIC

Composites with 3-1 connectivity have been made by aligning PZT rods in a plastic matrix. In the 3-1 model (eq 1), the piezoelectric effect of the composite depends on the volume fractions of the constituent phases, together with their permittivities,

piezoelectric coefficients, and elastic compliances. By varying the spacing between the PZT rods and their diameters, the conditions maximizing $\bar{d}_{33}$ and $\bar{g}_{33}$ are under study.

PZT rods are formed by extruding a slip of commercial PZT[a] in a PVA solution. The slip composition was 90 wt% PZT, 8% water, 2% PVA. Using dies of several different diameters, the slip was extruded onto a moving glass plate to ensure straightness of the green PZT rods. After drying for 24 hours at room temperature, the rods were cut into 35 mm segments and sintered at 1305°C for a half-hour.

Initially, the PZT rods proved difficult to pole because of air bubbles introduced during extrusion. To reduce the porosity and increase the electric breakdown strength, the sintered rods were refired in a hot isostatic press (HIP) for one hour at 1300°C under a 200 atmosphere pressure of argon. The final density was 7.82 g/cm^3. Rods of 0.84 mm diameter were used in the piezoelectric measurements, but thinner PZT rods of 0.66, 0.46, and 0.20 mm diameter have been produced by the same method.

A pair of brass disks with drilled holes were used to align the piezoelectric rods in parallel arrays (Fig. 3a). Four racks were made with different hole separations to give composites with 50, 40, 30, and 20 volume percent PZT. After alignment, the rack and rods were placed in a closed plastic tube and embedded in Spurrs epoxy[b]. Following a setting time of 16 hours at 70°C, the composite slug was sliced into disks with a diamond saw (Fig. 3b). Poling was carried out in an oil bath at 75°C by applying a field of 22 kV/cm for five minutes.

According to our theoretical model for parallel connectivity[1], the d_{33} coefficient for the composite is approximately equal to the d_{33} value of the piezoelectric phase if the piezoelectric is mechanically stiffer than the second phase. As long as the piezoelectric phase acts as the force-bearing component of the composite, $\bar{d}_{33}$ will be independent of volume fraction. Figure 4 shows the measured values for the PZT-Spurrs composites with 3-1 connectivity. The $\bar{d}_{33}$ values were measured with a Berlincourt d_{33} meter[c] using flat metal plates on the surfaces of the samples to distribute the weight evenly. As predicted by the model, the measured d_{33} values are independent of volume fraction, but are only about 75% of the d_{33} value of PZT 501A ceramic. This discrepancy may be due to incomplete poling of the rods, or perhaps to the approximations involved in the theory.

Electric permittivity and piezoelectric voltage coefficients are also plotted in Fig. 4. For idealized parallel connectivity, the permittivity of a diphasic composite is $v_I\varepsilon_I + v_{II}\varepsilon_{II}$, where v_I and V_{II} are the volume fractions of the two constituent phases with permittivities ε_I and ε_{II}. Since the dielectric constant of PZT ($\sim$ 2000) is much larger than that of Spurrs ($\sim$4), the dielectric constant of the composite is about 2000 v, where v is the volume fraction of PZT. This expression agrees well with the measurement.

The piezoelectric voltage coefficient g is defined as d/ε. Voltage coefficients for the PZT-Spurrs composites increase rapidly at low volume fractions of PZT because of the decrease in permittivity. Measured g values for the composite with 20% PZT were about 3.5 times larger than solid PZT.

Experiments are now underway with smaller volume fractions of PZT and with helical fibers (Fig. 3c). When arranged in bedspring arrays, the PZT spirals show some interesting piezoelectric effects. The helices were made in two ways: by extrusion and by casting. The extrusion technique is a variation on the method described earlier for making straight PZT rods. Immediately following extrusion, the green fibers were wrapped around a plastic mandrel to form spirals. After drying, the coils were slipped off the mandrel and sintered at 1300°C for 30 minutes in an alumina crucible. To protect the coils during sintering, they are buried in coarse PZT powder.

---

[a]PZT 501A, Ultrasonic Powders, Inc., South Plainfield, NJ 07080.
[b]Ernest F. Fullam, Inc., Schenectady, NY 12301.
[c]Channel Products, Inc., Chagrin Falls, Ohio 44022.

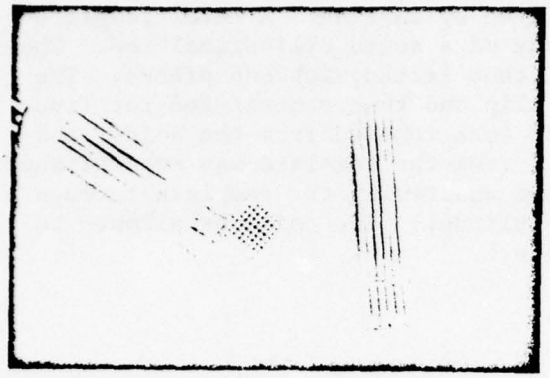

(a)

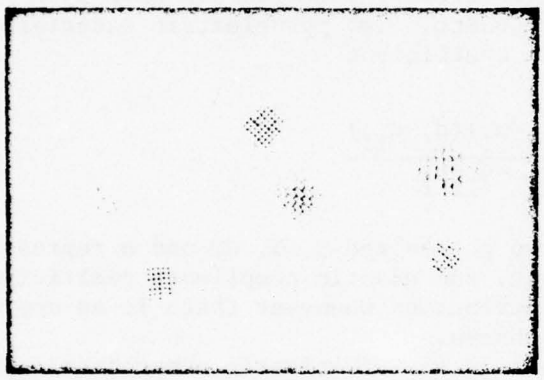

(b)

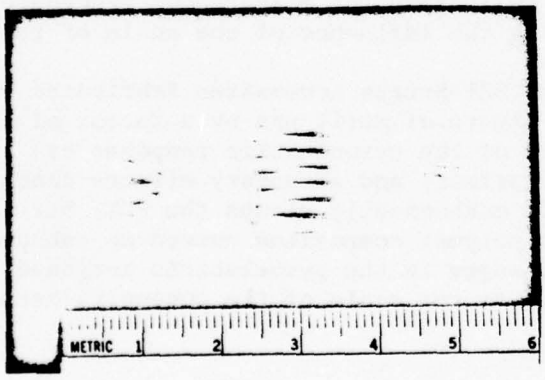

(c)

Fig. 3 (a) Alignment of the piezoelectric rods in parallel arrays for the composites with 3-1 connectivity. (b) PZT:SPURRS composite discs with various volume percent PZT. (c) Helical fibers made of PZT.

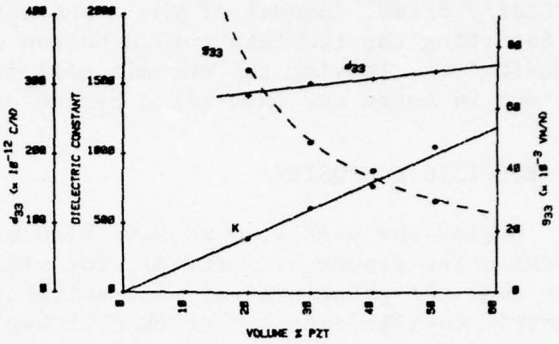

Fig. 4 Plots of K, d_{33} and g_{33} versus volume % PZT.

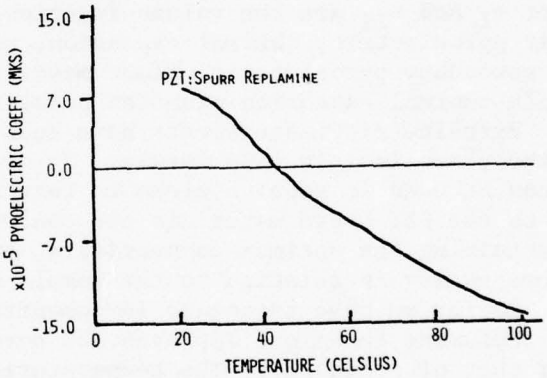

Fig. 5 Temperature dependence of the pyroelectric response in a PZT: SPURRS composite.

Spirals with rectangular cross-sections were made by casting. A metal template was made by machining a spiral groove on the surface of a solid cylindrical rod. The template was then inserted in a hollow cylindrical tube fitted with end pieces. The metal tube was then partially filled with PZT 501 slip and then centrifuged for five minutes at 3500 RPM. The template and cast ceramic were removed from the holder and partially dried. Removal of the green ceramic helix from the template was accomplished by inserting the template into a hollow cylinder and unscrewing the template through a blocking pin, leaving the ceramic coil inside the cylinder. The coil was allowed to dry for 24 hours and then fired by the usual procedure.

PYROELECTRIC COMPOSITES

During the past year we have also been studying pyroelectric composites, seeking to maximize the figure of merit p/ε for vidicon applications[1] for simple model systems suggest that two phase systems with suitably chosen connectivity patterns can have pyroelectric coefficients larger than either individual phase. Two pyroelectric materials connected in parallel have a composite pyroelectric coefficient

$$\bar{p} = v_I p_I + v_{II} p_{II} + \frac{v_I v_{II} (\alpha_{II}-\alpha_I)(d_I-d_{II})}{v_I s_{II} + v_{II} s_I}$$

where v_I and v_{II} are the volume fractions of the two phases and p, α, d, and s represent their pyroelectric, thermal expansion, piezoelectric, and elastic compliance coefficients. The secondary pyroelectric effect makes a major contribution whenever there is an appreciable thermal expansion mismatch between the two phases.

Pyroelectric measurements have been carried out on the PZT-plastic composites used in the piezoelectric experiments. Even though PZT is far from ideal as a pyroelectric, it can be used in model systems to test different composite geometries. Current studies on the PZT based materials are concerned with validating the measurement procedures, ascertaining the optimum connectivity, and exploring the influence of the scale of the heterogeneity in relation to the sample dimensions.

So far we have succeeded in demonstrating that PZT-Spurrs composites fabricated by the replamine technique improves the pyroelectric figure of merit p/ε by a factor of 6 over that of solid PZT. The temperature dependence of the pyroelectric response exhibits an interesting compensation point where the primary and secondary effects cancel out (Fig. 5). AT room temperature the hard plastic mechanically clamps the PZT, but at higher temperatures the plastic softens. PZT-soft polymer composites showed no enhancement of the pyroelectric figure of merit. Major changes in the pyroelectric response were noted when the sample thickness was comparable to the scale of the composite heterogeneity.

BORACITE COMPOSITES

Improper ferroelectrics such as the boracites ($M_3B_7O_{13}X$: M=Cu,Ni,Co,Fe,Mn; X=Cl, Br,I) possess unusual property coefficients, including a large figure of merit for pyroelectric vidicon applications.[7] The pyroelectric voltage coefficients of $Cu_3B_7O_{13}Cl$, $Ni_3B_7O_{13}Br$ and $Fe_3B_7O_{13}I$ are larger than that of deuterated triglycine fluoberyllate (DTGFB), but a number of problems remain to be solved before boracite crystals can be used for vidicon targets. Crystals larger than a few millimeters of acceptable chemical homogeneity and free from fracture are very difficult to grow and pole.

FERROELECTRIC CERAMIC-PLASTIC COMPOSITES

Boracite-plastic composites appear to be an attractive alternative to the single crystals. Some preliminary measurements were made using $Fe_3B_7O_{13}I$ crystallites obtained from the Plessey Company. The tiny crystals were crushed and screened between 100 and 200 mesh and then mounted in a Spurrs epoxy film. We found that the films became strongly pyroelectric after poling and that the signal level increases with the degree of poling. The figure of merit of the composites was the same as that of Fe-I boracite single crystals.

There are two excellent reasons why the boracite composites pole so easily: first, the dielectric constant of boracite is about the same as the plastic, and second, boracite has twelve domain orientations, far more than most ferroelectrics. Based on these encouraging results, it seems worthwhile to develop processing techniques for boracite composites and polycrystalline aggregates for pyroelectric applications.

ACKNOWLEDGMENTS

The boracite crystals used in the pyroelectric composites were supplied by Dr. Roger Whatmore of the Plessey Co. Some of the pyroelectric measurements were carried out in cooperation with Dr. Joseph Dougherty and Dr. Wallace Smith of the North American Philips Laboratories. The advice and assistance of our colleagues at Penn State and Dr. Robert Pohanka of the Naval Research Laboratory are also acknowledged with gratitude. This work was sponsored by the Department of Defense through contracts N00014-78-C-0291 and MDA 903-78-C-0306.

REFERENCES

1. R.E. Newnham, D.P. Skinner, L.E. Cross, Mat. Res. Bull. 13, 525 (1978).
2. S.T. Liu and W.B. Harrison, Ferroelectrics (this issue).
3. M. Miyashita, K. Takano, T. Toda, Ferroelectrics (this issue).
4. L. Bowen, T. Shrout, W. Schulze, J.V. Biggers, Ferroelectrics (this issue).
5. R.A. White, J.N. Weber, [illegible].W. White, Science,176, 922 (1972).
6. D.P. Skinner, R.E. Newnham, L.E. Cross, Mat. Res. Bull. 13, 599 (1978).
7. R.W. Whatmore, C.J. Brierley and F.W. Ainger, Ferroelectrics (this issue).

APPENDIX 11

K.A. Klicker, J.V. Biggers and R.E. Newnham. Composites of PZT and Epoxy for Transducer Applications.

COMPOSITES OF PZT AND EPOXY FOR TRANSDUCER APPLICATIONS

K.A. Klicker, J.V. Biggers, R.E. Newnham

Materials Research Laboratory
The Pennsylvania State University
University Park, Pennsylvania 16802

Introduction

Lead Zirconate titanate solid solutions (PZT) are currently used in many transducer applications. They have, however, limited utility in transducers used under hydrostatic conditions because their low hydrostatic piezoelectric coefficients (d_h) and voltage coefficient (g_h). The low coefficients are a result of the coupling of the d_{33} and d_{31} coefficients. Specifically

$$d_h = d_{33} + 2d_{31}$$

In PZT's d_{33} is about twice the magnitude and of opposite sign of d_{31} resulting in a very low value of d_h. The voltage coefficient (g_h) is related to d_h by

$$g_h = \frac{d_h}{\varepsilon_{33}}$$

and is also low because of the low d_h and high permittivity (ε_{33}) of PZT.

It is possible that a properly designed composite material of PZT and a polymer phase might decouple d_{33} and d_{31} and lower the permittivity resulting in improved values of d_h and g_h. In this paper we will describe a technique of producing composites of extruded and fired PZT rods embedded in a compliant polymer matrix.

Composites have been made using PZT particles bound in a matrix of silicon rubber.[1] These composites were not only flexible, but also exhibited good sensitivity to low frequency sound. Density of the composites varied from 6.2 - 3.9 g/cc depending on percent silicon rubber in the composite and the density of the PZT particles. Composites of polymer and PZT have also been prepared by use of the "replamine technique."[2] Using coral as a template, composites in which both the PZT and the polymer are three dimensionally connected have been made. These transducers also have low density and good sensitivity.

The properties of a composite are influenced by the connectivity[3] of the components of the composite. Connectivity is defined as the number of dimensions in which each phase is continuous. In the composite made by the replimine technique, for example, both the polymer and the PZT are continuous in all three dimensions and therefore the composite has 3-3 connectivity. A composite with 3-1 connectivity is shown in Figure 1. A theory for piezoelectric response has been developed[4] for composites of 3-1 connectivity in which rods of PZT (phase 1) are embedded in a three dimensionally continuous polymer. The PZT rods are poled along their length and therefore the 3 direction of the composite, as shown by Figure 1, is along the direction in which the rods are aligned. The theoretical equations for a composite with 3-1 connectivity are as follows:

$$\bar{d}_{33} = \frac{{}^1v\,{}^1d_{33}\,{}^2s_{33} + {}^2v\,{}^2d_{33}\,{}^1s_{33}}{{}^1v\,{}^2s_{33} + {}^2v\,{}^1s_{33}} \tag{1}$$

$$\bar{d}_{31} = {}^1v\,{}^1d_{31} + {}^2v\,{}^2d_{31} \tag{2}$$

$$\bar{\varepsilon}_{33} = {}^1v\,{}^1\varepsilon_{33} \quad {}^2v\,{}^2\varepsilon_{33} \tag{3}$$

where ${}^1v$, ${}^1d_{33}$, ${}^1d_{31}$, ${}^1g_{33}$ and ${}^1\varepsilon_{33}$ are respectively the volume fraction, piezoelectric coefficients, elastic compliance and permittivity of phase one. The average coefficients for the composite are $\bar{d}_{33}$, $\bar{d}_{31}$ and $\bar{\varepsilon}_{33}$.

If the following conditions are assumed:

$${}^1v = {}^2v = 0.5$$

$${}^1d_{33} >> {}^2d_{33}$$

$${}^1s_{33} << {}^2s_{33}$$

$${}^1\varepsilon_{33} >> {}^2\varepsilon_{33}$$

the theoretical results are:

$$\bar{d}_{33} \simeq {}^{1}d_{33} \tag{4}$$

$$\bar{d}_{31} \simeq 0.5\,{}^{1}d_{31} \tag{5}$$

$$\bar{\varepsilon}_{33} \simeq 0.5\,{}^{1}\varepsilon_{33} \tag{6}$$

The piezoelectric response to hydrostatic pressure (d_h) is defined as

$$d_h = d_{33} + 2d_{31} \tag{7}$$

The d_h coefficient for solid PZT is small because $d_{33} \simeq -2d_{31}$. If however d_{31} is reduced (if d_{33} is reduced at all) then the value of d_h will be greater than that for solid PZT. Substitution of equations (4) and (5) into equation (6) will have the result of

$$\bar{d}_h = \bar{d}_{33} + 2\bar{d}_{31} = {}^{1}d_{33} + 2(0.5\,{}^{1}d_{31}) \tag{8}$$

This theoretical value of $\bar{d}_h$ for the composite of 50 vol % PZT is greater than the d_h of solid PZT. Re-examination of equations (1), (2) and (7) shows that as the volume fraction of PZT is reduced from the value of 0.5 used above, d_{33} is constant but d_{31} will be further reduced and d_h will become even greater.

Another piezoelectric coefficient of interest is the hydrostatic voltage coefficient (g_h) which is defined as

$$\bar{g}_h = \frac{\bar{d}_h}{\varepsilon_{33}} \tag{9}$$

If the permittivity of phase one is much larger than the permittivity of phase two, equation (3) may be written as

$$\bar{\varepsilon}_{33} \simeq {}^{1}\varepsilon_{33}\,{}^{1}v \tag{10}$$

If the conditions assumed above are used equation (10) becomes

$$\bar{\varepsilon}_{33} \simeq 0.5(\varepsilon_{33}) \tag{11}$$

The theoretical value of $\bar{d}_h$ for a composite of 50 vol % has been shown to be greater than d_h of solid PZT (Equation 8) and $\bar{\varepsilon}_{33}$ is one half of ε_{33} (Equation 11). From equation (9), $\bar{g}_h$ will be much larger than g_h for solid PZT.

According to the theory, d_{33} is not a function of volume % PZT because the rods bear all the load in the 3 direction. If this is not strictly true, d_{33} will also be a function of volume % PZT. Figure 2 illustrates the theoretical behavior of $\bar{d}_h$ as a function of volume % PZT. Also shown is the behavior in a general case where $\bar{d}_{33}$ is a function of volume % PZT but to a lesser degree than d_{31}, and the case where both d_{33} and d_{31} are strictly a function of volume % PZT.

2. Procedure

Ninety weight percent PZT 501A* was mixed by hand in a plastic jar with a solution of 20 weight percent PVA and 80 weight percent water. After mixing the jar was tightly capped and put onto a ball mill rack and allowed to spin for 16 hours. The spinning helped to homogenize the batch. Further homogenization is done by extruding the batch through a 50 mm die several times. PZT rods are then extruded onto a moving glass plate. The rods are dried on the glass plates for ten hours at 120°C. Dried rods are cut into 3 cm lengths, laid on a platinum sheet and the binder is burned out at 550°C for 1/2 hour. Sintering takes place in a sealed alumina crucible at 1300°C for one half hour. A PbO vapor source of composition 97 mole % 501A and 3 mole % PbO is included in the crucible.[5]

In the larger extruded rods, porosity exists probably due to the multiple extrusions carried out to homogenize the batch before the final extrusion. To reduce this porosity, all sintered rods were re-fired in a hot isostatic press (HIP)[6] for one hour at 1300°C under a pressure of two hundred atmospheres of argon. Use of the HIP increases the average density

---

*Ultrasonics Powders, Inc., South Plainfield, NJ (PZT 501A).

of the rods from 7.45 to 7.7 - 7.8 gm/cc. Finished rods of diameters 840, 600, 400, 240 and 200 μm were made.

A fixture consisting of two brass discs in which an array of holes is drilled is used to align the rods. Several were made for each of the rod sizes so that composites of 50, 40, 30, 20 and 10 volume % PZT could be made. The polymer used in this work was an epoxy.* Once a rack had been filled with rods, the rack was placed in a plastic tube with two closed ends. The tube had a slot cut into one side so that the epoxy could be poured around the rods. To assure that complete investment of the rods by the epoxy would not be hindered by air bubles trapped between the rods, an apparatus was used which placed the plastic tube and its contents under vacuum while the epoxy was poured into the plastic tube. The epoxy was cured at 70°C for sixteen hours. Parts of thickness 1, 2, 3 and 4 mm were cut from the slug with a diamond saw. Some of these parts are seen in Figure 3. The excess epoxy around the composite was cut off so that only the composite volume remained.

Air dry silver electrodes were applied and the parts were poled in a 75°C oil bath with a field of 22 kv/cm for five minutes. Permittivity was measured at 1 KHZ. d_{33} was measured with a d_{33} meter** using the two rounded rams. The hydrostatic piezoelectric coefficient (d_h) was measured by changing pressure in an oil chamber at the rate of 500 psi/sec and collecting the charge with an electrometer in the feedback intergration mode which maintains nearly zero sample potential. Because of the possible influence of irreversible polarization and current effects, the values recorded are from many runs utilizing both increasing and decreasing pressure.

---

*Ernest F. Fullum, Inc., Schenectady, NY No. 5135
**Channel Products, Chesterland, Ohio, Model CPDT 3300.

3. Results and Discussion

According to the theory already described, d_{33} would not be a function of the volume fraction of PZT in the composite. This assumes an ideal situation in which the polymer phase is much more compliant than the PZT and that all the stress on the polymer phase is transferred to the PZT. That is, as the volume % PZT decreases, the pressure on the PZT increases proportionally so that the charge per unit area of the composite is constant. It is not necessary that d_{33} of the composite be constant with respect to volume % PZT for d_h to be enhanced in the composite. If, as the volume % PZT is decreased d_{31} decreases more rapidly than d_{33} , then d_h will be enhanced. Likewise, if $\bar{\varepsilon}_{33}$ decreases more rapidly than d_h, as the volume % PZT is decreased, then $\bar{g}_h$ will be enhanced.

3.1 d_{33} of the composites

In this work the following factors were varied: volume % PZT, diameter of PZT rods and sample thickness. The combination of the factors of rod diameter and volume % PZT brings in a fourth factor: the separation between the rods. Obviously, if the stress on the polymer is to be transferred to the PZT rods, the distance from a particular unit of load bearing polymer to the nearest rod is important. In the composites with the smaller rods at a fixed volume % PZT, the rods are much closer together. For this reason a point measurement of d_{33} on the composites should become more constant with respect to position on the composite surface at constant volume % PZT . Thus, if the rod diameter is decreased, the composite becomes more piezoelectrically homogeneous.

Figure 4.A shows that for volume fractions down to 40 volume % PZT the values of $\bar{d}_{33}$ are comparable to the value of d_{33} for solid PZT 501A of 400. Below 40 vol% PZT, the $\bar{d}$ values of all the composites decrease

but it is significant to note that the $\bar{d}_{33}$ of all the composites at 10 vol % are still greater than 220 c/N. If $\bar{d}_{33}$ had decreased strictly as a function of volume % PZT because the PZT rods were not bearing any part of the load on the polymer, the calculated $\bar{d}_{33}$ would be 10% of solid PZT or ~40 c/N. The method in which these $\bar{d}_{33}$ values were measured has somewhat effected the way d_{33} has varied as a function of volume fraction and rod diameter. The d_{33} meter measures the charge developed on a sample due to a stress from two rounded rams which stress the sample from the top and bottom. Whether or not the piezoelectric response of composites becomes more homogenous is hard to determine due to the size of these rounded rams with regard to the separation of the rods. If the rams are in physical contact with the rods then the force on the rods is transmitted directly by the ram and not to the rods via the polymer phase. It would not be justified to expect a similar $\bar{d}_{33}$ value when the composite is stressed hydrostatically by a fluid and a sizeable percentage of force (equal to the volume % of polymer) will fall directly on the polymer. For this reason the $\bar{d}_{33}$ values for lower volume fractions of PZT where the rams of the d_{33} meter may stress the polymer alone are probably closer to the true $\bar{d}_{33}$ of these composites. Each of the data points on Figure 4.A are an average of at least fifteen values measured at random over the electroded surface of the composite. The standard deviation of these values are shown in Figure 4.B. The piezoelectric response has indeed become more homogeneous as the rod diameters and the distance between piezoelectric elements are decreased. All the values shown in Figure 4 were measured on composites with a 4 mm thickness. The $\bar{d}_{33}$ of composites of 3, 2 and 1 mm thickness were also measured. A thickness effect was found. For all composites the $\bar{d}_{33}$ decreased as the composite thickness increased. This thickness effect was also a function of rod diameter and volume % PZT. $\bar{d}_{33}$ decreased as the separation between the rods increased.

3.2 d_h of the composites

In Figure 5, d_h is plotted as a function of composite thickness, rod diameter and volume % PZT. As was found with the measurements on the d_{33} meter, $\bar{d}_h$ is a function of composite thickness. This effect nearly disappears for the 400 micron rods. It should be noted that for most of the composites measured, regardless of composite thickness, rod diameter or volume % PZT, the $\bar{d}_h$ of the composite is greater than that for solid PZT 501A. PZT 501A pellets were cold pressed, sintered and fired in the HIP along with the rods used in the composites. An average $\bar{d}_h$ value of 30 - 32 c/N x 10^{-12} was measured on these pellets. Composites of the same PZT but with much lower volume fractions of PZT have higher values of d_h. The theory (Figure 2) predicted that $\bar{d}_{33}$ would be constant and that d_{31} would decrease linearly with the volume fraction PZT. If this were true, $\bar{d}_h$ would increase linearly as the value fraction of PZT was decreased. However, point probing indicates that $\bar{d}_{33}$ for all the composites decreased as the volume fraction of PZT decreased below 40 vol % PZT. If $\bar{d}_{31}$ decreased as the theory predicts and $\bar{d}_{33}$ decreased at a slower rate then d_h could either decrease, increase or be constant as the volume % PZT decreased. As shown by Figure 6, all of these occur. All the data in Figure 7 were measured on composites with a thickness of 4 mm. The composites of rods of 840 micron diameter show a decrease of $\bar{d}_h$ as volume % PZT decreases. From a volume fraction of 0.4 to a volume fraction of 0.1 its volume % PZT has decreased 75% but the $\bar{d}_h$ has decreased only 50%. For the composites of 600 micron rods $\bar{d}_h$ is nearly constant from 50 vol % down to 20 vol %. The composites of 400 micron rods actually show an increase of $\bar{d}_h$ going from 50 vol % down to 20 vol %. Although $\bar{d}_h$ at 10 vol % is the lowest for all the rod sizes these composites shown the largest increases in $\bar{d}_h$ with each reduction in rod

diameter. It appears that if the rod diameter could be further reduced, the 10 vol % composite would eventually have the greatest d_h. That the composite with the lowest volume fraction of PZT would have the highest $\bar{d}_h$ is predicted by the theory but the magnitude of the experimental $\bar{d}_h$ value are less than one third theoretical value. It must be remembered that the theory called for a phase 2 which was much more compliant than phase 1. As the epoxy is a stiff polymer, better agreement with the theory should be found when an elastomer is used as the phase two.

3.3 Effects on ε_{33} and g_h

The calculation of ε_{33} uses the equation for two capacitors in parallel and the value of $\bar{\varepsilon}_{33}$ varies linearly with the volume fractions of the two phases present. Since ε of the PZT is $\sim$1600 and that of the epoxy is $\sim$7, the value of $\bar{\varepsilon}_{33}$ may be approximated as 1600 x volume % PZT. The experimetal values of ε_{33} agree with calculated levels, as shown by Figure 7. Since $\bar{g}_h$ equals $\bar{d}_h$ divided by $\bar{\varepsilon}_{33}$, constant or increasing values of $\bar{d}_h$ with decreasing volume % PZT result in large increases in the value of g_h. Figure 8 is a plot of the $\bar{g}_h$ for the data shown in Figures 6 and 7. The dotted line in Figure 8 represents the $\bar{g}_h$ of solid PZT 501A. The 10 vol % composite of 254 micron rods has a $\bar{g}_h$ of better than twenty-five times that of the solid PZT. Although use of a more compliant matter would not appreciably affect ε_{33}, its enhancement of $\bar{d}_h$ would naturally cause a corresponding increas in $\bar{g}_h$.

Conclusions

1. A technique has been developed for fabrication of composites of extruded PZT rods and an epoxy matrix. These composites have 3-1 connectivity.

2. The values of $\bar{d}_h$ and $\bar{g}_h$ of such a composite have been found to be a function of the diameter of the PZT rods, the spacing between the PZT rods and the thickness of the composite.

3. $\bar{d}_h$ and $\bar{g}_h$ are probably also a function of the difference in the mechanical compliances of the PZT and the epoxy.

4. Composites with high values of $\bar{d}_h$ and $\bar{g}_h$ have bulk densities of less than 1.8 gm/cc.

5. Composites have been developed with a $\bar{d}_h$ three times that of PZT 501A and a $\bar{g}_h$ at least twenty-five times greater.

References

1. W. Harrison. Proceedings of the Workshop on Sonar Transducer Materials. Edited by P. Smith and R. Pohanka, Naval Research Laboratory, Washington, DC, 1976, pp. 257-268.

2. D.P. Skinner. Diphasic Piezoelectric Transducers. Ph.D. Thesis, The Pennsylvania State University, 1980.

3. R.E. Newnham, D.P. Skinner and L.E. Cross. Connectivity and Piezoelectric-Pyroelectric Composites. Mat. Res. Bull. 13, 525 (1978).

4. D.P. Skinner, R.E. Newnham and L.E. Cross. Flexible Composite Transducers. Mat. Res. Bull. 13, 599 (1978).

5. K.A. Klicker. Control of PbO Partial Pressure During the Sintering of PZT Ceramics. M.S. Thesis, The Pennsylvania State University, 1979.

6. L.J. Bowen, W.A. Schulze and J.V. Biggers. Hot Isostatic Pressing of Lamellar Heterogeneous Piezoelectric Devices. Electronics Division and IEEE Ferroelectrics Subcommittee, Fall Meeting, Dallas, TX, Sept. 1978.

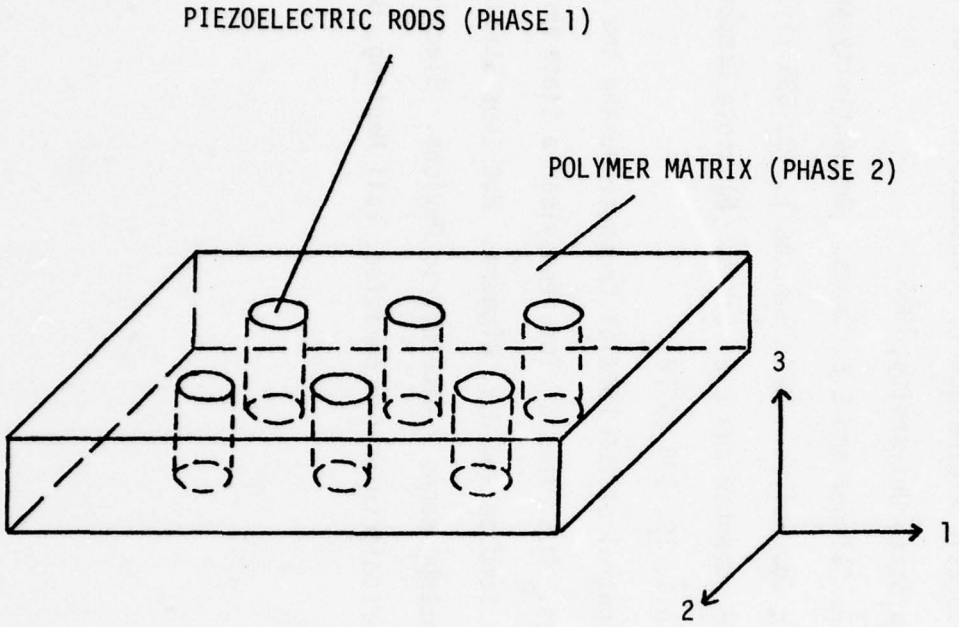

FIGURE 1. A COMPOSITE WITH 3-1 CONNECTIVITY.

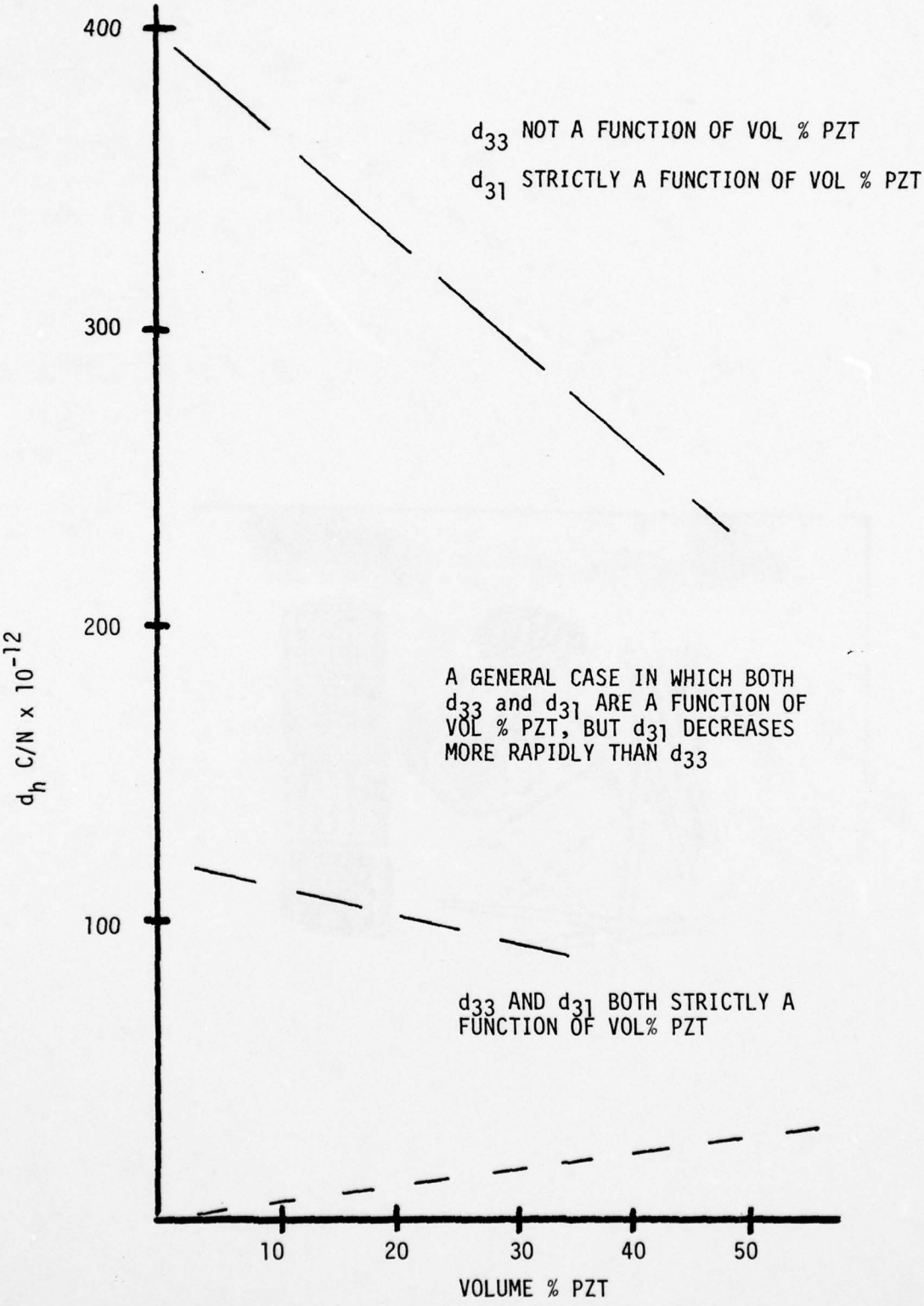

FIGURE 2. d_h AS A FUNCTION OF VOLUME % PZT, ASSUMING SEVERAL RELATIONS OF d_{33} and d_{31} TO VOLUME % PZT.

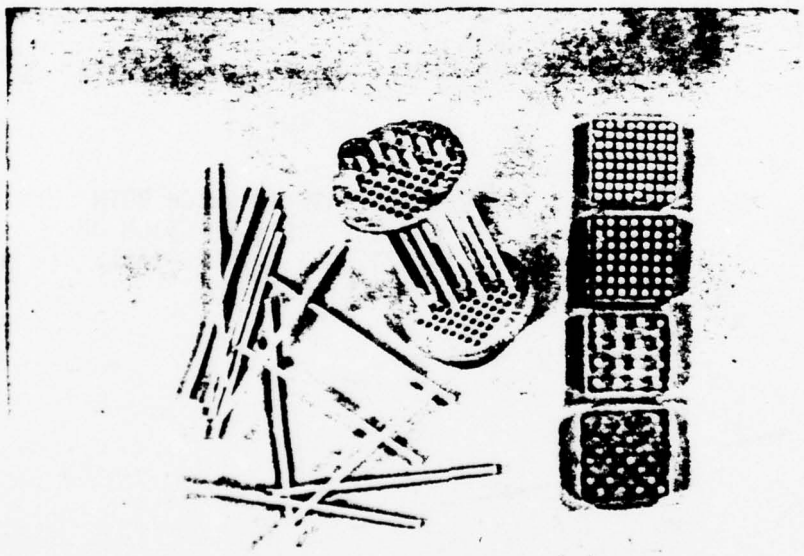

FIGURE 3. FIXTURE USED TO ALIGN RODS FOR INVESTMENT IN EPOXY AND COMPOSITES WHICH HAVE BEEN SLICED FROM THE CURED SLUG.

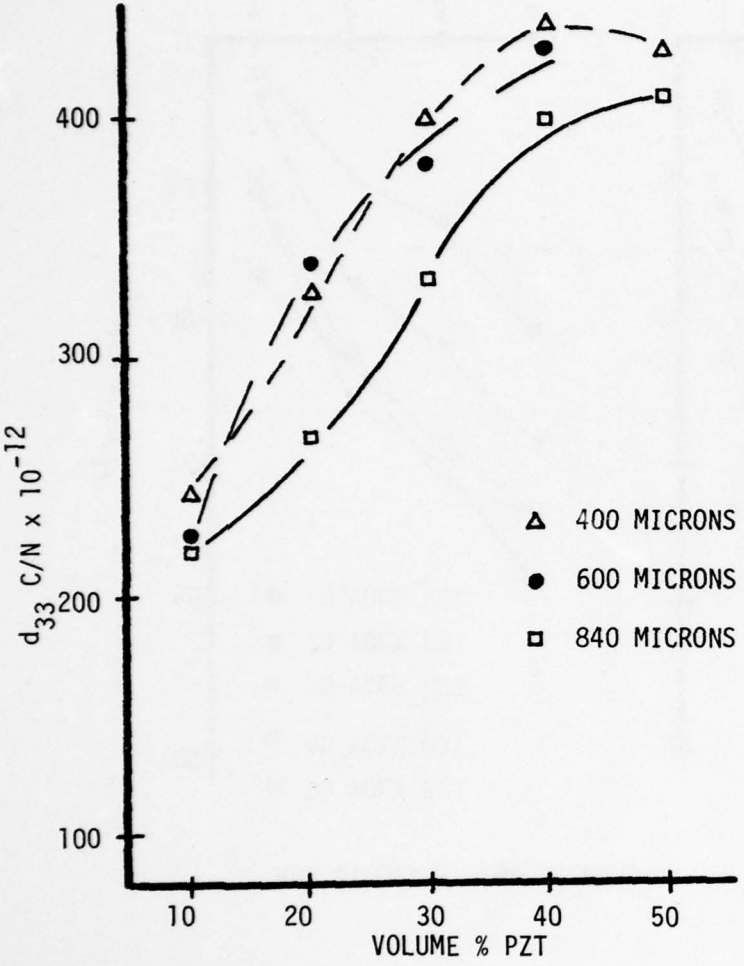

FIGURE 4A. d_{33} VS VOLUME % PZT.

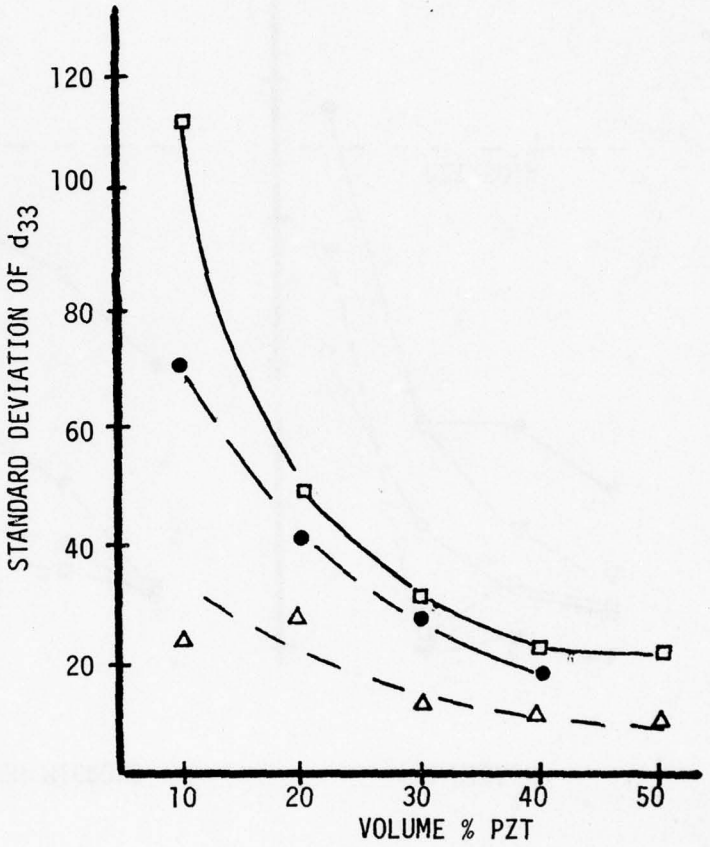

FIGURE 4B. STANDARD DEVIATION OF d_{33} VALUES AS A FUNCTION OF VOLUME % PZT.

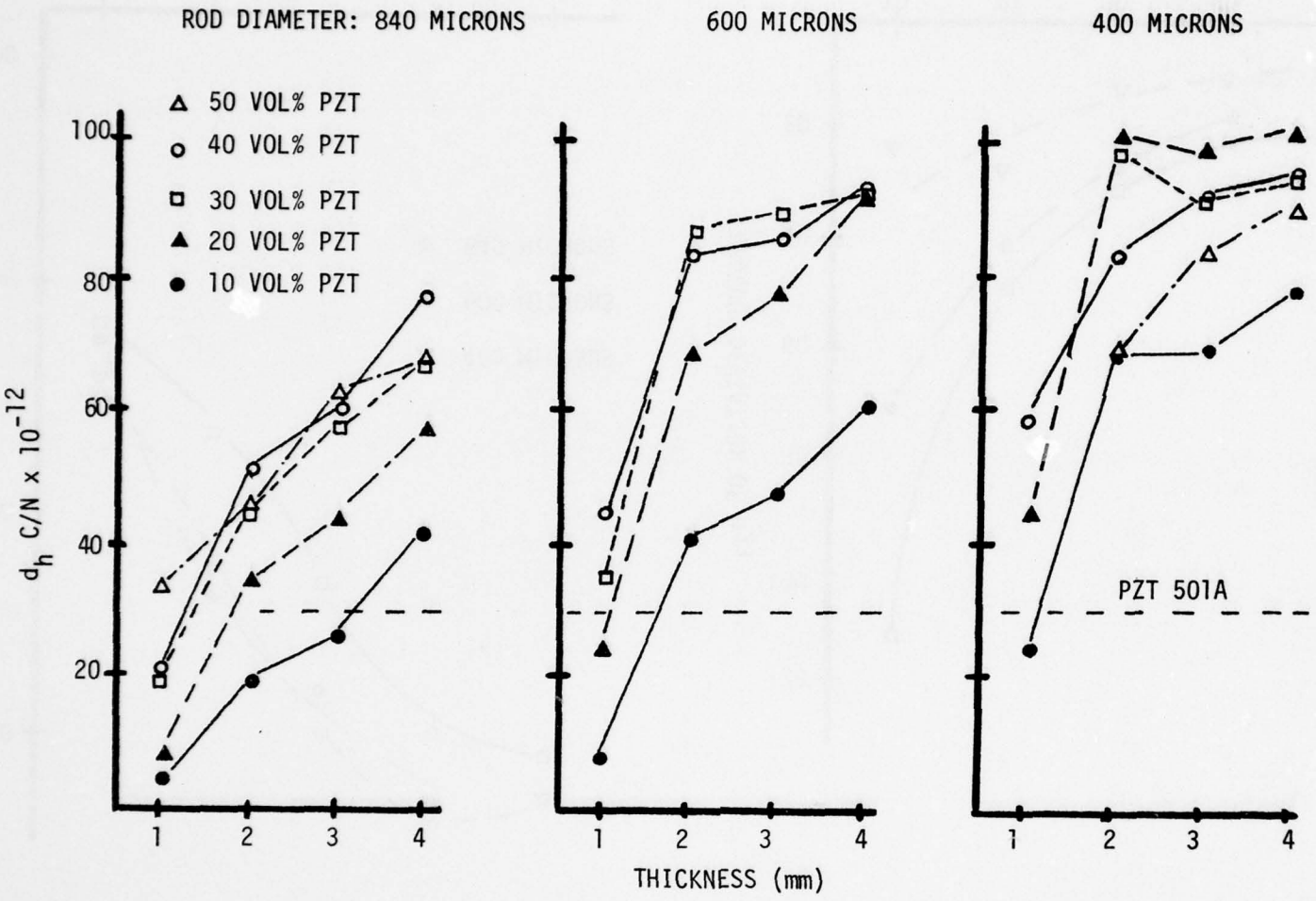

FIGURE 5. d_h AS A FUNCTION OF VOLUME % PZT, ROD DIAMETER AND COMPOSITE THICKNESS.

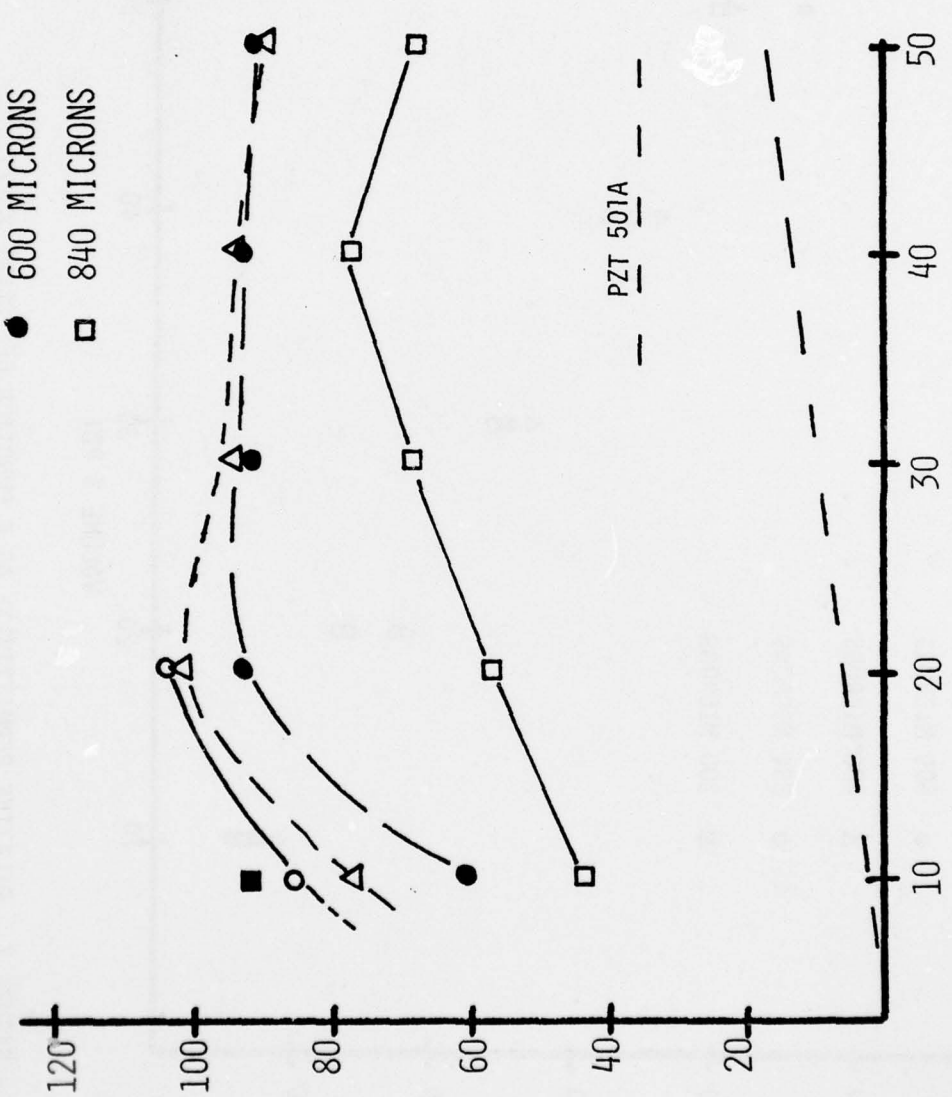

FIGURE 6. d_h AS A FUNCTION OF VOLUME % PZT AND ROD DIAMETER.

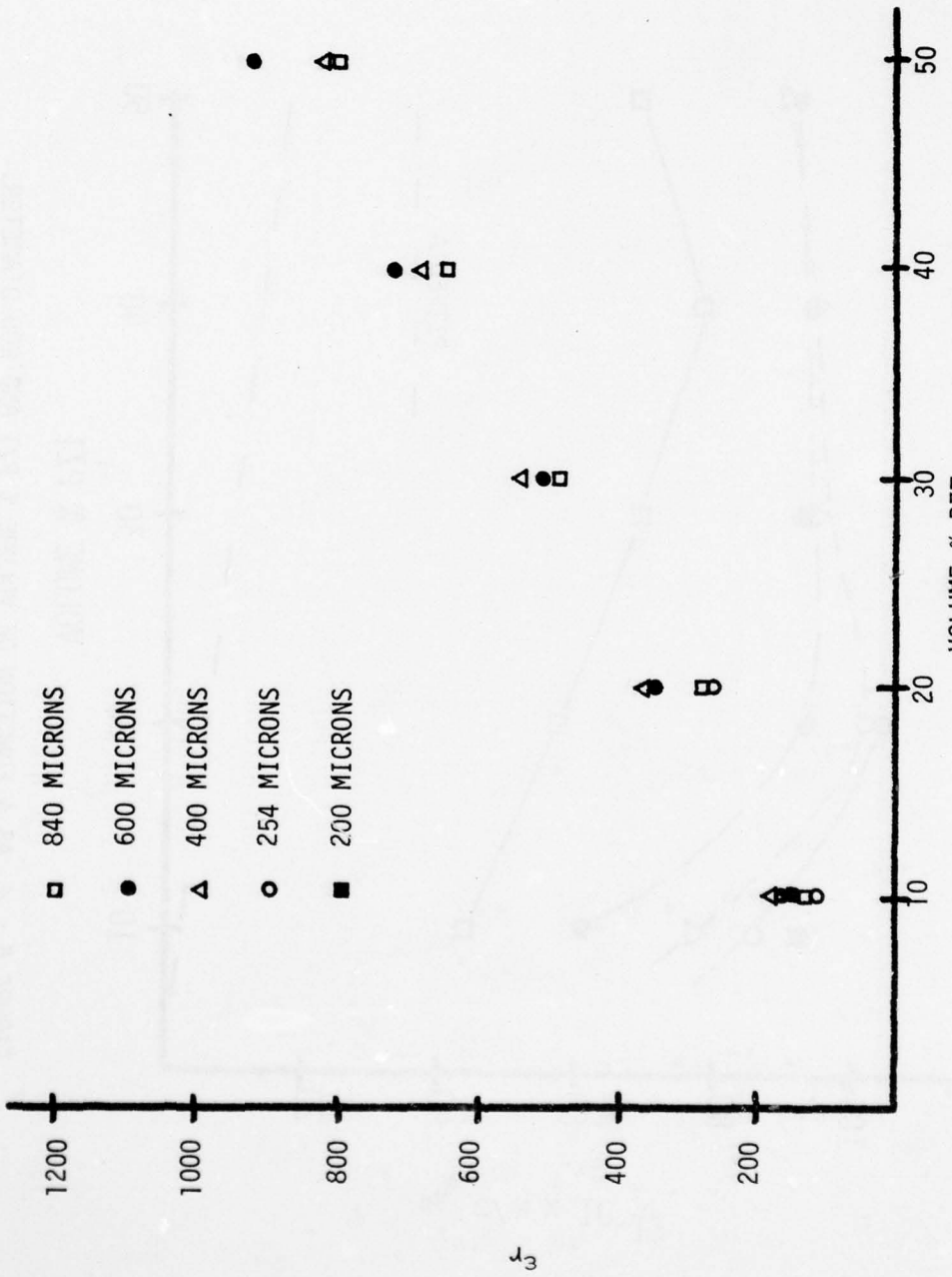

FIGURE 7. RELATIVE PERMITTIVITY AS A FUNCTION OF VOLUME % PZT.

AD-A079 400 PENNSYLVANIA STATE UNIV UNIVERSITY PARK MATERIALS RE--ETC F/G 9/1
TARGETED BASIC STUDIES OF FERROELECTRIC AND FERROELASTIC MATERI--ETC(U)
DEC 79 L E CROSS , R E NEWNHAM , G R BARSCH N00014-78-C-0291

UNCLASSIFIED NL

3 OF 4
AD A 079400

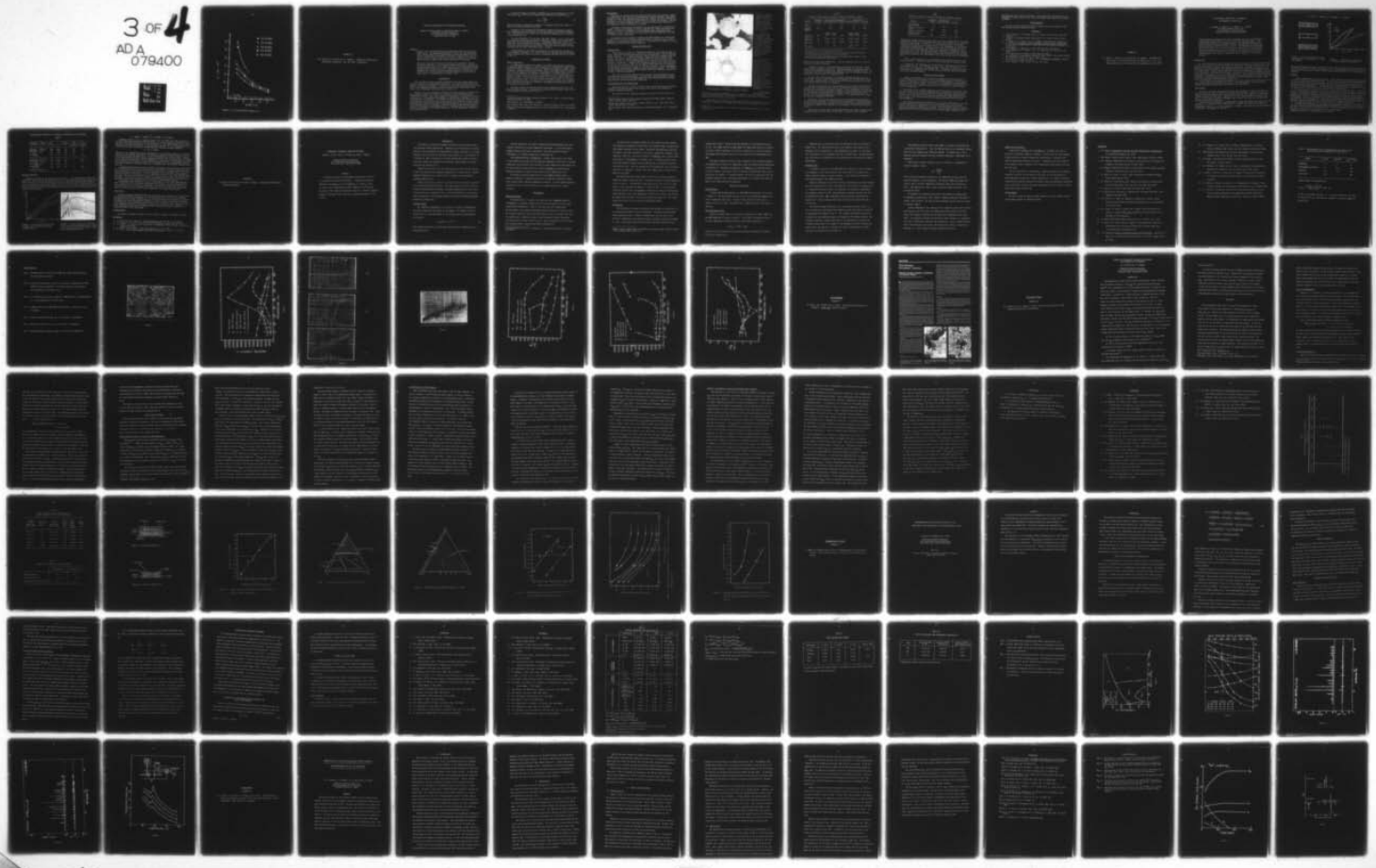

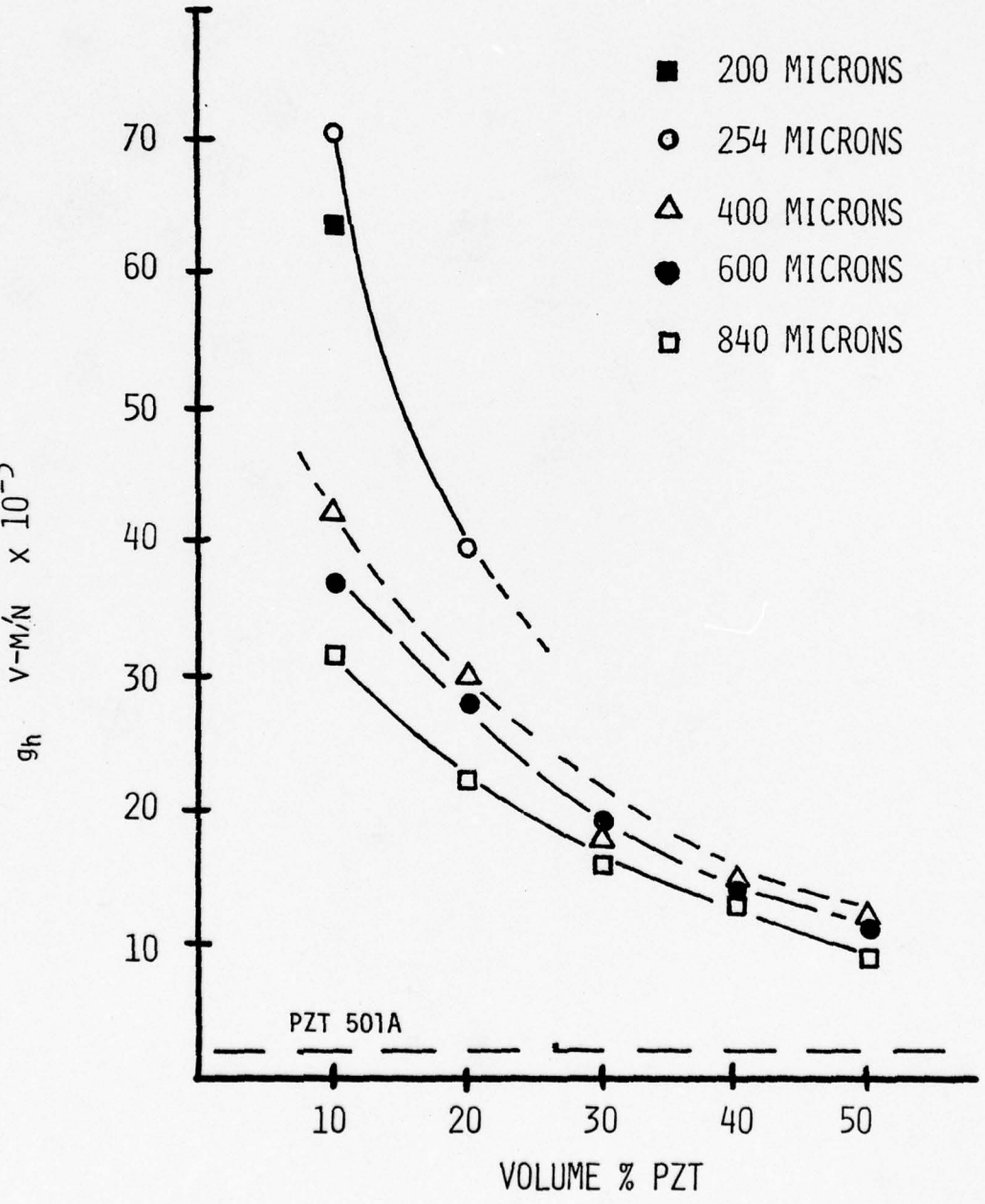

FIGURE 8. g_h AS A FUNCTION OF VOLUME % PZT.

APPENDIX 12

T.R. Shrout, W.A. Schulze and J.V. Biggers. Simplified Fabrication of PZT/Polymer Composites. Mat. Res. Bull. (submitted).

SIMPLIFIED FABRICATION OF PZT/POLYMER COMPOSITES

Thomas R. Shrout, Walter A. Schulze and James V. Biggers
Materials Research Laboratory
The Pennsylvania State University
University Park, PA 16802

ABSTRACT

Skinner, et al. prepared PZT/polymer composites using the coral replamine process. The composites were found to have, for certain applications, greatly improved electromechanical and physical properties over those of conventional piezoelectric materials. However, the coral replamine process requires natural coral from the ocean as the starting replica material, making this process industrially unfavorable.

This paper discussed PZT/polymer composites electromechanically and physically comparable to the Skinner replamine composites. Fabrication is simplified by the use of a compacted mixture of volatilizable plastic spheres and PZT powder, which when sintered yields a piezoelectric with a density of less than 2.9 g/cm^3, a permittivity of $\sim$120 and a d_{33} of 180×10^{-12} C/N. The improved connectivity increases d_h (hydrostatic) from $\sim 35 \times 10^{-12}$ C/N (solid PZT) to 100×10^{-12} C/N.

Introduction

Over the past few years, several researchers (1-5) have looked toward composites to improve electromechanical properties over those of present-day homogeneous piezoelectric materials. Specifically, we looked toward developing a composite with improved properties for use as a passive electromechanical transducer, e.g. hydrophones, medical acoustic devices, etc.

Skinner, et al. (1) developed a flexible PZT (lead zirconate titanate) polymer composite transducer in which the two phases formed interpenetrating 3-dimensional networks. This form of diphasic connectivity is referred to as a 3:3 structure (6). The composite was designed to take maximal advantage of the useful properties of each phase. The resultant composite had a low density for improved acoustic coupling to water or human tissue, was compliant to better resist mechanical shock and provide high damping (low mechanical Q), and could be flexible (depending on type of polymer). Flexibility offers the interesting possibility of fabricating a conformable detector. Most importantly, the composite was found to exhibit a very large piezoelectric voltage coefficient referred to as the g-coefficient.

The g-coefficient is defined in equation [1] as the piezoelectric strain coefficient d_{ijk} divided by the appropriate permittivity coefficient ϵ_{ij}.

$$g_{ijk} = \frac{d_{ijk}}{\epsilon_{ij}} . \qquad [1]$$

The g-coefficient as reported by Skinner, is commonly used as the "Figure of Merit" for passive sensing transducers.

Skinner, et al. prepared the PZT/polymer composites uitlizing a complex coral replamine process developed for the fabrication of prosthetic materials (7). This process is not likely to be industrially feasible and has problems in reproducibility (8).

It was the intention of this work, and other authors (4,5) to fabricate 3:3 connected PZT/polymer composites by utilizing a simpler fabrication technique than the coral replamine process. PZT/polymer composites, having 3:3 connectivity, were fabricated by sintering compacted mixtures of burnable (volatilizable) plastic spheres and PZT powder. The highly porous ceramic body produced can then be vacuum impregnated with a polymer.

Electromechanical and physical properties were measured and compared to those reported by Skinner (1,8). Materials and certain experimental procedures used by Skinner were chosen to justify a comparison (details can also be found in Ref. 8).

Experimental Procedure

Sample Preparation

A commercially available PZT powder[1] was thoroughly mixed with polymethyl methacrylate (PMM)[2] spheres in a 30/70 volume ratio. PMM spheres ranged between 50 and 150 microns in diameter and the PZT powder size range was between 1 and 4 microns. One-inch pellets were pressed, using a few weight percent polyvinylalcohol for enhancing green strength. The pellets were heated slowly to 400°C over a 12-hour period to volatilize the PMM spheres. A slow heating rate is needed to prevent excessive cracking. Sintering was done in closed high-purity alumina crucibles. The pellets were placed on Pt foil and lead zirconate was added as a source of PbO. A silicon carbide resistance furnace with a programmable controller was used, the heating rate being 200°C/hr with a soak temperature of 1305°C for a period of 0.5 hours. The samples were allowed to cool in the furnace with power off.

The highly porous pellets were easily vacuum impregnated with two of the polymers used by Skinner. A high-purity silicone rubber elastomer[3] and a stiff vinylcyclohexene dioxide epoxy[4] were used.

---

[1]Ultrasonic Powder PZT-501A, Ultrasonics Powders, Inc., 2383 S. Clinton Avenue, South Plainsfield, NJ 07080.

[2]Polysciences, Inc., Warrington, PA 18976.

[3]Dow Corning's MDX-4-4210, Dow Corning Co., Medical Products, Midland, MI 48640.

[4]Spurrs Low-Viscosity Embedding Media, No. 5135, Polysciences, Inc., Warrington, PA 18976.

Measurements

Electrodes of sputtered on gold and/or air-dry silver were applied. Dielectric permittivity and loss (tan δ) were measured using an automatic capacitance bridge[5] at 1 KHz. The composites were poled in a stirred oil bath at 80-90°C by applying a dc field ranging from 15-30 Kv/cm for at least five minutes. The completeness of poling was checked after 24 hours by measuring the piezoelectric d_{33} coefficient using a Berlincourt d_{33} meter[6].

Hydrostatic piezoelectic coefficient, d_h, was determined by a pseudostatic method. Pressure was changed at a rate of 500 psi/sec., while charge was collected by a Keithly Electrometer[7] in the feedback charge integration mode. Piezoelectric d_{33}, d_h and dielectric permittivity were also measured for flexed PZT/silicone rubber composites.

A resonance testing apparatus, based on the IRE Standards on Piezoelectric Crystals (9), was used to measure electromechanical coupling factors, Young's Modulus, and the mechanical quality factor Q. Measurements were made on both the PZT/Spurrs and PZT/silicone rubber materials.

Results and Discussion

Microstructure

Typical SEM micrographs of a PZT/Spurrs composite can be seen in Figs. 1a and b. This microstructure also typifies the microstructure of the PZT/silicone rubber composite. It is clearly seen that the two phases are randomly interconnected. The size of the PZT phase regions ranged from a few microns to 100 microns, whereas the polymer regions ranged from 20 to 120 μm and were quite spherical in nature. The interconnecting polymer regions could range from a few microns to 100 microns. Skinner's PZT replamine microstructure analysis showed a much more open structure with the PZT regions being about 200 μm in diameter and the polymer regions in the order of 500 μm in diameter. Vacuum impregnation of the polymer was complete, leaving no noticeable porous regions. The ability to apply large poling fields >30 Kv/cm before dielectric breakdown is also indicative of complete impregnation.

The finer 3:3 diphasic composite should exhibit more homogeneous electromechanical and physical properties. In other words, properties would be less area sensitive to location of measurement and allow the fabrication of thinner devices before deviation from bulk properties.

Electromechanical and Physical Data

Properties reported in Table 1 present direct comparisons between Skinner's replamine composites and those fabricated in this work to the homogeneous PZT-501A transducer material.

The densities of the composites fabricated in this work were found to be

---

[5]Hewlett Packard (Model 4270A) Automatic Capacitance Bridge, Hewlett Packard 1-59-1 Yoyogi, Tokyo, Japan 151.

[6]Berlincourt (Model 333) D_{33} Meter, Channel Products, Inc., 16722 Park Circle Drive, Chagrin Falls, OH 44020.

[7]Keithly (Model 616) Digital Electrometer, Keithly Instruments, Inc., Cleveland, OH.

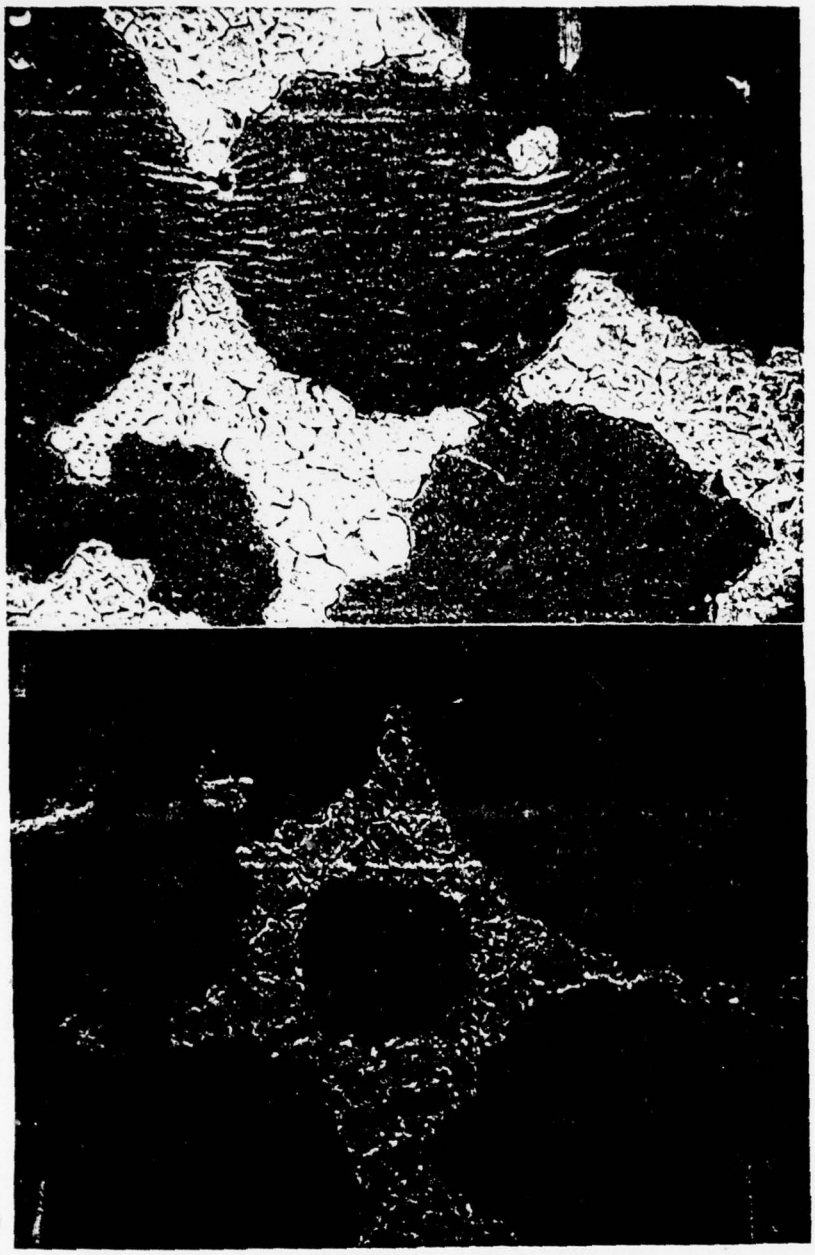

(a)

(b)

FIG. 1

Photomicrographs of PZT/Spurrs Composite (1000X).

lower (2.7 g/cc) than the replamine composites (3.3 g/cc). This should further improve acoustic impedance matching to water or body tissue over that of homogeneous PZT materials.

Elastic compliances were not reported for the replamine composites, but would be similar to those reported in this study. The composites, being much more compliant than the stiff PZT ceramic, would both be more resistant to mechanical shock.

The replamine composites were reported to exhibit dielectric breakdown strengths less than 20 Kv/cm, whereas the present composites break down at 25-30 Kv/cm. The lower breakdown strength is believed to be accredited to imcomplete vacuum impregnation brought about by the complex nature of the replamine fabrication technique.

It was expected that since the PMM composites contained the highest amount of polymer[8], they should have the lowest permittivities (10). This was not found to be the case. No reasonable explanation can be given at this time.

Piezoelectric d_{33} coefficients varied little between the replamine and PMM composites. Variations in d values were primarily due to breakage of ceramic

[8]Dielectric permittivities of the silicone rubber and Spurrs epoxy were 3 and 6, respectively.

TABLE 1

Comparison of Electromechanical and Physical Properties of PZT/Polymer Composites.

property	homogeneous PZT/501A[1]	Skinner's Replamine Composites PZT/Silicone Rubber		PZT/Spurrs	PMM Composites PZT/Silicone Rubber		PZT/Spurrs
density (g/cm^3)	7.9	3.3		3.3	2.8		2.8
dielectric breakdown (Kv/cm)	30-40	15-20		15-29	>25		25-35
		unbroken	broken		unbroken	broken	
dielectric constant (k)	2000	∿100	∿40	∿100	100-200	40-100	110-250
piezo d_{33} ($x10^{-12}$ C/N)	400	120-180	90-100	140-160	160-240	80-100	60-110
g_{33} ($x10^{-3}$Vm/N)	20	135-200	∿280	160-180	112-220	90-230	60-112
g_h ($x10^{-3}$Vm/N)	4	---	∿30[3]	---	190[4] 50-70	15-25	∿40

[1]Ultrsonic Powder, Inc., "Piezosonic Powders" data sheet.

[2]Unbroken PZT/silicone rubber composites before the 3:3 connectivity was disrupted (broken).

[3]The g_h-hydrostatic coefficient measured at 82 psi (reference 8).

[4]The g_h value recorded at applied pressures up to 500 psi before partial disruption of connectivity, and lower g_h values at higher pressures.

connections during sample preparation. This was especially true for the soft PZT/silicone rubber composites.

A thickness effect on electromechanical properties was indicated on PZT/Spurrs samples prepared in this work. Samples prepared for resonance, being (<0.08 cm) had degraded properties as compared to thicker samples (0.2 cm). It is believed that when the sample size approaches that of individual phases, the composite no longer depicts a homogeneous body.

The most important parameter for a passive receiver material is the g coefficient. The g_{33} values reported were computed from the measured d values and from the permittivities. The g values for PZT/silicone rubber were found to be similar for both types of composites.

Skinner found that when the ceramic connectivity was broken (flexible PZT/silicone rubber composites) the d values decreased less rapidly than did the permittivity, resulting in improved g values. Little improvement was found for the PMM prepared PZT/silicone rubber composites. Upon breaking the connectivity, the permittivity was only reduced by a factor similar to the reduction in d values. The g_{33} values remained on the order of 5-10 times larger than listed g_{33} values of homogeneous PZT-501A.

Hydrostatic g values were reported only for the flexible replamine PZT/silicone rubber composites. When a hydrostatic pressure of 82 psi was applied, the g_h value dropped from an initial value of $100x10^{-3}$ Vm/N to $30x10^{-3}$Vm/N due to an increase in permittivity induced by a closing-up of the interrupted connectivity.

Hydrostatic g values found for flexible PZT/silicone rubber composites fabricated in this work were from $15-25x10^{-3}$Vm/N. Values of g_h for unbroken

TABLE 2

Comparison of Physical and Electromechanical Properties Determined by Resonance.

property	homogeneous PZT-501A[1]	PMM composites PZT/Silicone Rubber	PZT/Spurrs
Young's modulus Y^E_{33} ($\times 10^{+10} N/M^2$)	6.8	0.25	1.3
thickness coupling coef. k_T (%)	~60	25-30	17-23
mechanical Q (thickness)	~70	10-15	16-25
frequency constant $N_{thickness}$ (Hz·m)	~2100	530-550	1050

PZT/silicone rubber composites were found to be nearly 200×10^{-3} Vm/N for applied pressures up to 500 psi. Pressures greater than that reduced the g_h values to around $50\text{-}70 \times 10^{-3}$ Vm/N. This was due to a partial breaking of the ceramic connectivity accredited to the high pressure. This phenomenon was verified by a reduction in permittivity. Hydrostatic g values for PZT/Spurrs composites were around 40×10^{-3} Vm/N and were found to be insensitive to pressure. Due to lack of g_h data on the replamine PZT/polymer composites, a reasonable comparison could not be made. The important point is that g_h values for all the PMM-PZT/polymer composites were considerably higher than the g_h value of homogeneous PZT.

Table 2 lists resonance data for PMM-PZT/polymer composites and the homogeneous PZT-501A. Skinner was unable to measure reliably any resonance data.

As expected, the compliance of the PZT/polymer composites was much higher than homogeneous PZT. The thickness coupling factor (k_t) was reduced by a factor of 2-3, as predicted in Reference (11). Mechanical Q values were found to be quite low, suggesting that the PMM composite material may be applicable with little external damping.

Summary and Conclusions

PZT/polymer composites were found to be comparable to those produced by Skinner while being fabricated by a relatively simple process. The process involved the sintering of compacted mixtures of volatilizable poly methyl methocrylate spheres and PZT powder. This process is industrially more feasible, as compared to the coral replamine process, for the production of passive piezoelectric transducers.

The reduced scale of these composites and the possibility of further reductions allow the use of composite piezoelectrics in thinner or higher frequency devices. The low density and natural low Q suggest that these composite materials may be used both in water and medical ultrasound applications with much less or none of the impedance matching and damping necessary with solid PZT active elements.

The improved hydrostatic sensitivity of the flexible PMM composite over the replamine material is encouraging, but the degradation of g_h with pressure found in both systems suggests that the high compliance (which allows rupture of the active phase)may be inherently unstable. The Spurrs/PZT composites, however, suggest that by varying the compliance of the organic phase a rigid but more

sensitive material could be fabricated. This would allow the production of a hydrophone of simple geometry that should be lighter and tougher than existing equipment.

Acknowledgement

We wish to thank the Office of Naval Research for their support of this work through Contract N00014-78-C-0291.

References

1. D. P. Skinner, R. E. Newnham, and L. E. Cross, Mat. Res. Bull. 13, 599 (1978).
2. R. Capek, "Multilayer Ceramic Capacitors," U.S. Patent 3,549,415 (Dec. 1970).
3. T. Shrout, W. A. Schulze, and J. V. Biggers, Ferroelectrics (submitted).
4. W. Harrison, Proceedings of the Workshop on Sonar Transducer Materials; P. Smith and R. Pohanka (Eds.), Naval Research Laboratory, Washington, DC (Feb. 1976).
5. M. Miyashita, K. Takano and T. Todo, Ferroelectrics (accepted).
6. R. E. Newnham, D. P. Skinner, and L. E. Cross, Mat. Res. Bull. 13, 525 (1978).
7. R. A. White and E. W. White, Science 176, 922 (1972).
8. D. P. Skinner, "Piezoelectric Composites," PhD Thesis, Solid State Science, The Pennsylvania state University (Nov. 1978).
9. B. Jaffe, W. R. Cook, Jr., and H. Jaffe, Piezoelectric Ceramics, Academic Press, London and New York (1971).
10. D. R. Biswas, J. Amer. Ceram. Soc. 61, 461 (1978).

APPENDIX 13

L.J. Bowen, T. Shrout, W.A. Schulze and J.V. Biggers. Piezoelectric Properties of Internally Electroded PZT Multilayers. Proc. Int. Symp. Applications of Ferroelectrics, Minneapolis, MN, June 1979.

PIEZOELECTRIC PROPERTIES OF INTERNALLY ELECTRODED PZT MULTILAYERS

L.J. BOWEN, T. SHROUT, W.A. SCHULZE, J.V. BIGGERS
Materials Research Laboratory
The Pennsylvania State University
University Park, Pennsylvania 16802

Platinum internal electrodes have been introduced into PZT compositions in a multilayer configuration by a conventional tape casting process. Electrical property data for the devices suggest that the piezoelectric coefficients of the multilayer configuration are approximately 20% lower than those of similar plain PZT devices. However, the applied voltage/displacement ratio is much lower in the multilayer compared to the plain devices. Resonant properties are almost unaffected by the presence of internal electrodes for hard PZT compositions. Piezoelectric transformers with multilayer primaries show improved transformer ratios compared to conventional devices.

INTRODUCTION

For electromechanical transducer applications, materials in the lead zirconate-lead titanate solid solution series are widely used because of their high piezoelectric coefficient and favorable chemical and mechanical properties. Although electrical driving conditions for PZT transducers vary depending on their composition and dimensions, for most applications a high driving voltage is required and consequently impedance matching can be difficult. Attempts have been made[1] to overcome this problem by bonding together electroded piezoelectric discs with organic adhesive to form internally electroded macrocomposites. Although success has been obtained in some applications using this approach it should be possible using existing multilayer capacitor technology to produce composites with improved electromechanical properties.

In this paper we investigate the effect of cofired internal electrodes on both resonant and displacement piezoelectric devices. The modifications result in greatly reduced operating voltages and in increased device capacitance.

EXPERIMENTAL

The basic electrode configuration used in the piezoelectric devices is shown in Fig. 1a and is the same as that used in multilayer capacitors. In such a device the poling of alternate layers is of opposite direction, but the responses are additive in either a driven or driver mode. Figure 1b is a plain device used as a control, and Fig. 1c is an exposed electrode "sandwich" used to test for effects of internal electrodes on electrical properties.

The devices were prepared by standard tape casting techniques using commercial PZT powder[a] and a commercial doctor blade media[b].[2] Internal electrodes were applied by

[a]Ultrasonic Powders, Inc., South Plainfield, NJ 07080. Type 501A soft and 401-888 hard.
[b]Cladan Inc., San Diego, CA, type B42.

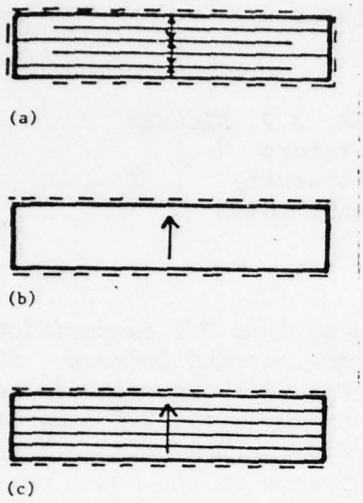

FIGURE 1. Device configurations under investigation (a) multilayer; (b) plain (c) sandwich.

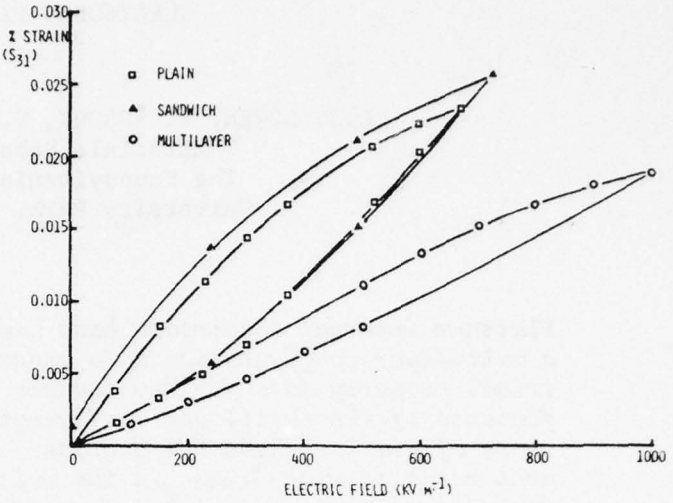

FIGURE 2. Strain/electric field data for devices prepared from 501A PZT.

screen printing platinum ink[c] onto the dried cast tape. Standard PZT firing techniques, described elsewhere,[3] yielded a 95% dense product, although some specimens fired in a hot isostatic press under 20 MNm^{-2} argon pressure had densities near to the theoretical maximum.

RESULTS

Table I summarizes the electrical data. Some reduction in permittivity was noted in the internally electroded structures. In the case of the multilayer devices this may be due to errors in the estimated active electrode area, although it is possible that increased porosity may have been present in the internally electroded devices which would lower the permittivity.[4] The piezoelectric coefficient d_{33} as measured on a Berlincourt meter[d] is affected only in the multilayer configuration.

The strain/field characteristics for the "soft" PZT are shown in Fig. 2. The electrodes in the sandwich structure act only as equipotential planes and have no effect on strain. The multilayer capacitor configuration, by its nature of two separate electrode systems and insulated electrode edges, has areas of inactive ceramic that can reduce displacement. Figure 3 illustrates this clamping effect by comparing displacements in the center of the active region to a partially clamped edge. Even though the strain is somewhat reduced by clamping, the voltage required to achieve an equivalent strain for the five layer test device is only one-third that of a solid ceramic part.

To demonstrate feasibility of a multilayer displacement transducer, a 100 layer device was constructed from PZT 401-888 (lower hysteresis than 501A) and driven through d_{33}. For this 25 mm long device a displacement of 4.5 μm was achieved with only 200 volts.

[c]Englehard Industries, East Newark, NJ 07029, Type E-305-A.
[d]Channel Products, Inc., Chagrin Falls, OH 44022.

TABLE I

Specimen Configuration	Poling Conditions	K (1 kHz, Low Field)	tan δ	d_{33} $CN^{-1}x10^{-12}$	d_{31} $CN^{-1}x10^{-12}$ (Low Field)	Q_M (Longitudinal Mode)
501A plain	3000 KV m^{-1}	1800	0.015	470	240	29
501A sandwich	2 minutes	1550	0.015	450	240	31
501A multi-layer*	100°C	1500	0.036	360	210	--
501A commercial data		2000	0.014	400	175	80
401-888 plain	2500 KV m^{-1}	936	0.002	295	--	397
401-888 sandwich	10 minutes	911	0.002	270	--	562
401-888 multi-layer*	125°C	794	0.003	210	--	--
401-888 commercial data		1000	0.003	215	95	1000

*Active area approximated

RESONANT PROPERTIES

Mechanical quality factor, Q_m, is listed in Table I. The experimental values were found to be lower than the manufacturer's values. This discrepancy may have arisen from differences in the ceramic processing and/or from differences in measuring technique, since the commercial data are from radial mode resonance, whereas the present data are from the fundamental longitudinal mode resonance of thin bars. When density effects were eliminated by hot pressing, PZT 401-888 material had a Q_m of 600 for both the plain and sandwich configurations.

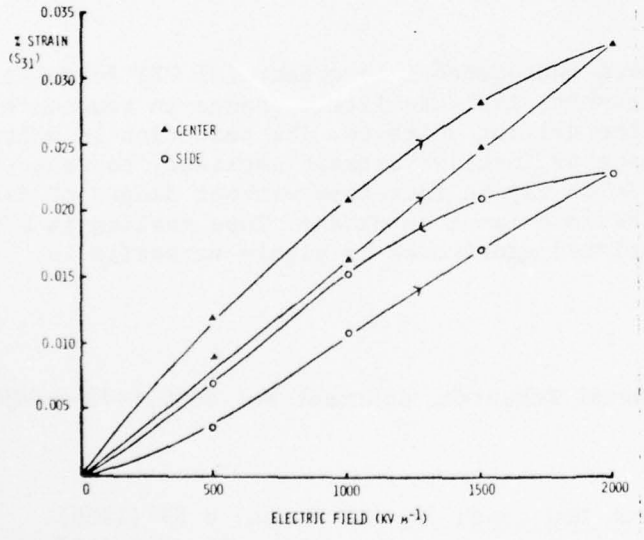

FIGURE 3. Strain/electric field data for 501A PZT illustrating the edge clamping effect.

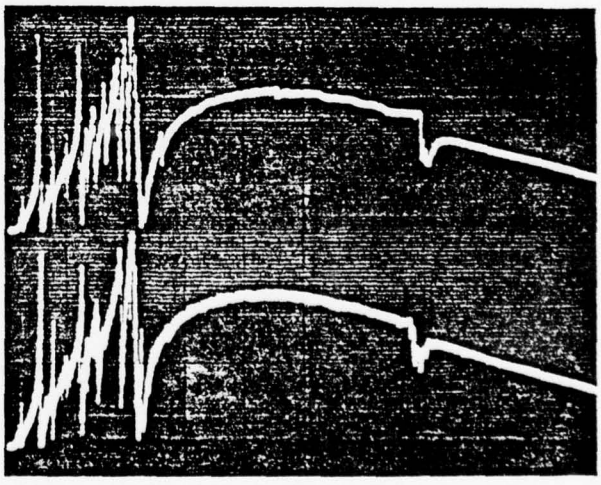

FIGURE 4. Resonance spectra for 401-888 PZT (horizontal scale 1MHz/division). Upper trace: plain material. Lower trace: internally electroded material.

Resonance spectra over a frequency range of 0.1 to 10 MHz show little difference for the control and internally electroded bars, the least variation occurring in composites of the high Q_m material, PZT 401-888 (Fig. 4). An understanding of the lack of influence of internal electrodes on the frequency constant, N, of a piezoelectric resonator can be better attained by considering the classical resonance equation:

$$N = f_r L \approx 1/2\sqrt{\rho S}$$

where f_r is the fundamental resonance frequency, L the governing dimension, ρ the density, and S the elastic compliance. The alternate metal and ceramic layers in the internally electroded specimens can be closely approximated by a series model[3]. Values of the mean density and mean elastic compliance derived from this model show an increase and a reduction respectively and thus compensate to some extent. In addition, for composites having a large ceramic-to-metal layer thickness ratio the series model predicts only small changes in frequency constant, in agreement with the observed change of less than 3%.

A resonance application in which internal electrodes may be useful is in increasing the voltage step-up ratio of the piezoelectric transformer. Here the transformer rate may be multiplied by the number of layers introduced into the primary end of the conventional bar-shaped transformer.[5] A second advantage is that the ends of the internal electrodes that act as the low side of the secondary circuit allow a more uniform poling and larger electrode area which increases the current capacity, hence the power of the secondary. If DC isolation of the primary and secondary is required a thin section of strip electrodes may be included as the low side of the secondary circuit.

Transformers with dimensions 15 x 6 x 1.5 mm with 10 active layer primaries were constructed and driven at resonance (approximately 100 kHz), and the voltage step-up ratio compared with conventional transformers. Although the transformer ratio was strongly dependent on load impedance for both types of device, the ratio in the multilayer case was increased over ten times compared to the conventional design.[3]

CONCLUSIONS

Platinum internal electrodes have been introduced into commercial PZT formulations by standard thick film techniques. The results indicate little change in resonance characteristics and large reductions in the driving voltages. The reduction in voltage is somewhat offset by the physical clamping of inactive ceramic necessary to separate electrode sets. The driving and poling fields may be increased without danger of dielectric breakdown because of the decreased ceramic layer thickness. Tape casting is a refined technique that along with screen printed electrodes is highly versatile in producing complex sizes and shapes.

ACKNOWLEDGMENT

For support we thank the Office of Naval Research, Contract No. N00014-78-C-0291.

REFERENCES

1. R. Holland and E.P. Earnisse. Research Monograph 50, MIT Press, p 89 (1969).
2. J.V. Biggers, T.R. Shrout and W.A. Schulze. Am. Cer. Soc. Bull. 58, 516 (1979).
3. L.J. Bowen, T.R. Shrout, W.A. Schulze and J.V. Biggers. To be published in Materials Research Bulletin.
4. K. Okazaki and N. Nagata. Proc. Int. Conf. lst. 4, 404 (1972).
5. H.W. Katz. Solid State Magnetic and Dielectric Devices. Wiley, Ch. 5 (1959).

APPENDIX 14

T.R. Shrout, W.A. Schulze and James V. Biggers. Temperature Compensated Composite Resonator.

TEMPERATURE COMPENSATED COMPOSITE RESONATOR

Thomas R. Shrout, Walter A. Schulze and James V. Biggers

Materials Research Laboratory
The Pennsylvania State University
University Park, Pennsylvania 16802

ABSTRACT

A composite resonator was designed and fabricated by the use of a multilayer tape casting technique. A multilayer composite composed of $Pb_3\ MgNb_2O_9$ and 0.8 $Pb_3MgNb_2O_9$ + 0.2 $PbTiO_3$ (chosen for their nearly compensating resonant temperature coefficients) was found to have improved temperature stability. Resonant frequency changes of <60 ppm/°C were found over a temperature range of -10°C to 80°C.

INTRODUCTION

Piezoelectric crystals and ceramics are widely used for most acoustic and ultrasonic device applications. Temperature and time stability of sound velocity, which determines the characteristic resonant frequency, is of great importance for both bulk (1) and surface wave devices (2). The stability as a function of time is influenced by crystal imperfections and/or the microstructure, whereas the temperature coefficients depend largely on crystal structure and orientation (3).

Single-crystal quartz is a well known example in which suitably chosen crystal cuts minimize the temperature dependence of sound velocity. However, minimized temperature cuts usually result in reduced electromechanical coupling properties (1).

Single crystals are, in general, costlier than polycrystalline materials such as modified ($Pb(Ti,Zr)O_3$) PZT. This realization has been the basis of extensive investigations attempting to minimize temperature and time coefficients by the use of additives (4-8). It was the intention of this work to show the feasibility of designing composite resonators exhibiting minimized temperature coefficients.

Composite Model

The temperature dependence of the velocity of sound is determined by the elastic moduli and the density of the medium. For example, the wave velocity (v) in a thin disk normal to the poling axis can be described by the relation

$$v = (S_{11}^{E}\rho(\sigma - 1)^2)^{-1/2} \tag{5}$$

with ρ being the density, S_{11}^{E} the short-circuit elastic compliance, and σ the poissons ratio.

For most materials, the elastic compliance increases gradually with temperature, producing a positive temperature coefficient. At structural phase changes, however, the elastic coefficients often show anomalous behavior, "softening," or a negative temperature coefficient (8).

Lead magnesium niobate ($Pb_3MgNb_2O_9$), a relaxor ferroelectric, was found to have regions of both positive and negative temperature coefficient, of elastic compliance, above and below the ferroelectric Curie temperature respectively (9). The solid solution system between the relaxor $Pb_3MgNb_2O_9$ and ferroelectric $PbTiO_3$ was reported to exhibit a wide range of Curie temperatures (10).

By suitably selecting compositions in the $Pb_3MgNb_2O_9$-$PbTiO_3$ family, a composite comprised of compensating positive and negative temperature coefficients should exhibit improved temperature stability. The low thermal expansion coefficients found in this system are also an added advantage for thermal stability.

EXPERIMENTAL

Sample Preparation

The compositions to be used in the composite were $Pb_3MgNb_2O_9$ (PMN) and $0.8Pb_3MgNb_2O_3 + 0.2PbTiO_3$ (.8PMN/.2PT) selected from Reference 10 with Curie temperatures (determined at 1 kHz) of 16°C and about 92°C respectively. Reacted powders were produced using mixed oxides calcined for 4 hours at 875°C. The calcined slugs were then ground sufficiently to pass a 325 mesh sieve. The fine powders and a commercial organic liquid suspension binder* were mixed to produce slips for tape casting (11-13). Tapes approximately 0.025 cm thick were produced using a procedure described in Reference 14.

---

*Claydon Binder B-62, Lot 117, Claydon Inc. 11404 Sorrento Valley, San Diego, CA, 92121.

Two and one-half centimeter squares of each composition were stacked and laminated in homogeneous "monolithic" and composite model configurations. Each sample consisted of four layers. Monolithic configurations consisted of layers of the same composition to be used as comparative standards. The composite, 50/50 V/O, consisted of layers of $Pb_3MgNb_2O_9$ tape in series (A/B) with layers of $0.8Pb_3MgNb_2O_9 + 0.2PbTiO_3$ tape. To prevent possible interaction and diffusion between the two compositions, an internal Pt barrier electrode was used. This was achieved by silk screening Pt ink on the green tape prior to lamination. Earlier work (12) suggests that a barrier layer might not be needed.

The multilayers were heated slowly to 700°C over a 30-hour period to remove any organic binder materials. Sintering was done in closed high-purity alumina crucibles. The multilayer tapes were placed on Pt foil and a small amount of lead zirconate was added as a source of PbO. A silicon carbide resistance furnace with a programmable controller was used, the heating rate being 200°C/hour with a soak temperature of 1275°C for a period of 0.5 hours. The samples were allowed to cool in the furnace with power off. The fired samples were found to be at least 93% theoretically dense.

Measurements

Electromechanical resonance properties were measured on disks about 0.5 cm in diameter and about 0.05 cm in thickness. The disks were electroded using sputtered-on gold. Dielectric permittivity and loss (tan δ) as a function of temperature were measured using an automatic capacitance bridge* at 1 kHz. Displacement-field (DE) hysteresis loops were observed using a

*Hewlett Packard (Model 4270 A) automatic capacitance bridge, Hewlett Packard 1-59-1 Yoyogi, Tokyo, Japan 151.

Sawyer Tower circuit. The DE loops were measured at room temperature and at 0.1 Hz. The .8PMN-.2PT and the PMN/.8PMN-.2PT samples were poled in a stirred oil bath at 90°C by applying a DC field of 15 Kv/cm for at least two minutes. The samples were allowed to age for 24 hours before further measurements were made.

The planar coupling coefficient (k_p), mechanical Q and resonant frequency were measured as a function of temperature using the resonance method described in Reference 15. Resonance measurements on $Pb_3MgNb_2O_9$ were conducted under a DC bias of 8Kv/cm, since above -16°C the material is paraelectric and a polarization must be induced. A blocking capacitor was used in conjunction with the resonance apparatus (16). Resonance measurements at a constant bias were also made on the .8PMN-.2PT and the composite.

RESULTS AND DISCUSSION

Microstructure

A typical SEM photomicrograph of a PMN/.8PMN-.2PT multilayer can be seen in Figure 1. The sharp change in grain size at the Pt interface suggests that little interaction took place. Further, little interaction was found in regions without a Pt layer, indicating that a diffusion barrier layer was not required.

Electromechanical Data

Dielectric permittivity as a function of temperature for PMN, .8PMN-.2PT, and PMN/.8PMN-.2PT are shown in Figure 2. Also shown are predicted values of K versus temperature calculated from the series model equation (17):

$$1/K_{calc} = V_1/K_1 + V_2/K_2$$

where V_1 and V_2 are volume fractions and K_1 and K_2 are dielectric constants for the two compositions.

Piezoelectric d_{33} and DE loop data are reported in Table 1 and shown in Figures 3a-c. The coercive field (E_c) of the composite was found to be an average of the two compositions. The experimental d_{33} value, for the composite, was found to be in agreement with the calculated value. The permittivity, d_{33}, and DE data all indicated that the composite may be described by a simple series model.

Resonance Data

A resonance spectrum for the PMN/.8PMN-.2PT composite is shown in Figure 4. The fundamental planar mode resonance (the large peak) was accompanied by a weaker resonance signal at a lower frequency. This signal was accredited to the strong resonance of the .8PMN-.2PT layer.

Spurious resonances due to the Pt barrier electrode were not found. Earlier work (18) reported that Pt layer electrodes had little effect on resonance due to a compensation between density and compliance in platinum to approximate the frequency constant of PZT. This matching of frequency constant can also be expected with PMN. PMN, being highly electrostrictive, maintained the generation of strong resonances well above the transition region with only 8 Kv/cm bias.

The planar coupling coefficient, k_p, and mechanical quality factor, Q, were calculated for multilayers both unbiased (poled) and biased as a function of temperature (See Figures 5 and 6). The coupling coefficient was found to be higher for the biased multilayers as compared to the unbiased samples. The coupling coefficient, being proportional to the piezoelectric constant and inversely proportional to the square of the appropriate elastic constants and permittivity, was expected to increase (5) since a biasing electric field decreases the permittivity (See Figure 2).

The mechanical quality factor Q was found to be lower with applied bias as reported in Reference 19. The Q for PMN was found to be considerably larger than Q for the composite and .8PMN-.2PT samples. It appears that a low Q material physically dampens the high Q material producing a nonaveraged low Q composite.

The relative resonant frequency, Δf_R, as a function of temperature is plotted in Figure 7, where

$$\Delta f_R = \frac{f_T - f_{RT}}{f_{RT}}$$

with f_T being the resonant frequency at any temperature and f_{RT} being the resonant frequency at room temperature. The biased .8PMN-.2PT samples were found to have a positive temperature coefficient above 70°C and negative below. PMN samples were found to have a positive coefficient above - 16°C and negative below.

As expected, the composite was found to have nearly an average value of temperature coefficients, with a greatly reduced coefficient (<60 ppm/°C) between -10°C and 80°C. The same relative frequency Δf_R was found for biased or unbiased samples.

Another advantage of the composite was its improved polarization stability. Both Figures 4 and 5 show that the .8PMN-.2PT depoled rapidly above 70°C, whereas the composite indicated little depoling at temperatures even above 120°C. The composite utilized the electrical control concept of a transpolarizer (20) to effectively stabilize the polarization. Such a composite should also be dielectrically more stable under high field cycling, as reported in Reference 12. Little aging of resonant frequency was found.

Summary and Conclusions

Compositions $Pb_3MgNb_2O_9$ and $0.8Pb_3MgNb_2O_9 + 0.2PbTiO_3$ were used to fabricate a multilayer composite resonator. As the result of nearly compensating positive and negative temperature coefficients, a composite with improved temperature stability was found. A change of less than 60 ppm/°C in the radial resonant frequency over a temperature range between -10°C and 80°C was shown.

Only the feasibility of fabricating a composite resonator with improved temperature stability was intended in this work, not the optimization of electromechanical properties. Further optimization of a composite resonator exhibiting both improved temperature stability and electromechanical properties may be realized by suitably selecting compositions from both sides of the PZT morphotropic phase boundary (3).

Acknowledgment

We wish to thank the Office of Naval Research for their support of this work through Contract No. N00014-78-C-0291.

References

1. W.P. Mason, Piezoelectric Crystals and Their Application to Ultrasonics (D. Van Nostrand Company, NY, 1950).

2. R.M. White, "Surface Elastic Waves," Proc. IEEE, 58[8], 1238-1277 (1970).

3. R.R. Zeyfang, "Temperature Coefficients of Sound Velocity in Piezoelectric Ceramics," Ferroelectrics 14, 743-748 (1976).

4. H. Thomann, "Stabilization Effects in Piezoelectric Lead Titanate Zirconate Ceramics," Ferroelectrics 4, 141-146 (1972).

5. B. Jaffe, W.R. Cook, Jr. and H. Jaffe, Piezoelectric Ceramics (Academic Press, London and NY, 1971).

6. H. Schichl, W. Christoffers and H. Hanisch, Piezo-Electric Ceramic Materials for SAW Devices," Mat. Res. Bull. 13, 1085-1093 (1978).

7. N. Ogowa and N. Toshio, Japan Kokai 76,125,900 (Nov. 1976).

8. H. Jaffe and D.A. Berlincourt, "Piezoelectric Transducer Materials," Proc. IEEE 53, 1372-1385 (1965).

9. L.E. Cross, S.J. Jang, R.E. Newnham, S. Nomura and K. Uchino, "Large Electrostrictive Effects in Relaxor Ferroelectircs" (to be published in Ferroelectrics).

10. S.J. Jang, L.E. Cross, K. Uchino and S. Nomura, "The Electrostriction Effects in Ceramic $Pb(Mg_{1/3}Nb_{2/3})O_3$:$PbTiO_3$ Solid Solutions" (to be published in Ferroelectrics).

11. R. Copek, "Multilayer Ceramic Capacitors," U.S. 3,549,415, Dec. 1970.

12. T. Shrout, W.A. Schulze and J.V. Biggers, "Electromechanical Behavior of Antiferroelectric-Ferroelectric Multilayer PZT Based Composites" (to be published in Ferroelectrics).

13. J.C. Williams, Treatise on Materials Science and Technology. Edited by F.Y. Wang, Vol. 9, Ceramic Fabrication Process, pp 173-198, Academic Press, NY (1976).

14. J.V. Biggers, T.R. Shrout and W.A. Schulze, "Densification of PZT Cast Tape by Pressing," Amer. Ceram. Soc. Bull. 58[5], 516-518; 521 (1979).

15. "IRE Standards of Piezoelectric Crystals: Measurements of Piezoelectric Ceramics, 1961," Proc. IRE 61, 1161-1169 (1961).

16. W.P. Mason, "Electrostrictive Effect in Barium Titanate Ceramics," Phys. Rev. 74[9], 1134-1147 (1948).

17. R.E. Newnham, D.P. Skinner and L.E. Cross, "Connectivity and Piezoelectric-Pyroelectric Composites," Mat. Res. Bull. 13, 525-530 (1978).

18. L. Bowen, T. Shrout, W. Schulze and J. Biggers, "Piezoelectric Properties of Internally Electroded PZT Multilayers" (to be published in Ferroelectrics).

19. G. Schmidt, H. Beige, G. Borchardt, J.V. Cieminski and R. Rossbach, "Some Special Properties of PLZT Ceramics," Ferroelectrics 22, 683-684 (1978).

20. C.F. Pulvari, "An Improved Field-Controlled Polarization-Transfer Device and the Operating Features of the Exploratory Content Addressable Memory System," IEEE Trans. Electron Dev. ED-16, 6, 580-587 (1969).

Table 1. DE hysteresis loop and piezoelectric d_{33} data for the various multilayer configurations (temp = 21°C).

Sample	E_c kV/cm	P_f NC/cm^2	$d_{33}(10^{-12}$ C/N)
$Pb_3MgNb_2O_9$	0	0	0
$0.8Pb_3MgNb_2O_9$-$0.2PbTiO_3$	2.1	22.4	240
Composite	1.1	1.5	160
Calculated*	1.05	--	185

*Based simply on averaging model.

** $d_{33} = \dfrac{V_1 {}^1d_{33}K_2 + V_2 {}^2d_{33}K_1}{V_1K_2 + V_2K_1}$ (Ref. 17)

V_1 and V_2 are volume fractions, K_1 and K_2 are dielectric constants and $^1d_{33}$ and $^2d_{33}$ are piezoelectric constants for PMN and .8PMN-.2PT respectively.

Figure Captions

Fig. 1 Photomicrograph of a PMN (1eft)/.8PMN-.2PT (right) multilayer with platinum barrier electrode.

Fig. 2 Dielectric permittivity (1 kHz) as a function of temperature for PMN, .8PMN-.2PT and the composite. Calculated values for the composite are represented by the dashed curve.

Fig. 3 (a-c) DE hysteresis loops for PMN (a), .8PMN-.2PT (b), and PMN/.8PMN-2PT (c). Loops measured at ∿2°C and 0.1 Hz.

Fig. 4 Resonance spectra for PMN/.8PMN-.2PT composite. Horizontal scale is 75 kHz/div.

Fig. 5 Planar coupling coefficient, k_p, as a function of temperature.

Fig. 6 Mechanical quality factor, Q, as a function of temperature.

Fig. 7 Relative resonant frequency (Δf_R) as a function of temperature.

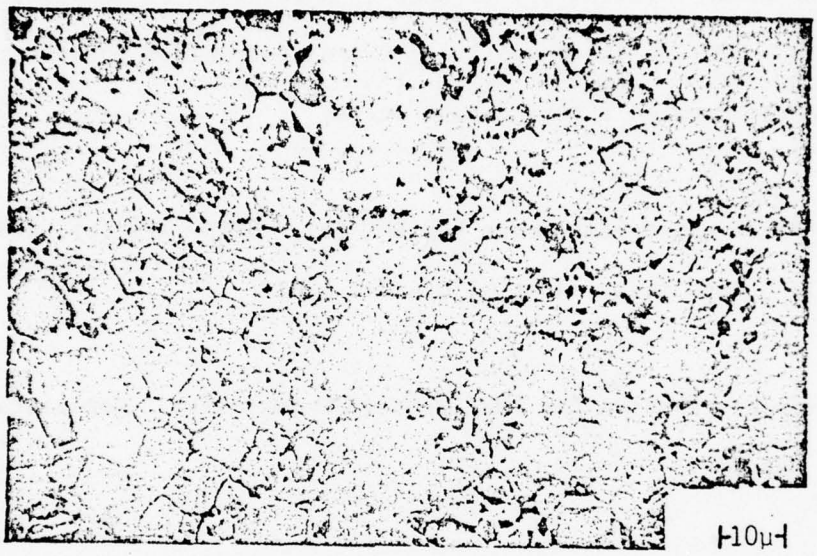

Figure 1

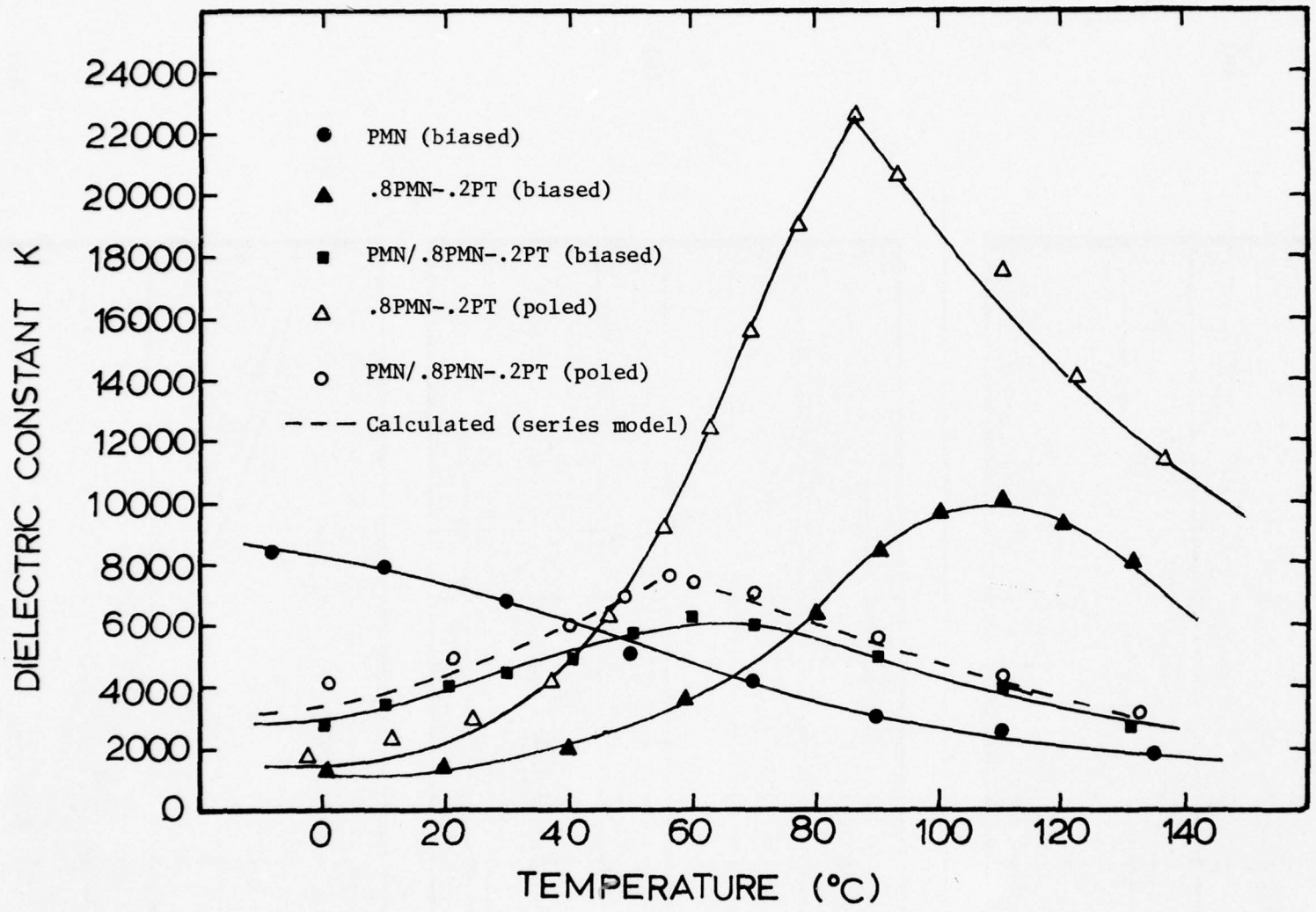
DIELECTRIC CONSTANT K
24000
22000
20000
18000
16000
14000
12000
10000
8000
6000
4000
2000
0
0
20
40
60
80
100
120
140
TEMPERATURE (°C)
PMN (biased)
.8PMN-.2PT (biased)
PMN/.8PMN-.2PT (biased)
.8PMN-.2PT (poled)
PMN/.8PMN-.2PT (poled)
Calculated (series model)

Figure 2

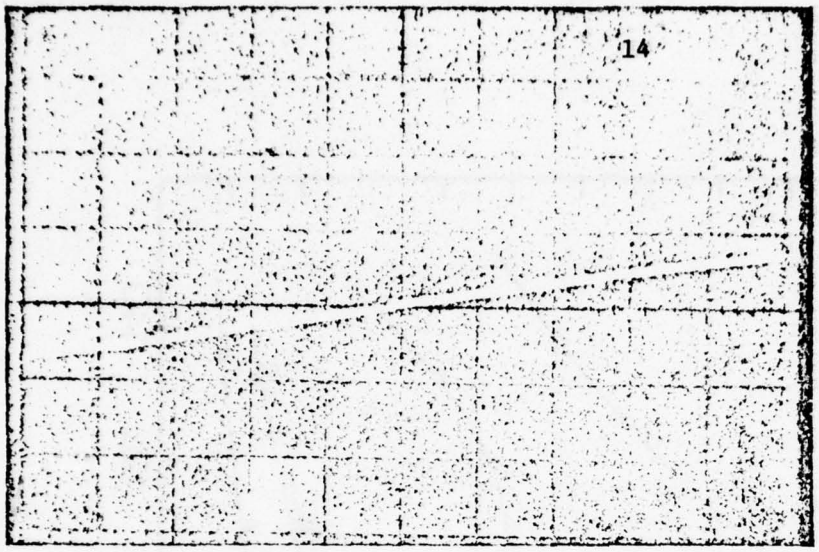

(a)

(b)

(c)

Figure 3

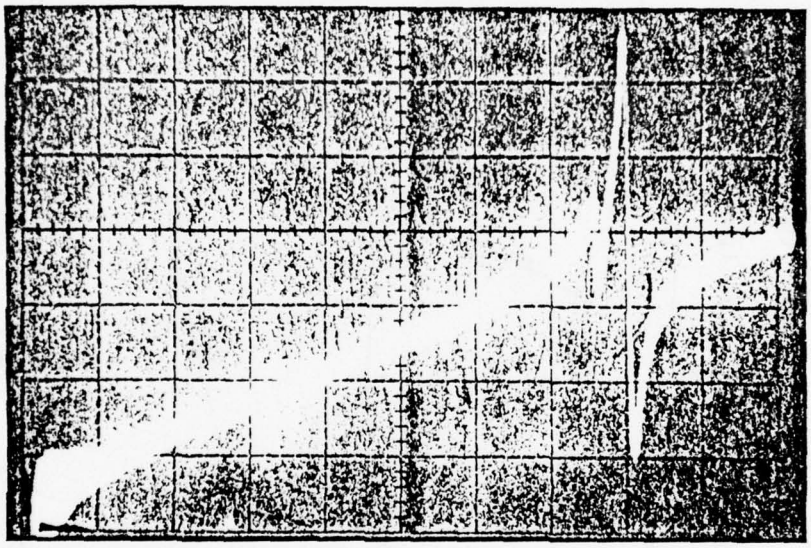

Figure 4

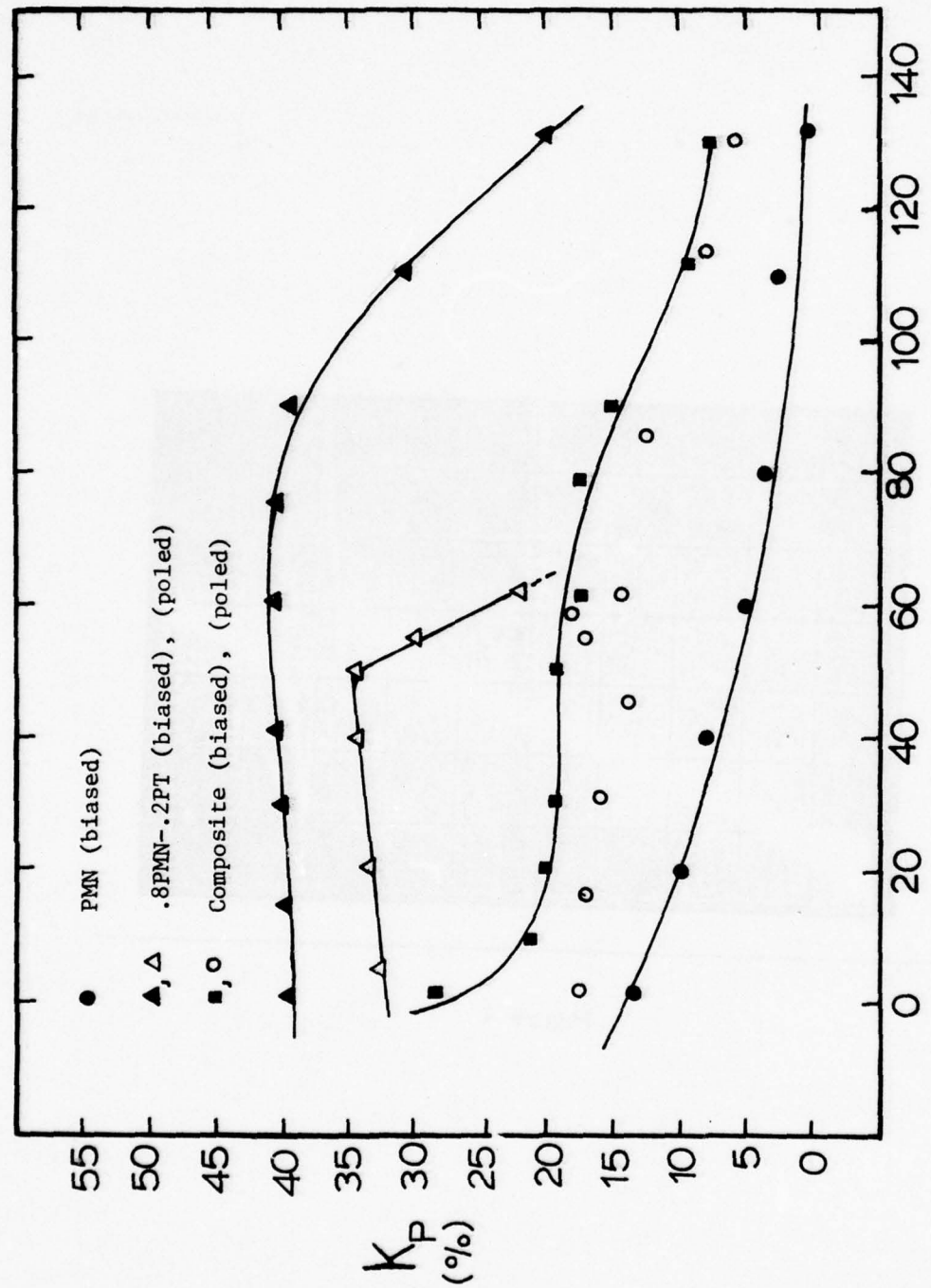
PMN (biased)
.8PMN-.2PT (biased), (poled)
Composite (biased), (poled)
K_p (%)
TEMPERATURE (°C)
0
5
10
15
20
25
30
35
40
45
50
55
0
20
40
60
80
100
120
140

Figure 5

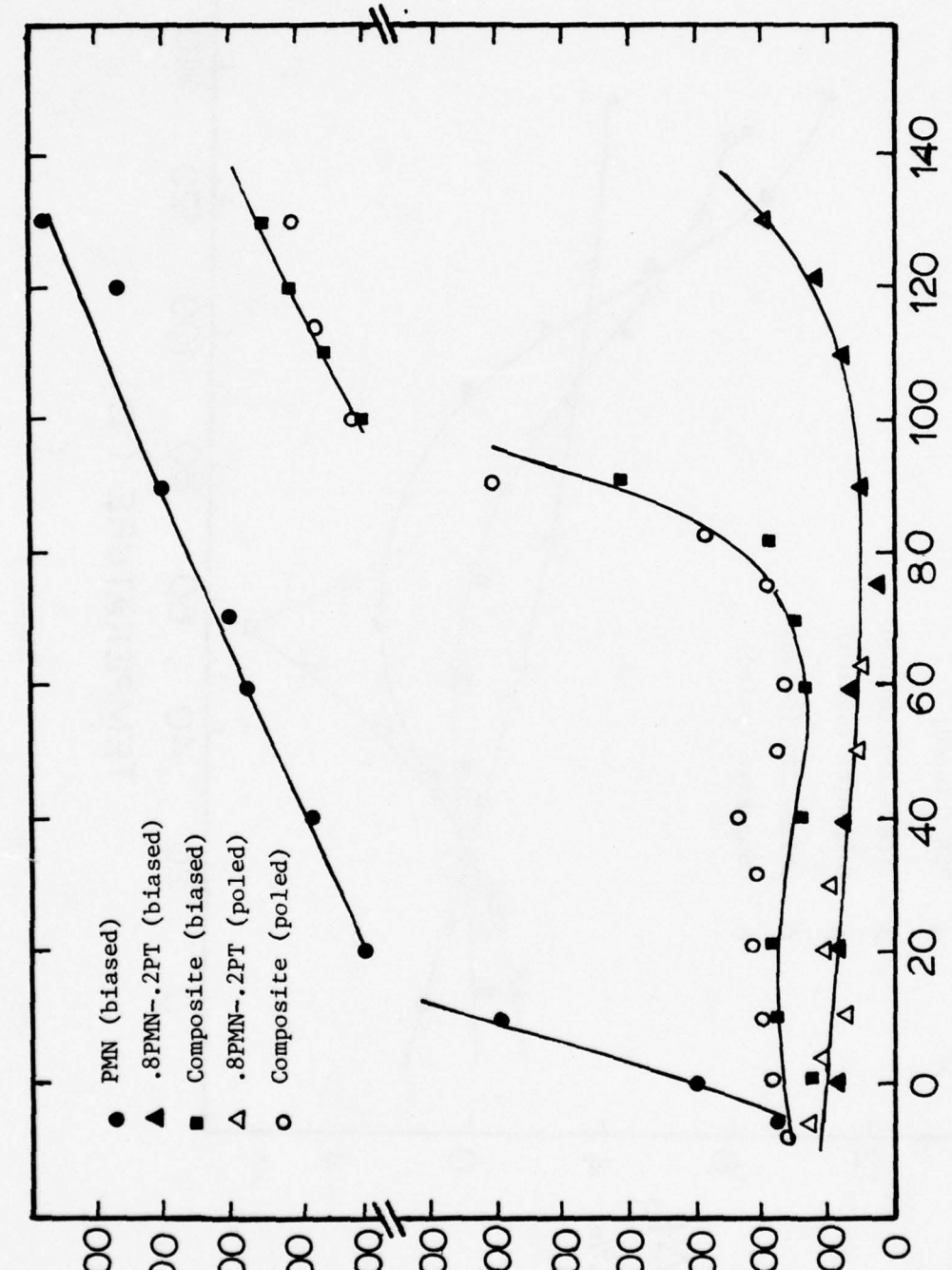
PMN (biased)
.8PMN-.2PT (biased)
Composite (biased)
.8PMN-.2PT (poled)
Composite (poled)
Q
9000
7000
5000
3000
1000
700
600
500
400
300
200
100
0
0
20
40
60
80
100
120
140
TEMPERATURE (°C)

Figure 6

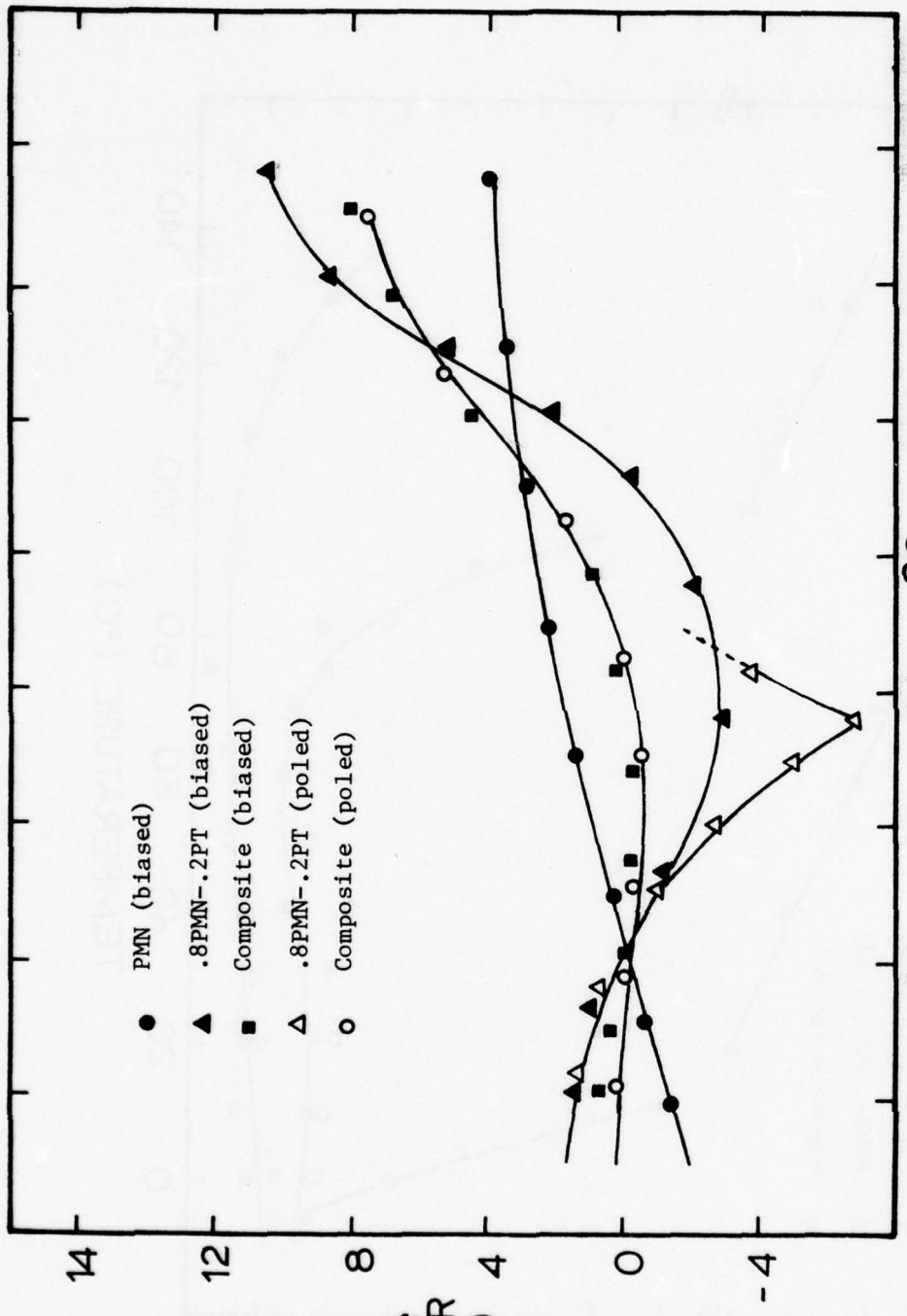
PMN (biased)
.8PMN-.2PT (biased)
Composite (biased)
.8PMN-.2PT (poled)
Composite (poled)
Δf_R (%)
14
12
8
4
0
-4
0
20
40
60
80
100
120
140
TEMPERATURE (°C)

Figure 7

GRAIN ORIENTED

APPENDIX 15

M. Holmes, R.E. Newnham and L.E. Cross. Grain-Oriented Ferroelectric Ceramics. Ceram. Bull. 58(9) 872 (1979).

NOTES

Grain-Oriented Ferroelectric Ceramics

MICHAEL HOLMES,* ROBERT E. NEWNHAM,* and LESLIE E. CROSS*

Pennsylvania State University, University Park

Electroceramic materials for piezoelectric transducer applications have in the past been based largely on pseudocubic phases of the perovskite family, such as $BaTiO_3$, $PbZrO_3$:$PbTiO_3$ (PZT), where the many available domain state orientations make it possible to pole a randomly axed assemblage of grains in the conventional polycrystalline ceramic to a strongly remanent polar state with high piezoelectric activity.

In these materials the original spherical macrosymmetry of the random array is modified by the poling to a conical symmetry (∞mm) with nonzero piezoelectric coefficients similar to those in the hexagonal point group $6mm$, and this resultant Curie group is independent of the symmetry of the initial ferroelectric species. The temperature range of strong piezoactivity is also limited by the range of Curie temperatures in the perovskites, and aging is a problem associated with the ferroelastic switching necessary to pole the randomly axed ceramic structure.

Clearly, a simple, inexpensive technique for achieving a strongly oriented (textured) grain structure in ferroelectrics of lower symmetry could relieve many of these constraints and lead to interesting new families with new Curie group symmetries, new combinations of usable piezocoefficients, and the possibility of exploiting the strong ferroelectric effects in lower symmetry prototype structures while still maintaining most of the ease of fabrication of ceramic processing.

In the present note a simple technique for producing powders with very marked shape anisotropy was applied to materials in the bismuth oxide layer structure family of ferroelectrics. The resulting anisotropic powders were used with several ceramic forming techniques to produce strongly textured bodies with orientation factors that heretofore had been produced only by the much more expensive uniaxial hot-pressing[1-2] and hot-forging methods.[3]

The technique consists of a molten salt synthesis step to produce discrete platelike grains (Arendt[4] and Rosolowski et al.[5] used the molten salt synthesis technique to produce single magnetic domain crystals and PZT powders). The powders thus produced are mixed with an organic binder, tape cast, and fired.

Specifically, this molten salt synthesis process consisted of mixing the component oxides, sodium chloride, and potassium chloride with an organic vehicle in a ball mill. Equal weights of the salts were used, and the weight ratio of the total salt to total oxide ranged from 0.45 to 0.90. After the composition was thoroughly mixed, it was put in covered alumina or platinum crucibles and fired in air. Upon cooling of the composition, the salt was removed by repeated washings with deionized water. Platelets of the bismuth compounds were left.

Figure 1 shows a photomicrograph of a bismuth tungstate (Bi_2WO_6) powder produced by firing the salt mixture at 1000°C for 1 h. Figure 2 is a similar photomicrograph of a bismuth titanate ($Bi_4Ti_3O_{12}$) powder produced under similar conditions, namely, 1150°C for 1 h. The very marked shape anisotropy of the small crystallites produced by this method is clearly evident in both pictures. With longer firing times and/or higher temperature, rather unexpectedly, the crystallites did not grow to significantly larger sizes, nor could we control the size effectively by changing the cooling rate imposed on the crucible.

Preliminary experiments using conventional tape casting to fabricate ceramics from these anisotropic powders show very promising results. For the Bi_2WO_6, X-ray diffraction patterns taken from ceramics fabricated from the fired tapes show only the (00l) peaks of a well-oriented sample. For $Bi_4Ti_3O_{12}$, the result is complicated by the presence of a small quantity of a second phase in the flux-produced powder. More detailed pole figures and property measurements are currently being conducted on tape-cast ceramics of both compositions.

Summary

The molten salt synthesis–tape casting technique appears to be a simple method of obtaining grain-oriented ferroelectric ceramics. The compounds Bi_2WO_6 and $Bi_4Ti_3O_{12}$ were prepared by this method because of their possible use in piezoelectric devices. This technique should, however, be applicable to any system in which crystallite shape can be used for alignment purposes.

References

[1] W. L. Streicher and D. A. Payne, "Electrical Properties of Hot-Pressed Bi_2WO_6," presented at the Fall Meeting of the Electronics Division of the American Ceramic Society, September 20, 1978; for abstract, see *Am. Ceram. Soc. Bull.*, 57 [8] 768 (1978).

[2] H. Igarashi, K. Matsunaga, T. Taniai and K. Okazaki, "Dielectric and Piezoelectric Properties of Grain-Oriented $PbBi_2Nb_2O_9$ Ceramics," *ibid.*, [9] 815–17.

[3] T. Takenaka, K. Shoji, H. Takai and K. Sakata, "Ferroelectric and Dielectric Properties of Press-Forged $Bi_4Ti_3O_{12}$ Ceramics," *Proc. Jpn. Congr. Mater. Res.*, 19, 230–33 (1976).

[4] R. H. Arendt, "The Molten Salt Synthesis of Single Magnetic Domain Barium Iron Oxide ($BaFe_{12}O_{19}$) and Strontium Iron Oxide ($SrFe_{12}O_{19}$) Crystals," *J. Solid State Chem.*, 8 [4] 339–47 (1973).

[5] J. H. Rosolowski, R. H. Arendt and J. W. Szymaszek, "Lead Zirconate Titanate (L/T) Ceramics," Annual Tech. Rept. to the Office of Naval Research, contract No. N00014-76-C-0659, June 1977. □

Fig. 1. Scanning electron photomicrograph of Bi_2WO_6 fired at 1000°C for 1 h in air (salt removed).

Fig. 2. Scanning electron photomicrograph of $Bi_4Ti_3O_{12}$ fired at 1150°C for 1 h in air (salt removed).

*Member, the American Ceramic Society.

Supported by the Office of Naval Research under contract No. N00014-78-C-0291 and by a Bismuth Institute graduate fellowship.

Received March 22, 1979; approved May 29, 1979.

PROCESSING STUDIES

APPENDIX 16

K.A. Klicker and J.V. Biggers. Control of the Partial Pressure of PbO During the Sintering of PZT Ceramics.

CONTROL OF THE PARTIAL PRESSURE OF PbO DURING THE SINTERING OF PZT CERAMICS

K.A. Klicker and J.V. Biggers

Materials Research Laboratory
The Pennsylvania State University
University Park, Pennsylvania 16802

INTRODUCTION

The manufacture of lead zirconate-lead titanate (PZT) ceramics requires that the partial pressure of PbO (P_{PbO}) be controlled during sintering. Ikeda[1] et al and Webster[2] et al have studied the effect of changes in the lead oxide content on the dielectric constant and electromechanical coupling coefficient of sintered PZT. Either positive or negative deviation of the PbO from stoichiometry affects both of these parameters. Most techniques for controlling partial pressure of PbO involve the use of a source material enclosed in the container with the parts to be fired. An ideal source material will produce a P_{PbO} so that the parts being sintered do not gain or lose PbO during the sintering process. If, however, the P_{PbO} atmosphere is higher than the P_{PbO} required by the part, the part will absorb PbO. Conversely, the part will lose PbO through vaporization if the P_{PbO} is lower than the than the P_{PbO} of the part. The P_{PbO} required by a PZT part is a function of the composition and temperature. When the part is in equilibrium with the atmosphere, neither vaporization from or absorption by the part will occur. Some of the commonly employed techniques for controlling the P_{PbO} include:

(a) Use of source pellets of a PZT composition which has a P_{PbO} higher than the P_{PbO} required by the PZT parts to be sintered[3,4].

(b) Use of source pellets of the PZT composition as the parts to be sintered but with addition of PbO[5].

(c) Burying the PZT parts in a powder, either calcined or sintered, of the same composition[6].

(d) Calculating the composition of the ceramic to include excess PbO. This excess PbO acts as a sintering aid and also helps to maintain a given P_{PbO}

about the parts[7].

All these techniques involve the use of compositions within the ZrO_3-TiO_3-PbO ternary system to provide a P_{PbO}. Despite this, no comprehensive studies have been reported in the literature that relate compounds in this system to P_{PbO}. The results of such a study will make it possible to choose a source composition that will provide a P_{PbO} near the P_{PbO} of parts to be sintered. It will also be possible to better understand the effectiveness of the various techniques listed above in providing the proper P_{PbO} so that sintered parts will undergo minimal compositional change during the sintering process.

PROCEDURE

The raw materials PbO[1], ZrO_2[2], and TiO_2[3] were weighed on an analytical balance in the proper proportions to form $PbZr_{0.55}Ti_{0.45}O_3$ and $PbZr_{0.6}Ti_{0.4}O_3$. Weight loss from calcination was found to be 0.51 weight percent. Of this weight loss, 0.31 weight percent was loss on ignition of organics from the oxide powders. The remaining 0.19 weight percent was assumed to be due to loss of PbO due to vaporization during calcining. The loss on ignition and loss due to vaporization were taken into account when the batch weights were calculated. The mixed oxides were ball milled in ethyl alcohol, using ZrO_2 milling media, for two hours and then pan dried. Calcination was done for one hour at 950°C in MgO crucible with a loose-fitting lid. The calcined slug was ground and passed through a 60-mesh screen. X-ray diffraction powder patterns showed only single-phase PZT. That portion of the batch to be used for sample pellets was mixed with a 15 weight percent PVA solution, dried,

---

[1]N.L. Industries, Inc., Highstown, NJ.

[2]Harshaw Chemical Corp., Cleveland, OH, Lot 1-75.

[3]Whittaker, Clark, and Daniels, Inc., South Plainfield, NJ, Lot 77G-27-8.

ground, and passed through a 60-mesh screen. The powder was pressed into pellets with a rotary press to a green density greater than 5.6 gm/sec. The pellet diameter was 5/8 inch and the average pellet weight was 1.2 grams. Before being weighed and sealed in crucibles, the sample pellets were put through a binder burn-out of 500°C for one hour. Preparation of the source materials depended on the firing configuration to be used.

Firing Configuration I

Figure 1A is a schematic of firing configuration I. All alumina discs and crucibles were McDanel 998[4] recrystallized alumina. Thin platinum sheets cut into discs were used at all places where thealumina might contact the PZT source pellets of PZT sample pellets. After being assembled as shown in Figure 1A, a 250 ml alumina crucible was inverted over the assemblage and the joint between the crucible and the large bottom alumina disc was sealed with calcium aluminate cement. The furance was preheated to 100°C and the crucible set in the furnace for 1/2 hour to permit the cement to dry.

Source compositions used with firing configuration I were

$$PbZr_{1-y}Yi_yO_3 + x \text{ mole \% } PbO,\ y = .4, .5, 5.5, 6, 7, 8, \text{ and } 1.0;$$

$$x = 0, .1, .3, .5, .7, .9, \text{ and } 1.0;$$

All source compositions used with firing configuration I are listed in Table 1. The PZT's used in source compositions were weighed, milled, dried, mixed with binder, ground, and screened as described above. Sixty grams of each composition used for firing was pressed into two thirty-gram, two-inch diameter pellets. Binder burn-out for the source pellets was two hours at 500°C.

Firing Configuration II

Figure 1B illustrates firing configuration II. The alumina ring was cut from a 4.8 mm ID alumina tube with a diamond blade and lapped flat on the ends. A platinum

[4]McDanel Refractory Porcelain Co., Beaver Falls, PA.

sheet was cut to obtain a disc that would rest on top of the bottom alumina disc and inside the alumina ring. Two different presintered granules were used to fill the volume of the crucible formed from the ring and the alumina disc. Granules of size greater than 30 mesh but less than 15 mesh of the same composition as the pellets were dusted onto the platinum sheet to form a thin layer onto which the green sample pellets were set. The sample pellets were then covered with a layer of this same powder. The remaining volume of the crucible was filled with the source granules which also were greater than 30 but less than Source compositons were:

$$PbZr_{1-y}Ti_yO_3 + x\text{mole \% } PbO,\ y = .55 \text{ and } .6$$

$$x = .1, .3, .5, \text{ and } .7$$

Source compositions used with firing configuration II are shown in Table 1. The ratio of weight of PZT to the weight of source powder was approximately 1:3. As shown by Figure 1B, a second alumina disc was set on top of the ring to close the crucible. The two joints of the ring and the alumina discs were sealed with calcium aluminate cement. The furnace was preheated to 100°C and the crucible set in the furnace for 1/2 hour to allow the cement to dry.

Both types of packing powder were presintered at 1330°C for 1/2 hour. The calcined powder was pressed into a two-inch diameter, 100 gram slug and had a binder burnout of 500°C overnight. Sintering took place in a crucible made of an alumina ring and two alumina discs, with all joints sealed with calcium aluminate cement. The alumina ring was cut so that the calcined slug would fit into it, leaving as little free volume as possible. Both top and bottom of the slug were covered with a platinum sheet immediately after the binder burnout, before they were placed in the crucible for firing. Sintering took place in a silicon carbide resistance furnace with a silicon carbide muffle.

A Data Trac 5310 programmable controller[5] was used to ensure that each sintering run was identical. The heat-up rate was 200°C/hours, followed by a soak period of one hour at 1330°C and cooling in the furnace with the power off. The sintered pellets were weighed on the same digital balance as before.

The number of pellets fired in each crucible with configuration I was as few as five and as many as nine. Only four pellets of this size could be fired in the same crucible with configuration II.

RESULTS AND DISCUSSION

When sintering PZT parts, the necessity of controlling the P_{PbO} makes selection of the PbO very important. Not only the composition of the source but also the amount of source and surface area of the source must be considered. Experimental data will be presented which describe the influence of each of these factors on the sintered PZT part.

Partial Pressure PbO as a Function of PZT Composition

There have been several papers published concerning the P_{PbO} of $PbZrO_3$ and $PbTiO_3$[8,9]. Härdtl and Rau measured the P_{PbO} of $PbZrO_3$, $PbTiO_3$, and several $PbZr_xTi_{1-x}O_3$ compounds using the Knudsen effusion method. At a fixed temperature, for equilibrium conditions, $PbZrO_3$ has a higher P_{PbO} than $PbTiO_3$. In terms of $PbZr_xTi_{1-x}O_3$ compounds, the equilibrium P_{PbO} of a compound decreases as the value of x decreases. This relationship of P_{PbO} to composition for the PZT compounds may also be stated in terms of the decrease in P_{PbO} as the Zr/Ti ratio decreases.

For the study described in this paper, weight change of PZT parts during sintering was used as an indicator of the relative P_{PbO} in which the parts were sintered. PbO, Pb and O_2 are the only volatile species found in PZT compounds[10].

---

[5] Research Incorporated, Minneapolis, MN.

When a PZT part equilibrates with the crucible atmosphere during firing, the interaction results in the absorption or vaporization of PbO by the part. This interaction may be measured by weighing the parts before and after sintering. If the P_{PbO} of the crucible atmosphere is higher than the P_{PbO} of the part, the part will absorb PbO. Conversely, the part will vaporize PbO if the crucible atmosphere is lower than the P_{PbO} of the part. The greater the weight change, the greater the difference between the P_{PbO} of the part and the source. These same relations hold true for weight losses.

Figure 2 shows the average percent weight change of PZT 55/45 ($PbZr_{.55}Ti_{.45}O_3$) parts as a function of source composition. The relationship of P_{PbO} to composition follows the trend reported by Härdtl and Rau. Those source compositions that have a P_{PbO} greater than the P_{PbO} of PZT 55/45 parts caused weight gains of the parts proportional to the difference in P_{PbO}. Likewise, the source compositions with lower P_{PbO} than the PZT 55/45 resulted in weight losses of the parts proportional to the difference in P_{PbO} of the source and the 55/45 parts. These results illustrate the validity of the use of weight change of PZT parts as an indication of the relative P_{PbO} of a particular source composition. This technique yields the relative P_{PbO} of a source composition because the technique indicates whether the P_{PbO} of a source is higher or lower than the P_{PbO} of the PZT parts and the relative difference in the P_{PbO} of the source and the parts, not the actual P_{PbO} of the source composition. The P_{PbO} that a source of a particular composition actually maintains will depend on the amount of source, the surface area of the source, the other material present in the crucible that will contribute to the P_{PbO}, and amount of PbO that leaks from the crucible. When only the relative P_{PbO} of a source composition is desired, these factors may be held constant. Choice of a particular firing rechnique fixes each of these factors and then the source composition may be chosen with regard to the

composition of the parts to be fired.

The binary phase diagram as prepared by Moon[11] contains a two-phase region on either side of the single phase $PbTiO_3$ region. According to the phase rule for condensed systems, P+F = C+1, where C equals the number of components in the system, P equals the number of phases in equilibrium and F equals the number of degrees offreedom or variance of the system. With regard to a two-phase region of a binary system, there is only one degree of freedom. By fixing the temperature this one degree of freedom is lost. Since the phase rule does not depend on the amount of the phases present but only on the number of phases that will be present at equilibrium, the composition of the two phases present in a two-phase region may not vary but the relative amounts of the two-phase present will vary across the region.

At a fixed temperature all compositions within the liquid + $PbTiO_3$ region have the same P_{PbO}. A material with a composition of liquid + $PbTiO_3$ may lose PbO, through vaporization for example, and maintain a constant P_{PbO} as long as the composition remains within the two-phase region. Such a material would be an ideal source material. PbO vapor lost from the crucible atmosphere due to interaction with the parts or leakage could be replenished by the source without a lowering of the P_{PbO} maintained by the source. As will be shown later, loss of PbO from most PZT + PbO compositions result in a decrease in the P_{PbO}.

The binary diagram for PbO-TiO_2 contains a second two-phase region of $PbTiO_3$+TiO_2. The binary diagram PbO-ZrO_2 also contains the two-phase regions. Four constant P_{PbO} sources are therefore available for use as source materials. Unfortunately, since $PbTiO_3$ has the lowest P_{PbO} and $PbZrO_3$ the highest P_{PbO} source materials will not provide the proper P_{PbO} for sintering the intermediate PZT compounds. In order to find a source with a relative P_{PbO} near to those of the PZT compositions, it is necessary to examine the PbO-ZrO_2-TiO_2 ternary diagram.

The $PbO-ZrO_2-TiO_2$ Phase Diagram

When considering small losses and gains of PbO from PZT compounds, the area of interest of the $PbO-ZrO_2-TiO_2$ phase diagram, as shown in Figure 3, is the portion immediately adjacent to the $PbZrO_3-PbTiO_3$ binary. Holman and Fulrath[9] have studied non-stoichiometry in the $PbTiO_3-PbZrO_3$ system. As was shown by the TiO_2-PbO binary loss of PbO from $PbTiO_3$ results eventually in the appearance of TiO_2 as a second phase. Loss of PbO from $PbZrO_3$ results eventually in the appearance of ZrO_2 as a second phase. For $PbZrO_3$, $PbTiO_3$ and all the PZT compounds lost of PbO results information of a defect structure, $Pb_{1-y}\square_y Zr_{1-x}Ti_xO_3$ with Pb vacancies. The width of this non-stoichiometric region is greatest for $PbTiO_3$ and $PbZrO_3$ and narrowest near $PbZr_{0.4}Ti_{0.6}O_3$. The P_{PbO} of a PZT drops rapidly as the composition passes through the non-stoichiometric region with loss of PbO. The non-stoichiometric region of the $PbO-ZrO_2-TiO_2$ ternary system, as determined by Holman and Fulrath, is shown in Figure 3. Webster, et al.[12], identified the phases present in the lower portion of Figure 4. As was found for $PbTiO_3$ and $PbZrO_3$, loss of PbO from non-stoichiometric $Pb_y\square_{xy}Zr_xTi_{1-x}O_3$ causes the appearance of a second phase. For most of the PZT compounds, the second phase which appears is ZrO_2.

The upper portion of Figure 3 was determined by Fushmi and Ikeda[13]. As with $PbTiO_3$ and $PbZrO_3$, absorption of PbO by any of the PZT compounds will result in the appearance of a liquid phase. Figure 4 is the upper portion of the $PbO-TiO_2-ZrO_2$ ternary at 1300°C, as derived by Fushmi and Ikeda. This diagram is of more interest than the 1100°C portion shown in Figure 3, since the sintering of most PZT takes place at a temperature near to 1300°C. The differences between the $PbO-PbTiO_3-PbZrO_3$ diagram at 1100°C and 1300°C are the extent of the liquid phase and the shift in the slope of the tie lines.

According to the phase rule, for the liquid plus solid solution region of the $PbO-PbTiO_3-PbZrO_3$ system, at a fixed temperature one degree of freedom remains. Therefore, the composition of the phases present within the two-phase region is not fixed. The composition of the phases present in a part which gains or losses PbO will not be unchanged and the P_{PbO} of the part will change as the overall composition of the part changes even though the composition remains within the two-phase region. The implication of this is that it is not possible to provide a P_{PbO} which is constant and equal to the P_{PbO} of a given PZT compound by using a PbO source of PZT+PbO, as was possible with $PbZrO_3$ and $PbTiO_3$.

This fact may be illustrated with Figure 4. Since the P_{PbO} of $PbZrO_3$ is higher than that of $PbTiO_3$ and the P_{PbO} of the various PZT's decreases as the Zr/Ti ratio decreases, the four PZT compounds shown in Figure 4 in order of decreasing P_{PbO} are A, B, C, and D.

As the dotted line on the figure shows, compositions H and G could be formed by intimately mixed PZT C with certain amounts of PbO. As previously predicted by the phase rule, neither compound H, G, or C is in equilibrium with either of the other two compounds. Compound H is in equilibrium with liquid F and PZT B. As PZT B has a higher P_{PbO} than PZT C and compound H is in equilibrium with PZT B, therefore compound H has a higher P_{PbO} than PZT C. The same argument proves that since compound G is in equilibrium with liquid E and PZT A, compound G has a higher P_{PbO} than either PZT B or PZT C. Although the effect has been exaggerated for illustrative purposes by using compounds as greatly different PbO contents it is certainly true for more practical compositions of PZT plus small amounts of PbO.

This illustration and the phase rule show that the use of any of the PZT compounds with addition of PbO as a source of PbO vapor will not provide a

contant P_{PbO}. The P_{PbO} of a particular PZT+PbO composition will depend on the composition of the PZT, the amount of PbO, and the ability of this source to vaporize PbO. With loss of PbO from the source through vaporization, the subsequent P_{PbO} of the source will decrease. A source of composition G would initially have a P_{PbO} equal to that of PZT A and subsequently decrease until a P_{PbO} equal to that of PZT C was established when all the excess PbO was vaporized and only PZT C remained.

Experimental verification of the relation of P_{PbO} to the amount of excess PbO in a source material was made firing parts of composition $PbZr_{0.6}Ti_{0.4}O_3$ with a source of composition $PbZr_{0.6}Ti_{0.4}O_3$+PbO where the amount of PbO was varied. Figure 5 shows that as the amount of excess PbO in the source was increased the weight gain of the parts increased. Source compositions containing less than four mole percent excess PbO caused a loss in PbO by the parts since the P_{PbO} of the source was lower than the P_{PbO} of $PbZr_{0.6}Ti_{0.4}O_3$. A similar relationship was found when parts of composition $PbZr_{0.55}Ti_{0.45}O_3$ were fired with a source composition $PbZr_{0.55}Ti_{0.45}O_3$+PbO.

A number of source compositions were used in firing PZT parts of composition $PbZr_{0.55}Ti_{0.45}O_3$. The composition of the source material was varied both in the composition of the PZT and the amount of excess PbO. The results of tehse findings is shown in Figure 6. Since all compositions which lie on a tie line are in equilibrium and have the same P_{PbO}, sources of these compositions will result in the same weight change of PZT parts. Comparison of the orientation of the equi-weight change lines of Figure 6 with the tie lines of Figure 4 shows good correlation. As predicted by the tie lines of Figure 4, a range of PZT+PbO compositions exist which provide the same P_{PbO}. For none of the PZT+PbO compositions used does the P_{PbO} remain constant with a change in the amount of excess PbO present.

Effects of the Amount of Source and Surface Area of Source

The inability of a PbO source of composition PZT+PbO to provide a constant P_{PbO} with loss of PbO makes the effects of the amount of each surface area of the source very important. Table 2 lists the weight losses of source pellets of several compositions when used in firing configuration I. In all cases the source pellets lost weight (thus implying a loss of PbO) but the amount of weight gained by the PZT parts being sintered never exceeded 2.5 wt %. The alumina crucible and discs exposed to the PbO atmosphere within the crucible had been used several times and therefore should not readily absorb PbO. The majority of the PbO lost by the source pellets must be attributed to leakage from the crucible. The P_{PbO} within the crucible must have decreased continually as the amount of PbO in the source decreased. The need for the source to vaporize PbO to replace PbO vapor lost due to leakage could be minimized by tightly sealing the crucible. Assuming that the practical limits of this have been reached, the only alternative method of minimizing compositional changes of the source is to maximize the amount of the source. For example, if 1 gram of PbO is to be lost by the source, the compositional change in a source of 20 grams will be much greater than a source of 40 grams. Because there are practical and economic limits to the amount of material which may be included in a crucible as a source material, the sources must be used in a form which most effectively makes use of the source material.

The vaporization of PbO in a surface phenomenon in the rate of vaporization of PbO is dependent on the surface area[14]. Therefore a granulated source material will much more easily and homogeneously vaporize PbO to maintain the partial pressure than a dense source pellet in which th bulk of the source material is unable to vaporize PbO. Since the vaporization is controlled by diffusion of PbO across a thickening PbO depleted surface layer, the P_{PbO} provided by the source will not be the P_{PbO} which corresponds to the bulk

source composition but will be determined by the ability of PbO to diffuse to the surface of the source material.

Firing configuration II is illustrated in Figure 1B. This configuration uses a source of granulated PZT+PbO. Source compositions used were the same as used with firing configuration I to provide a comparison of the effects on a granulated source. As predicted by the tie lines of the ternary diagram, addition of increasing amounts of PbO in the source composition resulted in larger weight gains of the parts. Figure 7 shows not only this effect but also compares the results with those obtained with firing configuration II. In all cases for a given weight change of the parts, the source composition of firing configuration II contained less excess PbO. As previously discussed, the influences on the P_{PbO} provided by the source include not only composition but also amount and surface area of the source and leakage of PbO vapor from the firing configuration. Table III compares several parameters of the the firing configuration. Assuming that leakage occurs at joints in the crucible, approximatly equal amounts of leakage of PbO vapor are expected as the length of sealed joint is nearly equal. The source in configuration II was less in mass but much higher in surface area. Therefore the effect of surface area on relative P_{PbO} of a source must surely be considered.

It has been established that the source material loses PbO to vaporization during the firing cycle. It has also been established that the P_{PbO} of a PZT+PbO composition decreases as the amount of PbO decreases. The effect of the decreasing P_{PbO} on the parts being sintered ought to be considered. The green parts are initially porous and have a high surface area at which to absorb PbO. These green parts experience the initially high P_{PbO} of the source. As the firing process continues, the P_{PbO} provided by the source decreases and the parts densify. If the compositional change of the source is great enough, the P_{PbO} within the crucible may decrease to the point that the parts being sintered will have to vaporize PbO. The sintered PZT parts

have a much lower surface area than the initially green parts which absorbed PbO. PbO will vaporize from the surface of the sintered PZT parts[14]. The properties of a PZT part with a PbO-rich bulk and a PbO-depleted surface could be quite complex. The use of final weight change of PZT parts as an indication of the P_{PbO} of the source must be made only with consideration of these implications. The final weight change of a part may be zero, but if the part has absorbed and then vaporized PbO while sintering it is doubtful that the part is homogeneous.

The effects of composition surface areas and amount of source on the weight change of PZT parts during sintering are described. If different amounts of source were used the results would differ but the trends would be the same. Not only the weight change of the parts must be considered but also the range of P_{PbO} which the parts experience. This study found that use of 60 grams of $PbZrO_3$ as a source in firing configuration I resulted in weight change greater than 1.8 wt% in parts of $PbZr_{0.55}Ti_{0.45}O_3$. Firings with successively smaller amounts of $PbZrO_3$ as a source will eventually reach an amount of $PbZrO_3$ which will result in zero final weight change of the parts. This study found that use of 60 grams of $PbZr_{0.55}Ti_{0.45}O_3$+11 mole % PbO as a source also resulted in zero weight change of $PbZr_{0.55}Ti_{0.45}O_3$ points. It has been shown previously that $PbZrO_3$ has a much higher P_{PbO} than does $PbZr_{.55}Ti_{.45}O_3$. Zero weight change may be achieved with a small amount of a high P_{PbO} source or a larger amount of a lower P_{PbO} source. Although the weight change is the same with either source, the range of P_{PbO} experienced by the parts during the sintering process would differ and possibly the degree of stoichiometry of the sintered parts.

CONCLUSIONS

1. The use of a composition $PbZr_xTi_{1-y}O_3$ + PbO as a PbO source will not provide a constant P_{PbO}, as the amount of PbO decreases.

2. As predicted by the lines for the $PbO-PbTiO_3-PbZrO_3$ ternary, a range of compositions of $PbZr_xTi_{1-y}O_3$ + PbO exist which have the same P_{PbO}, as indicated by the weight change of PZT parts during sintering.

3. The P_{PbO} which a source provides in a crucible is determined by source composition, amount of source, surface area of the source, and leakage of PbO vapor from the crucible.

REFERENCES

1. T. Ikeda, T. Okano and M. Watanabe, "A Ternary System PbO-TiO_2-ZrO_2," Jap. J. Appl. Phys. 1, 218 (1962).
2. A.H. Webster, J.B. Weston and N. Bright, "Effect of PbO Deficiency on the Piezoelectric Properties of Lead Zirconate-Titanate Ceramics," J. Amer. Ceram. Soc. 50(8) 490 (1967).
3. A.H. Webster, T.B. Weston and V.M. McNamara, "The Effects of Some Variations in Fabrication Procedure of Lead Zirconate-Titanate Ceramics Made from Spray-Dried Co-Precipitated Powders," J. Canad. Ceram. Soc. 35, 61-68 (1966).
4. A.H. Webster and T.B. Weston, "The Grain-Size Dependence of the Electromechanical Properties in Lead Zirconate-Titanate Ceramics," J. Canad. Ceram. Soc. 37, 42-44 (1968).
5. R.L. Holman and R.M. Fulrath, "Intrinsic Nonstoichiometry in Single-Phase $Pb(Zr_{0.5}Ti_{0.5})O_3$," J. Amer. Ceram. Soc. 55(4)192-195 (1972).
6. R.B. Atkin, R.L. Holman and R.M. Fulrath, "Substitution of Bi and Nb Ions in Lead Zirconate-Titanate," J. Amer. Ceram. Soc. 54(2)113-115 (1971).
7. S. Venkataramani, Private communication.
8. K.H. Härdtl and H. Rau, "PbO Vapour Pressure in the $Pb(Ti_{1-x}Zr_x)O_3$ System," Solid State Commun. 7(1)41-45 (1969).
9. R.L. Holman and R.M. Fulrath, "Intrinsic Nonstoichiometry in the Lead Zirconate-Lead Titanate System as Determined by Knudsen Effusion," J. Appl. Phys. 44(12)5227-5236 (1973).
10. D.A. Northrop, "Vaporization of Lead Zirconate-Lead Titanate Materials: II. Hot-Pressed Compositions at Near Theoretical Density," J. Amer. Ceram. Soc. 50(9)441-445 (1967).

11. R.L. Moon, "High Temperature Phase Equilibria in the Lead Zirconate-Lead Titanate System," Ph.D. Thesis, University of California, Berkeley, 1967; Tech. Rpt. UCRL-17545, 88 pp (1967).

12. A.H. Webster, R.C. MacDonald and W.B. Bowman, "System PbO-ZrO_2-TiO_2 at 1100°C," J. Canad. Ceram. Soc. 34, 97-102 (1965).

13. S. Fushimi and T. Ikeda, "Phase Equilibrium in the System PbO-TiO_2-ZrO_2," J. Amer. Ceram. Soc. 50(3)129-132 (1967).

14. D.A. Northrop, "Vaporization of Lead Zirconate-Lead Titanate Materials," J. Amer. Ceram. Soc. 50(9)441-445 (1967).

Table 1

SOURCE COMPOSITIONS--FIRING CONFIGURATION I
$PbZr_xTi_yO_3$ = x/y

Mole % PbO	40/60	50/50	55/45	60/40	70/30	80/20	100/0
0		I		I	I	I	I
1			II	I,II	I		
3			II	I,II	I		
5		I	I,II	I,II	I		
7	I	I	I,II	I,II	I		
9	I	I		I			
11	I	I		I			
13	I	I					

I = Source used with firing configuration I.

II = Source used with firing configuration II.

Table 2

FIRING OF SAMPLE PELLET COMPOSITION 60/40
SOURCE COMPOSITION PZT 60/40 + EXCESS PbO

Initial source composition (mole % PbO)	Mole % PbO lost by source	Final source composition (mole % PbO)	Total source weight loss (gm)	Total sample pellet weight change	Total weight PbO lost
6/4 + 9	2.4	6/4 + 6.6	1.29	+0.0297	1.26
6/4 + 7	2.4	6/4 + 4.4	1.22	+0.0100	1.21
6/4 + 5	2.2	6/4 + 2.8	1.02	+0.0060	1.01
6/4 + 3	1.88	6/4 + 1.2	0.80	-0.00206	0.802
6/4 + 1	0.86	6/4 + 0.14	0.38	-0.338	0.414

Table 3

COMPARISON OF PARAMETERS OF EACH TECHNIQUE

	Configuration I	Configuration II
Grams of source	60	40
Sealed joints (cm)[1]	2.26	3.02
Surface area of source (cm)[2]	31	176

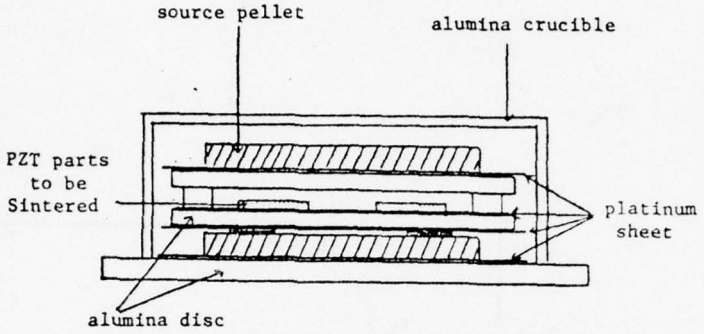

Figure 1A. Firing configuration I.

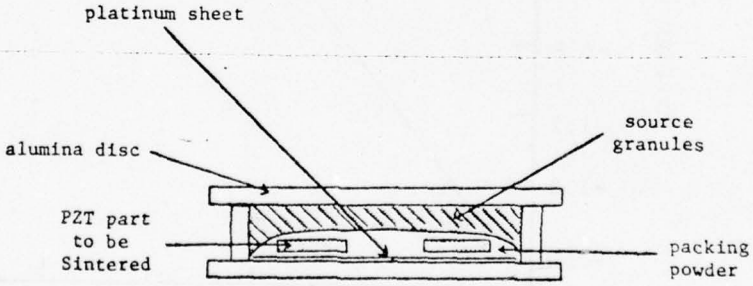

Figure 1B. Firing configuration II.

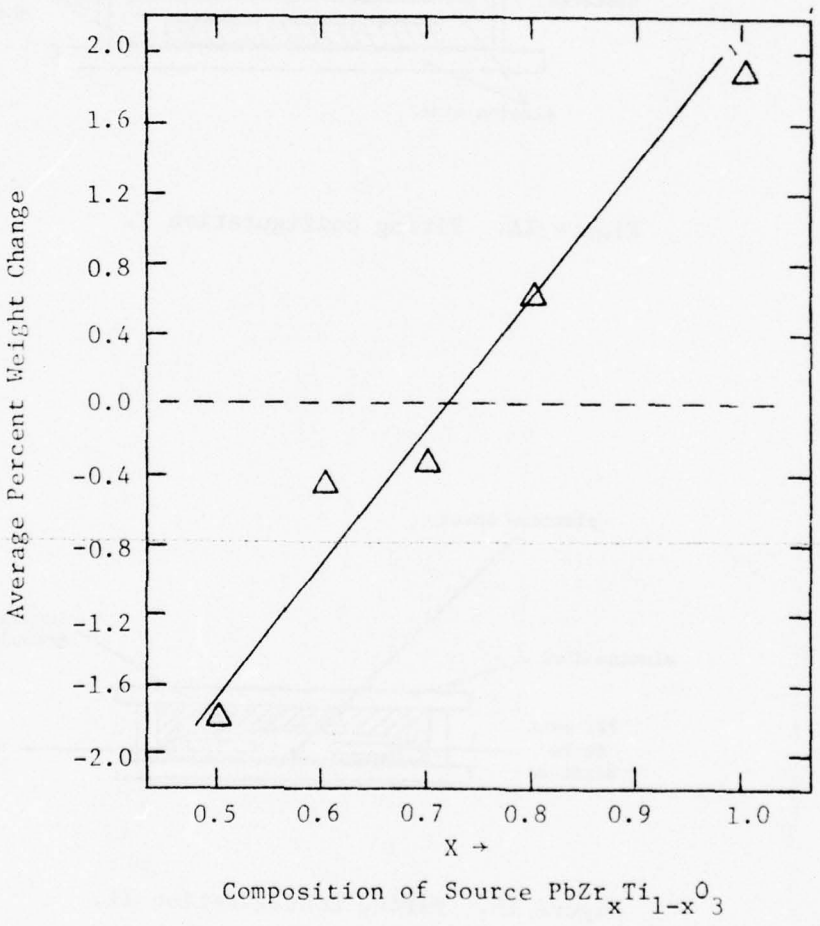

FIGURE 2. Average Percent Weight Change of PZT 55/45 Parts as a Function of Source Composition.

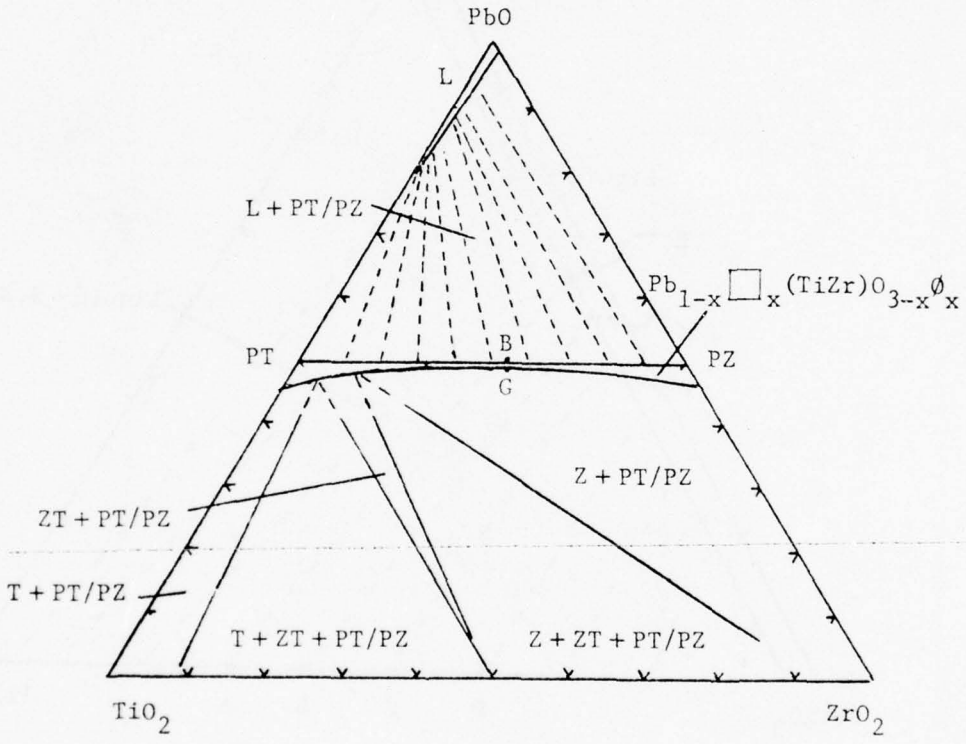

FIGURE 3. $PbO-TiO_2-ZrO_2$ Isothermal Diagram at 1100°C.

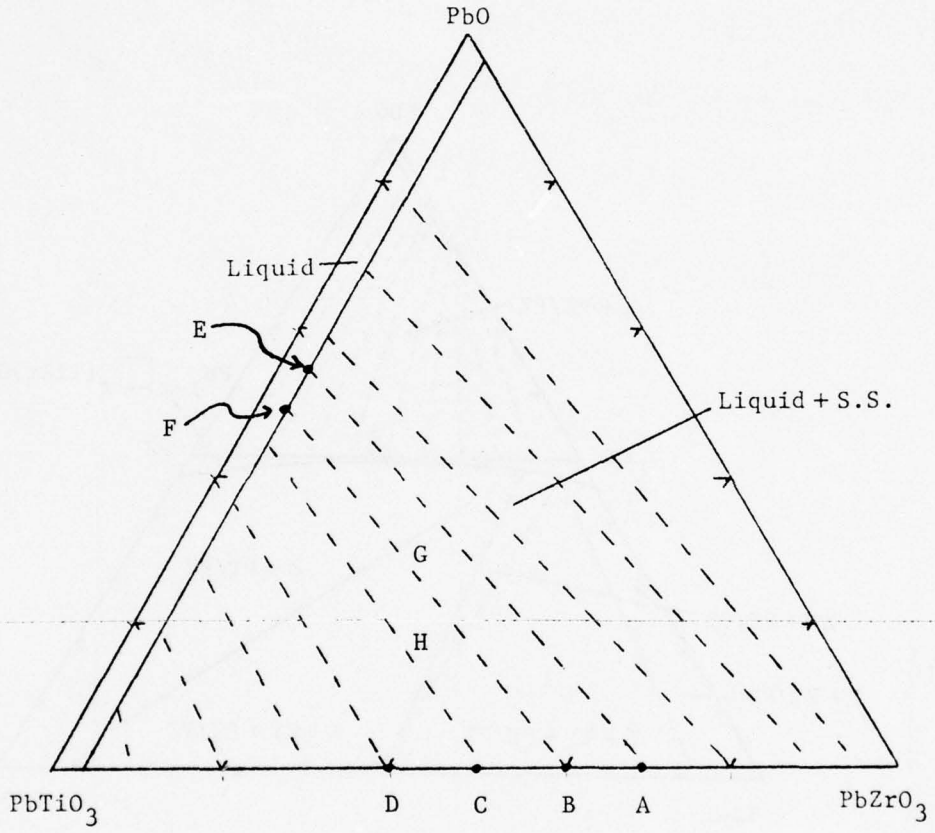

FIGURE 4. $PbO-PbTiO_3-PbZrO_3$ Isothermal Diagram at 1330°C.

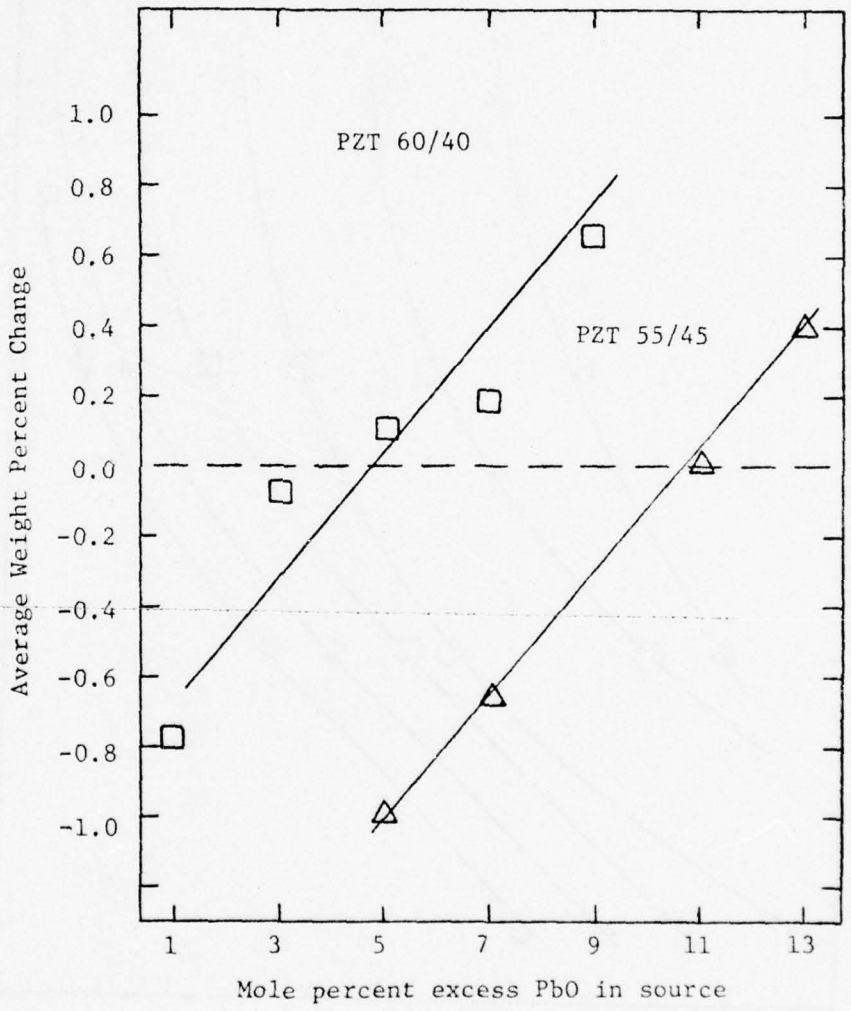

FIGURE 5. Average Weight Percent Change of PZT Parts as a Function of the Mole Percent Excess PbO in Source.

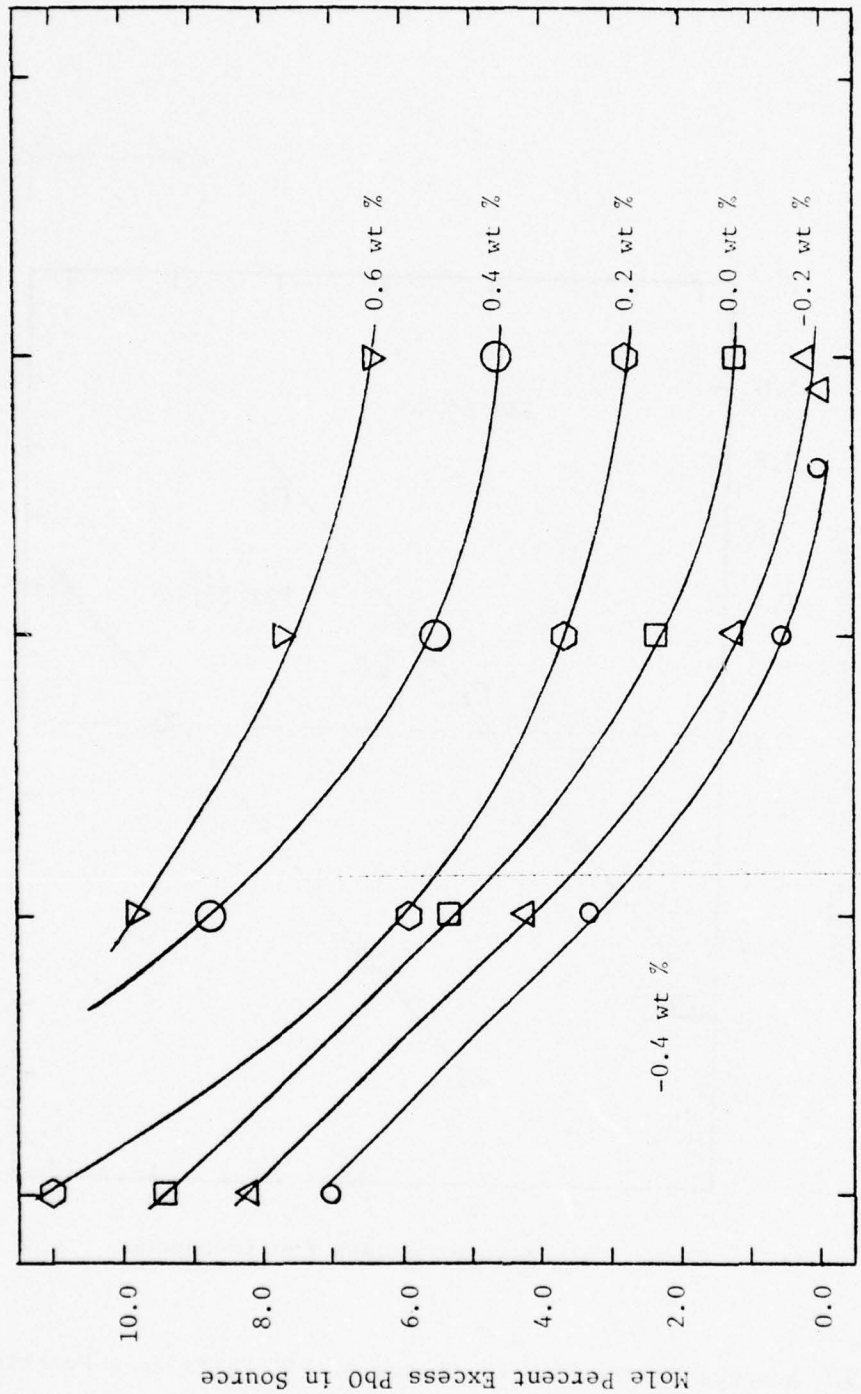

FIGURE 6. Average Percent Weight Change of PZT 55/45 Parts as a Function of Source Composition.

$[PbZr_xTi_{1-x}O_3 + PbO]$

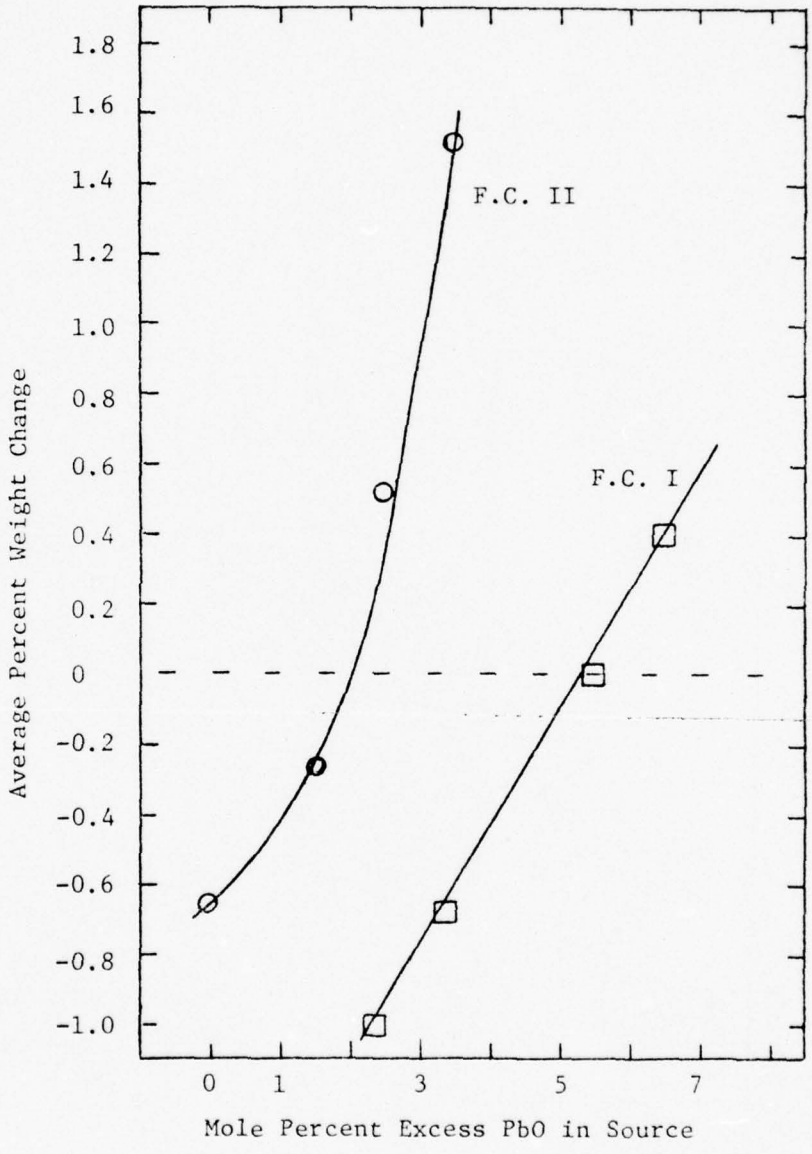

FIGURE 7. Average Percent Weight Change of PZT 55/45 Parts as a Function of Source Composition--Firing Configurations I and II.

PHENOMENOLOGICAL THEORY

APPENDIX 17

A. Amin, R.E. Newnham and L.E. Cross. Phenomenological and Structural Study of a Low Temperature Phase Transition in the $PbZrO_3$-$PbTiO_3$ System.

Phenomenological and Structural Study of a Low Temperature Phase Transition in the $PbZrO_3$-$PbTiO_3$ System

A. Amin, R.E. Newnham, L.E. Cross

Materials Research Laboratory
The Pennsylvania State University
University Park, Pennsylvania 16802

D.E. Cox

Physics Department, Brookhaven National Laboratory
Upton, New York 11973

ABSTRACT

The Landau-Ginsburg-Devonshire Phenomenological theory has been applied to the $PbZrO_3$-$PbTiO_3$ crystalline solid solution system to explore the behavior of the rhombohedral:tetragonal morphotropic phase boundary in the region below room temperature. The theory suggests that morphotropy is preserved, i.e. that the phase boundary occurs at nearly the same composition right down to 0 K.

The extension of the rhombohedral (R3m)-rhombohedral (R3c) phase boundary was investigated for a composition $PbZr_{0.6}Ti_{0.4}O_3$ using both neutron diffraction and pyroelectric measurements. Structures in both phases were refined by the neutron profile fitting technique. Values of the spontaneous polarization were obtained from the (Zr/Ti) shifts, and compared to those deduced from phenomenological theory.

INTRODUCTION

The perovskite solid solution between antiferroelectric $PbZrO_3$ and ferroelectric $PbTiO_3$ (PZT) contains a number of extremely important compositions used in the electronics industry (1). Many piezoelectric devices are made from poled PZT ceramics with compositions near the morphotropic phase boundary (MPB), the rhombohedral-tetragonal phase transition boundary in Fig. 1 where electromechanical coupling coefficients are unusually high.

In this work we report the low temperature results of the Landau-Ginsburg-Devonshire theory for PZT compositions near the morphotropic boundary. Using the Rietveld method (2), the $PbZr_{0.6}Ti_{0.4}O_3$ structure was refined above and below the low temperature phase transition. The transition temperature was determined by pyroelectric discharge experiments.

LANDAU-GINSBURG-DEVONSHIRE PHENOMENOLOGY

For many ferroelectric crystals it has proved useful to correlate the dielectric, piezoelectric, elastic, and thermal properties of the paraelectric and ferroelectric phases by a thermodynamic free energy theory. The Landau-Ginsburg-Devonshire (LGD) formalism gives an excellent description of these properties. A summary of past results can be found in the books of ferroelectricity by Jona and Shirane (3), Fatuzzo and Mertz (4), and Lines and Glass (5).

Consider the free energy function for a simple proper ferroelectric derived from a prototypic phase of symmetry Pm3m. For Brillouin zone center modes, the free energy may be written as a power series in dielectric polarzation P(6), and (7) as follows:

$$\Delta G = A(P_1^2+P_2^2+P_3^2) + B(P_1^4+P_2^4+P_3^4) + C(P_1^2P_2^2+P_2^2P_3^2+P_3^2P_1^2)$$
$$+D(P_1^6+P_2^6+P_3^6) + E(P_1^4(P_2^2+P_3^2) + P_2^4(P_1^2+P_3^2) + P_3^4(P_1^2+P_2^2))$$
$$+FP_1^2P_2^2P_3^2 + 1/2\ S_{11}^P(X_1^2+X_2^2+X_3^2) - S_{12}^P(X_1X_2+X_2X_3+X_3X_1) \qquad (1)$$
$$-1/2\ S_{44}^P(X_4^2+X_5^2+X_6^2) - Q_{11}(X_1P_1^2+X_2P_2^2+X_3P_3^2)$$
$$-Q_{12}(X_1(P_2^2+P_3^2)+ X_2(P_3^2+P_1^2)+X_3(P_1^2+P_2^2))$$
$$-Q_{44}(X_4P_2P_3+X_5P_1P_3+X_6P_1P_2)$$

where ABCDEF are related to the dielectric stiffness and higher order stiffness coefficients, S_{11}^P, S_{12}^P, S_{44}^P are the elastic compliances measured at constant polarization, and Q_{11}, Q_{12}, Q_{44} are the cubic electrostriction constants in polarization notation. The expression is complete up to all six power terms in polarization, but contains only first order terms in electrostrictive and elastic behavior.

Adjustable parameters in the free energy function which fit the observed $PbZrO_3$-$PbTiO_3$ phase diagram and the observed physical properties (dielectric, piezoelectric, and coupling coefficients) have been determined (8).

Numerical values of ΔG for the tetragonal modification (P4mm) are plotted as a function of composition in Fig. 2 for three different temperatures (-25°C, -175°C, and -265°C). The results are also given for the rhombohedral (R3m) and orthorhombic (Bmm2) cells. The rhombohedral-tetragonal degeneracy at the morphotropic phase boundary is temperature independent, in agreement with Fig. 1.

Based on the higher temperature phase diagram in Fig. 1, there is a rhombohedral-rhombohedral phase transition at low temperatures near the morphotropic boundary. The low temperature rhombohedral cell is twice the size of the high

temperature cell. Mechanical Q measurements by Kruger (9) seem to indicate such a transition. This is not, however, a reliable method of establishing phase boundaries.

To verify the existence of the transition, we have carried neutron diffraction experiments on $PbZr_{0.6}Ti_{0.4}O_3$ at three different temperatures (295 K, 200 K, and 9 K). The structures were refined by the Rietveld method (2). Low temperature pyroelectric discharge experiments established the transition temperature between the two phases.

SAMPLE PREPARATION

The $PbZr_{0.6}Ti_{0.4}O_3$ sample used for the neutron diffraction powder pattern and the pyroelectric discharge experiments was prepared by a chemical coprecipitation method. The starting materials [spectroscopic grade lead oxide, zirconium-tetra-n-butoxide (ZBT) and titanium-tetra-n-butoxide (TBT)] were weighed and blended with isopropyl alcohol in a mixer for 3 minutes while slowly adding deionized water. The white precipitated slurry was pan dried, then ball milled with ZrO_2 balls and distilled water for eight hours. The product was again pan dried and calcined at 600°C for 6 hours, followed by regrinding and recalcination at 800°C for 3 hours. X-ray powder patterns taken with CuK_α radiation showed sharp diffraction peaks up to high angles. There were no phases present other than rhombohedral (R3m) PZT.

NEUTRON DIFFRACTION STUDIES

Data Collection

Neutron data from a $PbZr_{0.6}Ti_{0.4}O_3$ pellet were collected at the Brookhaven high flux beam reactor at T = 295, 200, and 9 K. Pyrolytic graphite in the (002) and (004) reflection positions were used as monochromator and analyzer, respectively. The neutron wave length was 1.429 Å for the 200 K and 9 K patterns and 1.650 Å for the 295 K pattern. Higher order components were removed with a

pyrolytic graphite filter. Data were collected at 0.05 deg intervals over each peak within 2θ = 20 - 125° range for the 295 and 9 K scans and 20-60° for the 200 K scan.

The extra hkl reflections observed at 9 K were identified as the 311, 511, 531,... and other all odd reflections indexed on a doubled cell ($a \sim 8$ Å). The 295 and 200 K data showed no anomalies with all the observed reflection indexed on a small rhombohedral cell ($a \sim 4$ Å).

Structural Model and Data Reduction

Based on previous studies (10,11) the rhombohedral-rhombohedral transition was expected to stem from the tilt system $\bar{a}\ \bar{a}\ \bar{a}$ Glazer (12) or $\phi\ \phi\ \phi$ Aleksandrov (13). In the Glazer notation, the system of "rigid octahedra" tilts is represented by the symbol $a^{(i)}\ b^{(j)}\ c^{(k)}$ where a, b, and c represent rotations about the three pseudocubic axes. The superscripts (i), (j), and (k) denote the sense of rotations of adjacent corner-linked octahedra, such that (+) means the same sense, (-) means opposite sense, and (o) no rotation. Therefore, the tilt system $\bar{a}\ \bar{a}\ \bar{a}$ means three equal rotations of the Zr/TiO_6 octahedra about the pseudocubic axes <100>, with neighboring octahedra rotating in opposite senses. The tilt system $\bar{a}\ \bar{a}\ \bar{a}$ produces $R\bar{3}c$ (nonpolar) symmetry for the lower temperature phase (9 K). However, since this transition is expected to be similar to those reported previously for other PZT compositions (10,11), the structure was refined in space group (R3c). The polarity results from cation displacements along the rhombohedral [111] direction.

The $PbZr_{0.6}Ti_{0.4}O_3$ structures were refined by means of the profile-fitting technique (2,14). The following scattering lengths were used: Pb 0.94, Zr 0.71, Ti-0.34, O 0.58×10^{-12} cm. The refined parameters included a scale factor, three half-width parameters defining the Gaussian line shapes, a counter-zero error, isotropic temperature factors, atomic coordinates, and unit cell parameters.

In the rhombohedral phases we chose to use the double pseudocubic cell ($a \sim 8$ Å). The fractional atomic coordinates of the R3c phase are then given by:

	x	y	z
Pb	$\frac{1}{4} + S$	$\frac{1}{4} + S$	$\frac{1}{4} + S$
Zr/Ti	t	t	t
0	$-e + d$	$\frac{1}{4} - 2d$	$e + d$

S and t represent the fractional cation displacements along the three-fold axis, measured with respect to an origin lying midway between opposite faces of an oxygen octahedron. The parameter d is a measure of the octahedron distortion, which makes the upper and lower faces different. The e parameter indicates the rotation of an octahedron about the triad axis, with an angle of tilt ω, given by $\tan \omega = 4\sqrt{3}\ e$.

In the R3m phase there are no tilts and e is equal to zero. The pseudocubic cell is not doubled in this phase, but to facilitate comparison of the two phases we also used a doubled cell to describe R3m. This was accomplished for R3m by using the same symmetry operators used for R3c and adding the constraint $x=y$ for the prototype oxygen atom, in addition to $x+y+z = \frac{1}{4}$.

Table I summarizes the refined parameters in each phase. The numbers between brackets represent the standard deviation in the least significant digit. Figure 3 shows calculated and observed intensity profiles for the two phases. The fit between observed and calculated profiles is quite good. The metal oxygen bond lengths determined by neutron diffraction together with the sum of ionic radii "IR" of Shannon and Prewitt (15), are listed in Table II.

PYROELECTRIC DISCHARGE EXPERIMENT

The Chynoweth (16) technique used to determine the ferroelectric (R3m)-ferroelectric (R3c) phase transition temperature is shown in Fig. 4. The sample (a ceramic disc 2.8 mm in diameter and 0.11 mm thick) was electroded with evaporated silver and mounted on a glass substrate. Using an electric field of 20 kV/cm, the ceramic was poled at room temperature. Carbon black was coated on the upper silver electrode to absorb light. The sample was then mounted in a recessed copper holder and cooled with liquid helium in an Air Products LT-3-110 cold finger. A buffer FET preamplifier positioned within the cold finger was used to minimize loading capacitance on the sample, thereby maintaining reasonable signal levels. The sample was irradiated by a chopped defocused 4 mw He-Ne laser and the pyroelectric signal detected with a lock-in amplifier (PAR-HR8). The level of pyroelectric signal (mv) as a function of temperature for two heating/cooling cycles (H_1,C_1) and (H_2,C_2) is shown in Fig. 4. The heating/cooling rates were about 4-5 K/min.

The peak in the pyroelectric signal at 45 K is caused by changes in the spontaneous polarization at the rhombohedral-rhombohedral phase transition. The degradation of the pyroelectric signal as the sample was cycled through H_1, C_1, H_2, and C_2 is probably due to a depoling effect.

CORRELATION OF THE SPONTANEOUS POLARIZATION AND ATOMIC DISPLACEMENTS

Based on a survey of ten different ferroelectrics, Abrahams, Kurtz, and Jamieson (17) found that the spontaneous polarization P_S along the polar axis is linearly related to the homopolar atom shift δz (Å) by the relation,

$$P_S = K\,\delta z \qquad (2)$$

where K = 2.58 (9) C/m^2-Å.

A slightly different value of K = 2.51 (7) was found to hold for the $PbZrO_3$-$PbTiO_3$ system (18). Table III shows a comparison between P_S[111] as calculated from Eq (2) using the experimentally determined (Zr/Ti) shifts, and the P_S[111] values obtained from the (LGD) phenomenology. The agreement between the phenomenological P_S values and the values determined from Eq (2) is quite good.

SUMMARY AND CONCLUSIONS

A rhombohedra (R3m)-rhombohedral (R3c) phase transition was found to occur in $PbZr_{0.6}Ti_{0.4}O_3$ at T=45 K. The phase transition temperature was determined from pyroelectric measurements. The structures above and below the phase transition temperature were refined by the neutron profile fitting method (2,14).

The Landau-Ginsburg-Devonshire (LGD) phenomenological results showed no anomalies of morphotropic compositions below room temperature. The spontaneous polarization values P_S as determined from the phenomenological theory are in surprisingly good agreement with the values calculated from the (Zr/Ti) shifts using Abrahams, Kurtz and Jamieson relation.

Acknowledgments

Ahmed Amin wishes to thank the Brookhaven National Laboratory for the kind hospitality during his stay there. This work was supported by the Office of Naval Research, Contract No. N00014-78-C-0291.

REFERENCES

1. B. Jaffe, W.R. Cook and H. Jaffe, "Piezoelectric Ceramics," Academic Press, London (1971).
2. H.M. Rietveld, J. Appl. Cryst. 2, 65 (1969).
3. F. Jona and G. Shirane, "Ferroelectric Crystals," Pergamon Press, Oxford (1962).
4. E. Fatuzzo and W.J. Mertz, "Ferroelectricity," John Wiley and Sons, New York (1967).
5. E.M. Lines and A.M. Glass, "Principles and Applications of Ferroelectrics and Related Materials," Clarendon Press, Oxford (1977).
6. A.F. Devonshire, Phil. Mag. 40, 1040 (1949).
7. V. Ginsburg, J. Exp. Theor. Phys. SSSR, 15, 739 (1945).
8. A. Amin, B. Badger, Jr., H. McKinstry and L.E. Cross (to be published).
9. H.A. Kruger, "Final Technical Report," Clevite Corporation, Cleveland (1971).
10. C. Michel, J.M. Moreau, G.D. Achenbach, R. Gerson and W.J. James, Solid State Commun. 1, 865 (1969).
11. A.M. Glazer, S.A. Mabud and R. Clarke, Acta Cryst. B34, 1060 (1978).
12. A.M. Glazer, Acta Cryst. B28, 3384 (1972).
13. K.S. Aleksandrov, Ferroelectrics, 14, 801 (1976).
14. A.W. Hewat, J. Phys. C6, 2559 (1973).
15. R.D. Shannon and C.T. Prewitt, Acta Cryst. B25, 925 (1969).
16. A.G. Chynoweth, J. Appl. Phys. 27, 78 (1956).
17. S.C. Abrahams, S.K. Kurtz and P.B. Jamieson, Phys. Rev. 172, 551 (1968).
18. A. Amin, R.E. Newnham and L.E. Cross (to be published).

REFERENCES

1. B. Jaffe, W.R. Cook and H. Jaffe, "Piezoelectric Ceramics," Academic Press, London (1971).
2. H.M. Rietveld, J. Appl. Cryst. 2, 65 (1969).
3. F. Jona and G. Shirane, "Ferroelectric Crystals," Pergamon Press, Oxford (1962).
4. E. Fatuzzo and W.J. Mertz, "Ferroelectricity," John Wiley and Sons, New York (1967).
5. E.M. Lines and A.M. Glass, "Principles and Applications of Ferroelectrics and Related Materials," Clarendon Press, Oxford (1977).
6. A.F. Devonshire, Phil. Mag. 40, 1040 (1949).
7. V. Ginsburg, J. Exp. Theor. Phys. SSSR, 15, 739 (1945).
8. A. Amin, B. Badger, Jr., H. McKinstry and L.E. Cross (to be published).
9. H.A. Kruger, "Final Technical Report," Clevite Corporation, Cleveland (1971).
10. C. Michel, J.M. Moreau, G.D. Achenbach, R. Gerson and W.J. James, Solid State Commun. 1, 865 (1969).
11. A.M. Glazer, S.A. Mabud and R. Clarke, Acta Cryst. B34, 1060 (1978).
12. A.M. Glazer, Acta Cryst. B28, 3384 (1972).
13. K.S. Aleksandrov, Ferroelectrics. 14, 801 (1976).
14. A.W. Hewat, J. Phys. C6, 2559 (1973).
15. R.D. Shannon and C.T. Prewitt, Acta Cryst. B25, 925 (1969).
16. A.G. Chynoweth, J. Appl. Phys. 27, 78 (1956).
17. S.C. Abrahams, S.K. Kurtz and P.B. Jamieson, Phys. Rev. 172, 551 (1968).
18. A. Amin, R.E. Newnham and L.E. Cross (to be published).

Table I

REFINED PARAMETERS FOR $PbZr_{0.6}Ti_{0.4}O_3$

	Temperature	9 K	200 K	295 K
SHAPE PARAMETERS	Phase	F_R (LT)	F_R (HT)	F_R (HT)
	Space group	R3c (C_{3v}^6)	R3m (C_{3v}^5)	R3m (C_{3v}^5)
	a_h (Å)	5.7597 (5)	5.7682 (11)	5.7550 (4)
	c_h (Å)	14.2510 (12)	14.2529 (23)	14.2138 (11)
	2a (Å)	8.1730 (6)	8.1821 (15)	8.1618 (4)
	α (°)	89.614 (3)	89.667 (9)	89.676 (3)
DISTORTION PARAMETERS	S	0.0343 (3)	0.0343 (11)	0.0310 (4)
	t	0.0114 (5)	0.0110 (19)	0.0108 (7)
	d	-0.0028 (1)	-0.0026 (2)	-0.0023 (1)
	e	0.0105 (2)	---	---
	ω (°)	4.164 (1)	---	---
THERMAL PARAMETERS	B (Pb)	0.57 (5)	0.9 (5)	1.94 (1)
	B (Zr/Ti)	1.50 (2)	-1.2 (1.2)	1.10 (17)
	B (O)	1.24 (8)	1.4 (3)	1.57 (7)
STATISTICAL PARAMETERS	Number of Parameters (P)	15	13	13
	Number of Observations(N)	802	273	934
	Number of Reflections	48	16	45
	R_1%	1.68	3.08	4.85
	R_2%	10.37	9.79	11.08
	R_3%	11.70	12.54	14.28
	R_{exp}%	9.55	9.24	6.34

$R_1 = 100 \sum [I_{(obs)} - \frac{1}{C} I_{(calc)}]/\sum I_{(obs)}$

$R_2 = 100 \sum [y_{(obs)} - \frac{1}{C} y_{(calc)}]/\sum y_{(obs)}$

$R_3 = 100\sqrt{\sum w[y_{(obs)} - \frac{1}{C} y_{(calc)}]^2/\sum w[y_{(obs)}]^2}$

R_{exp} - the expected R-factor = $100\sqrt{(N-P+C)/\sum w[y_{(obs)}]^2}$

$I_{(obs)}$, $I_{(calc)}$ = observed and calculated integrated intensity of each reflection.

$y_{(obs)}$, $y_{(calc)}$ = observed and calculated profile data.

w = weight allotted to each data point.

$$R_1 = 100 \sum [I_{(obs.)} - \frac{1}{C} I_{(calc.)}]/\sum I_{(obs.)}$$

$$R_2 = 100 \sum [y_{(obs.)} - \frac{1}{C} y_{(calc.)}]/\sum y_{(obs.)}$$

$$R_3 = 100\sqrt{\sum w[y_{(obs.)} - \frac{1}{C} y_{(calc.)}]^2/\sum w[y_{(obs.)}]^2}$$

R_{exp} - the expected R-factor = $100\sqrt{(N-P+C)/\sum w[y_{(obs.)}]^2}$

$I_{(obs.)}$, $I_{(calc.)}$ = observed and calculated integrated intensity of each reflection.

$y_{(obs.)}$, $y_{(calc.)}$ = observed and calculated profile data.

w = weight allotted to each data point.

Table II

METAL-OXYGEN BOND LENGTHS

*Bond Type	T = 295 K	T = 200 K	T = 9 K	Sum of "IR"
$Zr/Ti-O_1$	1.995	2.003	2.005	2.07
$Zr/Ti-O_2$	2.098	2.100	2.101	
$Pb-O_1$	2.912	2.926	3.041	2.89
$Pb-O_2$	2.515	2.483	2.481	

*O_1 and O_2 represent the oxygen atoms in the upper and lower faces respectively of an octahedron viewed along [111].

Table III

(Zr/Ti) ATOM SHIFTS AND SPONTANEOUS POLARIZATION

T(K)	$(Zr/Ti)_O$ Shifts δz (Å)	P_S[111] C/m^2-Å from eq (2)	P_S[111] C/m^2-Å from (LGD) eq (1)
295	0.154 (9)	0.39 (3)	0.34
200	0.157 (27)	0.39 (6)	0.36
9	0.162 (7)	0.41 (2)	0.39*

*Taking into account the zone center mode only.

FIGURE CAPTIONS

Fig. 1 $PbZrO_3$-$PbTiO_3$ phase diagram (after Jaffe, Cook and Jaffe (1)).

Fig. 2 Elastic Gibbs free energy as a function of composition across the single cell region of the PZT phase diagram for three temperatures below room temperature.

Fig. 3 Observed (dots) and calculated (full line) neutron intensity profile for the two phases of $PbZr_{0.6}Ti_{0.4}O_3$. The lower trace in each case is the difference between observed and calculated profiles. (a) F_R(HT) at 295 K; (b) F_R(LT) at 9 K.

Fig. 4 Experimental arrangement and the pyroelectric signal as a function of temperature. The four curves represent successive heating and cooling cycles.

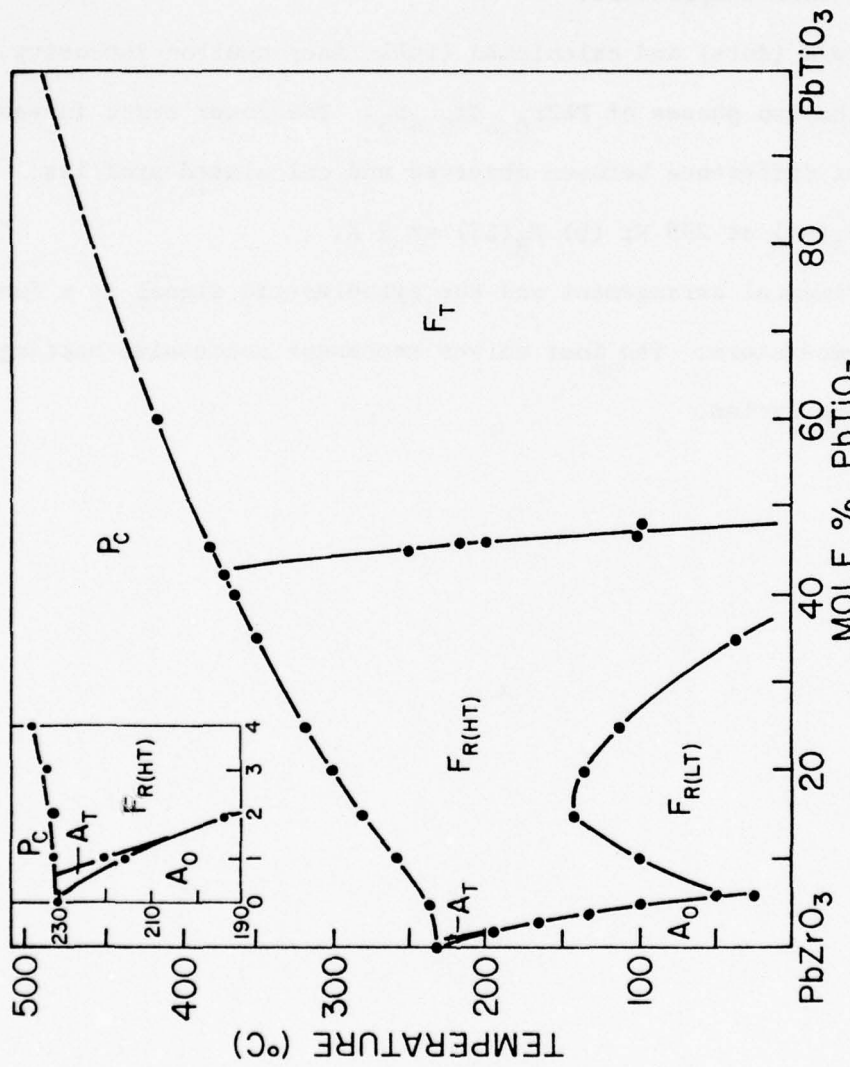
TEMPERATURE (°C)
500
400
300
200
100
PbZrO3
20
40
60
80
PbTiO3
MOLE % PbTiO3
Pc
FT
FR(HT)
FR(LT)
AT
AO
230
210
190
0
1
2
3
4

Figure 1

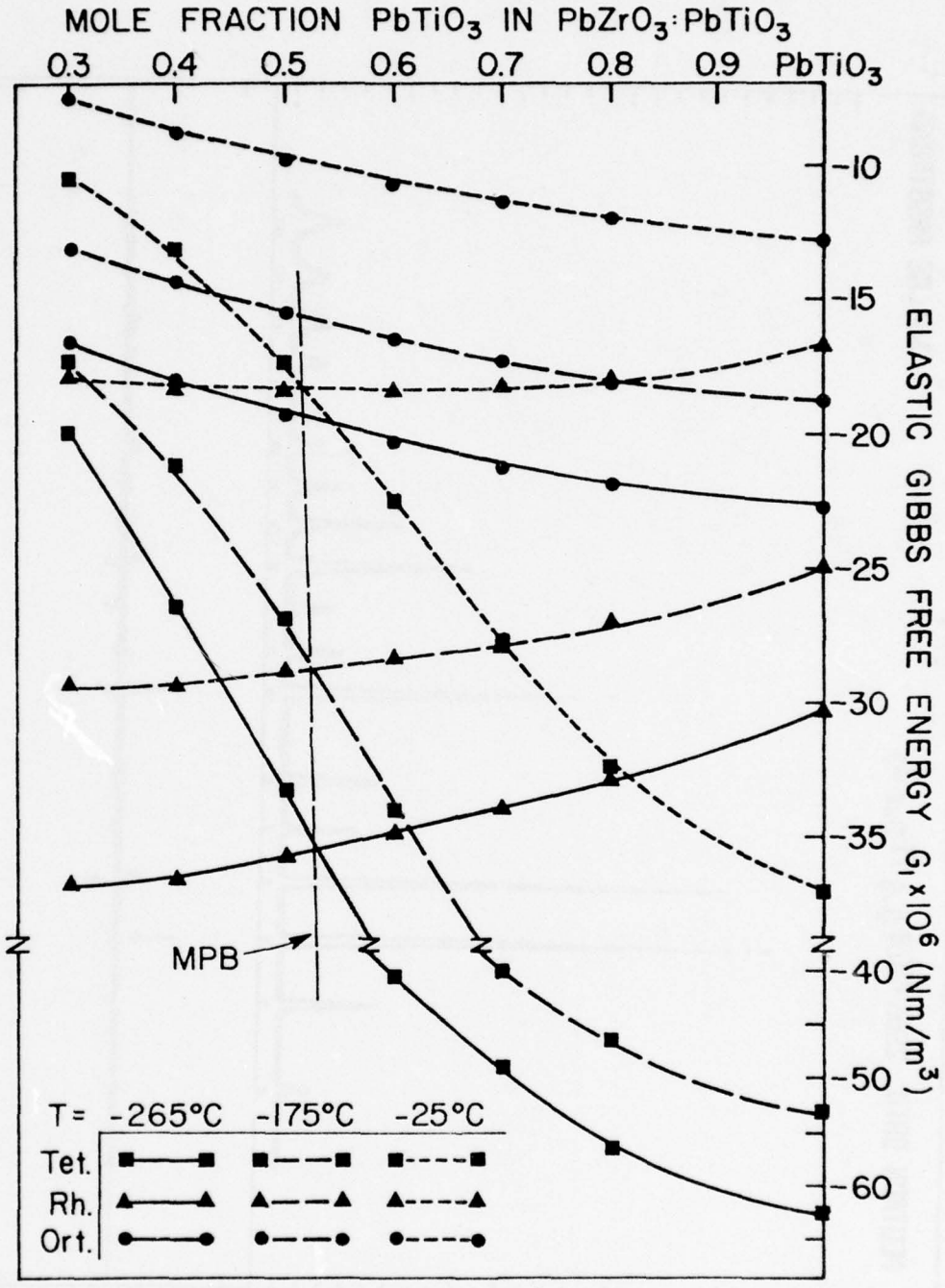
MOLE FRACTION $PbTiO_3$ IN $PbZrO_3$:$PbTiO_3$
0.3
0.4
0.5
0.6
0.7
0.8
0.9
$PbTiO_3$
-10
-15
-20
-25
-30
-35
-40
-50
-60
ELASTIC GIBBS FREE ENERGY $G_1 \times 10^6$ (Nm/m^3)
MPB
T= -265°C -175°C -25°C
Tet.
Rh.
Ort.

Figure 2

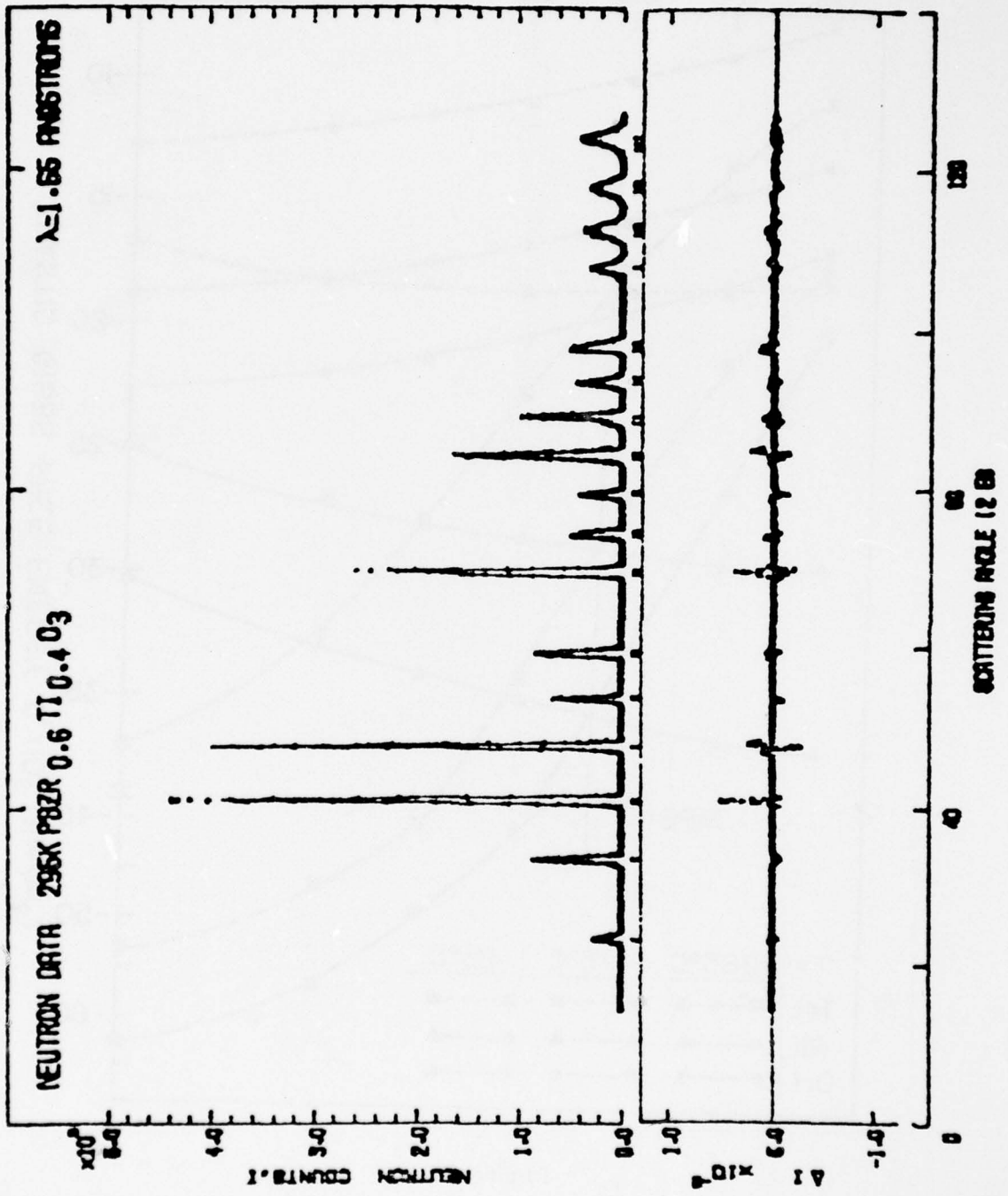
NEUTRON DATA 295K PBZR 0.6 TI 0.4 O3
λ=1.65 ANGSTROMS
NEUTRON COUNTS
SCATTERING ANGLE (2 θ)
Δ I

Figure 3a

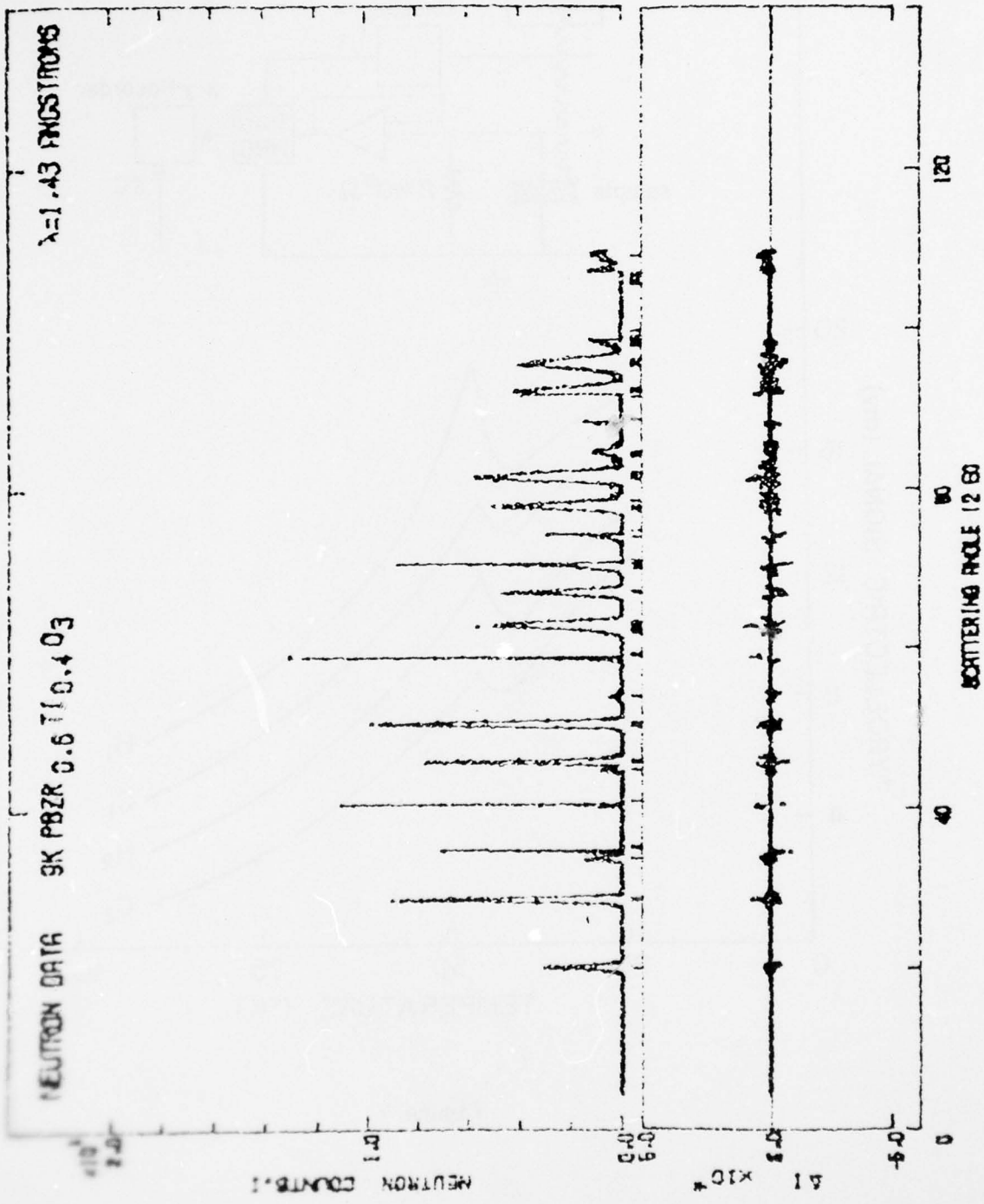
NEUTRON DATA 9K PBZR 0.6 TI 0.4 O3
λ=1.43 ANGSTROMS
NEUTRON COUNTS
SCATTERING ANGLE (2 θ)
0
40
80
120

Figure 3b

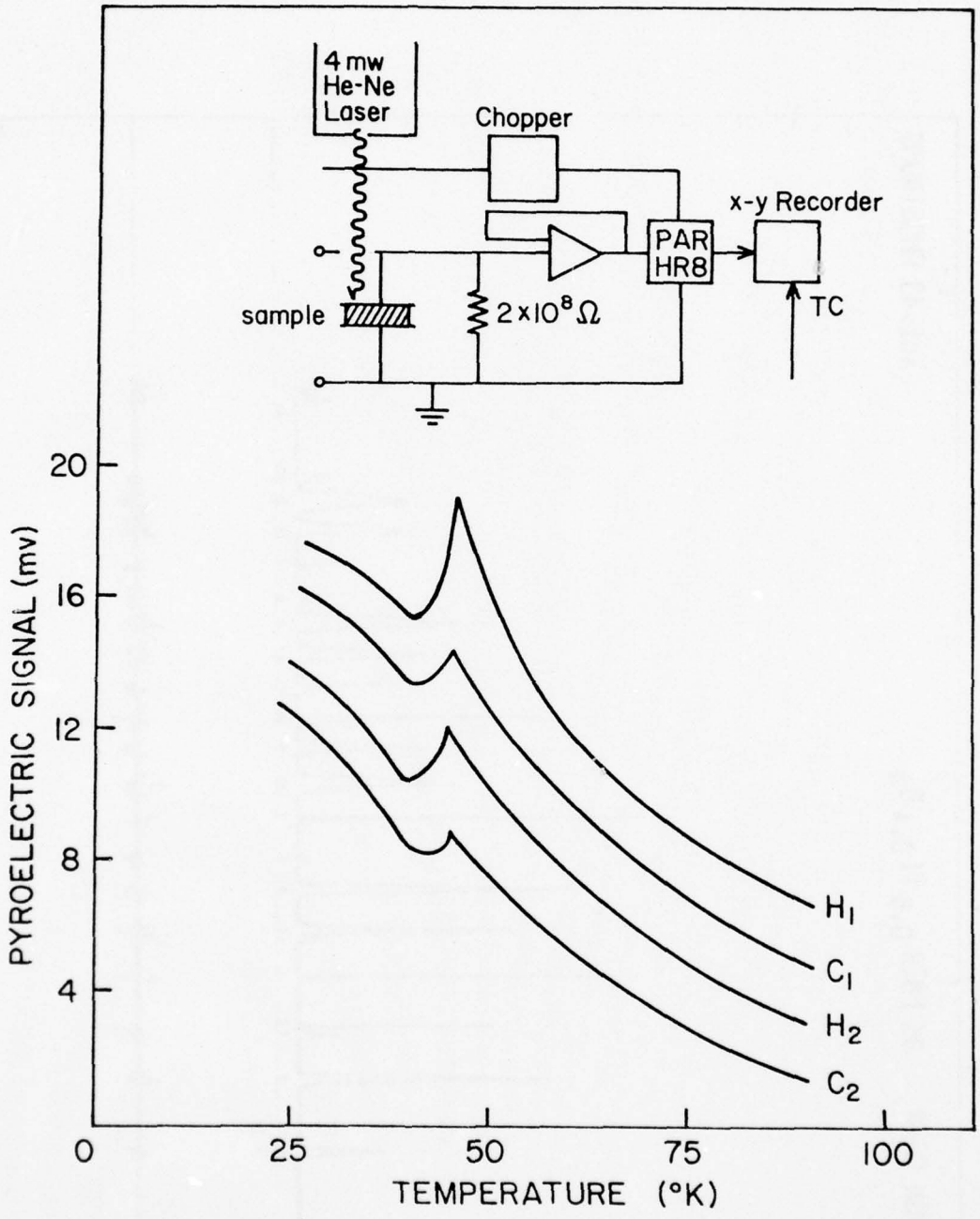
4 mw
He-Ne
Laser
Chopper
x-y Recorder
PAR
HR8
TC
sample
2x10^8 Ω
PYROELECTRIC SIGNAL (mv)
20
16
12
8
4
0
25
50
75
100
TEMPERATURE (°K)
H1
C1
H2
C2

Figure 4

MISCELLANEOUS

APPENDIX 18

L.L. Tongson, A.S. Bhalla, L.E. Cross and B.E. Knox. Investigation of $BaTiO_3$ and $Gd_2(MoO_4)_3$ Crystal Surfaces by Complementary AES and ISS Techniques. Appl. Surf. Sci. (accepted).

INVESTIGATION OF $BaTiO_3$ AND $Gd_2(MoO_4)_3$ CRYSTAL SURFACES BY COMPLEMENTARY AES AND ISS TECHNIQUES

L. L. Tongson, A. S. Bhalla, L. E. Cross and B. E. Knox

Materials Research Laboratory
The Pennsylvania State University
University Park, PA 16802

ABSTRACT

The chemical nature of the intrinsic surface layer in $BaTiO_3$ single crystals and the positive and negative surfaces of gadolinium molybdate have been determined using AES and ISS. Potassium and fluorine were detected in $BaTiO_3$ crystals grown by the Remeika method. The ratio of the AES 417 eV to 411 eV peaks of Ti in $BaTiO_3$ was stable under ion and electron beam irradiation. ISS showed that the positive and negative surfaces of gadolinium molybdate crystals were chemically identical, with both types exhibiting similar variations in the Gd and Mo signals with ion bombardment time. However, marked differences in the spectra of sputtered and scattered ions from each type were observed.

1. INTRODUCTION

Basic studies of ferroelectric crystal surfaces are of interest and importance for several reasons. First, the ferroelectrics are a subgroup of the much larger family of polar crystals. In all these materials the surface properties will be markedly modified by the orientation of the electric polarization vector with respect to the crystal surface. In ferroelectrics, because of the domain structure and switching possibility, these effects can be studied in a simple and controlled manner. Second, in many ferroelectrics, several experimental studies [1] have provided indirect evidence of the existence of a "modified" layer at the surfaces of these crystals. In general, two types of models have been proposed to explain observed data: (i) a physical model of space charge layers due to surface ionic vacancies [2], and (ii) a chemical model in which the thin layer is part of the crystal [3] and may be chemically different from the bulk [4-5]. Third, studies of ferroelectric surfaces are necessary in order to optimize the performance of these materials as stable and efficient electrodes for the photoelectrolysis of water in photoelectrochemical cells [6].

Another important feature in ferroelectrics is the apparent influence of the electric fields associated with the emergent spontaneous polarization on the chemical reactivities of the surfaces. Such differences in reaction rates have been utilized recently by Bhalla and Cross [7] to reveal the ferroelectric domains in gadolinium molybdate ($Gd_2(MoO_4)_3$ or GMO) crystals. When dipped in a dilute hydrofluoric acid, coherent and firmly adhering films of gadolinium fluoride are produced on the surface [8]. The thickness of the film differs for domains of opposite polarity, so that the underlying domain structure is revealed in reflected white light by clear interference colors.

In the present study, complementary techniques of Auger electron spectrometry (AES) and ion scattering spectrometry (ISS) have been utilized to

determine the chemical nature of (1) "as grown" $BaTiO_3$, and (2) polished surfaces of GMO single crystals. The latter samples were particular interesting because essentially single domain faces (i.e., either positive or negative) could be obtained easily. Specifically, we wanted to determine secondary effects (if any) in the ISS spectra such as (a) displacement of scattered peaks [9] and (b) displacement of the appearance threshold of sputtered ions due to the polar nature of these surfaces.

2. EXPERIMENTAL

The multi-domain, unpoled, $BaTiO_3$ single crystals used in this study were grown by the Remeika method in a potassium fluoride flux. The surfaces were examined in the "as-grown" condition, i.e., without etching or polishing to determine the intrinsic layer.

The GMO samples were cut from a single crystal boule to obtain 8 x 8 x 2 mm plates with the major faces perpendicular to the ferroelectric [001] axis. After polishing with 1/4 μm alumina powder, the plates were poled by applying a shear stress along a b axis. The existence of single domains was verified optically by a polarizing microscope while the polarity of the domain was determined by piezoelectric measurements on a Berlincourt d_{33} meter.

Our studies were conducted in an instrument which combines AES and ISS in the same ultrahigh vacuum chamber. The ISS unit is a sector-type 3M model 520, while the AES unit is a Physical Electronics Industries model 25-G double-pass cylindrical mirror analyzer with a coaxial electron gun. Samples mounted in a carousel-type target holder are inclined 45° relative to the ion beam for ISS. A 180° rotation of the target holder about the Z axis positions the sample (previously analyzed by ISS) normal to the electron beam for AES. All measurements were made at room temperature after achieving a base pressure of $\sim 1 \times 10^{-6}$ Pa without system bakeout.

The ISS data were obtained at typical current densities of about 20-25 $\mu A/cm^2$ using a 1-mm-FWHM-diam. 1500 eV He-4 ion beam. For studying oppositely poled surfaces of GMO, the spectra were recorded under identical experimental conditions, i.e., constant ion beam and charge neutralization currents.

The normally incident electron beam in AES caused charging problems in some cases. When no charging was encountered, the AES data were collected using a 0.25-mm-FWHM-diam. 2 KeV 15 μA primary electron beam, while a 2V peak-to-peak modulation voltage was used in recording the derivative spectra at a rate of 2 eV/sec.

3. RESULTS AND DISCUSSION

3.1 $BaTiO_3$ Crystals

Figure 1 shows the ISS data obtained from the "as-grown" $BaTiO_3$ crystal. The predominant impurities were potassium and fluorine. The plot shows that the Ba peak grows as the K peak decreases. The Ba signal assumed a stable value at the time that K was no longer detectable. Similar trends were observed in the oxygen and fluorine signals. Initial detection of Ba, Ti and oxygen suggested a non-uniform lateral distribution of impurities on the surface.

Inasmuch as the electron beam desorbs fluorine [8], the chemical composition profile of the intrinsic layer was not measured using AES. However, this technique was used to study the stability of titanium-to-oxygen bonding when these samples were irradiated with ion and electron beams.

An example of the Auger data on $BaTiO_3$ is shown in Fig. 2. The spectra were recorded after bombarding the crystal with 1.5 KeV Ar ions for 30 min. For purposes of comparison, the spectrum of Ti metal is included. One observes that significant changes occur in the LMM Auger transitions at ∿382 to 386 eV and in the valence band (LMV) transitions at ∿418 eV. The 382 eV and 386 eV

peaks of the metal appear as a single peak in Fig. 2(b). In addition, the Ti(418) peak in Fig. 2(a) is now split into two peaks at ∿411 eV and 417 eV in the titanate spectra. Such changes in the Auger spectra of Ti in Ti metal, TiO and TiO_2 were compared previously by Solomon and Baun [10]. In particular, differences in spectral shapes between TiO and TiO_2 were correlated with differences in the density of states of oxygen 2p and titanium 3d, 4s molecular orbitals.

The general features of Ti in $BaTiO_3$ were consistent with previously reported Auger spectra of Ti in TiO_2 [11], and in $SrTiO_3$ [12-13]. However, compared to TiO_2, the $BaTiO_3$ crystal surfaces exhibited greater stability under electron and ion beam irradiation. In TiO_2, Thomas [11] observed that the 417 eV/411 eV AES signal ratio changed from 0.31 to ∿1 when the surface was exposed to a 3 KeV, 15 μA electron beam for ∿2 min. More pronounced adverse effects of dissociation and reduction of the oxide were noted under 2 KeV, 9 μA Ar ion bombardment. In the $BaTiO_3$ crystals studied here, the corresponding 417 eV/411 eV ratios were stable, and varied from 0.14 to 0.23 among the samples. Incidentally, these values were similar to a ratio of ∿0.21 obtained from vacuum-fractured surfaces of $SrTiO_3$ by Henrich, et al. [12].

3.2 GMO Crystals

The composition of the outer surface of a GMO crystal polished with 1/4 μm alumina is revealed in a series of scans shown in Fig. 3. One interesting feature revealed by these spectra is the variation of the Mo signal relative to the Gd peak. Figure 4 is a plot of the Gd, Mo and O signals vs. ion bombardment time. Opposite trends are clearly indicated in the Gd and Mo profiles. Such changes could be due to initial shielding of Gd by Mo from the ion beam, or could be due to preferential sputtering of Mo from the surface. Regardless of the mechanism for these variations, no changes from the spectra

shown in Fig. 3(c) were observed even under prolonged ion bombardment.

The feature revealed by Fig. 3(a) was independent of surface preparation techniques: (1) mechanically polished (MP) with 1/4 μm alumina, (2) MP and annealed in air for 20 hours at 120°C, and (3) MP and chemically etched in HNO_3 acid. In addition, the variation of the Gd and Mo signals with ion bombardment time was the same for "positive" and "negative" surfaces. This can be readily understood inasmuch as switching from one polarity to the other involves less than 1Å displacements of oxygen atoms in the $(MoO_4)^{2-}$ tetrahedra [14].

Figure 5 shows the spectrum of sputtered and scattered ions for $^4He^+$ incident on the domain (a) with the positive end of the dipole on the surface, and (b) the negative domain of GMO. In Fig. 5(a), the position of the oxygen and gadolinium peaks are displaced from their normal values of 0.600 and 0.950 in 90° ISS. No shifts in position of the corresponding peaks for the negative domain was detected. Subtle differences in the energy distribution and intensity of sputtered ions from these two types of domains were also noted. In order to reveal such differences more clearly, a 500 eV Ne-20 ion beam was used.

Figure 6 shows a marked contrast in the energy distributions and intensities of the sputtered ions. Relative to the negative domain, Fig. 6(b), a considerable reduction in intensity accompanied by a broader distribution in energy was obtained in Fig. 6(a). In addition, the scattered peak in the latter was shifted to higher energies as observed previously in Fig. 5.

The displacement of ion scattering peaks from positions predicted by binary scattering was examined recently by Helbig, et al. [9]. They showed that displacement of ISS peaks to higher energies due to charging in insulating samples is caused by the repelling field which changes both the scattering angle and the impact energy of the incident ion during the collision. Similar

observations were obtained for a conducting target deliberately biased with a positive voltage. In the latter study, however, changes in the sputtered ions were not indicated.

Our own investigations [15] on sputtered and scattered peaks using a WC-Co composite target biased sequentially at -21.6, 0.00 and +21.6 volts relative to ground showed that the sputtered ions peak started at 0, 0 and ~12 V above ground, respectively. That is, at positive bias, the beginning of the sputtered peak is shifted towards higher energies.

The data shown in Fig. 5 and Fig. 6 do not show a shift in the appearance threshold of the sputtered peak. On this basis, the displacement of the scattered peaks cannot be attributed to build-up of surface charges alone. Additional work is necessary before an unambiguous interpretation of these effects can be made. In particular, the use of some other scheme of charge compensation, such as direct electron bombardment may be necessary. Nevertheless, the experimental data indicate that under identical instrumental conditions, significant differences were noted in the sputtered ion and scattered ion spectra obtained from positive and negative domains of GMO.

REFERENCES

[1] M. E. Lines and A. M. Glass, Principles and Applications of Ferroelectrics and Related Materials, Clarendon Press, Oxford, 1977, p. 117.

[2] W. Kanzig, Phys. Rev. 98 (1958) 549.

[3] M. E. Drougard and R. Landauer, J. Appl. Phys. 30 (1959) 1663.

[4] F. C. Lissalde and J. C. Peuzin, Ferroelectrics 4 (1972) 159.

[5] Yu. Ya. Tomashpolskii, E. N. Lubnin and M. A.Sevost'yanov, Sov. Phys. Crystallogr. 22 (1977) 330.

[6] R. D. Nasby and R. K. Quinn, Mat. Res. Bull. 11 (1976) 985.

[7] A. S. Bhalla and L. E. Cross, J. Mater. Sci. 12 (1977) 2346.

[8] A. S. Bhalla, L. L. Tongson, I. S. T. Tsong and L. E. Cross, Thin Solid Films 53 (1978) 55.

[9] H. F. Helbig, P. J. Adelmann, A. C. Miller and A. W. Czanderna, Nucl. Instrum. and Methods 149 (1978) 581.

[10] J. S. Solomon and W. L. Baun, Surf. Sci. 51 (1975) 228.

[11] S. Thomas, Surf. Sci. 55 (1976) 754.

[12] V. E. Henrich, G. Dresselhaus and H. J. Zeiger, Phys. Rev. B 17 (1978) 4908.

[13] W. J. Lo and G. A. Somorjai, Phys. Rev. B 17 (1978) 4942.

[14] E. T. Keve, S. C. Abrahams and J. L. Bernstein, J. Chem. Phys. 54 (1971) 3185.

[15] L. L. Tongson and B. E. Knox, unpublished data.

FIGURE CAPTIONS

Fig. 1. ISS signal vs. sputtering time for the intrinsic layer in Remeika grown $BaTiO_3$ crystals. Primary ion beam energy was 1500 eV.

Fig. 2. Partial AES spectrum of titanium obtained from (a) an evaporated Ti film, and (b) a $BaTiO_3$ crystal irradiated with 1.5 KeV Ar ions for 30 min.

Fig. 3. The spectrum of 1500 eV $^4He^+$ ions scattered from a GMO crystal at (a) 1 min, (b) 17 min., and (c) 40 min. of ion bombardment.

Fig. 4. Variation of gadolinium, molybdenum and oxygen ISS signals from GMO vs. ion bombardment time.

Fig. 5. Scattered and sputtered ion spectra for 1500 eV $^4He^+$ incident on (a) the domain with the positive end of the dipole on the surface, and (b) the negative domain of GMO crystals.

Fig. 6. Sputtered and scattered ion spectra for 500 eV $^{20}Ne^+$ ions incident on (a) the positive domain, and (b) the negative domain of GMO crystals.

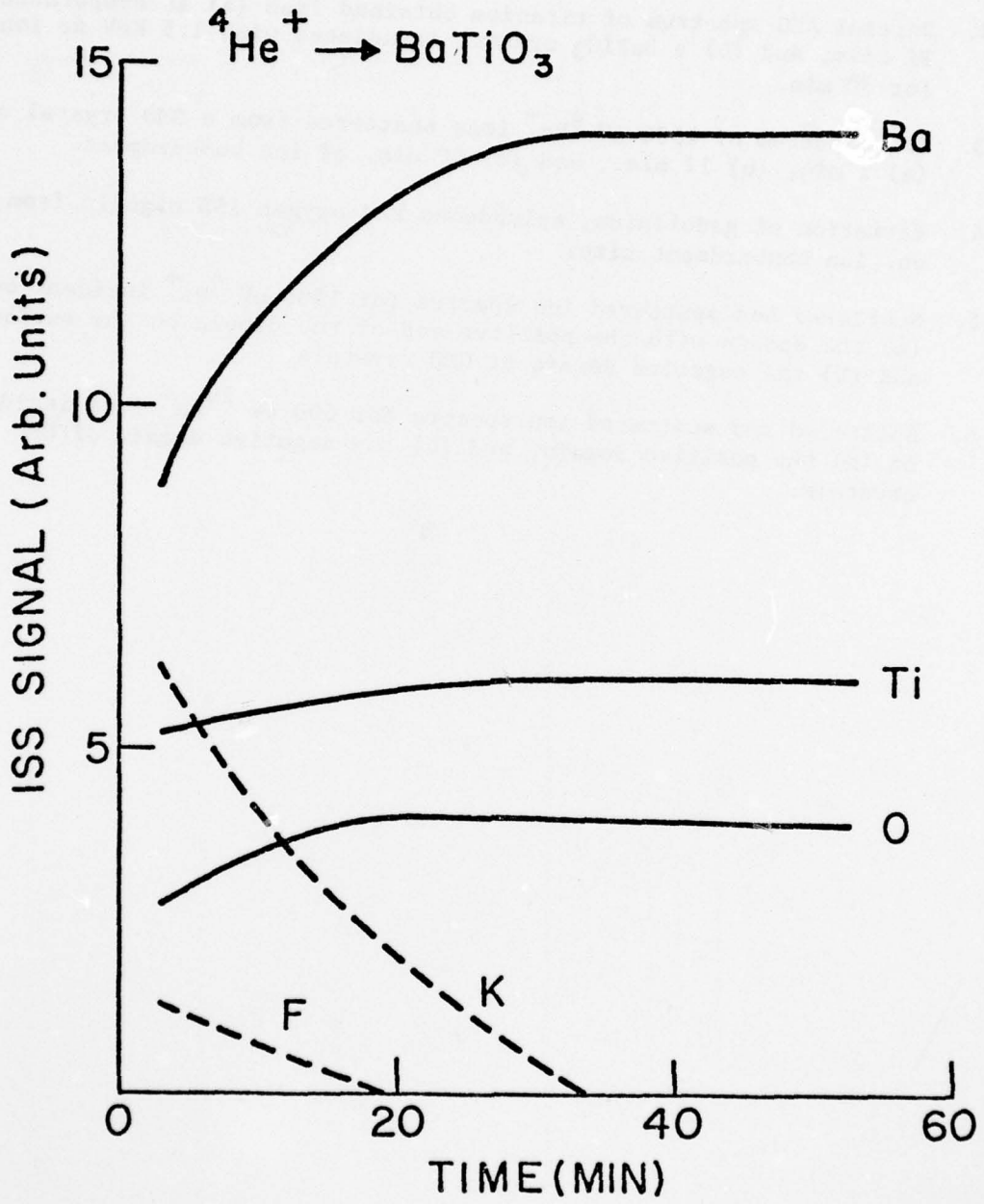
$^4He^+ \rightarrow BaTiO_3$
15
10
5
ISS SIGNAL (Arb. Units)
Ba
Ti
O
K
F
0
20
40
60
TIME (MIN)

Figure 1

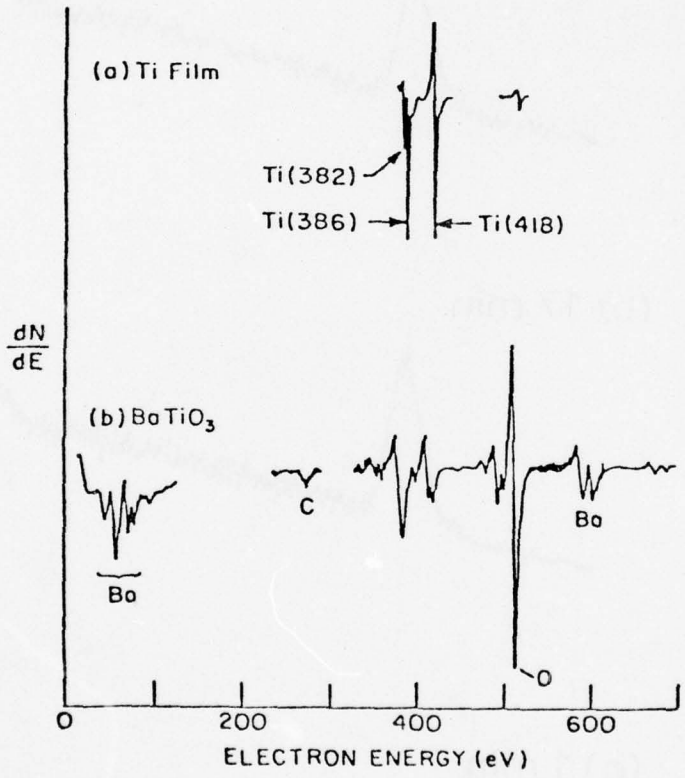
(a) Ti Film
Ti(382)
Ti(386)
Ti(418)
dN/dE
(b) BaTiO3
Ba
C
Ba
O
0
200
400
600
ELECTRON ENERGY (eV)

Figure 2

AD-A079 400 PENNSYLVANIA STATE UNIV UNIVERSITY PARK MATERIALS RE--ETC F/G 9/1
TARGETED BASIC STUDIES OF FERROELECTRIC AND FERROELASTIC MATERI--ETC(U)
DEC 79 L E CROSS , R E NEWNHAM , G R BARSCH N00014-78-C-0291

UNCLASSIFIED NL

4 OF 4
AD A 079400

END
DATE FILMED
2 -80
DDC

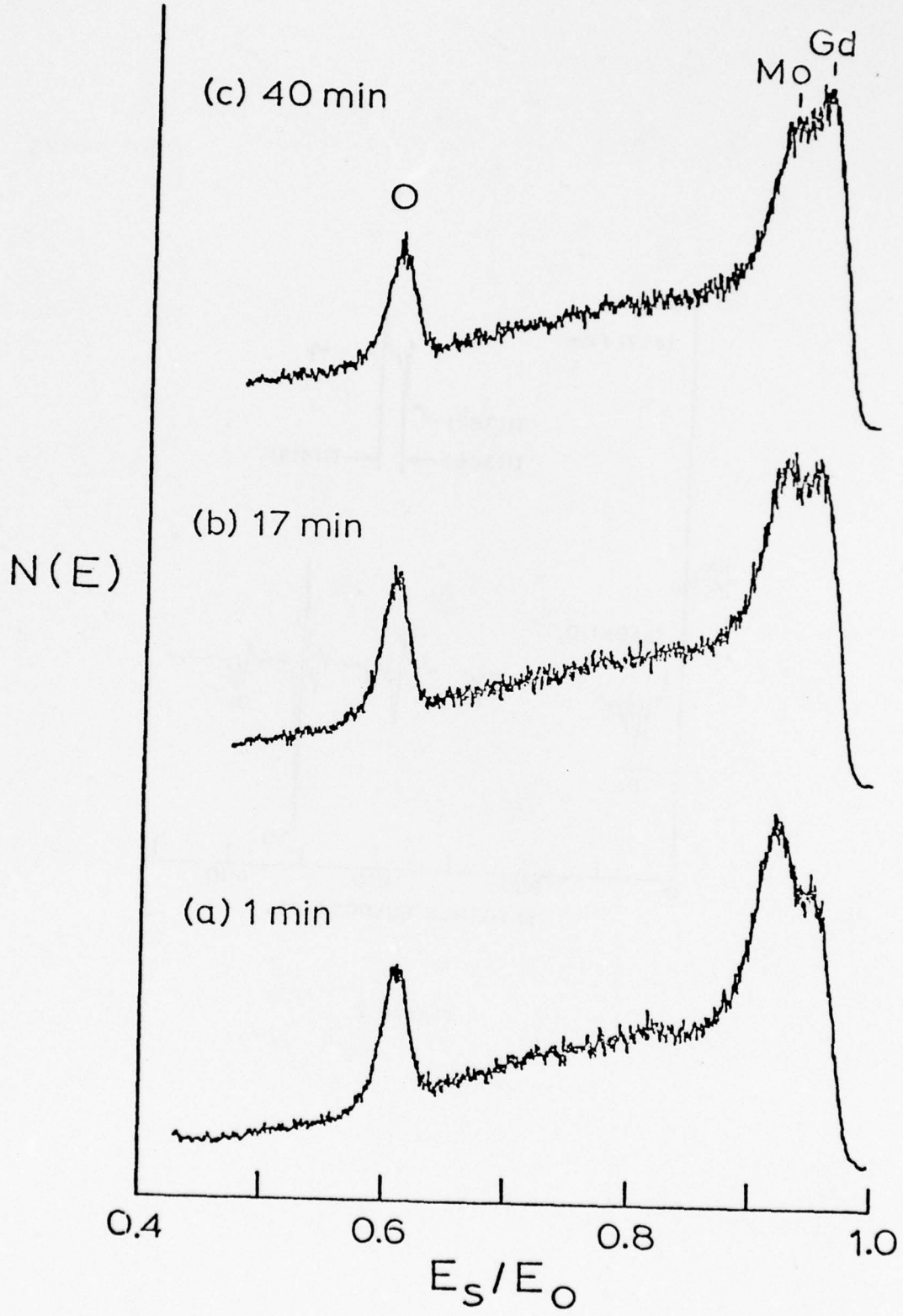

Figure 3

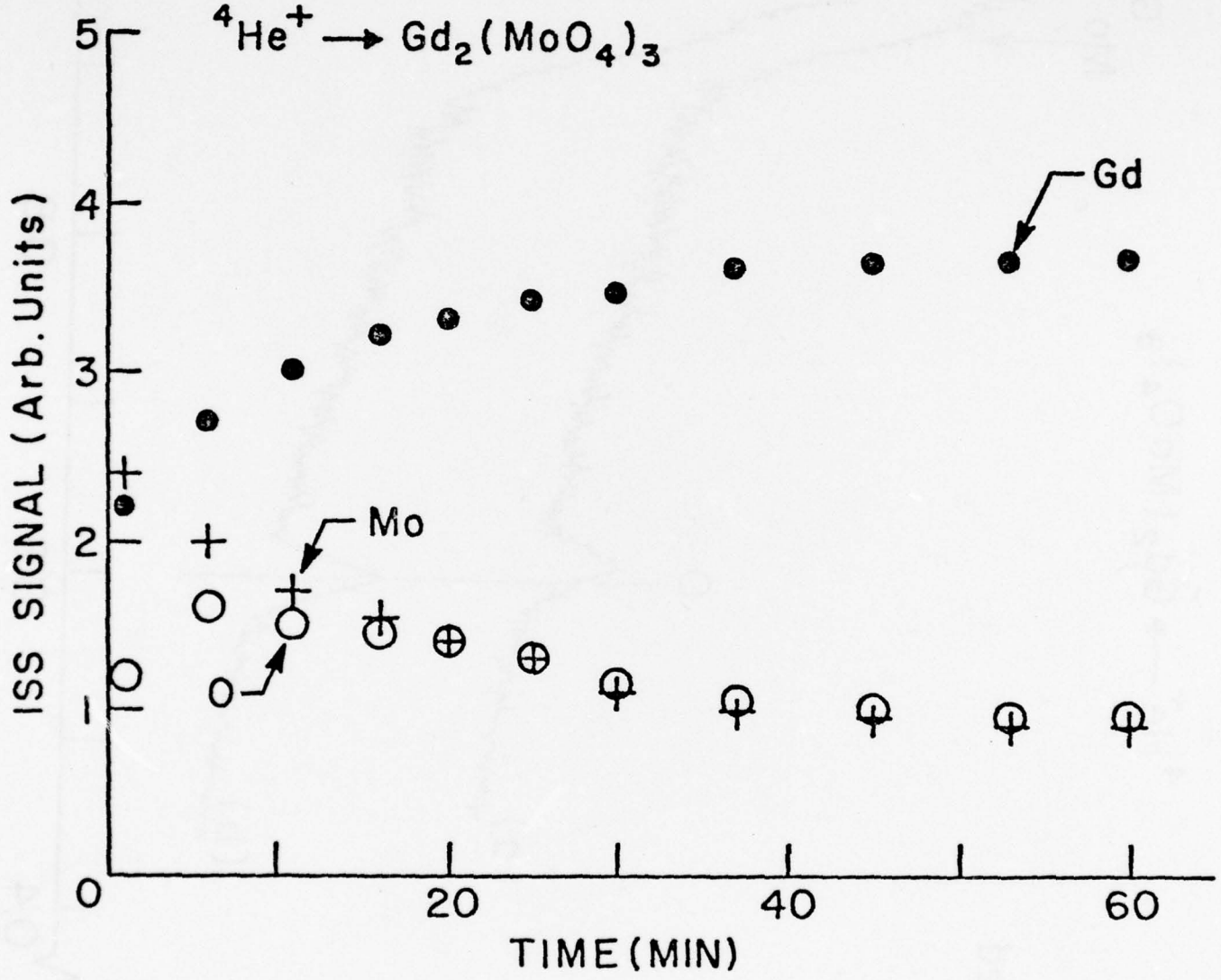
$^4He^+ \rightarrow Gd_2(MoO_4)_3$
ISS SIGNAL (Arb. Units)
TIME (MIN)
Gd
Mo
0
1
2
3
4
5
0
20
40
60

Figure 4

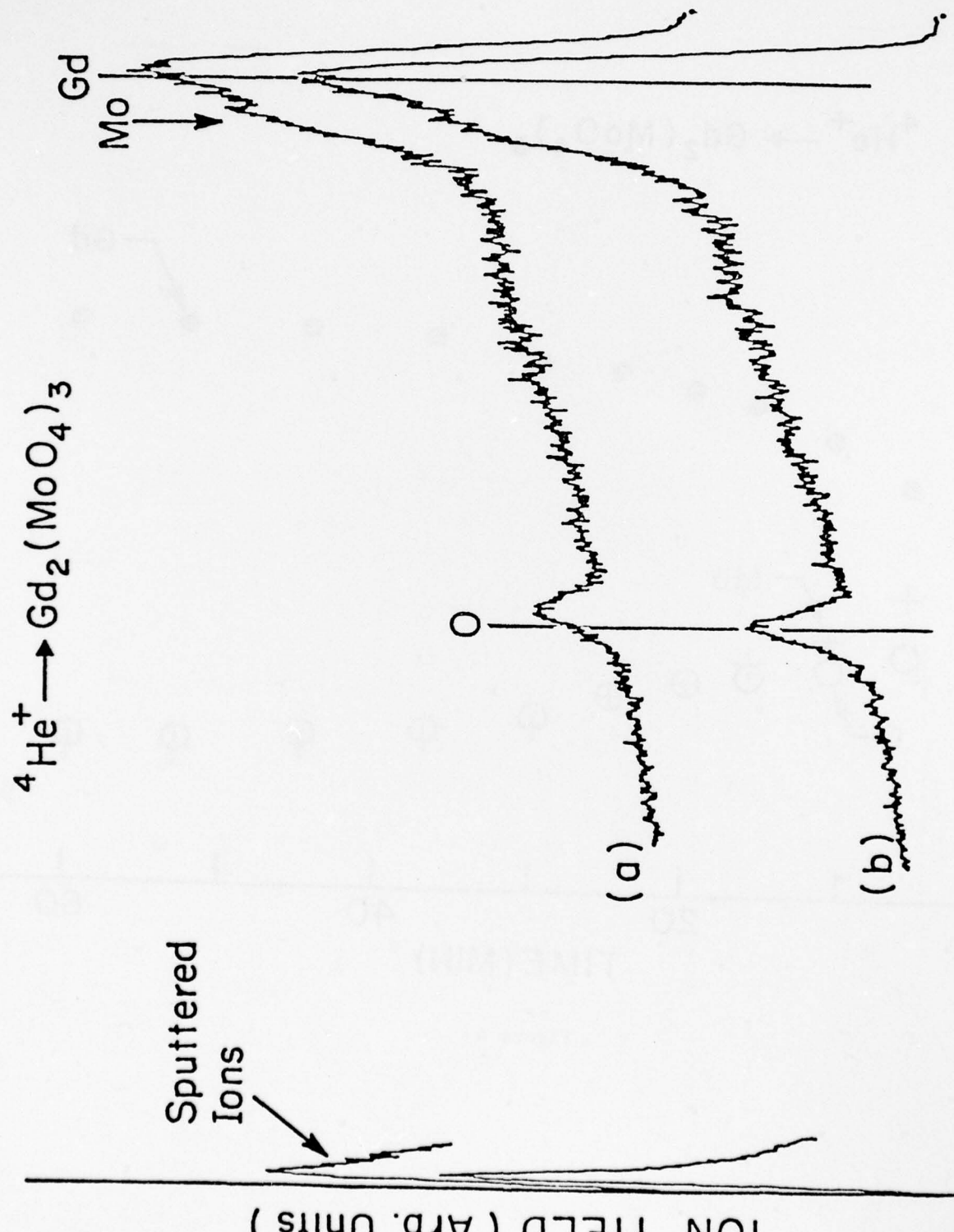
ION YIELD (Arb. Units)
Sputtered Ions
$^4He^+ \longrightarrow Gd_2(MoO_4)_3$
Gd
Mo
O
(a)
(b)
0.0
0.4
0.6
0.8
1.0

Figure 5

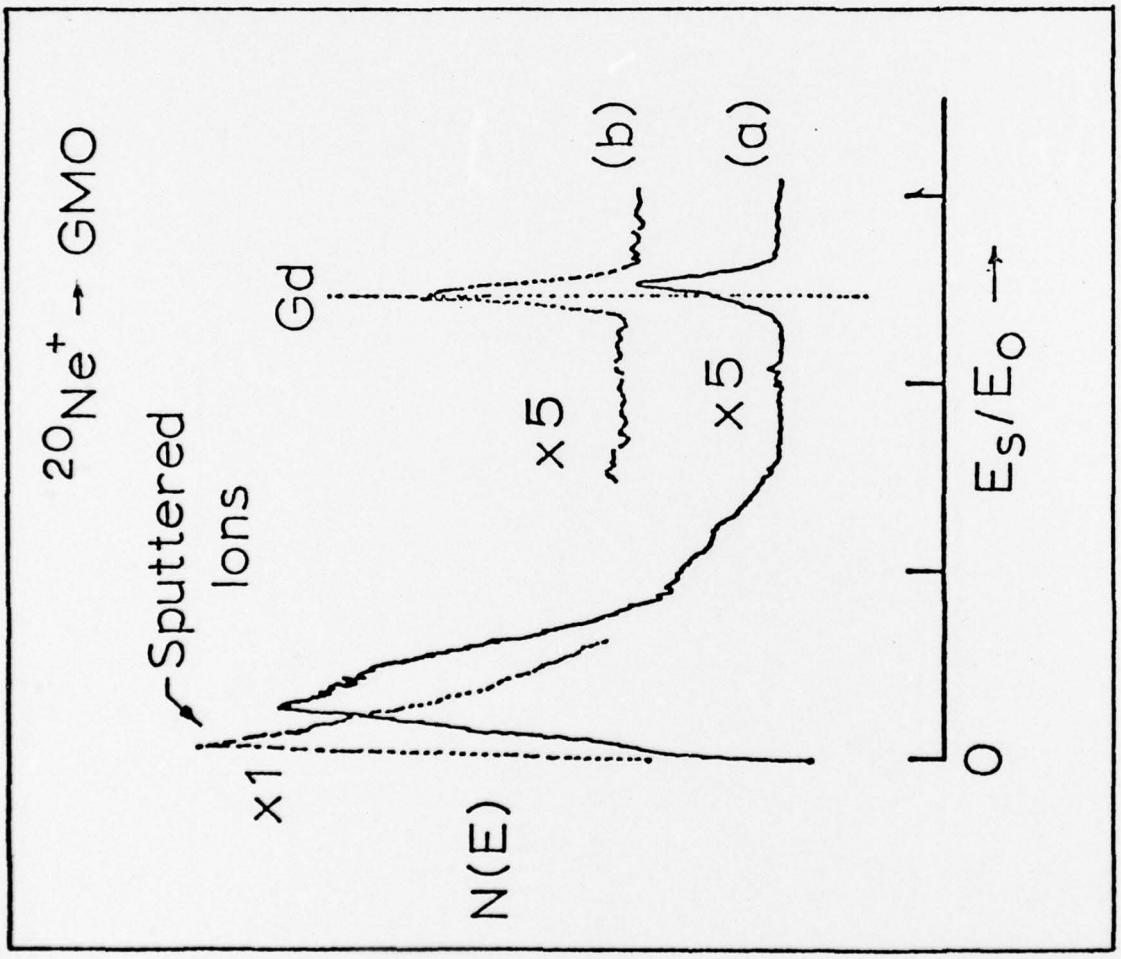

Figure 6

APPENDIX 19

K. Takahashi, L.H. Hardy, R.E. Newnham and L.E. Cross. Pyroeffect in $PbGe_3O_{11}$ and $Pb_5Ge_2SiO_{11}$ Crystals Prepared by Glass Recrystallization.

F - 11

Pyroeffect in $Pb_5Ge_3O_{11}$ and $Pb_5Ge_2SiO_{11}$ Monocrystals Prepared by Glass-recrystallization

Koichiro TAKAHASHI, L.H. HARDY*, R.E. NEWNHAM* and L.E. Cross*

Nat. Inst. for Res. in Inorg. Mat., Sakura-Mura, Ibaraki-Ken, JAPAN,
*Mat. Res. Lab., Penn. State Univ., University Park, PA., U.S.A.

Thin plate-like monocrystals of ferroelectric $Pb_5Ge_{3-x}Si_xO_{11}$ ($0 \leq x \leq 1.5$) with an orientation of the polar c-axis perpendicular to the surface were prepared by glass-recrystallization. For x=0 and x=1, temperature dependences of dielectric constant, dissipation factor, spontaneous polarization and coercive field were measured, to give sufficient ferroelectric quality equivalent to the crystals obtained by the Czochralski method. The pyroelctric responsivities R_v were recorded as large as about 3(V/W) at 14Hz with 10MΩ external resistance, whose performances are comparable to commercial detectors of TGS and $LiTaO_3$. The value of R_v for x=1 was greater than for x=0 because of a larger pyroelectric coefficient.

1. Introduction

Lead germanate $Pb_5Ge_3O_{11}$ (abbreviated as PGO here) and its isomorphs $Pb_5Ge_{3-x}Si_xO_{11}$ with $0 \leq x \leq 1$ are ferroelectric at room temperature,[1),2)] chemically stable, and have high pyroelectric coefficients as well as relatively low dielectric constants,[3),4)] being expected to be used as infrared detectors. Monocrystal boules of PGO and $Pb_5Ge_2SiO_{11}$ (abbreviated as PGSO here) have been grown by the Czochralski method.[3),5)] Takahashi et al.[6)] have succeeded in obtaining thick-film monocrystals with $0 \leq x \leq 1.5$, thin and wide enough to make pyroelectric infrared detector chips by the glass-recrystallization technique. The thickness of the crystals can be easily controlled by the amount of charged glass. The as-grown crystals themselves are possible to be directly used as detector elements; therefore, troublesome slicing and polishing processings are unnecessary. All it is required is to attach electrodes to the surface and the reverse side respectively, since the polar axis is perpendicular to the surface.

Only a few papers have referred to pyroelectricity of $Pb_5Ge_{3-x}Si_xO_{11}$. The study by Jones et al.[7)] is for the monocrystal of PGO prepared by the Czochralski method as well as the sintered body and that by Glass et al.[8)] for the glass-ceramics. Bordovskii et al.[9)] reported about pyrocurrents of the ceramics. For PGO and PGSO, together with TGS[10)] and $LiTaO_3$ (abbreviated as LT),[11)] commercially used as typical pyroelectric detector materials, Table 1 shows the pyroelectric coefficient $p=dP_s/dT$ (P_s: spontaneous polarization(C/cm^2); T(°K): temperature), the low frequency performance parameter p/c'_p

---

A part of this study was presented at the Annual Meeting of the Ceramic Society of JAPAN, May 1975.

(c_p'(J/cm^3°K): volume specific heat) and the high frequency performance parameter $p/\varepsilon c_p'$ (ε: dielectric constant). The values of these three parameters for PGO and PGSO are comparable to those of TGS and LT. Particularly, it is noted that the low frequency performance parameter of PGSO is largest among those four materials.

Table 1 The performances of the typical pyroelectric detectors.

Pyroelectric material	P [C/cm°K] x10^{-8}	P/c_p' [A·cm/W] x10^{-8}	$P/\varepsilon c_p'$ [A·cm/W] x10^{-10}	R_v* [V/W]
$Pb_5Ge_3O_{11}$	2.0	0.98	2.2	2.0
$Pb_5Ge_2SiO_{11}$	6.5	3.2	0.94	3.4
TGS	4	1.6	4.6	3.2
$LiTaO_3$	2.3	0.73	1.3	1.5

* When d=0.2mm, A=3.14mm^2, R=10MΩ, η=0.4 and f=14Hz

In this study are reported the results of the pyroelectric measurements of the PGO and PGSO thick-film monocrystals prepared by the glass-recrystallization, a very simple technique.

2. Experimental

Firstly the lead germanate silicate with the composition of $Pb_5Ge_3O_{11}$ and $Pb_5Ge_2SiO_{11}$ respectively was prepared, using Baker's Analyzed Reagent PbO, high-purity Eagle Picher GeO_2 and Aremco Products SiO_2 as starting materials. The polycrystalline powder of the materials with only one crystal phase was obtained by solid state reaction at 550°C for 100hr. Each powder of PGO and PGSO was melted in a gold crucible and held at 800-820°C for 20min., followed by being quenched in water for the former or poured on an aluminum plate for pressing with a domestic iron to make glass for the latter.

A few particles of the glasses were put on gold foil, remelted and then annealed at 600-720°C for recrystallization for 1-70hr., without being cooled down to room temperature, to give large hexagonal-shaped monocrystals up to 9mm in cross-section and 0.05 to 0.3mm in thickness,[6] which size is large enough to make an IR detector.

Prior to evaporation of Cr and Au on the as-grown crystal surface without slicing and polishing, the plate-like crystals were cut as large as 4x4mm^2 with a wire-saw. A front electrode was taken out of the Cr-Au evaporated surface and a back one from the gold foil.

Dielectric constant and dissipation factor were measured with the Hewlet-Packard automatic bridge, while spontaneous polarization and coercive field done with the Caborundum Sawyer-Tower circuit. For pyroelectric measurement, the surface was coated with black paint for sufficient IR absorption. For poling, DC bias of 3 times as large as the coercive field was applied to the samples parallel to the polar axis for a day. Pyroelectric voltage determination was carried out, using a 500°K blackbody IR source, a light chopper and the PAR-HR-8 lock-in amplifier.

3. Results and Discussion

From the results of back-reflection Laue photographs for the $Pb_5Ge_{3-x}Si_xO_{11}$ samples, the polar c-axis was found to be perpendicular to the surface; therefore, it is quite convenient for attachment of electrodes. The electrical and geometrical factors of the PGO and PGSO samples in this study are given in Table 2, where T_c: Curie temperature(°C), T_o(°C): paraelectric Curie temperature, C_o(°K): Curie constant, D(%): dissipation factor at 10kHz, ρ(MΩ cm): resistivity, E_c(kV/cm): coercive field, d(mm): thickness and A(mm^2): electrode area. The factors of ε_{33}, D, ρ, P_s and E_c are the values at room temperature. The temperature dependences of ε, D, P_s and E_c in the direction parallel to c-axis are shown in Fig.1 and Fig.2 respectively.

The above results show that the electrical properties of the PGO and PGSO samples in this study are quite comparable to those prepared by the Czochralski method.[3] Evidently the thick-film monocrystals of $Pb_5Ge_{3-x}Si_xO_{11}$ obtained by the glass-recrystallization, a quite simple technique, are sufficiently desirable in electrical properties.

The frequency dependences of responsivities R_v(V/W) of the PGO and the PGSO are shown in Fig.3. The difference in R_v between these two samples can be explained by using Putley's equation.[10]

$$R_v = \eta(\omega pAR/G)(1 + \omega^2\tau_E^2)^{-1/2}(1 + \omega^2\tau_T^2)^{-1/2} \qquad (1)$$

where η: the emmisivity of the electrode surface, ω(1/s): angular frequency($\omega=2\pi f$, f(1/s): frequency), R(Ω): the parallel resistance of the crystal-load circuit, G(W/°K): thermal conductance(G=Kd, K(W/m°K): thermal conductivity), τ_E(s): electrical time constant(τ_E=CR, C(F): the parallel capacitance of the crystal-load circuit), and τ_T(s): thermal time constant(τ_T=H/G, H(J/°K): heat capacity, H=c_p'Ad, $c_p'=c_pS$, c_p(J/kg°K): specific heat capacity, S(kg/m^3): density). Eq.(1) shows that R_v increases in proportion to f when $f<1/\tau_T$, varies as 1/f when $f>1/\tau_E$, and is constant in the intermediate frequency range; the variations of R_v's in Fig.3 are typical cases obeying this equation.

For the PGO and PGSO samples, the unknown values of η, S, c_p and K are estimated.

Table 2 Some properties of the thick-film PGO and PGSO monocrystals prepared by the glass-recrystallization technique.

	T_c [°C]	T_o [°C]	ε_{33} at R.T.	ε_{33} at T_c	C_o x10^4 [°K]	D [%]	ρ [MΩ·cm]	P_s [C/cm^2] x10^{-6}	E_c [KV/cm]	A [mm^2]	d [mm]	R_v [V/W]
$Pb_5Ge_3O_{11}$	178	173	44	820	0.69	0.3	13	3.5	11	2.09	0.146	2.50
$Pb_5Ge_2SiO_{11}$	45	32	340	720	1.5	3	0.18	1.5	6.4	1.92	0.265	2.99

ε_{33} at 10KHz, D at R.T. and 10KHz, ρ at R.T. and 10KHz, P_s at R.T., E_c at R.T. and R_v at R.T.

The magnitude of η assumed to be one when black paint is used. For S, the observed value of 7.33×10^3(kg/m^3) is used in the case of the PGO, while that of the PGSO (7.26×10^3) calculated from the observed lattice constants.[3] By the additivity law, the values of c_p are calculated from the observed ones of PbO, GeO_2 and SiO_2,[12] obtaining 2.78×10^2(J/kg°K) for PGO and 2.79×10^2 for PGSO respectively. The values of K(W/m°K) for PGO and PGSO, respectively, are presumed to be in the range 2.7-14 since K=2.77 for PbO[13] and 7.2-14 for SiO_2 quartz.[14]

Calculating $(\omega\tau_E)^2$ and $(\omega\tau_T)^2$ at 14Hz, respectively, using the above deduced and observed values in Table 1 and 2, we obtain $(\omega\tau_E)^2<<1$ and $(\omega\tau_T)^2>>1$ for the PGO and PGSO samples, and therefore, Eq.(1) is simplified as:

$$R_v = (\eta pR)/(c_p Sd) \qquad (2)$$

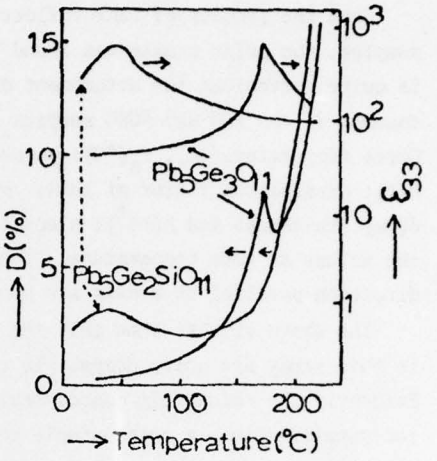

Fig. 1 The temperature dependences of the dielectric constant ε_{33} and dissipation factor D(%) for PGO and PGSO.

Hence, it is noted that R_v is independent of ω and G. If η=1, we obtain R_v= 6.7(V/W) for the PGO sample and 8.7 for the PGSO, respectively. Either of the observed R_v's is less than above calculated values, for it is thought that the effective η's might be

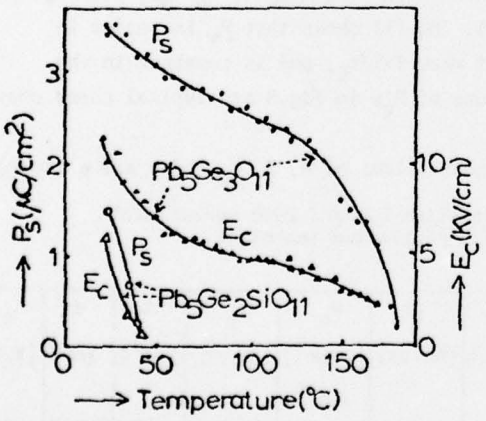

Fig. 2 The temperature dependences of the spontaneous polarization P_s(μC/cm^2) and coercive field E_c(kV/cm) for PGO and PGSO.

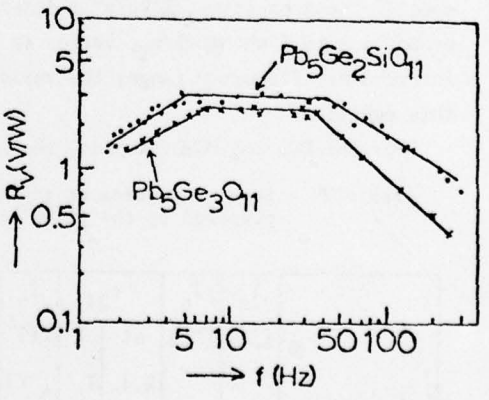

Fig. 3 The frequency dependence of the pyroelectric responsivity R_v(V/W) for the PGO and PGSO samples.

as small as 0.36<1. Expressing the ratio of R_v for the PGSO to that for the PGO as r, the observed r_{obs}= 1.2 agrees approximately with the calculated r_{cal}= 1.3 within the experimental errors. The reason why R_v(PGSO) is greater than R_v(PGO) is considered to result mainly from a larger pyroelectric coefficient for PGSO as indicated in Eq.(2).

In Table 1 are listed R_v's for the PGO and PGSO samples in comparison with the commercial pyroelectric detectors(TGS and LT) at the same geometry(d=0.2mm, A=3.14mm^2) and the same conditions(R=10MΩ, f=14Hz, η=0.4); wherein, it is evident that the pyroelectric performances of PGO and PGSO are comparable to those of the commercial detectors; furthermore, particularly PGO and PGSO are superior to TGS in chemical stability.

As a conclusion, as far as the glass-recrystallization technique is concerned, there are many advantages as follows; 1) This technique is quite simple, which requires no sophisticated and large-scale apparatus, 2) Crystal size obtained is good enough for a pyroelectric detector, 3) Thickness of as-grown crystal is thin enough to be directly used as a detector element and can be controlled by varying the amount of charged glass; thus, troublesome slicing and polishing processings become useless, 4) For $Pb_5Ge_{3-x}Si_xO_{11}$, the monocrystal of the desired composition can be prepared in the range $0 \leq x \leq 1.5$, moreover, it is convenient for a detector assembly that the polar axis is perpendicular to the crystal surface.

Acknowledgement

The authors are much indebted to Dr. Toshiaki Ohsaka(NIRIM) and Mr. Kazuyuki Kakegawa(Chiba Univ.) for valuable discussions, and Dr. Walter A. Schulze, Dr. Terry Cline, Mr. Brenneman(MRL), Mr. Kohji Ogura as well as Mr. Yasuji Masuda(NIRIM) for help with the experiments.

K. Takahashi was sent to the U.S.A. on Exchange Program sponsored by the Japanese Government.

References

1) S. Nanamatsu, H. Sugiyama, K. Doi and Y. Kondo, "Ferroelectricity in $Pb_5Ge_3O_{11}$", J. Phys. Soc. Japan 31, 616 (1971)

2) H. Iwasaki, K. Sugii, T. Yamada, N. Niizeki, "$5PbO \cdot 3GeO_2$ Crystal; a New Ferroelectric", Appl. Phys. Letters 18, 444 (1971)

3) H. Iwakaki, S. Miyazawa, H. Koizumi, K. Sugii and N. Niizeki, "Ferroelectric and Optical Properties of $Pb_5Ge_3O_{11}$ and its Isomorphous Compound $Pb_5Ge_2SiO_{11}$", J. Appl. Phys. 43, (12), 4907 (1972)

4) W. Eysel, R. W. Wolfe and R. E. Newnham, "$Pb_5(Ge,Si)_3O_{11}$ Ferroelectrics", J. Am. Ceram. Soc., 56, (4), 185 (1973)

5) K. Sugii, H. Iwasaki and S. Miyazawa, "Crystal Growth and Some Properties of $5PbO \cdot 3GeO_2$ Single Crystal", Mat. Res. Bull. 6, 503 (1971)

6) K. Takahashi, L. E. Cross and R. E. Newnham, "Glass-recrystallization of Ferroelectric $Pb_5Ge_3O_{11}$", Mat. Res. Bull. 10, 599 (1975)

7) G. R. Jones, N. Shaw and A. W. Verre, "Pyroelectric Properties of Lead Germanate", Electronics Letters, 8, (14), 345 (1972)

8) A. M. Glass, K. Nassau and J. W. Shiever, "Evolution of Ferroelctricity in Ultrafine-grained $Pb_5Ge_3O_{11}$ Crystallized from the glass", J. Appl. Phys. 48, (12) 5213 (1977)

9) G. A. Bordovskii, V. A. Izvochikov, V. T. Avanesyan, V. A. Bordovskii and K. L. Kozhevnikov, "Pyroelectric and Thermally Stimulated Currents in system $PbO-GeO_2$", Ferroelectrics, 18, 109 (1978)

10) E. H. Putley, "The Pyroelectric Detector", Semiconductors and Semimetals, vol.5, R. K. Williams and A. C. Beer, Editors (Academic Press, N. Y., 1970)

11) C. B. Roundy and R. L. Byer, "Sensitive $LiTaO_3$ Pyroelectric Detector", J. Appl. Phys. 44, (2) 929 (1973)

12) I. Barin and O. Knacke, Editors, "Thermochemical Properties of Inorganic Substances", (Springer-Verlag, N. Y., 1973)

13) C. T. Lynch, Editor, "Handbook of Material Science", vol.1, (1974), CRC Press, Ohio, USA.

14) "American Institute of Physics Handbook", 2nd Edition, McGraw-Hill, N. Y., (1963)

BASIC DISTRIBUTION LIST

Technical and Summary Reports April 1978

(12) Defense Documentation Center
Cameron Station
Alexandria, VA 22314

Office of Naval Research
Department of the Navy
800 N. Quincy Street
Arlington, VA 22217

ATTN: Code 471
Code 102
Code 470

Commanding Officer
Office of Naval Research
Branch Office
Building 114, Section D
666 Summer Street
Boston, MA 02210

Commanding Officer
Office of Naval Research
Branch Office
536 South Clark Street
Chicago, IL 60605

Office of Naval Research
San Francisco Area Office
One Hallidie Plaza Suite 601
San Francisco, CA 94102

Naval Research Laboratory
Washington, DC 20375

ATTN: Codes 6000
6100
6300
6400
2627

Naval Air Development Center
Code 302
Warminster, PA 18964
ATTN: Mr. F. S. Williams

Naval Air Propulsion Test Center
Trenton, NJ 08628
ATTN: Library

Naval Construction Batallion
Civil Engineering Laboratory
Port Hueneme, CA 93043
ATTN: Materials Division

Naval Electronics Laboratory
San Diego, CA 92152
ATTN: Electron Materials
Sciences Division

Naval Missile Center
Materials Consultant
Code 3312-1
Point Mugu, CA 92041

Naval Surface Weapons Center
White Oak Laboratory
Silver Spring, MD 20910
ATTN: Library

David W. Taylor Naval Ship
Research and Development Center
Materials Department
Annapolis, MD 21402

Naval Undersea Center
San Diego, CA 92132
ATTN: Library

Naval Underwater System Center
Newport, RI 02840
ATTN: Library

Naval Weapons Center
China Lake, CA 93555
ATTN: Library

Naval Postgraduate School
Monterey, CA 93940
ATTN: Mechanical Engineering
Department

BASIC DISTRIBUTION LIST (cont'd)

Naval Air Systems Command
Washington, DC 20360
ATTN: Codes 52031
52032

Naval Sea System Command
Washington, DC 20362
ATTN: Code 035

Naval Facilities Engineering Command
Alexandria, VA 22331
ATTN: Code 03

Scientific Advisor
Commandant of the Marine Corps
Washington, DC 20380
ATTN: Code AX

Naval Ship Engineering Center
Department of the Navy
Washington, DC 20360
ATTN: Code 6101

Army Research Office
P.O. Box 12211
Triangle Park, NC 27709
ATTN: Metallurgy & Ceramics Program

Army Materials and Mechanics Research Center
Watertown, MA 02172
ATTN: Research Programs Office

Air Force Office of Scientific Research
Bldg. 410
Bolling Air Force Base
Washington, DC 20332
ATTN: Chemical Science Directorate
Electronics & Solid State Sciences Directorate

Air Force Materials Laboratory
Wright-Patterson AFB
Dayton, OH 45433

Library
Building 50, Rm 134
Lawrence Radiation Laboratory
Berkeley, CA

NASA Headquarters
Washington, DC 20546
ATTN: Code RRM

NASA
Lewis Research Center
21000 Brookpark Road
Cleveland, OH 44135
ATTN: Library

National Bureau of Standards
Washington, DC 20234
ATTN: Metallurgy Division
Inorganic Materials Div.

Director Applied Physics Laboratory
University of Washington
1013 Northeast Forthieth Street
Seattle, WA 98105

Defense Metals and Ceramics Information Center
Battelle Memorial Institute
505 King Avenue
Columbus, OH 43201

Metals and Ceramics Division
Oak Ridge National Laboratory
P.O. Box X
Oak Ridge, TN 37380

Los Alamos Scientific Laboratory
P.O. Box 1663
Los Alamos, NM 87544
ATTN: Report Librarian

Argonne National Laboratory
Metallurgy Division
P.O. Box 229
Lemont, IL 60439

Brookhaven National Laboratory
Technical Information Division
Upton, Long Island
New York 11973
ATTN: Research Library

Office of Naval Research
Branch Office
1030 East Green Street
Pasadena, CA 91106

SUPPLEMENTARY DISTRIBUTION LIST October 1977

Technical and Summary Reports

Dr. W.F. Adler
Effects Technology Inc.
5383 Hollister Avenue
P.O. Box 30400
Santa Barbara, CA 92105

Dr. G. Bansal
Battelle
505 King Avenue
Columbus, OH 43201

Dr. R. Bratton
Westinghouse Research Lab.
Pittsburgh, PA 15235

Dr. A.G. Evans
Rockwell International
P.O. Box 1085
1049 Camino Dos Rios
Thousand Oaks, CA 91360

Mr. E. Fisher
Ford Motor Co.
Dearborn, MI

Dr. P. Gielisse
University of Rhode Island
Kingston, RI 02881

Dr. M.E. Gulden
International Harvester Company
Solar Division
2200 Pacific Highway
San Diego, CA 92138

Dr. D.P.H. Hasselman
Montana Energy and MHD Research
and Development Institute
P.O. Box 3809
Butte, Montana 59701

Mr. G. Hayes
Naval Weapons Center
China Lake, CA 93555

Professor A.H. Heuer
Case Western Reserve University
University Circle
Cleveland, OH 44106

Dr. R. Hoagland
Battelle
505 King Avenue
Columbus, OH 43201

Dr. R. Jaffee
Electric Power Research Institute
Palo Alto, CA

Dr. P. Jorgensen
Stanford Research Institute
Poulter Laboratory
Menlo Park, CA 94025

Dr. R.N. Katz
Army Materials and Mechanics
Research Center
Watertown, MA 02171

Dr. H. Kirchner
Ceramic Finishing Company
P.O. Box 498
State College, PA 16801

Dr. B. Koepke
Honeywell, Inc.
Corporate Research Center
500 Washington Avenue, South
Hopkins, MN 55343

Mr. Frank Koubek
Naval Surface Weapons Center
White Oak Laboratory
Silver Spring, MD 20910

E. Krafft
Carborundum Co.
Niagara Falls, NY

SUPPLEMENTARY DISTRIBUTION LIST (Cont'd) October 1977

Dr. F.F. Lange
Rockwell International
P.O. Box 1085
1049 Camino Dos Rios
Thousand Oaks, CA 91360

Dr. J. Lankford
Southwest Research Institute
8500 Culebra Road
San Antonio, TX 78284

Library
Norton Company
Industrial Ceramics Division
Worcester, MA 01606

State University of New York
College of Ceramics at Alfred University
Attn: Library
Alfred, NY 14802

Dr. L. Hench
University of Florida
Ceramics Division
Gainesville, FL 32601

Dr. N. MacMillan
Materials Research Laboratory
Pennsylvania State University
College Park, PA 16802

Mr. F. Markarian
Naval Weapons Center
China Lake, CA 93555

Dr. Perry A. Miles
Raytheon Company
Research Division
28 Seyon Street
Waltham, MA 02154

Mr. R. Rice
Naval Research Laboratory
Code 6360
Washington, D.C. 20375

Dr. Robert C. Pohanka
Room 619, Ballston Tower
800 N. Quincy Street
Arlington, VA 22217

Dr. J. Ritter
University of Massachusetts
Department of Mechanical Engineering
Amherst, MA 01002

Professor R. Roy
Pennsylvania State University
Materials Research Laboratory
University Park, PA 16802

Dr. R. Ruh
AFML
Wright-Patterson AFB
Dayton, OH 45433

Mr. J. Schuldies
AiResearch
Phoenix, AZ

Professor G. Sines
University of California, Los Angeles
Los Angeles, CA 90024

Dr. N. Tallan
AFML
Wright-Patterson AFB
Dayton, OH 45433

Dr. T. Vasilos
AVCO Corporation
Research and Advanced Development Division
201 Lowell Street
Wilmington, MA 01887

Mr. J.D. Walton
Engineering Experiment Station
Georgia Institute of Technology
Atlanta, GA 30332

Dr. S.M. Widerhorn
Inorganic Materials Division
National Bureau of Standards
Washington, DC 20234

SUPPLEMENTARY DISTRIBUTION LIST (Cont'd) October 1977

Dr. S.A. Bortz
IITRI
10 W. 35th Street
Chicago, IL 60616

Mr. G. Schmitt
Air Force Materials Laboratory
Wright-Patterson AFB
Dayton, OH 45433

Dr. D.A. Shockey
Stanford Research Institute
Poulter Laboratory
Menlo Park, CA 94025

Dr. W.G.D. Frederick
Air Force Materials Laboratory
Wright-Patterson AFB
Dayton, OH 45433

Dr. P. Land
Air Force Materials Laboratory
Wright-Patterson AFB
Dayton, OH 45433

Mr. K. Letson
Redstone Arsenal
Huntsville, AL 35809

Dr. S. Freiman
Naval Research Laboratory
Code 6363
Washington, DC 20375

Director
Materials Sciences
Defense Advanced Research Projects Agency
1400 Wilson Boulevard
Arlington, VA 22209

Dr. James Pappis
Raytheon Company
Research Division
28 Seyon Street
Waltham, MA 02154

Major W. Simmons
Air Force Office of Scientific Research
Building 410
Bolling Air Force Base
Washington, DC 20332

Dr. P. Becher
Naval Research Laboratory
Code 6362
Washington, DC 20375

Mr. L.B. Weckesser
Applied Physics Laboratory
Johns Hopkins Road
Laurel, MD 20810

Mr. D. Richarson
AiResearch Manufacturing Company
4023 36th Street
P.O. Box 5217
Phoenix, AZ 85010

Dr. H.E. Bennett
Naval Weapons Center
Code 3818
China Lake, CA 93555

Mr. G. Denman
Air Force Materials Laboratory
Code LPJ
Wright-Patterson AFB
Dayton, OH 45433

Dr. D. Godfrey
Admiralty Materials Laboratory
Polle, Dorset BH16 6JU
UNITED KINGDOM

Dr. N. Corney
Ministry of Defense
The Adelphi
John Adam Street
London WC2N 6BB
UNITED KINGDOM

SUPPLEMENTARY DISTRIBUTION LIST (Cont'd)

Dr. L.M. Gillin
Aeronautical Research Laboratory
PO Box 4331
Fisherman's Bend
Melbourne, VIC 3001, AUSTRALIA

Dr. G. Ewell
MS6-D163
Hughes Aircraft Co.
Centinela and Teale Streets
Culver City, CA 90230

Dr. R.E. Tressler
Ceramic Science Section
226 Steidle Bldg
The Pennsylvania State Univ.
University Park, PA 16802

Dr. R.E. Newnham
Materials Research Laboratory
The Pennsylvania State Univ.
University Park, PA 16802

Dr. K.D. McHenry
Honeywell, Inc.
Corporate Technology Center
10701 Lyndale Avenue South
Bloomington, MN 55420

Dr. R.A. Queeney
Prof. Engr. Mech.
Hammond Bldg
The Pennsylvania State Univ.
University Park, PA 16802

Dr. George W. Taylor
Princeton Resources, Inc.
PO Box 211
Princeton, NJ 08540

Dr. Herb Moss
RCA Laboratories
Princeton, NJ 08540